Workshop of

Experimental Nuclear and Particle Physics

2017

14.–21. 01. 2017, Bílý Potok

Faculty of Nuclear Sciences and Physical Engineering
Czech Technical University in Prague

Workshop of Experimental Nuclear and Particle Physics 2017
Editors: J. Cimerman, K. Kohoutová, R. Lavička, R. Novotný
Issued by: Czech Technical University in Prague
Faculty of Nuclear Sciences and Physical Engineering
Address: KF FJFI ČVUT, Břehová 7, 115 19 Praha 1
novotr14@fjfi.cvut.cz, +420731891801
Available at http://wejcf2017.ejcf.cz/wejcf2017_proceedings.pdf
First edition. 162 pages.

Contents

Foreword

This year, for the 11^{th} time, students, graduates, and teachers from the field of Experimental Nuclear and Particle Physics at FNSPE CTU met at the annual winter workshop. The meeting was held during the week of 14.–21. 01. 2017 at *Penzion Krakonoš* in the Jizera Mountains in the Czech Republic. The main goal of the workshop is to follow the progress of students, discuss problems and experiences and also to get to know each other better. Each participant gave a talk about their work or progress during the previous year. Extended abstracts of these talks are published in the proceedings you are holding now.

Editors

ALGORITHMS OF JET RECONSTRUCTION

Veronika Agafonova*

Faculty of Nuclear Sciences and Physical Engineering, Brehova 7, Prague, Czech Republic

* corresponding author: v.d.agafonova@gmail.com

Abstract. The nuclear-nuclear collisions at energies attainable on the accelerator RHIC in BNL in the United States are an ideal environment to study nuclear matter under extreme conditions of high temperature and energy density. One of the most important probes of the nuclear matter is studying the production of jets. There are different algorithms for their identification which can be divided into two types: cone jet finding algorithms and cluster type jet finding algorithms. In this paper the second type of jet reconstruction algorithms will be described and its advantages and disadvantages will be discussed.

Keywords: jet, jet reconstruction, algorithm.

1. Introduction

The central concepts in the discussions of the QCD aspects of high energy collisions are quarks and gluons (or partons). Because of the inability to observe partons, jets are measured instead. A jet is a narrow cone of hadrons and other particles produced by the hadronization of a quark or gluon in particle physics or heavy ion experiment (Fig.1). Jets are measured in particle detectors and studied in order to determine the properties of the original quarks. They are also very important in analysing data from hadronic colliders.

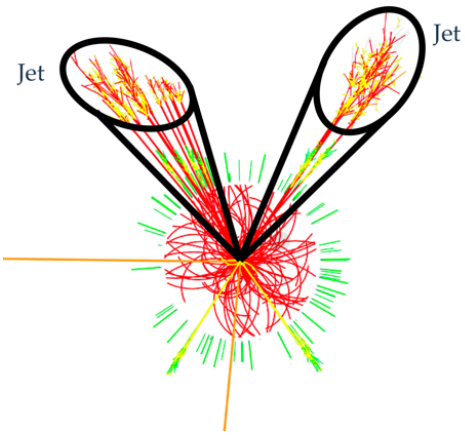

Figure 1: An example of jet.

There are two types of jets: regular or "soft-resilient" and less regular or "soft-adaptable". Having a regular jet can simplify some theoretical calculations as well as eliminate some parts of the momentum resolution loss caused by underlying event (UE) and pile-up contamination. Meanwhile, in the second type an infrared and collinear (IRC) safe algorithm can stimulate irregularities in the boundary of the final jet.

To reconstruct jets different algorithms are used. Jet finding algorithms can be divided into two types: cone jet-finders and sequential-clustering jet-finders.

In this paper the cluster jet finding algorithms will be described. In addition, the FastJet packagery will be briefly introduced.

2. Cluster type jet finding algorithms

Cluster-type jet algorithms are based on successive pair-wise recombination of particles. They are infrared safe. The wide usage of sequential-clustering jet algorithms on the different accelerators, such as Tevatron in Fermilab and the LHC at CERN, led to intense discussions concerning the advantages of various types of jet algorithms. One part of the discussion has concentrated on the merits of sequential recombination (k_t and Cambridge/Aachen) and cone algorithms, another has centered on anti-k_t jet-finder. The difference between the k_t and cone methods is in their sensitivity to non-perturbative effects like hadronization and underlying event (UE) contamination.

Two types of distances are defined in jet-finding algorithms. The first is the distance d_{ij} between entities i and j. The second one is the distance d_{iB} between the particle i and the beam B. These distances are defined as follows

$$d_{ij} = \min(k_{ti}^{2p}, k_{tj}^{2p}) \frac{\Delta_{ij}^2}{R^2}, \tag{1}$$

$$d_{iB} = k_{ti}^{2p}, \tag{2}$$

where $\Delta_{ij}^2 = (y_i - y_j)^2 + (\phi_i - \phi_j)^2$ and k_{ti}, y_i, ϕ_i and R are the transverse momentum, rapidity, azimuth and radius parameter of particle i respectively. A parameter p is used to take control of the relative power of the energy versus geometrical (Δ_{ij}) scales.

The algorithm identifies d_{min}, the smallest of the distances, and if it is d_{ij} then it recombines the entities i and j, otherwise, if the smallest distance is d_{iB}, it

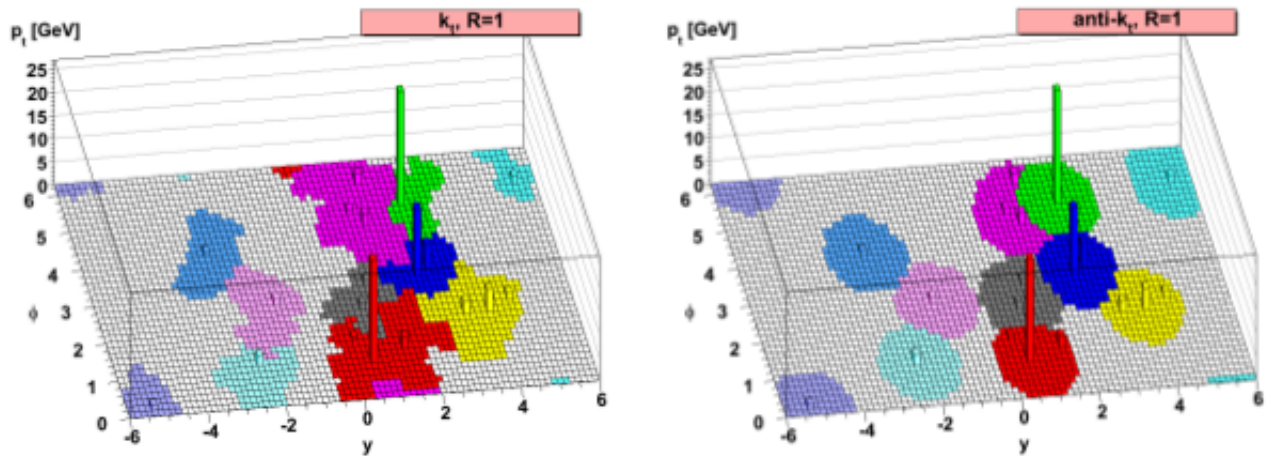

Figure 2: A sample parton-level event generated with Herwig clustered with the k_T and anti-k_T algorithms [1].

calls i a jet and removes it from the list. The procedure is repeated until no particles are left.

Depending on the parameter p the algorithms are divided into three types: k_t, anti-k_t and Cambridge/Aachen algorithm. Hereafter, the first two algorithms will be described in more detail.

2.1. k_T ALGORITHM

For this type of jet finding algorithm $p = 1$. After finding the minimum distance d_{min} between all the d_{ij} (1) and d_{iB} (2) there could be two situations: $d_{min} = d_{ij}$ or $d_{min} = d_{iB}$.

In the first case, the particles i and j are merged, summing their four-momenta. In the second one, a particle is declared to be a final jet and next is removed from the list.

This algorithm has its advantages and disadvantages. The first advantage is the explicit imitation of a walk through the QCD branching sequence. This means, that the largest part of the particles radiated from an original hard parton is clustered in the reconstructed jets. That gives better particle mass measurements, general kinematic reconstruction and gaps-between-jets identification. The second advantage of the k_T algorithm is jet disintegration into constituent subjets. That is useful for identifying decay products of fast-moving heavy particles. The main disadvantage of the k_T jet-finder is its algorithmic slowness: to cluster N particles into jets requires $\mathcal{O}(N^3)$ operations. For instance, the cluster time would grow to an unsustainable $\mathcal{O}(10^5 s)$, i.e more than a day, for a typical heavy-ion event at the LHC, $N = \mathcal{O}(50000)$. That is why the k_t jet-finder slowness has been one of the instigating factors behind proposals for alternative algorithms. The second disadvantage is the sensitivity of the jet-finder to a background in comparison with the other algorithms. Therefore, the k_T jet finding algorithm is mostly used for the background subtraction.

2.2. ANTI-k_T ALGORITHM

For this type of jet finding algorithm $p = -1$. The behaviour of the anti-k_t algorithm can be explained on the event containing a few well-separated hard particles with transverse momenta k_1, k_2, ... and many soft particles. In contradiction to the k_T jet-finder, the hardest particle is found first and after that the algorithm searches for the distances between the hard particle "1" and soft particles. These lengths are defined only by the hard particle's transverse momentum and the Δ_{1i} separation. The shape of the final jet depends on the distance between the two hard particles.

In case there are no other hard particles within a distance of $2R$ from the given hard particle, the hard particle that does not have any other hard particles around itself within a distance of $2R$ from it will easily collect all the soft particles within a circle radius R. The result will be a perfect conical jet. If $k_{t1} \gg k_{t2}$, the first jet will have a conical shape and the second jet will be partly conical since it will miss the part crossing the first jet. If $k_{t1} = k_{t2}$, neither of two jets will be conical and the overlying area will be easily divided by a straight line into the two equal parts. In general state, when $k_{t1} \sim k_{t2}$, a boundary b defined as $\Delta R_{1b}/k_{t1} = \Delta_{2b}/k_{t2}$ will be pruned both of cones.

In case $\Delta_{12} < R$ two particles will cluster to form a single jet. If $k_{t1} \gg k_{t2}$, it will be a conical jet centered around k_1. If $k_{t1} \sim k_{t2}$, it will be the union of cones with radius $< R$ around each hard particle plus one cone with radius R centered on the final jet.

Fig.2 shows the behaviour of the k_T and anti-k_T algorithms. A parton-level event was taken together with $\sim 10^4$ random ghost particles and then clustered with four different algorithms. It can be seen that the pair of jets near $y = 2$ and $\phi = 5$ presents an interesting example in the respect of jet shapes. The left-handed one is much softer than the right-hand one. Also the k_t has irregular boundary between jets, while the anti-k_t have circular generated hard jet, which

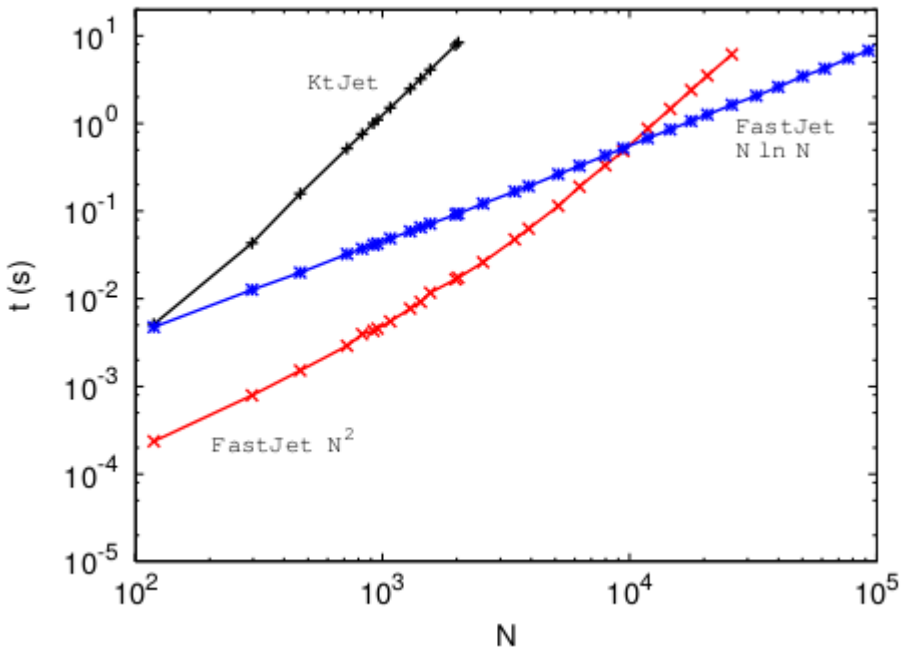

Figure 3: The running times of k_T jet-finder and FastJet implementations of the k_T clustering algorithm versus the number of initial particles [2].

trims a lens-shaped region out of the soft one, leaving behind a crescent.

Area related properties

There are two types of jet areas: passive and active. The first type measures jet's susceptibility to point-like radiation. The second one measures its susceptibility to diffuse radiation. The passive area $a_{JA,R}(\Delta_{12})$ in usual IRC safe jet algorithms (JA) is πR^2 only when $\Delta_{12} = 0$, but when Δ_{12} is increased, it changes. For comparison, the passive area of anti-k_T jets is always independent of Δ_{12}: $a_{anti-k_T,R}(\Delta_{12}) = \pi R^2$, since its boundaries are unaffected by soft radiation. For the anti-k_T algorithm also applies that the passive and active areas are identical.

Back reaction

Suppose one has a hard scattering event that leads to a set of jets $\{J_i\}$. After adding a soft event (UE, pile up) and rerunning the algorithm one gets a set of jets $\{\widetilde{J}_i\}$ that differ in two ways. First of all, the soft energy will be added to each jet. Secondly, there could be a change of the distribution of the particles from the hard event: in case a $\widetilde{J}_i$ that is close to the original J_1 will be found, then two jets will not consist from the same subset of particles from the original hard event. This is called "back reaction".

It can be shown for the anti-k_T algorithm that the back reaction probability is suppressed not by the amount of back reaction itself, but by the transverse momentum of the jet, p_t, that leads to a much smaller effect.

3. FastJet

FastJet is a software package where most of jet finding algorithms are implemented. Identifying each particles geometrical nearest neighbour with a help of a Voronoi diagram and a Delaunay triangulation it isolates the geometrical aspects of the problem. Due to this, the FastJet requires only $\mathcal{O}(N \ln N)$ operations versus the k_t jet-finder. Fig.3 compares the running time of the FastJet with the k_t jet-finder.

4. Conclusion

In this paper the cluster type jet finding algorithms were discussed. As it was shown the anti-k_T jet-finder is the most used algorithm because of its insensitivity to a background and ability to reconstruct perfect conical or partly conical jets. However, the k_T jet-finder that is sensitive to a background is also widely used, but mostly for the background subtraction. The reduce of the k_t algorithm complexity from N^3 to $N \ln N$ operations opens up the previously unconvincing usage of the k_t jet-finder for the large values of N that rise when considering all cells of a finely segmented calorimeter and for heavy-ion events.

References

[1] G. S. Matteo Cacciari, Gavin P. Salam. The anti-kt jet clustering algorithm. *JHEP* 2008.

[2] G. P. S. Matteo Cacciari. Dispelling the n^3 myth for the k_t jet-finder. *Phys Lett* 2006.

ENTANGLED PHOTONS AND THEIR INTERACTION WITH BIOLOGICAL STRUCTURES

Elisabeth Andriantsarazo[a,*]

[a] *FNSPE CTU, Brehova 7, Praha 1, Czech republic*

[b] *FNSPE CTU, Brehova 7, Praha 1, Czech republic*

[*] corresponding author: andrieli@fjfi.cvut

Abstract. Is quantum mechanics consistent with so called Local hidden variable theories (LHVT) that Einstein, Podolsky and Rosen (EPR) came up with? John S. Bell provided us with a way to experimentally confirm or reject the idea of hidden variables via his Bell inequalities. By simple probabilistic theory arguments he mathematically reformulated EPR Gedankenexperiment and showed that certain correlation measure cannot exceed particular value if some LHVT was describing our world better than quantum mechanics. Certain systems (for example Bell states) permitted greater values providing us with a conclusion that quantum mechanics describes our world more accurately than any LHVT. In our experiment we want to create and measure quantum entangled states and make them interact with biological structures. These interactions are going to be further explored.

Keywords: Quantum entanglement, Bell states, Bell inequalities.

1. Introduction

In 1935 Einstein, Podolsky and Rosen (EPR) brought a paradox considering quantum entanglement to wider attention. Entangled state of two particles can be written as follows:

$$|\phi\rangle = \frac{1}{\sqrt{2}}(|01\rangle - |10\rangle) \tag{1}$$

which shows that the state of one particle cannot be written without referring to the state of the second particle. Provided these particles were one light year apart, as soon as we measure one of the particles, we would immediately know the state of the second particle. This nonlocal actions at a distance would immediately happen, no matter how distant the entangled particles were and such fact is not only paradoxical but also seems to defy the laws of relativity. EPR pointed this out, hence the EPR paradox. Local realistic theories were explored by an Irish physicist John Stewart Bell in 1964. He stated that the class of local realistic theories could never be consistent with quantum mechanics which was mathematically formalized in what is called Bell inequalities nowadays. These inequalities are a way not only to decide which theory gives better prediction, but also to show the presence of quantum entangled particles.

2. Setup

The aim is to create entangled photons and to detect the entanglement. Using the two nonlinear beta barium borate (BBO) crystals with identical optical axes rotated by 90° with respect to the other the creation of entangled photon pairs is achieved thanks to a process called Spontaneous parametric down-conversion (SPDC).

Experimental setup used for production of polarization-entangled photons is shown on 1. The laser diode produces monochromatic ultraviolet beam (405 nm) which traverses through a polarizer (which linearly polarize the laser beam at an angle θ from the vertical) and a birefringent plate (that shifts the phase of one polarization component). This makes the photons reaching the pair of BBO crystals circular polarized so that as many incoming photons as possible are observed by the crystals and then spontaneously down-converted. Original light beam is then stopped by a beam stopper but the downconverted photons emerge on opposite sides at the same time and reach the mirrors which reflect them to the detectors, two single-photon counting modules. These detectors are both preceded by linear polarizers to block any scattered light. To detect the photon pair coincidence detection unit is used to select entangled photon pairs from the background.

3. Spontaneous parametric down-conversion

SPDC is one of the simplest ways to create polarization correlated photons. This method is easily available at laboratory thanks to modern diode laser technology and avalanche photodiodes that are able to register single photons. This process is generated spontaneously, hence the name. The photon that downconvertes and creates correlated pair is called pump (γ_p). Splitting of the γ_p occurs in accordance with conservation law and requires γ_p to be partially or fully polarized in an extraordinary direction relative to the crystal's optical axis. SPDC has two different varieties. We use what is called Type-I which means both outgoing photons are ordinary in their polariza-

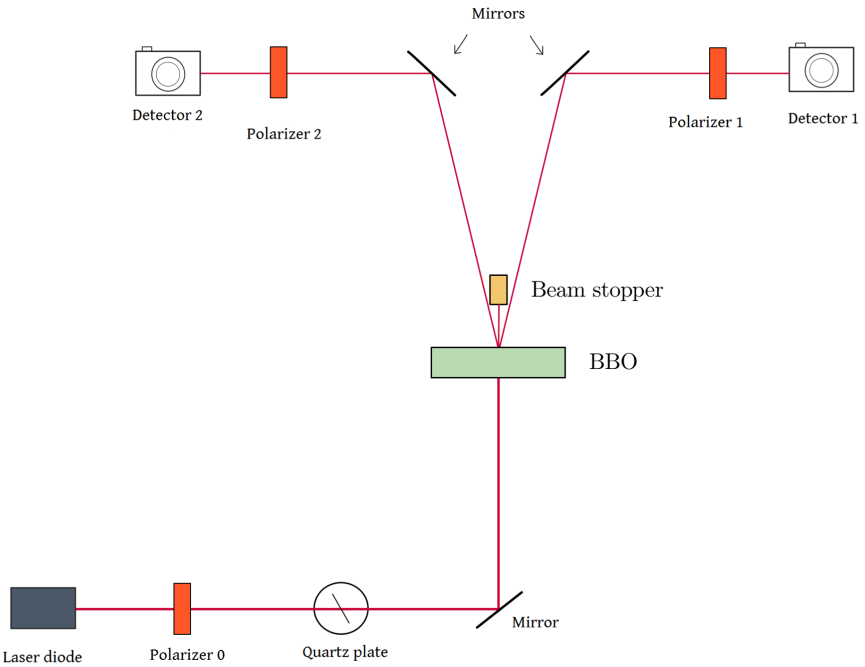

Figure 1: Schematic of our experimental setup.

tion. Plus their polarization is orthogonal to that of the γ_p. Emerging photons are for historical reasons called signal and idler (γ_s, γ_i). As previously said two BBO crystals are used in our alignment. That is because γ_p is seen as a superposition of ordinary and extraordinary polarizations until it interacts with one of the crystals. So the SPDC may occur if one of the crystals observes an extraordinary pump.

4. Detection of entangled states

Once the pump photon downconverts to idler and signal photon following state can be described as follows:

$$|\phi\rangle = \frac{1}{\sqrt{2}}(|V\rangle_s|V\rangle_i + |H\rangle_s|H\rangle_i), \tag{2}$$

where $|V\rangle$ is vertical and $|H\rangle$ is horizontal polarization state. Subscript s/i is for signal/idler photon respectively. Let's say the polarization plane of polarizer 0 was rotated by α. The previous description of state $|\phi\rangle$ can be rewritten as follows:

$$|\phi\rangle = \frac{1}{\sqrt{2}}(|V_\alpha\rangle_s|V_\alpha\rangle_i + |H_\alpha\rangle_s|H_\alpha\rangle_i). \tag{3}$$

In our setup polarizers 1 and 2 are placed in the signal and idler paths. The first polarizer is rotated by angle α and the second by angle β. We measure the polarization of downconverted photons by placing these rotated polarizers and the probability of such coincidence detection for both photons vertical is then given by:

$$P_{VV}(\alpha, \beta) = |\langle V_\alpha|_s \langle V_\beta|_i |\psi_{DC}\rangle|^2, \tag{4}$$

where $|\psi_{DC}\rangle$ is the state of downconverted photons emerging from BBO crystals. For any pair of polarizer angles (α, β) there are four possible outcomes $V_\alpha V_\beta, V_\alpha H_\beta, H_\alpha V_\beta, H_\alpha H_\beta$. By placing all these outcomes in following expression

$$E = P_{VV}(\alpha, \beta) + P_{HH}(\alpha, \beta) - P_{VH}(\alpha, \beta) - P_{HV}(\alpha, \beta) \tag{5}$$

we calculate

$$S = E(\alpha, \beta) - E(\alpha, \beta') + E(\alpha', \beta) + E(\alpha', \beta'). \tag{6}$$

For arbitrary $\alpha, \alpha', \beta, \beta'$ Clauser, Horne, Shimony and Holt proved following Bell inequality:

$$|S| \leq 2. \tag{7}$$

5. Conclusions

We described how photon entanglement is created in laboratory and how we detect it. Subsequent plan is to make the polarizer 1 and 2 fully automatic. That's because it won't be necessary for us to lift the cover of our experiment that provides us with complete darkness every time we want to change the angle. Furthermore we plan to add biological structures such as microtubules or unicellular organisms in the paths of γ_s, γ_i to see how the entangled pair is going to interact with them.

Acknowledgements

References

MASS COMPOSITION, ENERGY SPECTRUM AND PROPAGATION OF ULTRA-HIGH ENERGY COSMIC RAYS

Alena Bakalová*

Faculty of Nuclear Science and Physical Engineering, Czech Technical University, Břehová 7, Prague, Czech Republic

* corresponding author: bakalale@fjfi.cvut.cz

Abstract. The origin of cosmic ray particles of ultra high energies is still unknown and is a subject of current research. While cosmic ray particles propagate through the universe they lose energy and are also subjected to nuclear transformation due to photodisintegration. By measurement of the cosmic ray showers created in the Earth's atmosphere we are able to reconstruct the maximum of the shower development X_{max}, which is sensitive to the mass composition of the primary particles. Interpretation of recent data from fluorescence detectors indicates that for the highest energies the combined mass spectrum of primary particles shifts towards higher nuclear mass numbers. The shower universality is a promising method to study mass composition with surface detectors.

Keywords: cosmic rays, mass composition, shower universality.

1. Introduction

It is more than hundred years since the discovery of cosmic rays and more than fifty years after the discovery of cosmic rays of ultra high energies, yet the origin of these most energetic particles with energies $E > 10^{18}$ eV is still unknown. Since the energy spectrum of cosmic rays decreases approximately as E^{-3}, the most energetic events are very rare. When a primary cosmic ray particle penetrates into the Earth's atmosphere, it interacts with air nuclei and a shower of secondary particles is created. Therefore observatories of large areas are constructed in order to study the cosmic ray physics, such as The Pierre Auger Observatory in Argentina covering an area of 3000 km^2 [1] or Telescope Array in the USA with detectors distributed across 762 km^2 [2].

2. Mass composition

The shower maximum X_{max} is one of the most sensitive quantities to the mass composition of primary particles. It can be reconstructed from the signal of fluorescence detectors [1]. Such reconstruction has a strong disadvantage, namely it can not be used at all times, but only when there is minimal background light. This was a motivation for the invention of a new procedure to reconstruct shower maxima, which would use only information from surface detectors. It is interesting because it can increase the statistics for mass composition studies. Such a procedure was recently presented in [3, 4]. This reconstruction procedure, called shower universality, considers the four components of the detected shower

(1.) the muonic component,

(2.) the electromagnetic component originating from muon interactions and muon decay,

(3.) the purely electromagnetic component and

(4.) jet component, which is the electromagnetic component from low-energy hadrons [4].

A shower is characterized by its energy E, shower maximum X_{max}, zenith angle θ, air density on the ground ρ^{air}_{ground} and number of muons N_μ. The signal induced in surface detectors is then parametrized as

$$S(r,\Psi|E,X_{max},N_{mu},\theta,\rho^{air}_{ground}) = \sum_{i=1,..,4} S^i_0(r,\Delta X|E)\cdot f^i mod(r,\Psi|\theta) \cdot f^i_{atm}(r|\rho^{air}_{ground})\cdot f^i_{conv}(r,\Delta X,\Psi|\theta) \cdot f^i_{N_\mu fluc}(r|N_\mu), \quad (1)$$

where ΔX depends on the set of parameters (r,Ψ,θ,X_{max}) and i refers to the four electromagnetic components of the shower [4]. Successive terms in the sum correspond to the signal released by an ideal detector, correction for atmospheric effects, conversion factor for a realistic detector and a factor expressing fluctuations in muon number N_μ.

In Figure 1 the energy dependence of the mean shower maximum is reconstructed using fluorescence detectors [5]. We can see that the mass composition shifts towards heavier primary particles with increasing energy. For the highest energies, there are no data shown due to small statistics. If we were to use the shower universality reconstruction, the statistics would grow and we could see if the behavior is similar even for the highest energies.

We made simulations of cosmic ray showers in CONEX [6, 7] for four types of primary particles and energies from 10^{14} eV to 10^{20} eV and two models of hadronic interactions EPOS-LHC [8, 9] and QGSJet

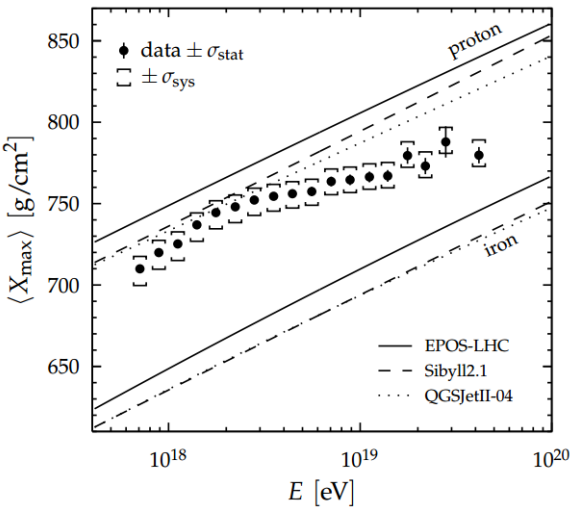

Figure 1: Energy dependence of the mean value of shower maxima measured by fluorescence detectors compared with predictions of different hadronic interaction models [5].

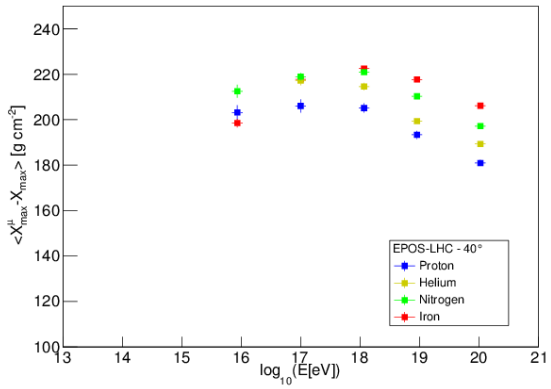

Figure 2: Energy dependence of the mean value of difference between muon maximum X^{μ}_{max} and shower maximum X_{max} for EPOS-LHC and zenith angle 40°.

II-04 [10]. We defined the muon maximum X^{μ}_{max} as the atmospheric depth, where the shower contains the highest number of muons above an energy of 1 GeV. The energy dependence of the mean value of the difference between muon maximum and shower maximum is shown in Figure 2 for EPOS-LHC and zenith angle 40°. We can see that for the highest energies this quantity is clearly dependent on mass composition of primary particles. For the lowest energies there are no data shown due to applied cuts and subsequent small statistics. Similar behavior was found for zenith angles 0° and 60° and for QGSJet II-04. Moreover the mean value of $X^{\mu}_{max} - X_{max}$ was found to be only weakly model dependent. This quantity is not measurable at this time, but it would be interesting to include such an observable (or a similar one that can be measured - MPD [11]) into mass composition studies in future projects, which would allow such reconstruction.

3. Conclusions

We plan to analyse the surface detector data from the Pierre Auger Observatory and apply new means of shower maximum reconstruction, using shower universality for the reconstruction. Comparing the mean values of shower maximum with hadronic interaction models, it seems that the ultra-high energy cosmic ray particles become heavier with increasing energy. In our next work we will be developing models for placement of sources of cosmic rays of ultra-high energies in simulation program CRPropa3 [12], so that the results from simulations would be in an agreement with the energy spectrum and mass composition observed at the Pierre Auger Observatory.

References

[1] The Pierre Auger Collaboration. The Pierre Auger Cosmic Ray Observatory. *NIMA* **798**:172–213, 2015.

[2] H. Kawai, et al. Telescope Array Experiment. *Nuclear Physics B Proceedings Supplements* **175**:221–226, 2008.

[3] M. Ave, et al. A generalized description of the time dependent signals in extensive air shower detectors and its applications. *Astroparticle Physics* **88**:46–59, 2017.

[4] M. Ave, et al. A generalized description of the signal size in extensive air shower detectors and its applications. *Astroparticle Physics* **87**:23–39, 2017.

[5] The Pierre Auger Collaboration. Depth of maximum of air-shower profiles at the Pierre Auger Observatory. I. Measurements at energies above $10^{17.8}$ eV. *Physical Review D* **90**(12):122005, 2014. 1409.4809.

[6] T. Bergmann, et al. One-dimensional hybrid approach to extensive air shower simulation. *Astroparticle Physics* **26**:420–432, 2007. astro-ph/0606564.

[7] T. Pierog, et al. First results of fast one-dimensional hybrid simulation of EAS using CONEX. *Nuclear Physics B Proceedings Supplements* **151**:159–162, 2006. astro-ph/0411260.

[8] S. A. Bass, et al. Microscopic models for ultrarelativistic heavy ion collisions. *Progress in Particle and Nuclear Physics* **41**:255–369, 1998. nucl-th/9803035.

[9] M. Bleicher, et al. Relativistic hadron-hadron collisions in the ultra-relativistic quantum molecular dynamics model. *Journal of Physics G Nuclear Physics* **25**:1859–1896, 1999. hep-ph/9909407.

[10] S. Ostapchenko. Monte Carlo treatment of hadronic interactions in enhanced Pomeron scheme: QGSJET-II model. *Physical Review D* **83**(1):014018, 2011. 1010.1869.

[11] The Pierre Auger Collaboration. Muons in air showers at the Pierre Auger Observatory: Measurement of atmospheric production depth. *Physical Review D* **92**(1):019903, 2015.

[12] R. Alves Batista, et al. CRPropa 3-a public astrophysical simulation framework for propagating extraterrestrial ultra-high energy particles. *Journal of Cosmology and Astroparticle Physics* **5**:038, 2016. 1603.07142.

STUDY OF DIFFRACTION PROCESSES AT LHC

Dagmar Bendova*

FNSPE CTU, Brehova 7, Praha 1, Czech republic

* corresponding author: Dagmar.Bendova@fjfi.cvut.cz

Abstract. Diffraction processes represent a large contribution to the total inelastic cross-section in proton- proton collision. It is therefore very important to understand these processes to provide a better descrip- tion of the experimental data from LHC experiments. This thesis is devoted to study of diffraction. Particularly properties of the diffraction were studied in inclusive events and in cases with at least two jets with $p_T > 20$ GeV simulated by MC generator Pythia 8.186 at the center-of-mass energy $\sqrt{s} = 7$ TeV.

The distribution of fractional momentum loss of the incident proton for various pomeron fluxes is studied. Then other observables are discussed for Minimum Bias Rockefeller flux, namely square of the four-momentum transfer, invariant mass of the diffractive system and number of charged particles. Finally, the distribution of the rapidity gap size as published by ATLAS for both inclusive and dijet events is compared with predictions of Pythia 8 using single diffractive, double diffractive and non-diffractive processes and observed differences are briefly discussed.

Keywords: diffraction, jets, MC generator Pythia 8, rapidity gaps.

1. Introduction

As the diffraction creates a considerable contribution to the inelastic cross-section in high-energy collisions of hadrons, it is very important to develop and improve its theoretical description in order to better understand the experimental results. The H1 Collaboration at HERA accelerator brought new results on the diffraction occurring in deep inelastic scattering in ep collisions. Very precise measurements were executed which led to the improvement of the understanding the diffractive processes. This success was followed by experiments at the Tevatron, where protons and antiprotons were collided, and even more precise results and new observations were acquired. With the construction of the Large Hadron Collider at CERN new and even more precise results have been expected and diffraction in pp collisions is now an object of interest of the large part of particle physics community as it can provide further improvements in our understanding of the Standard Model and physics beyond it.

2. Theoretical description

We distinguish several classes of diffractive processes. The most frequent one is the single diffraction (SD). In this process one of the interacting protons dissociates into the mass system denoted as X and other one is rescattered under the very small polar angle. The system X and rescattered proton are separated by a large gap in rapidity where no hadronic activity can be detected. Other processes involve double diffraction, in which both protons are dissociated, and central diffraction.

Diffraction is dominated mainly by soft processes with small momentum transfer where a perturbative approach of QCD can not be used. Instead phenomenological models based on Regge theory are applied. Regge theory was developed in late 1960s as a theory providing the description of the strong interaction. Although succeeded by QCD, it still holds its importance in the field of elastic scattering and diffraction. It is based on properties of scattering amplitudes and S-matrix evolving the initial state into the final one. Interaction is then described as an exchange of so called Regge trajectories (or Regge poles) in t-channel

$$\alpha(t) = \alpha(0) + \alpha\hat{\mathrm{A}}\dot{t}t, \tag{1}$$

first term being called reggeon intercept and second reggeon slope of the trajectory. A trajectory dominant in high energies with intercept $\alpha(0) < 1$ and carrying quantum numbers of vacuum is named pomeron.

At a hard scale a pQCD can be applied and pomeron is introduced in terms of QCD as a color singlet object with an internal structure and can be described by diffractive parton dostribution functions (DPDF) similar to commom particle PDFs. Because of the large momenta transfer various high-p_T objects can be produced, e.g. a jet production can occur. Important progress in understanding the diffraction at the hard scale was acomplished in the DIS experiments performed by H1 and ZEUS collaborations at HERA and led to the predictions for the diffractive processes behavior in $p\bar{p}$ collisions at Tevatron. However Tevatron data revealed to be suppressed by a constant factor approximately 10

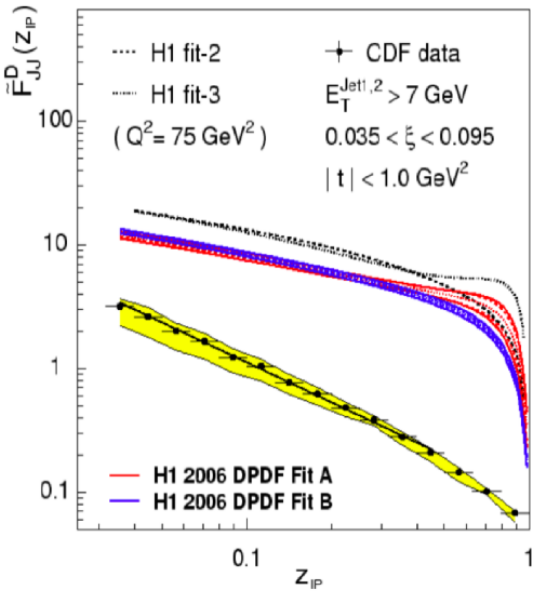

Figure 1: Tevatron data (yellow band) on the DPDFs as a function of the momentum fraction carried by the parton from the pomeron involved in hard subprocess compared to the predictions based on the H1 measurements. [2]

when compared to the expectations based on the HERA data as can be seen on Figure 1. As a result the so called factorization breaking of the cross-section in hadron-hadron collision was shown to occur due to additional soft partonic interactions. More detailed information on the theoretical description of the diffraction can be found in [1].

Therefore the gap survival probability factor S^2 was introduced as a probability that the soft interactions do not spoil the gap and that the event survives them. The soft survival probability was found to be $S^2 \approx 0.1$ in Tevatron single diffraction dijet events and using the so called KMR model it was predicted to be similar or slightly smaller in the LHC collisions at $\sqrt{s} = 7$ TeV. Diffractive dijet measurements carried out by the CMS Collaboration and compared with predictions of MC event generators gave two compatible results, namely $S^2 \approx 0.12 \pm 0.04$ and $S^2 \approx 0.08 \pm 0.04$, when compared to the LO (resp. NLO) matrix elements, which seems to be in an agreement with the theoretical prediction [3]. Also the ATLAS Collaboration estimation [4] $S^2 = 0.16 \pm 0.04(\text{stat.})pm0.08(\text{exp.syst.})$, which is based on the comparison of the data and predictions of the MC models based on DPDFs, shows a reasonable agreement with both theoretical prediction and CMS result. The ATLAS Collaboration members also published several other measurements of the diffractive processes of which already mentioned paper [4], related thesis [3] and paper [5] will form the basis of the results presented in this paper.

We describe diffractive events using several common observables. The rescattered proton can be characterized using fractional momentum loss of the incident proton defined as

$$\xi = \frac{(P - P') \cdot q}{P \cdot q} \tag{2}$$

where P and P' are momenta of the incident and rescattered proton and q is the transferred momentum in the collision.
We also use the invariant mass of the dissociated system which can be calculated as a standard Mandelstam variable or using ξ and centre-of-mass energy one can get

$$M_X = \sqrt{s\xi}. \tag{3}$$

Probably the most important feature is the existence of large rapidity gap (LRG) which is a region in pseudorapidity devoid of any hadronic activity. They are formed due to color singlet exchange in the t-channel associated with the pomeron exchange. Size of the gap is taken from the edge of the detector in pseudorapidity to the first registered particle and it satisfies

$$\Delta\eta \approx -\ln\xi. \tag{4}$$

3. Results

We will focus on the basic diffractive properties shown on the samples of events generated using Monte Carlo generator Pythia 8.1 [6]. Diffractive and also non-diffractive events are examined in two cases, the inclusive events, which are dominated by soft processes, and dijet events defined by an existence of at least two jets with transverse momentum $p_T > 20$ GeV. An anti-k_t clustering algorithm [7] from the Fastjet package [8] with the jet radius $R = 0.6$ was used for the jet reconstruction.

3.1. Pomeron flux and ξ

First we examine distributions of ξ in various pomeron fluxes available in Pythia 8.1 settings. The environment of Pythia 8.186 offers five different pomeron flux models which affect the mass spectrum of diffractive system and the t spectrum of the exchange. Their comparison can be seen in Figure 2 for inclusive single diffractive events (top) and for dijet events(bottom). The Schuler-Sjostrand (option 1) and Bruni-Ingelman (option 2) fluxes are based on critical pomeron which is the strong-coupling solution of Reggeon Field Theory and a conventional Pomeron description is the basis of Berger-Streng (option 3) and Donnachie-Landshoff (option 4) fluxes. The Minimum Bias Rockefeller (MBR, option 5) flux is based on simulations of (anti)proton-proton collisions and offers various optional parameters. The MBR flux provides the most satisfactory description of SD dijet events, based on results from CMS [9],

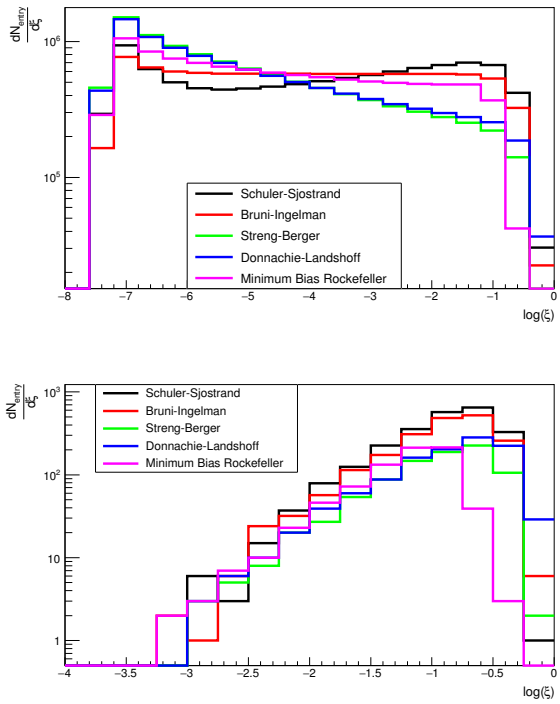

Figure 2: Distributions of ξ in inclusive (top) and dijet (bottom) SD events for different pomeron fluxes in samples generated using Pythia 8.186 at $\sqrt{s} = 7$ TeV.

and therefore it was chosen to be used in our further examination of the properties of diffractive processes.

As we can see in Figure 2 all fluxes provide a steep rise in small values of ξ reaching its maximum at $\approx 10^{-7}$. For larger values of ξ all distributions are nearly flattened out, only Berger-Streng and Donnachie-Landshoff fluxes rather show a small decrease. All fluxes then drop at very high values of $\xi \approx 1$, especially Minimum Bias Rockefeller flux. In dijet case when compared to the inclusive one we see very low values of ξ being completely cut out, then a slow rise is observed up to the values around $\xi \approx 10^{-1} - 10^{-0.5}$ where a sudden drop occurs. It implies that cases with higher fractional momentum loss of the incident proton are preferred in SD dijet events, which is indeed expectable as the condition on jet's p_T requires particles with relatively high p_T in the central detector and hence large invariant masses of the system as $\xi \approx \frac{M_X^2}{s}$.

3.2. Rapidity gaps

Large rapidity gaps (LRG) are the regions of rapidity (or pseudorapidity) devoid of any hadronic activity. Measurements of the differential cross sections in forward rapidity gap size in pp collisions at $\sqrt{s} = 7$ TeV were performed with the ATLAS detector for inclusive events and published in 2012 [5], and for dijet events in 2015 [4]. In this section, we will try to reconstruct these measurements using Pythia 8.186 MC generator. In accordance with papers [5] and [4], the edge of the detector is located at $|\eta| = 4.9$ resp. $|\eta| = 4.8$, therefore expected gap sizes can be $\Delta\eta < 9.8$ and only particles with $p_T > 200$ MeV were accepted to the calculation process. Lower transverse momentum particles are not taken into account during the evaluation of the data because of the tracking acceptance. Technical information concerning the ATLAS detector can be found in [10].

In the top part of Figure 3 we can see the differential cross-section as a function of the gap size $\Delta\eta$ for inclusive SD, DD and ND events and their sum compared to the data from [5].
It is clearly obvious that in low $\Delta\eta$ values non-diffractive processes form the main contribution to the inelastic cross-section and single diffractive and double diffractive contributions are rather negligible. However with increasing $\Delta\eta$ the ND contribution falls exponentially and for $\Delta\eta \approx 3$ it is insignificant when compared to SD and DD.
At high values of $\Delta\eta$ we observe a forming plateau caused by diffractive effects, SD and DD contributions are almost equal in these regions, and for values $\Delta\eta \approx 6$ and higher a slow rise of the differential cross-section occurs which is caused mainly by SD events. This rise is believed to be a consequence of the dynamics of SD and DD processes [5].
As can be seen from attached ratio plot, Pythia 8 describes the data reasonably in the region of $\Delta\eta < 3$ but at higher values of the gap size they do not describe the plateau and consecutive rise in the differential cross-section very well. This behavior is in agreement with observations made in [5] where Pythia 8 was also used for the simulations, but with a Schuler-Sjostrand pomeron flux. The double diffractive contribution to the inelastic cross-section seems to be very similar to the one in the [5]. However the single diffractive contribution is much smaller which is caused by the choice of pomeron flux. It is clearly obvious from Figure 3 that MBR flux causes bigger suppression of high values of ξ than Schuler-Sjostrand flux. As these high values of fractional momentum loss of the proton cause events with small rapidity gaps, the contribution of the low $\Delta\eta$ cases is hence suppressed because of the MBR flux choice.

The differential cross-section as a function of the gap size with cut for at least two jets with $p_T > 20$ GeV is depicted in the bottom part of Figure 3. The anti-k_t clustering algorithm with radius $R = 0.6$ was used for the jet reconstruction.
It is important to note that in the analysis presented in [4] a rather different cuts for the selection of particles were used compared to the analysis [5]. Here a gap is defined as a region of pseudorapidity absent of neutral particles with $p > 200$ MeV and charged particles with $p > 500$ MeV or $p_T > 200$ MeV. Similarly as in analysis [4], we normalized the ND

contribution to match the data in the first gap bin. The normalization factor is 0.75 which is slightly different, but very close, with respect to the factor 0.71 used in [4]. The difference can be explained by the fact that the factor 0.71 comes from the detector-level comparison, however we are working at the particle level.

As in the previous inclusive case the main contribution to the differential inelastic cross-section is produced by ND events in low values of $\Delta\eta$ where they fit the data reasonably, and with increasing $\Delta\eta$ ND is gradually balanced by SD and DD contributions. The differential cross-section also falls exponentially for ND events. ND contribution seems to fit the data reasonably within first four bins and is also in accordance with the Pythia 8 model presented in [4], except the region $\Delta\eta$ where the disagreement is caused by the low statistics in our model.

For SD and DD events and the sum we do not observe the plateau and the small rise of the cross-section as in the inclusive case. Exponential tendency of the differential cross-section in dijet case is, together with the non-existing plateau, a consequence of reduced phase space available for the gap occurrence, caused by the requirement of at least two jets with $p_T > 20$ GeV.

For a better consistency with simulations in analysis [4], SD and DD differential cross-sections as functions of the gap size are also provided using Donnachie-Landshoff flux choice. As can be seen, a suppression of high ξ cases is again present in the MBR flux, therefore a contribution of SD events is rather smaller in the region of low $\Delta\eta$ than the contribution of single diffractive events with D-L flux choice. Despite the same D-L flux used in our analysis and analysis [4], differences are seen for SD predictions. They may be caused by slightly different version of Pythia 8 and possible additional tunes used. No additional tunes were implemented in our case.

Very interesting phenomenon may be observed for DD events. Contrary to SD events, for double diffraction Donnachie-Landshoff flux choice results up to 10 times lower values of differential cross-section than MBR flux. Sadly this phenomenon could not be compared to the results from [4] as DD case is not depicted separately there.

The sum of SD, DD and ND contribution seems to be in accordance with the data and the simulations presented in [4] in the region of $\Delta\eta < 4$. For higher vaules of $\Delta\eta$ the model do not fit the data so accurately. But statistical uncertainties are not negligible in this region.

4. Conclusions

Main topic of the work was a study of the properties in inclusive and dijet diffractive events. Presented results are part of the work accomplished within the author's bachelor thesis [11] where more detailed informations and descriptions of the diffractive

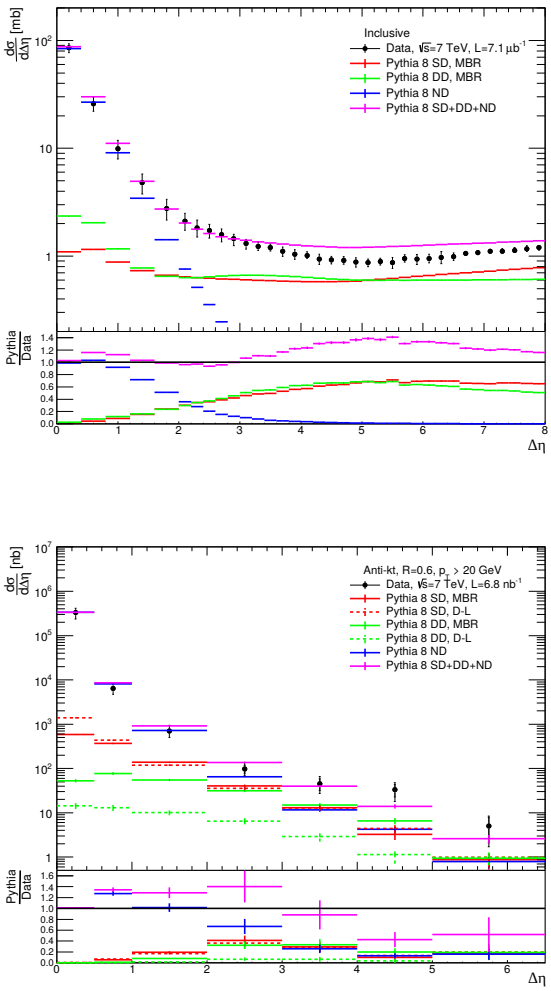

Figure 3: Inelastic differential cross-section in forward RG size $\Delta\eta$ for inclusive (top) and dijet (bottom) events. The color lines shows predictions of Pythia 8.816 with Minimum Bias Rockefeller flux choice for SD, DD and ND events and their sum at $\sqrt{s} = 7$ TeV compared to the data from [4] and [5] depicted by the black dots.

characteristics can be found.

Dijet events were selected using the cut on existence of at least two jets with minimal transverse momentum $p_T > 20$ GeV and jet radius $R = 0.6$. First of all a comparison of the distribution of the fractional momentum loss of the incident proton ξ was provided for five available pomeron flux choices. For the rest of the analysis the Minimum Bias Rockefeller flux was chosen based on the CMS Collaboration results which consider this flux the best choice for the description of single diffractive dijet events.

The very important feature of the diffractive events are large rapidity gaps which provide an effective tool for the detection of diffraction. Therefore there are great efforts to study this phenomenon. In

this paper we focused on the differential cross-section as a function of rapidity gap size. A discussion of Pythia 8 predictions for SD, DD and ND contribution to the inelastic cross-section and its comparison to the published ATLAS data was performed. For inclusive events we acquired reasonably accurate results which were found to be in accordance with the data for low $\Delta\eta$ values where ND component gave the main contribution to the inelastic cross-section. However at values of $\Delta\eta \approx 3$ and higher an overestimation of the Pythia 8 prediction is clearly obvious and the plateau with subsequent rise of the differential cross-section was not observed. But this behavior is still in agreement with the Pythia 8 simulations performed in [5].

In dijet events we observe an exponential decrease of the total inelastic cross-section with increasing gap size which is governed by the dominant contribution of ND over almost all region of gap size. The plateau observed in inclusive events is not seen here as a consequence of the requirement on the presence of jets. Our simulations based on D-L flux are in a fair agreement with the data and more or less with simulations used in [4], especially in the region of lower values of $\Delta\eta$. Therefore we conclude that Pythia 8.186 without any additional tunes and parameter settings provides a good description of the ATLAS data which is also a conclusion achieved in the analysis [4]. This means that no soft survival probability S^2 is needed (i.e. $S^2 = 1.0$) for this particular model and pomeron flux. In the next steps, we are going to compare these ATLAS data with a more recent Pythia model 8.2 with dynamically generated value of S^2 [12].

Acknowledgements

I would like to express my gratitude to my supervisor Dr. Marek Tasevsky for his guidance during my work.

References

References

[1] S. Donnachie, G. Dosch, P. Landshoff and O. Nachtmann, *Pomeron Physics and QCD*, Cambridge University Press, 2002, ISBN 0-521-78039-X.

[2] T. Affolder et al. (CDF Collaboration), *Diffractive Dijets with a Leading Antiproton in pp Collisions at* $\sqrt{s} = 1800$ GeV, Phys. Rev. Lett. 84 (2000) 5043.

[3] V. Kus, *Study of diffractive processes at the ATLAS Experiment*, Doctoral thesis, 2015.

[4] ATLAS Collaboration, *Dijet production in* $\sqrt{s} = 7$ TeV *pp collisions with large rapidity gaps at the ATLAS experiment*, Phys.Lett. B754 (2016) 214-234.

[5] ATLAS Collaboration, *Rapidity gap cross sections measured with the ATLAS detector in pp collision at* $\sqrt{s} = 7$ TeV, Eur. Phys. J. C72 (2012) 1926.

[6] T. Sjostrand, S. Mrenna and P. Skands, *A Brief Introduction to PYTHIA 8.1*, JHEP05 (2006) 026, Comput. Phys. Comm. 178 (2008) 852.

[7] M. Cacciari, G. P. Salam and G. Soyez, *The anti-k_t jet clustering algorithm*, JHEP04 (2008) 063.

[8] M. Cacciari, G. P. Salam and G. Soyez, *FastJet user manual*, Eur. Phys. J. C72 (2012) 1896.

[9] V. Khachatryan et al. (CMS Collaboration), *Measurement of diffractive dissociation cross sections in pp collisions at* $\sqrt{s} = 7$ TeV, Phys. Rev. D 92 (2015) 012003.

[10] ATLAS Collaboration, *The ATLAS Experiment at the CERN Large Hadron Collider*, J. Instrum. 3 (2008) S08003.

[11] Bendova D., *Study of Diffraction Processes at LHC*, Bachelor thesis, 2016.

[12] C. O. Rasmussen, T. Sjostrand, *Hard Diffraction with Dynamic Gap Survival*, J. High Energ. Phys. (2016) 142.

GIANT DIPOLE RESONANCE EXCITATION BY FEMTOSECOND GAMMA RAY PULSES

Lucie Celbová*

Faculty of Nuclear Sciences and Physical Engineering, Czech Technical University, Břehová 7, Prague, Czech Republic

* corresponding author: celboluc@fjfi.cvut.cz

Abstract. In 1979 John M. Dawson and Toshiki Tajima presented a new method of accelerating particles, accelerating by plasma waves which are induced by laser pulses. Plasma-based accelerators are considered the future of accelerating physics. The produced high-energy electron bunches can be, among other things, used to excite the giant dipole resonance.

Keywords: plasma based acceleration, electron acceleration, giant dipole resonance.

1. Introduction

Laser accelerators or plasma-based accelerators (LPA) bring a new view of accelerating physics. Nowadays, the average acceleration yeilds electrons with energies of the order of hundreds MeV. Those electrons can be used in inverse Compton scattering to produce high energy photons and those can subsequqently excite the giant dipole resonance.

2. Plasma wave acceleration

Accelerating gradients in linear accelerators are limited aproximately to $100MV/m$, while the ionized plasma can sustain waves with electric field given by the cold nonrelativistic wave breaking field

$$E_0 \simeq 96\sqrt{n_0(cm^{-3})} \tag{1}$$

where n_0 is the ambient electron number density. For example, a plasma density of $n_0 = 10^{18}cm^{-3}$ yields $E_0 \simeq 96GV/m$ [1]. In addition to this significant difference, the length of the accelerating wave in a plasma-based accelerators is approximately the plasma wavelength

$$\lambda_p \simeq 3.3 \times 10^{10}/\sqrt{n_0(cm^{-3})} \tag{2}$$

for example for $n_0 = 10^{18}cm^{-3}$ we get $\lambda_p \simeq 33\mu m$. Furthermore, plasma accelerators, typically driven by femtosecond laser pulses, are sources of femtosecond electron bunches which are synchronized to the those pulses [1].

In LPAs, wakefields are driven via the ponderomotive force

$$F_p = -m_e c^2 \nabla(a^2/2) \tag{3}$$

where a is the normalized vector potential and m_e is the mass of the electron [1]. Ponderomotive force can also be understood as the radiation pressure, it is responsible for expelling electrons from the front of the pulse (we neglect the motion of the ions due to their big mass with respect to that of electrons).

The plasma wave generated in an initially uniform plasma is described by

$$\left(\frac{\partial^2}{\partial t^2} + \omega_p^2\right)\frac{\delta n}{n_0} = c^2\nabla^2 a^2/2, \tag{4}$$

$$\left(\frac{\partial^2}{\partial t^2} + \omega_p^2\right)\phi = \omega_p^2 a^2/2, \tag{5}$$

where $\frac{\delta n}{n_0} = \frac{(n-n_0)}{n_0}$ is the normalized density perturbation associated with the electrostatic wake ϕ in the limit $a^2 \ll 1$ [1]. The solution for the electric field of the wake is

$$\frac{E}{E_0} = -c\int_0^t \mathrm{d}t' \sin[\omega_p(t-t')]\nabla a^2(r,t')/2 \tag{6}$$

and for the density perturbation

$$\frac{\delta n}{n_0} = (c^2/\omega_p)\int_0^t \mathrm{d}t' \sin[\omega_p(t-t')]\nabla^2 a^2(r,t')/2 \tag{7}$$

Equations (6) and (7) describe plasma waves generated at the frequency ω_p and are valid for $E \ll E_0$, where $E_0 = (m_e c\omega_p)/e$ is the cold nonrelativistic wave breaking field. Solutions to (6) and (7) indicate that wakefields will be generated most efficiently when the envelope scale length is of the order of the plasma wavelength $\lambda_p = 2\pi c/\omega_p$ [1].

3. The Giant Dipole Resonance

The giant dipole resonance (GDR) is usually interpreted as the excitation of a collective nuclear vibration in which all the protons in the nucleus move collectively against all the neutrons providing a separation between the centres of mass and charge, thus creating an electric dipole moment and occurs for gamma ray energies from 7 up to 40 MeV depending on the material. Experimentally, the GDR is well established as a general feature of all nuclei . During the resonance a neutron or a photon can be emitted

and hence the resonance can be used for example as the source of neutrons. A lot of models which try to describe the GDR exist and one can learn more about them for example at [2]. In here, we will discuss the electromagnetic excitations. In relativistic reaction between heavy ions, the strong transverse electric field

$$E_{tr}(t) = -\frac{Z_p e\gamma b}{(b^2+\gamma^2 v^2 t^2)^{3/2}} \tag{8}$$

dominates [2]. Here the projectile of charge Z_p is travelling on a straight line trajectory defined by the impact parameter b and a constant velocity v. Hence the excitation of the transverse GDR degrees of freedom in a nucleus is due to the interaction of protons with the electric field. Therefore the interaction energy

$$W(t) = ZeE_{tr}(t)z = F_{ext}(t)z, \tag{9}$$

where z is the displacement in transverse direction [2]. Then the collective Hamiltonian is of form

$$M\frac{\mathrm{d}^2 z}{\mathrm{d}t^2} + M\gamma\frac{\mathrm{d}z}{\mathrm{d}t} - Kz = F_{ext}(t), \tag{10}$$

where $F_fric = -M\gamma\frac{\mathrm{d}z}{\mathrm{d}t}$ is the frictional force. The solution to this equation is

$$F_{ext}(t) = F_0 e^{-i\omega_{ext}t} \tag{11}$$

where ω_{ext} is the field frequency [2]. (The physical external forces are real, so only the real part is meaningful.) With the above field, the motion of the dipole is

$$z(t) = \frac{1/M}{\omega^2 - \omega_{ext}^2 - i\gamma\omega_{ext}} F_0 e^{-i\omega_{ext}t} \equiv \Pi(\omega_{ext}) F_0 e^{-i\omega_{ext}t} \tag{12}$$

where the operator $\Pi(\omega_{ext})$ gives the response of the system to an external field at the frequency ω_{ext}. In order to compute the average rate of energy lost per unit time, we compute

$$P = \overline{Re(F_{ext}(t))Re(\dot{z}(t))} = \frac{F_0^2}{M}\frac{\gamma\omega_{ext}^2}{(\omega^2-\omega_{ext}^2)^2+\gamma^2\omega_{ext}^2} \tag{13}$$

where $\overline{XX}$ means the average over time. We got the equation which is nothing but the Lorentzian shape [2]. Here we took as an example the Coulomb excitation but the same arguments hold for the photoabsorption and indeed this shape correctly describes the observed GDR data in heavy nuclei.

4. Conclusions

The plasma-wave acceleration is a new way of accelerating particles, however nowadays we effectively accelerate only electrons. But it is obvious that any charged particle can be accelerated by that mechanism, since this method is based on the difference between electric potentials. Once we have the accelerated electrons, we can use them to accelerate photons in inverse Compton scattering process. If we let those photons (with energies in exact interval, depends on material) intereact with a nuclei, a giant dipole resonance can occur. Many theories of the origin of GDR are available, in here we discussed the electromagnetic excitation, which provides a clear insight into topic. The GDR can then be used for example as the source of neutrons.

References

ANISOTROPY OF HADRON PRODUCTION IN ULTRARELATIVISTIC NUCLEAR COLLISIONS

Jakub Cimerman*

Czech Technical University in Prague, FNSPE, Břehová 7, 11519 Prague 1, Czech Republic

* corresponding author: jakub.cimerman@gmail.com

Abstract. Scientists in world laboratories investigate high energy collisions of atomic nuclei for several decades. One of their objectives is research of quark-gluon plasma, which is created in these collisions. After the collision, the plasma changes into a gas of hadrons. The hot drop of matter is customarily called fireball. This fireball isn't homogeneous and expands anisotropically due to inhomogeneities of the initial energy density distribution. This leads to measurable anisotropy of the distribution of the produced hadrons. The anisotropy of the fireball can show up in its shape and expansion. To find out the properties of fireball, we have to create its theoretical model. We can simulate data from the model, which we can compare with experimentally measured data. However, measuring momentum spectrum isn't enough to determine the properties. Due to this we also measure the correlation radii. Azimuthal dependence of these quantities can tell us more about the properties of the fireball by comparing it with our model.

Keywords: space anisotropy, flow anisotropy, corelation radii.

1. Introduction

Ultra-relativistic heavy-ion collisions at colliders like LHC or RHIC produce strongly interacting quark-gluon plasma. Due to large energy density, plasma expands and cools and gradually changes into a gas of hadrons. The hot drop of matter is customarily called fireball. This fireball continues expanding until hadrons are too distant from each other to interact strongly, so they are emitted from fireball and measured by detectors. This process is called freeze-out.

The fireball isn't homogeneous and expands anisotropically due to inhomogeneities of the initial energy density distribution. This leads to measurable anisotropy of the distribution of the produced hadrons.

2. Blast wave model

The fireball can be characterized by several theoretical models. We use blast-wave model [1], in which the source is modelled an emission function

$$S(x,p)\mathrm{d}^4x = \frac{m_t \cosh(\eta - Y)}{(2\pi)^3}\mathrm{d}\eta\mathrm{d}x\mathrm{d}y\frac{\tau\mathrm{d}\tau}{\sqrt{2\pi}\Delta\tau} \times \exp\left(-\frac{(\tau-\tau_0)^2}{2\Delta\tau^2}\right)\exp\left(-\frac{p^\mu u_\mu}{T}\right) \times \Theta\left(1-\overline{r}\right). \quad (1)$$

Emission function is the Wigner phase space density of particle emission. Here, we use space-time rapidity η and longitudinal proper time τ instead of t and z

$$z = \tau\sinh\eta \quad (2a)$$

$$t = \tau\cosh\eta. \quad (2b)$$

We also use scaled radius of fireball defined as $\overline{r} = r/R(\theta)$.

The anisotropy of the fireball can show up in its shape and expansion. The spatial anisotropy is characterized by radius of fireball

$$R(\theta) = R_0\left(1 - \sum_{n=2}^{\infty} a_n \cos\left(n(\theta-\theta_n)\right)\right). \quad (3)$$

The flow anisotropy is parametrized through rapidity

$$\rho(\overline{r},\theta_b) = \overline{r}\rho_0\left(1 + \sum_{n=2}^{\infty} 2\rho_n \cos\left(n(\theta_b-\theta_n)\right)\right), \quad (4)$$

where θ_b is angle perpendicular to fireball surface. Real fireball can have both anisotropies simultaneously.

3. Anisotropy of single-particle spectrum

The single-particle spectrum is obtained by integrating the emission function

$$P(p_t,\phi) = \frac{\mathrm{d}^3N}{p_t\mathrm{d}p_t\mathrm{d}Y\mathrm{d}\phi} = \int S(x,p)\mathrm{d}^4x. \quad (5)$$

This spectrum is azimuthally dependent, so we can decompose it into Fourier series

$$P(p_t,\phi) = \frac{1}{2\pi}\frac{\mathrm{d}^2N}{p_t\mathrm{d}p_t\mathrm{d}Y}\bigg|_{Y=0} \times \left(1 + \sum_{n=1}^{\infty} 2v_n(p_t)\cos(n(\phi-\theta_n))\right). \quad (6)$$

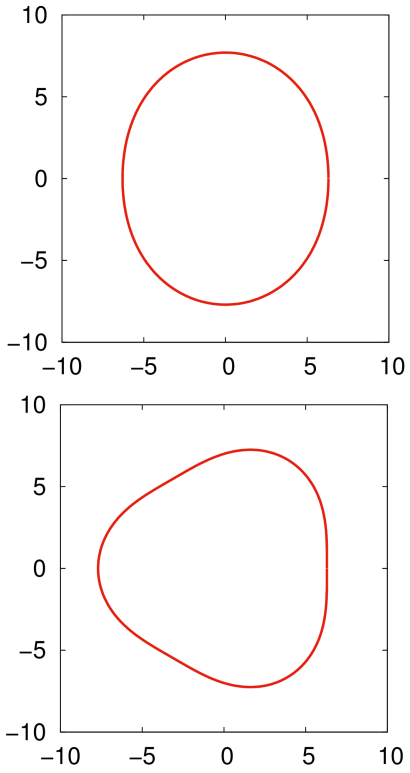

Figure 1: The shape of the fireball with second order spatial anisotropy $a_2 = 0.1$ (upper) and third order $a_3 = 0.1$ (lower). Both pictures are plotted for $R_0 = 7$ fm.

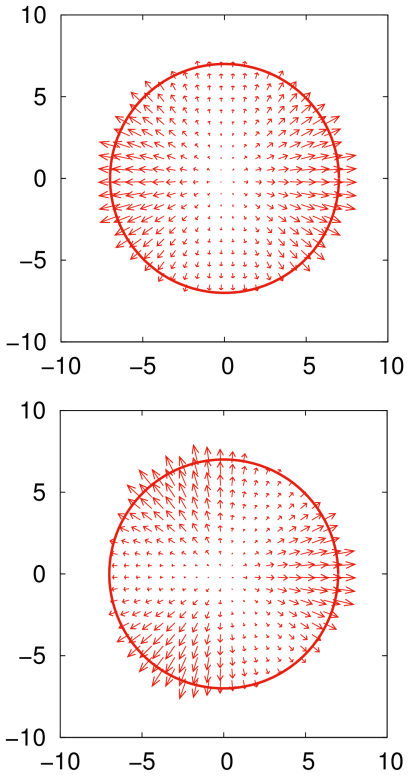

Figure 2: The shape of the fireball with second order flow anisotropy $\rho_2 = 0.3$ (upper) and third order $\rho_3 = 0.3$ (lower). Both pictures are plotted for $R_0 = 7$ fm.

The result of the calculation would depend on the value of the phase difference $\Delta = \theta_3 - \theta_2$. In experimental analysis, one effectively takes an average over all its possible values. We thus have to integrate the spectrum over Δ and then we can calculate Fourier coefficients as

$$v_n(p_t) = \frac{\int_0^{2\pi/3} d\Delta \int_0^{2\pi} P(p_t,\phi)\cos(n(\phi-\theta_n))\mathrm{d}\phi}{\int_0^{2\pi/3} d\Delta \int_0^{2\pi} P(p_t,\phi)\mathrm{d}\phi}. \tag{7}$$

Fourier coefficients v_2 and v_3 are measurable quantities, so we calculated their dependence on the anisotropy coefficients a_n and ρ_n. We have checked that both v_2 and v_3 basically depend only on coefficients of the same order. In Fig. 3 we show the contour plots, where dependence on both spatial and flow anisotropy can be seen.

We can see, that measuring of v_2 and v_3 can't tell us values of anisotropy coefficients, due to degree of freedom on plots in Fig. 3. Therefore we need another measurable quantity, which we can compare with data.

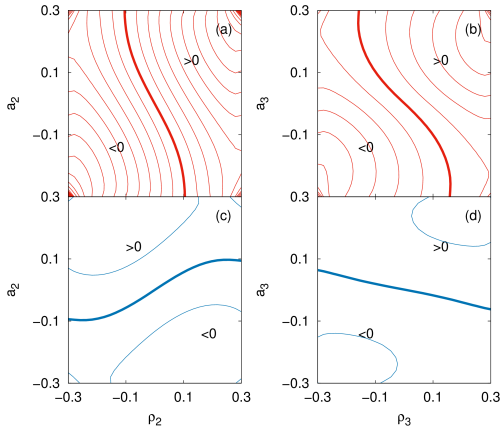

Figure 3: Dependence of v_2 and v_3 on spatial anisotropy a_n and flow anisotropy ρ_n for pions (upper row) and kaons (lower row). Thick line means $v_n = 0$ and thin lines are separated by 0.005. Results are calculated with parameters $T = 120$ MeV, $\rho_0 = 0.8$, $R_0 = 7$ fm, $\tau_0 = 10$ fm/c and $p_t = 300$ MeV.

4. HBT RADII

The femtoscopic technique which uses two-particle correlations is standard tool for measuring the space-time characteristics of the emitting source. From the correlation function we can derive correlation radii (also called HBT radii). Here we use the out-side-longitudinal reference frame, in which the outward direction is identified with the direction of the transverse component of $K = \frac{1}{2}(p_1 + p_2)$ and longitudinal axis is parallel to the beam. In this system we can

write correlation radii as

$$R_o^2(K) = \left\langle \left(\tilde{x}_o - \beta_o \tilde{t}\right)^2 \right\rangle (K) \tag{8a}$$
$$R_s^2(K) = \left\langle \tilde{x}_s^2 \right\rangle (K) \tag{8b}$$
$$R_l^2(K) = \left\langle \left(\tilde{x}_l - \beta_l \tilde{t}\right)^2 \right\rangle (K) \tag{8c}$$
$$R_{os}^2(K) = \left\langle \left(\tilde{x}_o - \beta_o \tilde{t}\right) \tilde{x}_s \right\rangle (K) \tag{8d}$$
$$R_{ol}^2(K) = \left\langle \left(\tilde{x}_o - \beta_o \tilde{t}\right) \left(\tilde{x}_l - \beta_l \tilde{t}\right) \right\rangle (K) \tag{8e}$$
$$R_{sl}^2(K) = \left\langle \left(\tilde{x}_l - \beta_l \tilde{t}\right) \tilde{x}_s \right\rangle (K). \tag{8f}$$

In Fig. 4 we can see the azimuthal dependence of one of the correlation radii. Although we calculated only with third order anisotropy, we can see that there is also another higher order sinusoidal element, because the curve isn't horizontally symmetrical.

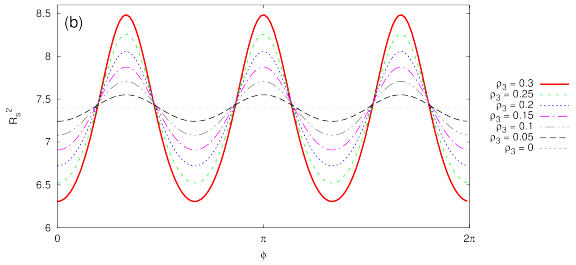

Figure 4: Dependence of R_s^2 on flow anisotropy ρ_3 for pions. Results are calculated with parameters $T = 120$ MeV, $\rho_0 = 0.8$, $R_0 = 7$ fm, $\tau_0 = 10$ fm/c and $K_o = 500$ MeV.

Now we can again decompose the correlation radii into Fourier series and plot contour graphs. Then we can easily overlay plot of spectrum Fourier coefficients and correlation radii Fourier coefficients to get Fig. 5. Now by measuring v_3 and $R_{o,3}^2/R_{o,0}^2$ we can definitely get anisotropy coefficients a_3 and ρ_3.

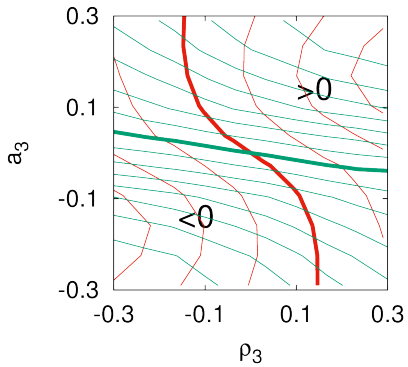

Figure 5: Overlay of contour plots. Red plot shows dependence of v_3 and green plot dependence of $R_{o,3}^2/R_{o,0}^2$ on spatial and flow anisotropy for pions. Results are calculated with parameters $T = 120$ MeV, $\rho_0 = 0.8$, $R_0 = 7$ fm, $\tau_0 = 10$ fm/c and $K_o = 500$ MeV.

5. Conclusions

We showed, that if we want to know spatial and flow anisotropy coefficients, we have to measure more than just single-particle spectrum. It appears, that correlation radii and their Fourier coefficients are helpful quantity, because we can measure it and with coefficients v_2 and v_3 they give us definitely anisotropy coefficients.

Interesting conclusion is that even if we calculate only with second and third order anisotropies, the results contain also fourth and sixth Fourier coefficients. Therefore if we measure fourth or sixth order anisotropy, it does not necessary implies fourth or sixth order of spatial and flow anisotropy.

References

[1] B. Tomášik. Disentangling spatial and flow anisotropy. *Acta Phys Polon B* **36**:2087–2104, 2005.

[2] J. Cimerman, et al. Higher-order anisotropies in the blast-wave model - disentangling flow and density field anisotropies. `arXiv:1702.01735`.

[3] M. Csanád, et al. Interplay among the azimuthally dependent hbt radii and the elliptic flow. *Eur Phys J A* **37**:111–119, 2008.

[4] U. Heinz, et al. Symmetry constraints for the emission angle dependence of hanbury brown–twiss radii. *Phys Rev C* **66**:044903, 2002.

[5] W. Florkowski. *Phenomenology of Ultra-Relativistic Heavy-Ion Collisions*. World Scientific, 2010.

LASER DRIVEN PHOTOPRODUCTION OF RADIOISOTOPES

Pavel Gajdos*

CTU FNSPE, Brehova 7, Prague, Czech Republic

* corresponding author: gajdopa1@fjfi.cvut.cz

Abstract. A brief introduciton to acceleration of electrons using laser induced plasma wakefield. The experimental setup for production of radioisotopes by Bremsstrahlung γ-rays via (γ, n) and $(\gamma, 2n)$ reactions and analysis of products using γ-spectroscopy and half-life time measurements.

Keywords: radioisotopes, wakefield, photonuclear.

1. Introduction

The first proposal of electron acceleration using laser-driven plasma wakefield was by Tajima and Dawson in 1979. This technique allows acceleration of particles to high energies in a small distance because of its acceleration gradient, which is approximately a thousand times bigger than that in conventional accelerators. Hence a thousand times smaller accelerators are needed to achieve the same energy. Several experiments has shown acceleration of electrons with energies over 100 MeV. This paper will show the basic principle of laser wakefield acceleration in Section 2 and demonstrate the possible use of relativistic electron beam to produce radioisotopes in Section 3. The experiment will be held in the PALS research centre.

2. Electron acceleration

2.1. Acceleration in plasma

Using plasma-based acceleration is very effective, because of its ability to sustain large acceleration gradients, whereas acceleration gradients in conventional accelerators are limited due to a material breakdown in the chamber, when high electric field is applied. Plasma can sustain electric fields in excess of [1].

$$E_0(\mathrm{V/m}) \simeq 96\sqrt{n_0(\mathrm{cm}^{-3})}, \qquad (1)$$

where n_0 is the ambient electron density. Moreover, plasma-based accelerators are able to produce ultrashort electron bunches in order of femtoseconds. The following paragraph will describe the basic principle of electron acceleration using plasma wakefield.

2.2. The principle of laser wakefield acceleration

A single, ultrashort, high intensity laser pulse is shot into an appropriate gas (e.g. Helium). It ionizes the medium in a front of the pulse and subsequently free electrons are expelled around the laser pulse envelope due to its ponderomotive force. In the back of the pulse envelope electron trajectories are crossed, where a huge electron density is created, whilst inside the envelope the electron density is very low. hence the electric field is created. If the electron density in the back of the pulse envelope is at its maximum, other incoming electrons are not able to go through it and they are repelled. Some of them may slip into the pulse envelope in an accelerating phase, and therefore they are accelerated. This is the simplest method of electron injection.

3. Experimental setup

The schematic experimental setup is shown in Fig: 1. Firstly, mirror M1 reflects the laser beam onto the off-axis parabolic mirror, which reflects it onto mirror M2 and subsequently the beam is focused onto the gas jet. The electron beam is accelerated and interacts with a solid target, in which it is stopped creating Bremsstrahlung γ-rays, that are used to activate the target material. To carry out a high number of products we will focus on a two types of reactions (γ, n) and $(\gamma, 2n)$ with thresholds around 10 MeV for (γ, n) reaction and 25 MeV for $(\gamma, 2n)$ reaction. The whole experiment is placed in the vacuum chamber, a 150 μm beryllium table will be used to separate the target and the vacuum chamber, so the detection will be possible immediately after the activation. Hence radioisotopes with shorter half-lifes might be detected. A 1.5×1.5 cm Timepix detector will be used for detection. Products will be analyzed by γ-spectroscopy for identification. The reaction products might be also analyzed by measuring only activity. Produced radioisotopes have different half-life, so it is possible to determine their quantity.

3.1. Target

Here is a list of elements, that are avaliable to use as a target: Al, Ti, Fe, Ni, Cu, Zn, Zr, Mo, Cd, In, Sn, W. To produce a good quality isotopes, not all of these elements will be used. Target proportions are $5 \times 5 \times 1$ mm. The list of expected reactions is shown in Tab. 1 with the energy of the characteristic γ-ray emission, natural abundance and the half-life time [2]. The products were chosen to provide a detectable radiation with emission probability over 10% and half-lifes from 5 minutes to 3 days. In the ideal case we

Target	**Target isotope**	**Nat. Abn.** [%]	**Product**	**E$_\gamma$ [keV]**	**I$_\gamma$** [%]	**T1/2**
Fe	^{54}Fe	6.9	^{53}Fe	378	42	8.5 m
			^{52}Fe	168	99	8.3 h
Ni	^{58}Ni	68.1	^{57}Ni	1378	82	35.6 h
Cu	^{63}Cu	69.2	^{61}Cu	283	12	3.3 h
				656	11	
Zn	^{64}Zn	48.6	^{62}Zn	41	25	9.2 h
				596	26	
	^{70}Zn	0.6	^{69m}Zn	438	95	13.8 h
Mo	^{92}Mo	14.8	^{90}Mo	122	64	5.6 h
				257	78	
	^{94}Mo	9.3	^{93m}Mo	263	57	6.9 h
				685	99	
				1477	99	
Cd	^{106}Cd	1.3	^{104}Cd	84	47	57.7 m
				710	20	
In	^{113}In	4.3	^{112m}In	157	13	20.6 m
			^{111}In	171	90	2.8 d
				245	94	
			^{111m}In	537	87	7.7 m
Sn	^{124}Sn	5.8	^{123m}Sn	160	86	40.1 m

Table 1: Reactions: Natural Abundance, Energy of emitted γ-ray, Probability of emission, Half-life (m=minute, h=hour, d=day)

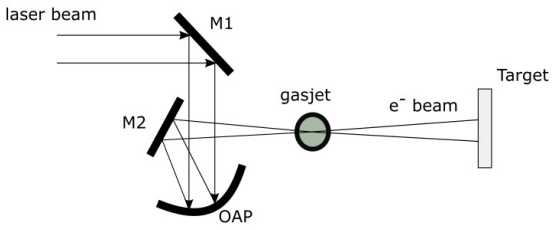

Figure 1: Experimental setup: laser pulse is refected by the mirror (M1) onto the off-axis parabolic mirror (OAP), which focuses it after another reflection by the mirror (M2) onto a gasjet. Thus, a high energy electron beam is created and interacts with a solid target

would like to measure out 1000 counts of γ-rays with relevant energy emitted from a radioisotopes to get a small statistical relative error $\sigma_{rel} \simeq 3$ %.

3.2. The number of laser pulses

To estimate how many laser pulses will be needed to produce sufficient number of reaction products, we will use the next formula for number of reactions in a thin target, taken from [3]

$$C = N_0 n \sigma x, \tag{2}$$

where C is th number of reactions, N_0 is the number of γ-photons in the beam, n the number of target particles per unit volume, σ the collision cross-section and x thickness of the target. A rough calculation of a number of laser pulses for ^{58}Ni (γ, n) reaction has been made in the approximation of a perfect detector and even energy distribution of the photon beam.

$$^{58}Ni \ + \ \gamma \ \rightarrow \ ^{57}Ni \ + \ n \tag{3}$$

We suppose photon beam energy spread from 10 to 50 MeV with 10^7 photons per pulse. The simple redioactive decay formula is [3]

$$A(t) = A_0 e^{-\lambda t}, \tag{4}$$

where $A(t)$ is the quantity of radioisotopes at time t, A_0 is the initial number of radioisotopes and λ is given by

$$T_{1/2} \ = \ \frac{ln2}{\lambda}, \tag{5}$$

where $T_{1/2}$ is the half-life of the radioisotope. Using (4) and choosing counting time $t = 1$ h with ^{57}Ni half-life $T_{1/2} = 35.6$ h, we estimate, that we need to produce approximately $N_0 = 65 \cdot 10^3$ radioisotopes to measure 1000 counts. From equation (2) and a cross-section taken from Exfor database [4] (using trapezoidal rule for numerical integration), we calculated (with approximations mentioned earlier) that ~ 500 of ^{57}Ni radioisotopes are produced in one shot. That leads to need of a 130 shots to produce a sufficient number of reaction products.

4. Conclusions

Experimental setup for producing radioisotpoes using laser wakefield accelerator was demostrated. When assuming the perfect detector, 130 laser pulses were estimated to be needed for producing a sufficient number of ^{57}Ni radioisotopes from a Ni target. The number of laser pulses needed to measure out the same number of events will be a lot bigger, when using a Timepix detector. Therefore, we will use not only γ-spectroscopy for identifiaction but also a half-life time measuremnts.

References

[1] C. B. S. E. Esarey, et al. Physics of laser-driven plasma-based electron accelerators. *Rev Mod Phys* **81**(3):1229–1285, 2009.

[2] Lund/lbnl nuclear data search.

[3] W. Williams. *Nuclear and particle physics*. Oxford at the Clarendon, 1991.

[4] L. Katz, et al. The solution of x-ray activation curves for photonuclear cross sections. *Canadian Journal of Physics* **29**:518, 1951.

MEASUREMENT OF QUARKONIA PRODUCTION IN HEAVY-ION COLLISIONS WITH THE ATLAS DETECTOR

Petr Gallus for ATLAS collaboration*

Czech Technical University in Prague, Brehova 7, Prague 5, Czech Republic

* corresponding author: petr.gallus@fjfi.cvut.cz

Abstract. The suppression of quarkonia production observed in heavy-ion collisions relative to proton-proton collisions is a phenomenon that may be connected to the formation of a Quark Gluon Plasma. In addition to hot effects in the dense heavy-ion fireball, cold nuclear matter effects, may also be in play in quarkonia production. To distinguish between these two, we compare A+A collisions containing both hot and cold effects with p+A collisions in which only cold effects are expected. The ATLAS experiment has studied prompt and non-prompt J/ψ and $\psi(2S)$ via the dimuon channel using both p+A and A-A systems and Upsilon(nS) in p+A collisions. These data were taken using collision with center-of-mass energy per nucleon pair of 5.02 TeV in 2013 for p+A and 2015 for A+A and p+p. Measurements will be presented including excited-to-ground state and nuclear modification factors as a function of transverse momentum, rapidity and centrality.

Keywords: ATLAS, LHC, Quarkonia, Heavy Ions.

1. Introduction

We need some type of probe to study the properties of Quark Gluon Plasma, so in 1986 two theoretics, Matsui and Satz [1], propose to use the quarkonia and their states. The J/ψ and other quarkonia give us well measured bounded state with know bounding energy, this can serve as a thermometer to measure temperatures and could indicate the creation of deconfined hot nuclear matter. Inside collisions of two nuclei, the quarkonia state is interacting with matter by two types of effects, first hot nuclear matter effects are connected with QGP, for example, Color-Screening - this describes how temperature can melt a bound between quarks because energy of media is higher than energy of bound, or there is Regeneration where two free quarks can create new quarkonia. The second type of effects are so-called cold nuclear matter effects, these occur in media of dense nuclear matter but without free energy from temperature, to separate this types of Prompt we use hadron-nucleus collisions.

To find out how much is quarkonia production affected by media, we create observable nuclear modification factor, which can be defined for each centrality class as:

$R_{AA} = \frac{N_{AA}}{\langle T_{AA} \rangle \times \sigma_{pp}}$

where N_{AA} is the per-event quarkonia yield, T_{AA} is the mean nuclear thickness function and σ_{pp} is the corresponding cross-section of quarkonia in proton-proton collisions with the same energy.

As we propose earlier, effect of the QGP does interact with quarkonia differently based on their bounding energy, so it is important to compare not only pp with PbPb but also effects on quarkonia with different bounding energy, in our case we compared J/ψ with $\psi(2S)$, both states decay into the muon and antimuon. So we can create a double ratio of R_{AA} of J/ψ and $\psi(2S)$.

The last concept we need to introduce is the Prompt and Non-prompt fraction of quarkonia. The Prompt J/ψ is meson which was created in the moment of collision and then must propagate through media to before decay, non-prompt J/ψ originate mainly from b quarks decay which so itÂt's decay is delayed and quarkonia do not interact with hot nuclear matter.

2. ATLAS Detector, Events and Data selection

The ATLAS detector is one of the big experiment on LHC and it is designed as a multi-purpose detector which covers almost solid angle around collision point. For this analysis, we used an Inner detector and muon spectrometer. We choose dimuon pairs with opposite charge and each of the muons must pass trigger and momentum requirements.

This analysis [2] uses data from Pb+Pb collisions at a nucleon-nucleon centre-of-mass energy of $\sqrt{s_{NN}} = 5.02TeV$ and pp collisions at centre-of-mass energy of $\sqrt{s_{pp}} = 5.02TeV$ recorded by ATLAS in 2015. The integrated luminosity of the analysed samples is $0.49nb^{-1}$ for Pb+Pb collisions and $25pb^{-1}$ for pp collisions.

3. Results

Central observable discussed in this note is the ratio of nuclear modifications factors of two charmonia states: $/psi(2s)$ and J/ψ. This ratio provide important cross-check: if non-prompt fraction originate from decay of b quarks, it should correspond to the branching ratio similar to the pp collisions, we should observe the only suppression of b quarks, but it should be the same

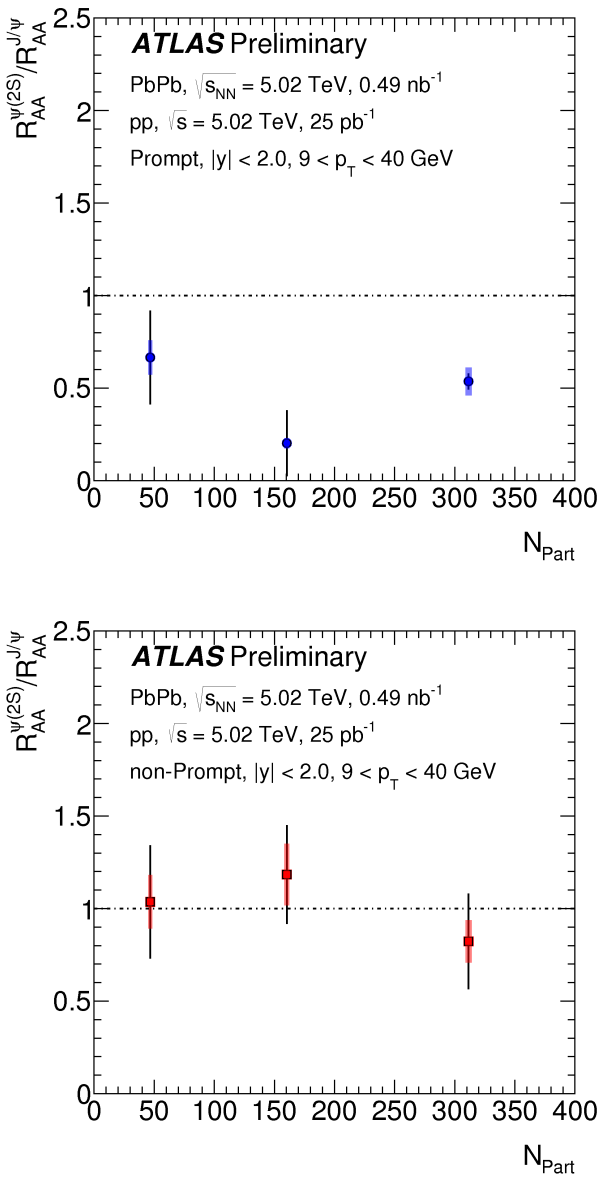

Figure 1: Double ratio of $\psi(2S)$ and $J/\psi(2S)$ for Prompt fraction (top) and Non-prompt fraction (bottom) [2].

for both states, this mean that ratio should be unity independently on momentum, rapidity of centrality. For prompt fraction it is different, suppression should depend on binding energy, which will create lower R_{AA} for $\psi(2S)$ compare to the J/ψ.

The result is shown in Figure 1, where we can see that our analysis support this statement. In those plots, we observe this ratio as a function of a number of participants in a collision, for prompt (top) and non-prompt (bottom) fractions. The data support suppression of prompt $\psi(2S)$, so ratio is below unity, and also statement about non-prompt fraction, where we measured ratio around unity, that show same suppression independently on binding energy.

4. Conclusions

The ratio of $\psi(2S)$ to J/ψ meson production is measured for both prompt and non-prompt mesons and shown as a function of centrality. Values are consistent with unity for a non-prompt fraction and for prompt fraction we observe values below unity, which can be interpreted as stronger suppression of higher states in heavy ion collisions. This pattern is consistent with proposed thesis of a dependence of suppression on binding energy, in prompt case, and that mesons originate from b quarks decays do not interacts with hot nuclear matter.

Acknowledgements

References

[1] T. Matsui, et al. J/ÏĹ suppression by quark-gluon plasma formation. *Physics Letters B* **178**(4):416 – 422, 1986.

[2] Study of $J/\psi \to \mu^+\mu^-$ and $\psi(2S) \to \mu^+\mu^-$ production with 2015 PbPb data at $\sqrt{s_{NN}} = 5.02$ TeV and pp data at $\sqrt{s} = 5.02$ TeV with the ATLAS detector. Tech. Rep. ATLAS-CONF-2016-109, CERN, Geneva, 2016.

MEASUREMENT OF J/ψ AZIMUTHAL ANISOTROPY IN U+U COLLISIONS AT $\sqrt{s_{\rm NN}} = 193$ GEV

Alena Harlenderova*

Faculty of Nuclear Sciences and Physical Engineering of the Czech Technical University in Prague, Brehova 78/7, 11000 Praha, Czech Republic

* corresponding author: alena.harlenderova@fjfi.cvut.cz

Abstract. Lattice Quantum Chromodynamics (QCD) predicts Quark-Gluon Plasma (QGP), a new state of matter consisting of deconfined quarks and gluons, at hight temperatures or densities. One of the most prominent signatures of the QGP is J/ψ suppression due to color screening of the quark-antiquark potential in the deconfined medium. However, an interpretation of the measured J/ψ yield modification is complicated by a contribution of competing mechanisms. Measurements of the second-order harmonic coefficient (v_2) of J/ψ azimuthal distribution can help to disentangle contribution of $c\bar{c}$ recombination and primordial direct pertubative processes to J/ψ production. In this proceedings, a first measurement J/ψ v_2 in U+U collisions at $\sqrt{s_{\rm NN}} = 193$ GeV from the STAR experiment is presented for $0 < p_T < 10$ GeV/c. In this kinematic region and at this energy, v_2 of J/ψ in U+U collisions is measured to be consistent with zero for p_T higher than 2 GeV/c favouring rather non-significant contribution of $c\bar{c}$ recombination to J/ψ production.

Keywords: J/ψ, azimuthal anizotropy,quark-gluon plasma, U+U collisions.

1. Introduction

In common matter which surrounds us and from which we are made of, quarks are bound in sets of two or three in the so called hadrons. Different state of matter called Quark-Gluon Plasma (QGP) is predicted by lattice Quantum Chromodynamics (QCD) at high energy densities and/or temperatures. Under these extreme conditions, quarks and gluons are asymptotically free. QGP existed at the beginning of the Universe and it is expected that scientists are able to recreate similar conditions for a brief time in ultra-relativistic collisions of heavy ions.

Various probes of QGP were proposed. One of the most prominent is a suppression of J/ψ meson yields in heavy-ion collisions compared to elementary p+p collisions scaled by a number of binary collisions. It is supposed that quark potential of c and $\bar{c}$ quarks in J/ψ is screened in the deconfined medium. As a result, J/ψ is dissociated. Consequently, J/ψ yields should be suppressed in the presence of the QGP. However, an interpretation of the observed yield modification is complicated because of a contribution of competing mechanisms such us $c\bar{c}$ recombination. An exact fractions of the J/ψ yield which are produced or suppressed by these individual mechanisms are so far not know.

Measurement of J/ψ azimuthal distribution, particularly its second Fourier coefficient v_2, can help us to disentangle contribution of the $c\bar{c}$ recombination from the potentially suppressed direct perturbative QCD (pQCD) production. In case the J/ψ is produced at the beginning of the collision by direct pQCD processes, it is in the form of colourless meson after its formation. Thus, it should not interact strongly with the deconfined color charges in the surrounding QGP. On the other hand, J/ψ produced by $c\bar{c}$ recombination inherits flow of its constituent quarks. Heavy quarks are more resistant to changes in velocity and and to subsequent thermalization than light quarks which exhibit clear collective motion. However, recent D_0 elliptic flow measurements in Au+Au collisions and its comparison to models have shown that charm quarks probably also flow with the medium [1].

We used U+U collisions for the analysis of J/ψ v_2 presented in these proceedings since there is approximately 20% higher energy density in the initial stage of the U+U collisions in comparison to Au+Au collisions [2]. Subsequently, the medium in U+U collision should reach higher degree of thermalization and particles are then expected to attain higher elliptic flow. There is indeed an observation of higher v_2 of charged particles measured in U+U collisions than in Au+Au collisions [3]. These particles consist mostly of light quarks, but the free charm quarks are also expected to develop higher v_2.

2. Data analysis

Minimum bias and high tower triggered data were used for this analysis. High tower triggered events are rich in J/ψ since these events were selected by requiring high energy to be deposited in the Barrel Electromagnetic Calorimeter (BEMC), which usually corresponds to non-fotonic electron.

J/ψ were reconstructed via dielectron decay channel $J/\psi \rightarrow e^+e^-$ with branching ratio 5.9%. Main detectors used for J/ψ reconstruction are Time Pro-

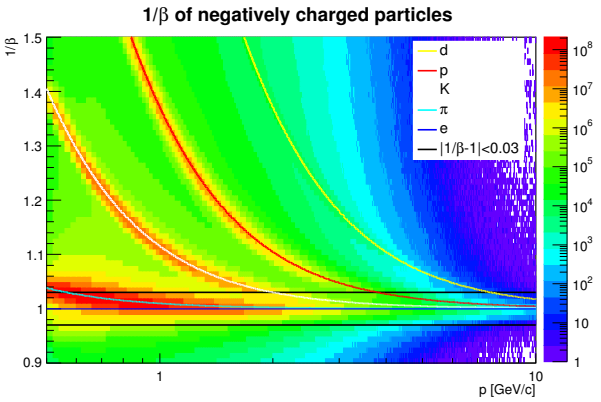

Figure 1: TOF $1/\beta$ distributions for negatively charged particles in U+U collisions together with theoretical $1/\beta$ functions of deuterons, protons, kaons, pions and electrons. Cut used for electron identification in this analysis is indicated by black lines.

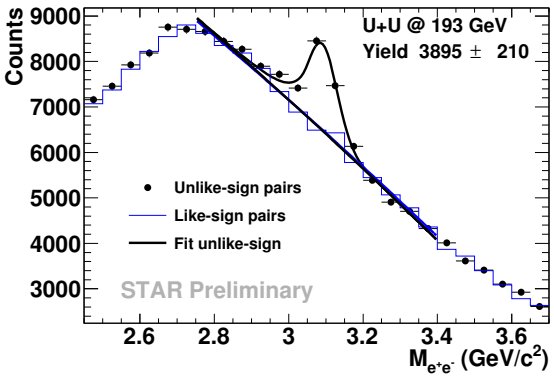

Figure 2: Invariant mass distribution of unlike-sign electron pairs (black points) fitted by Crystal Ball function plus second order polynomial (fitting function and polynomial from fitting function are shown as black curve). Blue curve corresponds to like-sign pair yield. The figure is taken from [4].

jection Chamber (TPC), Time of Flight (TOF) and BEMC. TPC provides excellent tracking of charged particles and their identification via specific particle energy loss (dE/dx). Tracks in the TPC are curved in applied magnetic field. particle momenta can then be calculated from the curvature of the tracks. For J/ψ reconstruction, we use electrons and positrons with momentum $p_1 > 1.2$ GeV/c for slower daughter particle and $p_2 > 1.4$ GeV/c for faster one. TOF with its timing resolution < 100 ps provides particle identification via $1/\beta$. Hadrons and electrons are well separated by TPC and TOF information for $p < 1.5$ GeV/c. For higher momenta, it is useful to include also information about the energy deposited in the BEMC.

In this analysis BEMC cut $0.3 < pc/E < 1.5$ is used. Here p is the momentum of the particle as measured by the TPC and the E is the energy deposited in the BEMC. Electrons should deposit all their energy in the BEMC resulting in $pc/E \sim 1$. Electrons are light particles and as such their velocity β is close to one in the measured momentum region, as can be seen in the Figure 1. Since the measured β statistically fluctuates around the expected mean values TOF cut $|1/\beta - 1| < 0.03$ is used.

There are three sets of applied cuts for electron identification. They are listed in the Table 1 in third to fifth column. Each line correspond to one set of cuts. If one set is fulfilled, we take particle as electron or positron. In the one case, particle fulfills both, BEMC and TOF cut. However, particle can be taken as electron or positron also in the case that only BEMC or TOF cut are fulfilled, however corresponding $n\sigma_a$ cuts are tighter. Further, we demand daughter particles to fulfill also cut for minimal momenta p_1 and p_2 listed in first and second column in the Table 1.

Example of reconstructed J/ψ invariant mass distribution for $0 < p_T < 2$ GeV/c is shown in the Figure 2. The distribution is fitted by a Crystal Ball function plus second order polynomial. Background reconstructed from like-sign pairs is also plotted in the Figure 2 for comparison. Similarly, invariant mass distribution was reconstructed for p_T bins $2 < p_T < 5$ GeV/c and $5 < p_T < 10$ GeV/c.

For measurements of elliptic flow we first need to determine the event plane in each collision. For this analysis a second order event plane is calculated from charged TPC tracks with $0.15 < p_T < 2$ GeV/c. Correction for non-uniform acceptance of detectors was applied in order to suppress detector effects.

The elliptic flow v_2 was calculated by two methods, event plane method and invariant mass method.

In the event plane method, parameters of Crystal Ball fit are fixed with the exception of the normalization for each p_T bin and after that J/ψ yields are reconstructed for five bins in $\phi - \Psi$, where $\phi - \Psi$ is the relative angle between J/ψ (ϕ) and event plane (Ψ). Subsequently, yield vs. $\phi - \Psi$ are fitted by the function $N \cdot [1 + 2 \cdot v_{2,obs} \cdot \cos(2 \cdot (\phi - \Psi))]$ and v_{obs} is extracted. Final v_2 is obtained by dividing $v_{2,obs}$ by event plane resolution averaged over all used centralities. In order to estimate our systematic uncertainties, yields in $\phi - \Psi$ bins are extracted by three submethods. At first, yields are fitted by Crystal Ball function plus second order polynomial and yields are obtained by subtracting the polynomial from the fitting function. Yields obtained in this way for $0 < p_T < 2$ GeV/c are shown in the Figure 3 and corresponding v_2 for all p_T bins in the Figure 5 in blue. In the second submethod, yields are obtained by counting unlike-sign yield bin by bin and subtracting the polynomial from previous submethod. Corresponding v_2 is shown by gray in the Figure 5. In the last submethod shown in green, we at first subtract bin by bin like-sign from unlike-sign yield. Afterwards, yields are fitted by Crystal Ball function plus first order polynomial and final yields are obtained by subtracting polynomial from

p_1 (GeV/c)	p_2 (GeV/c)	TPC $n\sigma_e$ cut	TOF cut	BEMC cut
> 1.5	> 1.5	$-0.6 < n\sigma_e < 3$		$0.3 < pc/E < 1.5$
> 1.2	> 1.4	$-0.3 < n\sigma_e < 3$	$\lvert 1/\beta - 1\rvert < 0.03$	
> 1.2	> 1.4	$-1 < n\sigma_e < 3$	$\lvert 1/\beta - 1\rvert < 0.03$	$0.3 < pc/E < 1.5$

Table 1: Table of applied cuts for electron and positron identification. If set of cut in one line is fulfilled, partice is taken as electron or positron. p_1 and p_2 are daughter momenta.

the fitting function.

In the invariant mass method of obtaining the v_2, yields in each p_T bin are fitted by Gaussian function which describes the signal ($Sg(M_{e^+e^-})$) plus second order polynomial describing the background ($Bg(M_{e^+e^-})$). In the next step v_2 of unlike-sign pairs is calculated, for each bin in the invariant mass of the pair $M_{e^+e^-}$, as an average $\cos 2(\phi - \Psi)$ divided by eventplane resolution. This $v_2(M_{e^+e^-})$, shown in Figure 4, contains contribution from the signal as well as from the background. It is then fitted by the following function:

$$\frac{v_2^{J/\psi} \cdot Sig(M_{e^+e^-}) + (a_0 + a_1 \cdot M_{e^+e^-}) \cdot Bg(M_{e^+e^-})}{Sig(M_{e^+e^-}) + Bg(M_{e^+e^-})},$$

, where $v_2^{J/\psi}$ is the elliptic flow of J/ψ meson and a_1 and a_0 are coefficients of linear function. The a_0, a_1 and v_2 J/ψ are free parameters of the fit. This method assumes that J/ψ has constant v_2, whereas v_2 of background is linear function of $M_{e^+e^-}$, as can be seen from the fitting formula. The results from the invariant mass method are shown in red in the Figure 5. Full circles correspond to v_2 calculated with standard cuts, which were described in this chapter. Open circles correspond to tighter cuts which are used to estimate effects of hadron contamination on v_2. As can be seen, hadron contamination does not considerably affect the final v_2 values, especially in the first two p_T bins. v_2 results for different methods and two sets of cuts were used for calculation of systematic errors. Event plane method points obtained by fitting unlike-sign distribution are used as final v_2 values. They are shown as red points in the Figure 6 and are compared to v_2 of J/ψ in Au+Au (black circles) and non-flow effect estimation for Au+Au (gray band). As can be seen the v_2 of J/ψ in U+U is consistent with zero above p_T of 2 GeV/c. However, real physical value of v_2 can be lower due to non-flow effects. Particles that have non-flow correlations with J/ψ are more likely to fly from collision under similar azimuthal angle. Due to this effect, event plane angle is calculated closer to the azimuthal angle of the J/ψ and the measured v_2 of the J/ψ hence rises.

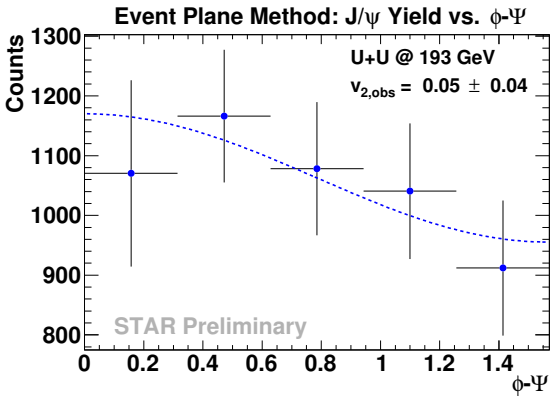

Figure 3: Event plane method: Yield extracted by fitting unlike-sign distribution vs. relative angle between J/ψ (ϕ) and event plane angle (Ψ) fitted by the function $N \cdot [1 + 2 \cdot v_{2,obs} \cdot \cos(2 \cdot (\phi - \Psi))]$. The figure is taken from [4].

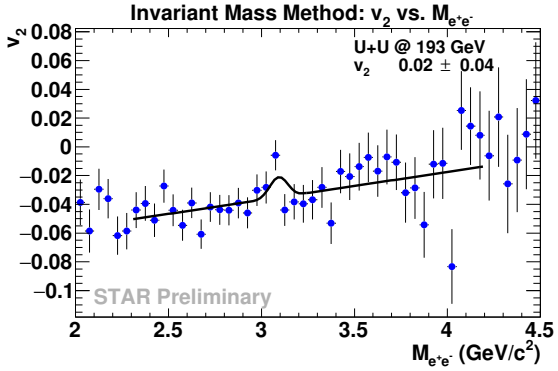

Figure 4: Invariant mass method: Elliptic flow v_2 of unlike-sign pairs as a function of $M_{e^+e^-}$ fitted by the function 2. The figure is taken from [4].

3. Conclusions

Measurement of J/ψ elliptic flow can help to disentangle contribution of $c\bar{c}$ recombination and direct primordial processes to the J/ψ production. J/ψ v_2 as a function of p_T for centrality $0 - 80\%$ in U+U collisions at $\sqrt{s_{\rm NN}} = 193$ GeV measured by the STAR experiment can be seen in a Figure 6. The minimum bias and high tower triggered data were used for this analysis. For comparison, J/ψ v_2 from Au+Au collisions at 200 GeV [5] is also plotted in the Figure 6. The results from U+U and Au+Au collisions are consistent with each other and at the same time they are consistent with zero for $p_T > 2$ GeV/c. These results favour the case of rather non-significant contribution of $c\bar{c}$ recombination to the J/ψ production at these center-of-mass energies and in this kinematic region. This is further supported by the fact that real

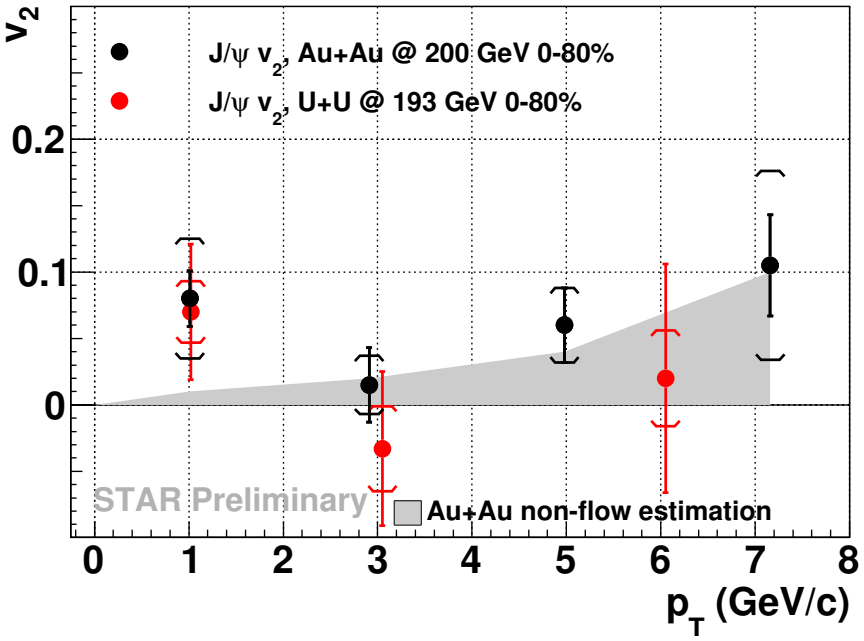

Figure 6: Results on elliptic flow v_2 of J/ψ vs. p_T in U+U (red circles) compared to the STAR results from Au+Au (black circles). The brackets denote systematic errors. Non-flow effect estimation is shown by a gray band. The figure is taken from [4]. Au+Au data points and non-flow effect estimation are taken from [5].

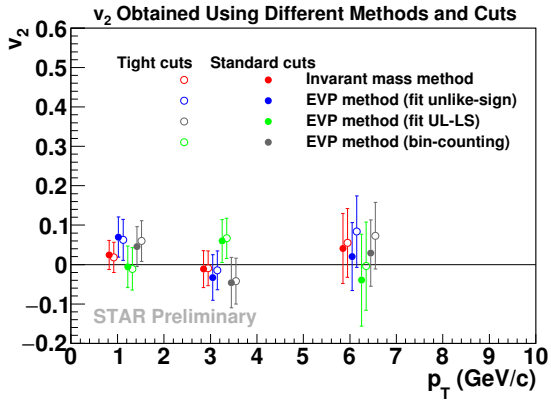

Figure 5: J/ψ v_2 vs. p_T calculated by event plane method (with three methods of yield extraction) and invariant mass method. Both methods are shown with a use of standard and tight cuts. The figure is taken from [4].

physical values of v_2 are probably even lower due to non-flow contribution.

References

[1] M. R. Lomnitz. Measurement of D-meson azimuthal anisotropy in Au+Au GeV collisions at RHIC. *Nucl Phys* **A956**:256–259, 2016. 1601.00743.

[2] D. Kikola, et al. Prospects for quarkonia production studies in U + U collisions. *Phys Rev* **C84**:054907, 2011. 1111.4693.

[3] Y. Pandit, et al. Azimuthal anisotropy in u+u collisions at $\sqrt{s_{NN}}$ = 193 gev with star detector at rhic. *Journal of Physics: Conference Series* **458**(1):012003, 2013.

[4] A. Harlenderova for the STAR Collaboration. Measurement of J/ψ azimuthal anisotropy in U+U collisions at $\sqrt{s_{\rm NN}} = 193$ GeV by the STAR experiment. *Quark Matter 2017* .

[5] R. Ma. J/ψ and Υ measurements via the di-muon channel in Au + Au collisions at $\sqrt{s_{NN}} = 200$ GeV with the STAR experiment. *Nucl Phys* **A956**:725–728, 2016. 1512.08713.

SIGNAL EXTRACTION IN J/Ψ PHOTOPRODUCTION WITH ALICE

Tomáš Herman*

Faculty of Nuclear Sciences and Physical Engineering, Czech Technical University in Prague , Břehová 7, Prague, Czech Republic

* corresponding author: hermato8@fjfi.cvut.cz

Abstract. The behaviour of the gluon distribution in protons and nuclei can be studied with ALICE at the LHC using exclusive photoproduction of J/Ψ. When the J/Ψ are measured in the dilepton decay channel, the yield is extracted by modelling the invariant mass distribution of the decay products. The most frequently used model is called Crystal Ball. But recently there has been proposed a new model called GaussExp [1], which is allegedly better suited for analysis of high energetic peaks with radiation tails. Performances of these two models will be tested on both Monte Carlo and real data, to establish which one of them is superior. This is important because signal extraction is one of the largest contributors to the total systematic uncertainty of the measurement. The hope is that the new model may help in reducing the systematic uncertainty from signal extraction.

Keywords: signal extraction, GaussExp, Crystal Ball.

1. Introduction

The composition of the proton is described by parton distribution functions $xf(x, Q^2)$, where x is the fraction of the momentum of the proton carried by the parton and Q^2 is the four momentum transferred in the scattering (between the parton and the used probe). Each type of parton f (quarks/gluons) has its own distribution function. In leading order $xf(x, Q^2)$ can be interpreted as the number of the given parton in the proton.

The parton composition of the proton is not constant, as can be seen in Figure 1. At large x the proton is composed of 1/3 down quarks and 2/3 up quarks. This is not surprising, because one up and two down quarks are the valence quarks of a proton. However, when we measure at small x the valence quarks become negligible and other partons become significant. First of them are sea quarks, which are virtual quark-antiquark pairs and second are gluons.

The distribution function is also proportional to the cross section for given parton. And at some point the cross section of the partons would become bigger than that of the proton, which is impossible. Therefore a process referred to as saturation must occur. Saturation is one of the main areas of study in pQCD today. UPC measurements can shed light on this phenomenon from the experimental side.

2. Deep-inelastic scattering

Deep-inelastic scattering is one of the processes used to measure parton distribution functions. A high energy lepton is collided with a hadron and they interact through photon exchange. This photon has very high momentum (low wavelength), therefore it interacts only with one parton in the hadron. The energy

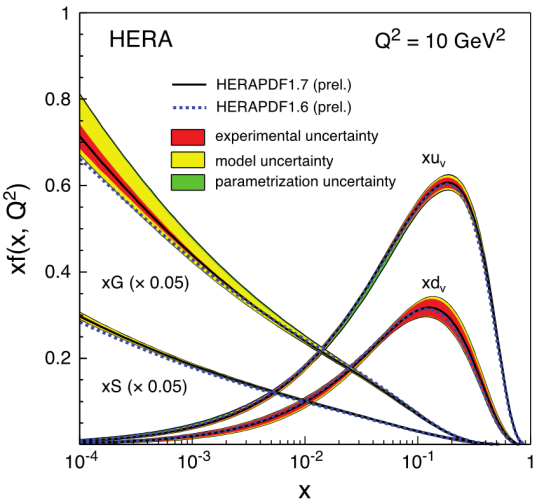

Figure 1: The parton distribution functions from HERA at $Q^2 = 10$ GeV^2. The gluon and sea quarks distributions are scaled down by a factor of 20. [2]

transfer in the collision is so massive that the proton is shattered after the collision.

3. Ultra-peripheral collisions

A process similar to deep-inelastic scattering can be studied in hadron colliders in so called ultra-peripheral collisions (UPC). Collisions in hadron colliders can be classified by their centrality. For this we need to introduce the concept of the impact parameter, which is the distance between the centres of the two incoming particles in the plane transverse to the direction of their movement. When the impact parameter b is approximately 0, the collisions is called central (or head on), when the impact parameter is not 0, but

still smaller then the sum of the radii of the colliding particles, the collision is called semi-central or for larger impact parameters, peripheral. When the impact parameter is larger then the sum of the radii of the two colliding particles, the collision is called ultra-peripheral.

When an ion (e.g. lead) is accelerated nearly to the speed of light, its electromagnetic field is flattened to a circular shape. This flat electromagnetic field can be then described as an arrangement of virtual photons and these photons can collide with the proton.

4. Analyses

We are interested in UPC where one J/Ψ is produced. We measure the J/Ψ using its decay into a pair of leptons: e^+e^- or $\mu^+\mu^-$. When traversing a medium such particles lose energy via radiation of photons, which are not detected by the detector, therefore we do not measure the complete energy of the produced particle. This effect causes a different shape of the measured signals. They are not classical Gaussian but a Gaussian with a tail. We use special models to fit this kind of signals.

4.1. Crystal Ball

The most commonly used model to fit the invariant mass distribution from the decay of a J/Ψ is called Crystal Ball.

$$\begin{aligned} f(x;\alpha,n,\bar{x},\sigma) &= e^{-\frac{1}{2}\left(\frac{x-\bar{x}}{\sigma}\right)^2} \quad \text{for} \quad \frac{x-\bar{x}}{\sigma} > -\alpha \\ &= \left(\frac{n}{|\alpha|}\right)^n e^{-\frac{|\alpha|^2}{2}} \left(\frac{n}{|\alpha|} - |\alpha| - \frac{x-\bar{x}}{\sigma}\right)^{-n} \\ &\qquad \text{for} \quad \frac{x-\bar{x}}{\sigma} \leq -\alpha \end{aligned} \tag{1}$$

Here x stands for the invariant mass of a given lepton pair. The disadvantage of this formula is the fact that it contains parts like $\left(\frac{n}{|\alpha|}\right)^n$. That is the fraction of two fit parameters to the power of one of the parameters. Such expressions are extremely hard to fit with good precision.

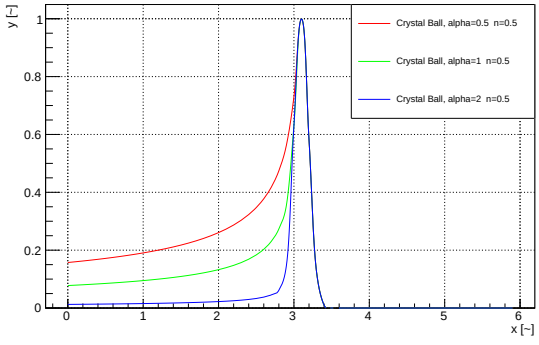

Figure 2: Crystal Ball function drawn with changing α parameter.

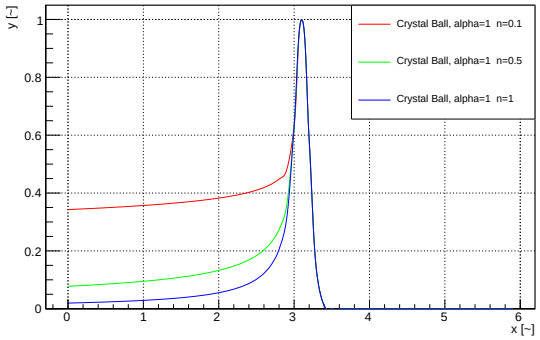

Figure 3: Crystal Ball function drawn with changing n parameter.

Figures 2 and 3 show the behaviour of the Crystal Ball function for different values of its parameters. The α parameter mainly influences the position of the tail and the n parameter influences the shape of the tail.

4.2. GaussExp

GaussExp function [1] is a new model proposed to be better suited to describe the invariant mass distribution of dileptons coming from a J/Ψ.

$$\begin{aligned} f(x;k,\bar{x},\sigma) &= e^{-\frac{1}{2}\left(\frac{x-\bar{x}}{\sigma}\right)^2} \quad \text{for} \quad \frac{x-\bar{x}}{\sigma} \geq -k \\ &= e^{\frac{k^2}{2}+k\left(\frac{x-\bar{x}}{\sigma}\right)} \quad \text{for} \quad \frac{x-\bar{x}}{\sigma} < -k \end{aligned} \tag{2}$$

The formula seems simpler then that of CB model and does not contain any part with parameter to the power of parameter. The goal of my thesis is to study the performance of this new model when compared to the CB model.

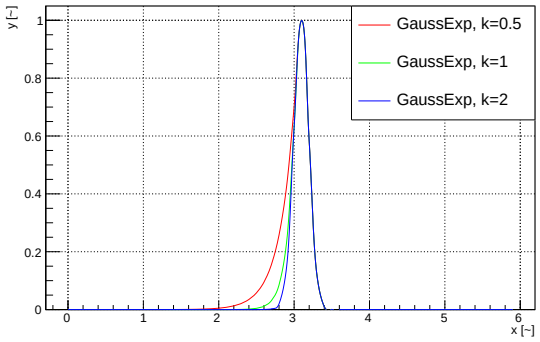

Figure 4: GaussExp function with changing k parameter.

The GaussExp function has only one parameter, unlike the Crystal Ball, so this parameter is responsible for both the position and shape of the tail, as can be seen on Figure 4.

On Figure 5 can be seen a comparison of both models with classical Gaussian function.

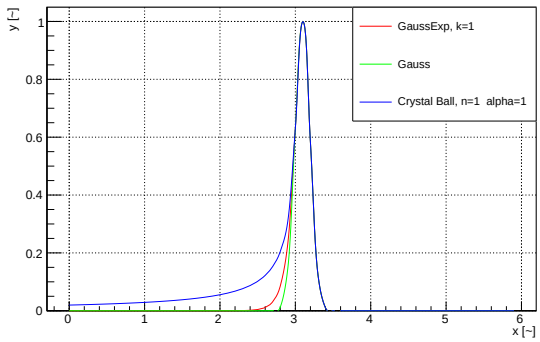

Figure 5: Comparison of Crystal Ball and GaussExp models with Gaussian.

GaussExp and Crystal Ball models will be tested on various Monte Carlo data with clean signal and also with different backgrounds. After that they will be also tested on real data from ALICE.

5. Conclusions

These studies are important because signal extraction is one of the largest contributors to the total systematic uncertainty of the measurement. The hope is that the new model may help in reducing the systematic uncertainty from signal extraction.

References

[1] S. Das. A simple alternative to the Crystal Ball function 2016. 1603.08591.

[2] R. Placakyte. Parton Distribution Functions. In *Proceedings, 31st International Conference on Physics in collisions (PIC 2011): Vancouver, Canada, August 28-September 1, 2011*. 2011. 1111.5452.

ANALYSIS OF THE IS521 EXPERIMENT DATA

Lukas Holub*

Czech Technical University, Brehova 7, Prague, Czech republic

* corresponding author: holubl11@fjfi.cvut.cz

Abstract.

The aim of this work is to perform energy calibration of the Broad Energy Germanium (BEGe) detector which was used in experiment IS521 at CERN-ISOLDE facility. The main goal of this experiment was to explore shape coexistence in odd-Au isotopes. Physical background and technical details of the IS521 experiment are presented. The energy calibration was performed using two different approaches, results are compared. The stability of the elctronics and detector was investigated in a great detail.

Keywords: calibration of the detector, TATRA system, BEGe detector .

1. Introduction

The age of nuclear detectors started with the Geiger-Muller counters which were able to detect radiation such as alpha particles, beta particles and also gamma rays. They were using the ionization effect produced in a Geiger-Muller tube which was constructed in 1928.

Progress in detectors which are able to detect radiation or any particles is huge in last few decades. A quality of these detectors rises. Advances in materials, particularly ultra-pure materials, and methods of fabrication was critical to the creation of new and better detectors which are used in experiments nowdays.

For accurate determination of energy of released radiation in nuclear-structure experiments is necessary to have suitable detectors which measure in appropriate range of energy. This range can be affected by outside radiation from different sources. Example of such a detector is novel Broad Energy Germanium (BEGe) detector. The goal of this work is to calibrate BEGe detector which was used in IS521 experiment at CERN-ISOLDE facility.

The work is devided into three chapters. In the first chapter, we described physical background of this experiment which includes the Beta decay, interaction of the gamma radiation with the matter, internal conversion of electrons, Augger effect and briefly phenomenon of the shape coexistence in atomic nuclei. Subsequently, in the second chapter we describe experimental devices and facilities such as the ISOLDE, the BEGe detector and system which was used in IS521 experiment. Expecially, in this chapter we describe TATRA tape trasportation system which was designed and constructed at the Institute of Physics of Slovak Academy of Science in Bratislava. In third chapter we describe a way how we performed energy calibration of the data and which computer programmes we used for reading of the energy spectrum.

2. Physical part of the experiment

2.1. Beta decay

2.1.1. β^- decay

It is an emission of negative electrons from the nucleus where one neutron decays via β^- decay into a proton. The basic equation for this case is:

$$ {}^1_0n \rightarrow {}^1_1 p + e^- + \bar{\nu}_e, \tag{1}$$

and the general equation of the β^- decay is:

$$ {}^A_Z X \rightarrow {}^A_{Z+1} Y + e^- + \bar{\nu}_e, \tag{2}$$

where ${}^A_Z X$ is a initial element, ${}^A_{Z+1}Y$ is a final element, e^- is an electron and $\bar{\nu}_e$ is an electron anti-neutrino.

Total released energy Q in a given nuclear decay is given by equation:

$$ Q_{\beta^-} = [m_N({}^A_Z X) - m_N({}^A_{Z+1}Y) - m_{e^-} - m_{\bar{\nu}_e}]c^2, \tag{3}$$

2.1.2. β^+ decay

It is the second type of the beta decay in which the weak interaction converts a proton inside a nucleus into a neutron while releasing a positron e^+ and electron neutrino ν_e. This process is described as:

$$ {}^1_1p \rightarrow {}^1_0 n + e^+ + \nu_e. \tag{4}$$

The general equation for this decay is:

$$ {}^A_Z X \rightarrow {}^A_{Z-1} Y + e^+ + \nu_e, \tag{5}$$

where ${}^A_Z X$ is a initial element, ${}^A_{Z-1}Y$ is a final element, e^+ is a positron and ν_e is an electron neutrino.

The energy released in this decay is given by equation:

$$ Q_{\beta^+} = [m_N({}^A_Z X) - m_N({}^A_{Z-1}Y) - m_{e^+} - m_{\nu_e}]c^2, \tag{6}$$

2.1.3. Electron capture

It is a nuclear process in which the nucleus of the electrically neutral atom absorbs an inner electron most likely from the K or L electron shell. During this process the nuclear proton changes into the neutron and it causes the emission of the electron neutrino:

$$ {}^{1}_{1}p + e^{-} \rightarrow {}^{1}_{0}\, n + \nu_e. \tag{7} $$

Electron capture takes place only in proton rich nuclei and proceeds as:

$$ {}^{A}_{Z}X + e^{-} \rightarrow {}^{A}_{Z-1}\, Y + \nu_e, \tag{8} $$

where ${}^{A}_{Z}X$ and ${}^{A}_{Z-1}Y$ are initial and final element, e^{-} is the electron and ν_e is the electron neutrino.

Let us derive value of the released energy Q_{CE}. Generally, the equation for released energy is:

$$ Q_{CE} = [m_N({}^{A}_{Z}X) + m_e - m_N({}^{A}_{Z-1}Y) - m_{\nu_e}]c^2, \tag{9} $$

2.2. Photoelectric effect

The photoelectrin effect, which was for the first time explained by Albert Einstein it is an another process in which the photon interacts with the electron is a process in which a gamma photon interacts with an orbital electron of the atom. During this interaction, the energy of the photon is absorbed by the atom. The entire photon energy is transferred to the electron of the atom and this electron is released from the atom. The kinetic energy of the ejjected electron is given by the equation:

$$ E_{electron} = h\nu_{photon} - W, \tag{10} $$

where W is minimum energy required to remove electron from the surface of the metal, h is the Planck constant and f is the frequency of the incident photon.

2.3. Compton effect

During this interaction the photon with the energy E_γ imparts only a fraction of its energy to the electron and then this photon is scattered with energy $E^{'}_{\gamma}$ at an angle Θ, while the bombarded electron is ejected at an angle Φ to the trajectory of the incident photon. The shift in wavelengths of incident and scattered photon is created. This shift is given by equation:

$$ \lambda^{'} - \lambda = \frac{h}{m_0 c}[1 - cos(\Theta)], \tag{11} $$

where $\lambda^{'}$ is the wavelength after scattering, λ is the initial wavelength, h is Planck constant, c is speed of light, m_0 is the electron rest mass and Θ is the scattering angle.

2.4. Electron - positron pair production

It is a formation of pairs of electrons and positrons, usually in the vicinity of an atomic nucleus. This process has threshold of 1.022 MeV Consequently, this process is a direct conversion of energy to a matter. Posintron is than passing through the matter loosing the kincetic energy in collisions with atoms. As soon as it is in rest it undergoes the annhilation process. Result of this is emmision of two 511 keV gamma quanta. If this happens in the gamma detector three scenarious are possible:

- both 511 keV photons are absorbed in the detector: these events contribute to the photopeak
- one of the 511 keV photons escapes from the detector: in this case an artificial peak with energy of E_γ - 511 keV appears in the spectrum
- both 511 keV photons escape from the detector: in this case an artificial peak with energy of E_γ - 1022 keV appears in the spectrum

If positron annihilates in surrounding materials, the 511 keV line appears in the spectrum. Therefore, if the source emmiting gamma rays well above 1022 keV for lines instead of one are expected in the spectrum.

2.5. Internal conversion

It is a process when the excitation energy is transformed from atomic nucleus onto one of the atomic electrons, which leaves the atom. This leaves a vacancy in the atomic shell therefore, similar atomic relaxation processes (X-rays fluorescence, Auger electron emmision). Kinetic energy of the electron is given as:

$$ E_e = (E_i - E_f) - E_b, \tag{12} $$

where E_e is the kinetic energy of the emitted electron from the atom, E_i and E_f are energy states of the nucleus and E_b is the binding energy of the electron.

The ratio of internal conversion to gamma emission photons is known as the internal conversion coefficient α :

$$ \alpha = \frac{N_e}{N_\gamma}, \tag{13} $$

where N_e is the number of de-excitation via electron emmision and N_γ is the number of de-excitations via γ-ray emission. For total number of passes in atomic nucelus, let us lable N_T, we have $N_T = N_\gamma + N_e$. Using the internal conversion coefficient α we obtain:

$$ N_T = N_\gamma(1 + \alpha). \tag{14} $$

Internal conversion coefficients are functions of transition energy, proton number and transition multipolarity and can be calculated theoretically. Usefull tool is the BRICC software developed at the Australian National University in Canberra, which is available online, see http://bricc.anu.edu.au/.

2.6. Auger effect

It is a physical phenomenon in which the filling of an inner-shell vacancy of an atom is accompanied by the emission of an electron from the same atom. When a core electron is removed, leaving a vacancy, an electron from a higher energy level may fall into the vacancy, resulting in a release of energy. Although

most often this energy is released in the form of an emitted photon, the energy can also be transferred to another electron, which is ejected from the atom, this second ejected electron is called an Auger electron.

2.7. Shape coexistence

The shape of a nucleus is one of the most fundamental properties of an atomic nuclei. It is governed by the interplay of macroscopic, liquid-drop like properties of the nuclear matter and microscopic shell effects. The shape of atomic nucleus is determined by number of nucleons present in the the nucleus and the interaction between them. For example, if the proton and neutron shells are completely filled than atomic nucleus in ground state has a spherical shape. In case, that nucleus is in excited state or some nucleons are added, the long-range correlations between valence nucleons disrupt the sferical symmetry and shape of the atomic nucleus becomes deformed. The simplest type of the deformation is axially symmetric rotiational ellipsoid, which has either prolate (rugby-ball-like) or oblate (discus-like) shape. It has been found in the nature that prolate shape dominates. If all three principal axes of the nucleus are different than nucleus is called triaxial. Few nuclei have been found to have a static octupole deformation (pear shaped nuclei).

In some areas of the nuclear chart the shape is very sensitive to structural effects and can change from one nucleus to its neighbor. In addition to shape changes with proton or neutron number, the shape can also change with excitation energy or angular momentum within the same nucleus. Such changes are caused by a rearrangement of the orbital configuration of the nucleons or by the dynamic response of the nuclear system to rotation.

3. Technical part of the experiment

3.1. ISOLDE

Nowadays, very progressive technique for experimental nuclear physics is production of radioactive-ion beams. The worldwide leading facility in the research area is ISOLDE (The Isotopes mass Separator On-Line DEtector), which is operational at CERN since 1965. Excepts of nuclear physics, ISOLDE covers fields of atomic physics, chemistry, biology, medicine, solid state physics, fundamental physics and nuclear astrophysics. The ISOLDE facility is operated and maintained by the ISOLDE collaboration which is a consortium of 17 countries.

For radioactive-ion beam production ISOLDE is using infrastructure of pre-accelerators of the LHC. The beam of protons with energy of 1.4 GeV delivered by the PS Booster impinges on thick target inducing spallation nuclear reactions. The reaction products are ionized using various technique, extracted from the ion source, mass separated and delivered to experimental station. If needed the beam can be post-accelerated using the REX and HIE-ISOLDE linear accelerators, which are able to accelerate the beam up to 5.5 MeV/nucleon.

ISOLDE offers option of using of so called travelling detection setups. These are systems developed at home institutes and subsequently transported to CERN here they are connected to the dedicated ISOLDE beamline (denoted as LA1). The radioactive beam is then delivered. Example of this is the TATRA system developed at the Institute of Physics, Slovak Academy of Sciences in Bratislava for precise β-decay studies.

3.2. TATRA

TATRA system is a unique tape transportation system that was used in IS521 experiment. The TATRA system provides a high quality of the vacuum. Another good properties of this system are the low weight and thus posibility of easy transport to CERN, versatility and simple connection with the source of the beam line of any low-energy radioactive-ion beam facilities.

The TATRA system is housed in a cylindrical vacuum, steel chamber with diameter 425mm and a height of 160mm. Inside the chamber the heart of the system is situated. This heart is created from the metallic tape, tape reel, beam dump, measurement position, ballance lever, viton wheels, capstan and several pulleys. Metallic tape has a width of 6mm and a length of 25m. It is created at the Institute of Physics, by special technique that is called the Planar flow casting technique. A sample of radioactive isotopes is produced by a deposition of the radioactive-ion beam onto the metallic tape Using capstan and two additional wheels, that are made from Viton rubber, the tape with radioactive nuclides is driven to the measurement position where detectors are located and measure nuclear activity. The capstan is connected to an externally-mounted stepper motor. The diameter of the capstan is 32mm. After measurement, the tape passes through the capstan and reels on the tape reel from the outside then it is pulled from the centre of the reel. This process is repeated periodically. The deposition and measurement times are selected according to the half life of the studied isotopes and to the yield of the radioactive ion beam.

There are together seven flanges from the outside of the cylindrical chamber. On the top are two flanges, one for vacuum measurement gauge and another one for standart mechanical manometer. Next flange deserves on the connection of the chambre and radioactive-ion beam line facility. The fourth flange is connected with the vacuum pump. A value of the vacuum that is created in the chamber is less than $10^{-5}Pa$. Two more flanges are used for connection with picoampermeters. The last flange is connected with the container with nitrogen. This nitrogen is used for creation of atmospheric pressure in the chamber. The reason, why we use nitrogen and not atmospheric

air is, that nitrogen from bottle is dry while the air contains a humidity which might harm this apparatus.

During the experiment is really important to suppress all possible vibration from different sources (e.g. turbomolecular pump, radioactive-ion beam facility, vibration from the outside), because of these vibration could cause deterioration of the energy resolution of conversion electrons detector. To suppress a shock wave in a tape during quick start and stop the balance lever is used, because the inertia of the tape reel and tape might tear the tape at the exit of the reel.

3.3. BEGe detector

Radiation due to samples of Hg isotopes is detected by germanium detectors when a samples of radioactive isotopes reaches the measurement position. There were two types of detectors which were used in this experiment. The first one was coaxial High Purity Germanium (HPGe) detector with relative efficiency of 80% and second one was a modern detector of type Broad Energy Germanium (BEGe). Let us describe features and benefits of BEGe detector.

The energy range of this detectors is from 3 keV up to 3 MeV. At low energies, the resolution of the detector is equal to the resolution of The Low Energy Germanium (LEGe) detector and vice versa at high energies the resolution is similar to The Standart Electrode coaxial Germanium (SEGe) detector. However, BEGe detectors are approriate especially for detection of radiation with energy below 1 MeV because of, its a short, planar shape which was chosen for improvement of the efficiency of typical real samples in the energy range that is the most important for routine gamma analysis.

The BEGe detector is designed with an electrode structure that enhances low energy resolution and is fabricated from selected germanium having an impurity profile that improves charge collection at high energies.

3.4. Data Acquisition system - DAS

Output of pre-amplifier of germanium detectors is voltage signal is exponentialy decaying voltage pulse. This pulse was futher amplified by dedicated circuits designed at the University of Liverpool. They increased the amplitude of the signal without shaping. For the analysis of the signal fully digital data acquisition system was used. The system is based on commercial digitizer Pixie-16 that operate on the PXI bus. PIX bus is a rugged PC-based platform for measurement and automation systems. PXI combines PCI electrical-bus features with the modular, Eurocard packaging of CompactPCI and then adds specialized synchronization buses and key software features. Analog singnal is digitized with the sampling frequency of 250 MHz. Subsequently, digital trace of the signal is analyzed by processor onboard of the Pixie-16 module. For each signal the amplitude is calculated.Signals are timestamped and transfered to the PC via optical cable. They are recorded on the RAID6 with four disks, 4 TB each.

4. Results

Very important part of the whole experiment was calibration of the detectors. The calibration is process of finding a relationship between arbitrary units of the data acquisition system (channels) and energy in units of keV. In this work a relative calibration was used, which means that energy was measured and calculated relative to known γ rays of ^{241}Am, ^{133}Ba, ^{152}Eu, and ^{137}Cs standards. Using of online Table of Radioactive Isotopes [*http : //nucleardata.nuclear.lu.se/toi/*], we assigned energy value to each isotope, see in (Tab.1)

Channel	Ch.err	Energy	E.err	Isotope
2029.96	0.0035	59.5412	0.0002	^{241}Am
2762.54	0.038	80.9971	0.0014	^{133}Ba
4154.97	0.031	121.7817	0.0003	^{152}Eu
8351.72	0.1	244.6975	0.0008	^{152}Eu
9433.11	0.13	276.398	0.002	^{133}Ba
10337.98	0.078	302.853	0.001	^{133}Ba
11751.77	0.06	344.2785	0.0012	^{152}Eu
12152.19	0.044	356.017	0.002	^{133}Ba
22586.26	0.043	661.657	0.003	^{137}Cs
26588.42	0.19	778.904	0.0018	^{152}Eu
29609.36	0.45	867.378	0.004	^{152}Eu

Table 1: Energies and channels of isotopes which was used for relative calibration

Whole process was done step by step. Firstly, fitting function had to be created. For this, we used channels and energies of isotopes from (Tab.1). These functions are

$$E = 0.067605 + 0.029292ch \quad (15)$$

$$E = 0.087622 + 0.029288ch + 1.269210^{-10}ch^2, \quad (16)$$

where E and ch means energy and channel respectively. These functions were used for chalculating of energies for ^{183} Hg decay.

For calibration was necessary to use appropriate software, in which one could see all energy peaks very clearly. Such the suitable software was "*tv*". It is a spectra-analysis and matrix-analysis program which runs under the operating system UNIX.

After creating of spectrum, we had to fit each peak of the spectrum because any background was also presented there. The numbers of the channel of the fitted peaks and calculated energies are written in the table which is not presented here because of size of this table.

During the analyses of the data we also found out that electronics did not flow, what means that there were not any significant vibration from vacuum pump or radioactive-ion beam facility.

5. Conclusions

The goal of the work was investigation of the energy calibration of the novel BEGe detector. The data arise from the IS521 experiment performed at the CERN-ISOLDE facility. BEGe detector is a planar detector with excellent energy resolution. For the energy calibration, ^{152}Eu, ^{133}Ba, ^{241}Am and ^{137}Cs standards were used. Linear and quadratic polynomial functions were used to calibrate the detector. After the energy calibration, the energies of gamma rays in the spectrum of the decay of mass-separated ^{183}Hg samples were determined. The difference between these two calibration curves was manifested. The difference is up to 100 eV. However, the IS521 experiment is intended to measure γ-ray energies precisely, therefore this difference cannot be ignored and calibration must be carefully investigated for the final analysis. The stability of the detector and electronics was investigated using peaks of the ^{183} Hg decay spectrum. No significant floating of peaks was observed.

References

COHERENT PHOTOPRODUCTION OF ρ^0 MESON IN PB-PB ULTRA-PERIPHERAL COLLISIONS AT ALICE

David Horak*

FNSPE CTU in Prague, Brehova 7, Praha 1, Czech republic

* corresponding author: david.horak@cern.ch

Abstract.

The LHC is not only the most powerful collider for proton-proton and heavy-ion collisions, but it is also the most powerful source of photon collisions. The relativistic protons and ions carry an electromagnetic field, which can be viewed as a beam of photons. Photon-photon and photon-proton (or proton-lead) processes can be studied in ultra-peripheral collisions (UPC). These processes, in particular photoproduction of vector mesons, offer an unique opportunity to study fundamental interactions in QED and QCD.

Keywords: ALICE, photoproduction, ultra-peripheral collision, rho meson.

A collision of two particles is characterized by an impact parameter b, which is defined as the perpendicular distance between the path of the two particles. When two fast charged particles collide with an impact parameter larger than the sum of nuclear radii, the strong interaction is suppressed due to its short range and only electromagnetic interactions may occur. This we call an ultra-peripheral collision. The electromagnetic field of relativistic nuclei is contracted and its intensity (and the number of virtual photons surrounding the nucleus) is proportional to Z^2 [1].

In ultra-peripheral collisions it is possible to study exclusive photoproduction of ρ^0 meson. This process can be coherent or incoherent. In the former, the transversal momentum p_T of created vector meson is very low and creates diffractive peaks. In the latter the p_T is shifted to the higher values. The ALICE experiment provides a great oportunity to study ultra-peripheral collisions thanks to its good resolution at low p_T. The ρ^0 meson decays dominantly into a $\pi^+\pi^-$ pair.

The photoproduction of ρ^0 was measured at ALICE at the LHC using Run 1 data at $\sqrt{s_{NN}} = 2.76\,\text{TeV}$. The measured cross section was in agreement with STARLIGHT [2] and the calculation by Gonçalves and Machado (GM) [3], while the Glauber-Donnachie-Landshoff (GDL) prediction [4] overestimate the data of factor of 2. This result indicate that further work is needed to understand this process [5].

For Run 2 new detectors at ALICE were installed. One of them was ALICE Diffractive (AD) Detector, which is formed by two scintillation arrays on both sides (ADA and ADC). The ADA covers a pseudorapidity interval: $4.8 < \eta < 6.3$ while the ADC covers: $-7.0 < \eta < -4.9$ [6]. This detector provides better acceptance for rejection of beam-gas and dissociative background. The new measurement in Run 2 will be at higher energy at $\sqrt{s_{NN}} = 5.02\,\text{TeV}$.

A typical UPC event is characterized by a small number of tracks. The beam-gas background events can be rejected by online trigger using V0 and AD detectors, which have to be by empty when the ρ^0 is produced. Then pions are identified by means of ionization losses in a time projection chamber (TPC). Also these events should have opposite charge. If not, it means that there are lost tracks and those ones can be used to determine the number of lost good tracks.

The invariant mass of $\pi^+\pi^-$ pair has not a Breit-Wigner shape due to two pion non-resonant production. This shape can be described by the Soeding formula or by the Ross-Stodolski formula [5]. In Run 2 also ω resonance is expected to be visible, which causes a "kink" in the invariant mass spectrum.

Run 2 provides more than an order of magnitude more data than Run 1. That allows precise measurement of rapidity and t–dependence of the protoproduced ρ^0 meson at higher energy. Also the new data may offer the possibility of measuring new particles that were never measured in UPC before.

References

[1] C. A. Bertulani, et al. Physics of ultra-peripheral nuclear collisions. *AnnRevNuclPartSci* **55**:271–310, 2005. nucl-ex/0502005.

[2] S. R. Klein, et al. STARlight: A Monte Carlo simulation program for ultra-peripheral collisions of relativistic ions. *Comput Phys Commun* **212**:258–268, 2017.

[3] V. P. Gonçalves and V. T. Machado. Photoproduction of Rho0 meson in ultraperipheral heavy ion collisions at the BNL RHIC and CERN LHC. *Phys Rev* **C 80**(054901), 2009.

[4] L. Frankfurt, M. Strikman, and M. Zhalov. Signals for black body limit in coherent ultraperipheral heavy ion collisions. *PhysLett* **B537**:51–61, 2002.

[5] ALICE Collaboration. Coherent ρ^0 photoproduction in ultra-peripheral Pb–Pb collisions at $\sqrt{s_{\rm NN}} = 2.76$ TeV 2015. 1503.09177.

[6] G. Herrera Corral. Diffractive Physics with ALICE at the LHC: the control of quantum collisions. *Conference Series 624* **012008**, 2015.

CP VIOLATION IN THE $B_S^0 \to J/\psi\phi$ DECAY ON ATLAS

Tomas Jakoubek*

Institute of Physics of the Czech Academy of Sciences, Na Slovance 1999/2, Prague, Czech Republic

* corresponding author: tomas.jakoubek@cern.ch

Abstract. An overview of a measurement of time-dependent CP asymmetry parameters in $B_s^0 \to J/\psi(\mu^+\mu^-)\phi(K^+K^-)$ decays from a 14.3 fb^{-1} data sample of pp collisions collected with the ATLAS detector during the 2012 $\sqrt{s} = 8$ TeV LHC run, combined with previous ATLAS measurement using 4.9 fb^{-1} of 2011 $\sqrt{s} = 7$ TeV data, is presented. In the Standard Model CP violation is described by a phase in the CKM matrix. One of the manifestations of this complex phase is a phase shift between direct and mixing-mediated B_s^0 decays producing a common final state. In the case of $B_s^0 \to J/\psi(\mu^+\mu^-)\phi(K^+K^-)$ this phase shift is predicted to be small $\phi_s = -0.0368 \pm 0.0018$ rad. New physics can enhance ϕ_s whilst satisfying all existing constraints. Results presented in this talk are compatible with the Standard Model predictions and with other LHC measurements.

Keywords: CP Violation, Bs J/psi Phi, ATLAS, CERN, B Physics, Flavor Physics.

1. Introduction

The $B_s^0 \to J/\psi\phi$ decay channel is expected to be sensitive to new physics contributions in CP violation field of study. In this channel, CP violation occurs due to interference between direct decays and decays occurring through $B_s^0 - \overline{B_s^0}$ mixing. The frequency of this mixing is characterized by the mass difference ΔM_s between light (B_L) and heavy (B_H) mass eigenstates. Difference between decay widths can be described using a CP-violating phase ϕ_s

$$\Delta\Gamma_s = \Gamma_L^s - \Gamma_H^s = 2\,|\Gamma_{12}^s|\,\cos\phi_s, \qquad (1)$$

where Γ_L^s and Γ_H^s are decay widths of B_L and B_H states respectively. ϕ_s is small in the context of the Standard Model and can be related to CKM quark mixing matrix via the relation

$$\phi_s \simeq -2\,\arg\left(-\frac{V_{ts}V_{tb}^*}{V_{cs}V_{cb}^*}\right). \qquad (2)$$

Predicted value is $\phi_s = -0.0368 \pm 0.0018$ rad. Many new physics models predict large ϕ_s values whilst satisfying all existing constraints, including the precisely measured value of ΔM_s.

2. Data, Reconstruction, and Candidate Selection

The analysis is based on 4.9 fb^{-1} of $\sqrt{s} = 7$ TeV data from proton-proton collisions collected with the ATLAS detector in the year 2011 (separate study [1], published in 2014), combined with 14.3 fb^{-1} of $\sqrt{s} = 8$ TeV data from the year 2012 into the complete Run 1 results presented here [2].

To be selected, events must contain at least one reconstructed primary vertex, formed from at least four Inner Detector (ID) tracks, and at least one pair of oppositely charged muons reconstructed using information from the Muon Spectrometer (MS) and the ID. Pairs of oppositely charged muon tracks are refitted to a common vertex and the pair is accepted if $\chi^2/\text{ndf} < 10$. In order to account for varying mass resolution in different parts of the detector, the $|\eta(\mu)|$ dependent J/ψ mass cuts are applied. Decays $\phi \to K^+K^-$ are reconstructed from all pairs of oppositely charged particles with $p_\text{T} > 1$ GeV and $|\eta| < 2.5$ that are not identified as muons. Candidates for B_s^0 are selected by fitting the four tracks to a common vertex with J/ψ mass constrain [3]. Candidate is accepted if the vertex fit has $\chi^2/\text{ndf} < 3$ and $|m(K^+K^-) - m_\text{PDG}(\phi)| < 11$ MeV. If there is more than one accepted B_s^0 candidate in the event, the one with the lowest χ^2/ndf is selected.

For each B_s^0 candidate the proper decay time t is calculated:

$$t = \frac{L_{xy}\; m(B_s^0)}{p_\text{T}(B_s^0)},$$

where $p_\text{T}(B_s^0)$ is the transverse momentum of the B_s^0 meson and $m(B_s^0)$ is the mass of the B_s^0 meson, taken from [3]. The transverse decay length L_{xy} is the displacement in the transverse plane of the B_s^0 meson decay vertex with respect to the primary vertex, projected onto the direction of the B_s^0 transverse momentum.

Flavour tagging is used to improve this CP violation measurement. Initial flavour of (neutral) B_s^0 can be inferred using the other B-meson, typically produced in the event (so called "Opposite-Side Tagging" method). To study and calibrate these methods, events containing the decays of "self-calibrated" channel $B^\pm \to J/\psi K^\pm$ can be used (flavour of the B-meson at production is provided by the kaon charge).

Detector effect have been studied using Monte Carlo (MC) samples. So-called "acceptance maps" (relying

on three angles and p_T) have been created and applied to the data. Also an observed time dependence of the muon trigger have been corrected by weighting function (derived using real data and MC).

3. Results

Time-angular unbinned maximum likelihood fit have been then performed on B_s^0 candidates within a mass range of 5.15 GeV $< m(B_s^0) <$ 5.65 GeV to extract the parameters characterising the decay. The full fit contains 25 free parameters. Below the important physical parameters are summarized: mean B_s^0 lifetime, the decay width difference $\Delta\Gamma_s$, and the CP-violating week phase ϕ_s. All results (2011, 2012, and the full Run 1 statistical combination) are consistent with the world average values. Mass and lifetime fit projections are shown in Figure 1 and Figure 2 respectively. Comparison with other experiments is shown in Figure 3.

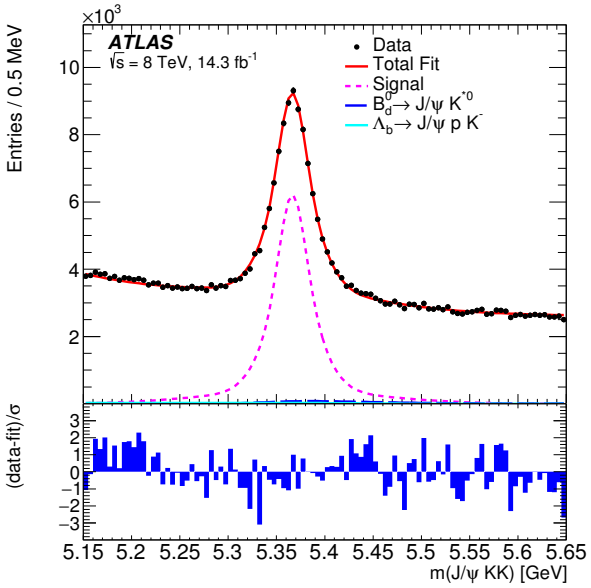

Figure 1: Mass fit projection for the 2012 data. The red line shows the total fit, the dashed green line shows the signal component while the long-dashed blue line shows the contribution from $B_d^0 \to J/\psi K^{0*}$ events.

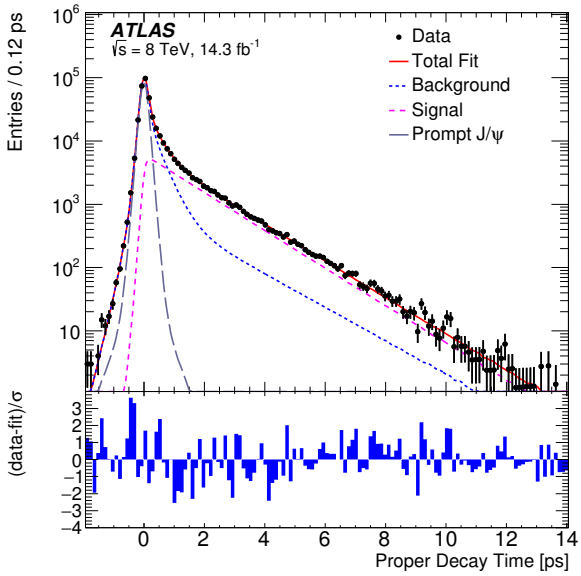

Figure 2: Proper decay time fit projection for 2012 data. The red line shows the total fit while the green dashed line shows the total signal. The total background is shown as a blue dashed line with a long-dashed grey line showing the prompt J/ψ background.

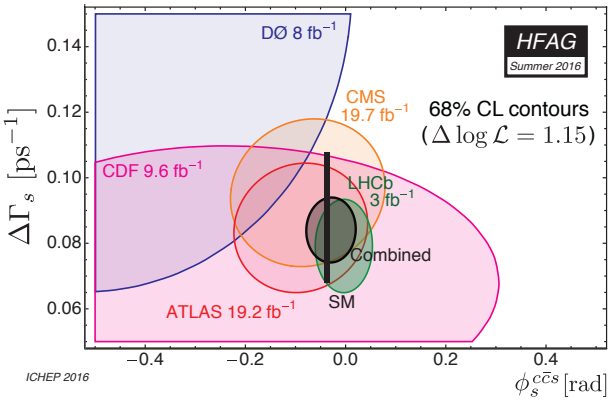

Figure 3: Plot of the 68% confidence-level contours in the ϕ_s – $\Delta\Gamma_s$ plane with the individual contours of ATLAS, CMS, CDF, DØ, and LHCb experiments, their combined contour (solid line and shaded area), as well as the Standard Model predictions (thin black rectangle). [4]

References

[1] G. Aad, et al. Flavor tagged time-dependent angular analysis of the $B_s \to J/\psi\phi$ decay and extraction of $\Delta\Gamma$s and the weak phase ϕ_s in ATLAS. *Phys Rev* **D90**(5):052007, 2014. 1407.1796.

[2] G. Aad, et al. Measurement of the CP-violating phase ϕ_s and the B_s^0 meson decay width difference with $B_s^0 \to J/\psi\phi$ decays in ATLAS. *JHEP* **08**:147, 2016. 1601.03297.

[3] C. Patrignani, et al. Review of Particle Physics. *Chin Phys* **C40**(10):100001, 2016.

[4] Y. Amhis, et al. Averages of b-hadron, c-hadron, and τ-lepton properties as of summer 2016 2016. 1612.07233.

	8 TeV data			7 TeV data			Run 1 combined		
Par	Value	Stat	Syst	Value	Stat	Syst	Value	Stat	Syst
ϕ_s [rad]	-0.110	0.082	0.042	0.12	0.25	0.05	-0.090	0.078	0.041
$\Delta\Gamma_s$ [ps^{-1}]	0.101	0.013	0.007	0.053	0.021	0.010	0.085	0.011	0.007
Γ_s [ps^{-1}]	0.676	0.004	0.004	0.677	0.007	0.004	0.675	0.003	0.003

Table 1: Current results using data from 8 TeV pp collisions, the previous measurement using 7 TeV data, and the values for the parameters of the two measurements, statistically combined.

MEASUREMENTS OF LIGHT YIELD OF SCINTILLATORS

Michal Kocan*

CTU Prague, Brehova 7, Prague, Czech Republic

* corresponding author: kocanmi3@fjfi.cvut.cz

Abstract. This contribution deal with different types of scintilators and how to measure the their yield.

Keywords: scintilators, yield .

1. Introduction

The light yield of scintillators is one of the most important characteristics of scintillators. The light yield depends not only on the material but also on the temperature and on the value of the deposited energy in the scintillators. This energy unproportional dependence can be up to 30% for CsI crystals.[1] The absolute light yield of scintillators is defined as the ratio of the total energy of scintillation photons to the energy deposited by ionizing radiation in the scintillator and is characterized by the number of photons in scintillation per 1 MeV energy radiation absorbed by the scintillator. [2] For the measuring photons from the scintillator is using a photomultiplier, a photodiode, an avalanche photodiode or a silicon photomultiplier. The silicon photomultiplier for its characteristics is becoming popular in nowadays. In our measurements, we are going to use the photomultiplier and the silicon photomultiplier.

For the measurements of the light yield is possible to use several methods, but the most common one is the single-electron method. In the single-electron method is compared the signal amplitude of photopeak with the value of the amplitude of the single electron distribution. If the photodiode is using, the signal amplitude of the photopeak is compared with the signal of X-ray of well-known energy. During the light yield measurement, we want to get all produced photons to the photosensitive device. For this reason, it is using the reflector all around the scintillator except the side where the device is placed. One of the best reflectors and our choice is Teflon. Because the photon now has more chances to be detected, we have to modify the quantum efficiency of the photosensitive device. [2] To enhance the probability, that the photon reaches the surface of the photosensitive device, is possible to use the optical coupling compound. Unfortunately, this is possible only for the (avalanche-)photodiode and the silicon photomultiplier. It is not recommended to use the optical coupling with photomultiplier because the quantum efficiency specified by manufacture is measured with photons incident perpendicular to the PMT. But with optical coupling photons can incident in various angle with unknown quantum efficiency. [2] If we want to use the silicon photomultiplier, we need to choose the right number of pixels (N_{pixels}) and also the size of a pixel pitch. The size of the pixel pitch affects the main properties of the silicon photomultiplier, such as a photon detection efficiency (PDE), dark count, gain, cross-talk, capacitance and afterpulses. The number of fired pixel (N_{fired}) for a number of incidents photons (N_γ) can be estimated by the semi-empirical equation (1).

$$N_{fired} = N_{pixels}\left(1 - e^{\frac{-N_\gamma \cdot PDE}{N_{pixels}}}\right) \qquad (1)$$

In our measurements, we are using the silicon photomultiplier and evaluation circuit from Hamamatsu Photonics. [3] For our purposes we chose the silicon photomultiplier with 3600 pixels with the pixel pitch of 50 microns. In the future, we will also use the one with 14400 pixels with the same pixel pitch. For the first tests, we have constructed a few nanoseconds LED pulse circuit. [4] With this LED pulse we tested different setups of a circuit to achieve the best energy resolution. Then we use the organic scintillator with dimensions $2,5\text{x}2,5\text{x}5\text{mm}^3$ and put it into the Teflon reflector. As a gamma source, we use ^{137}Cs and ^{60}Co. The measured spectrum of ^{60}Co is shown in the figure 1 . As we can see, there is no visible photopeak. This is caused by a type of scintillator, which is a plastic scintillator. These scintillators have a small probability of photo effect. This is a reason, why we will use the Compton edge for determining the light yield of the scintillator.

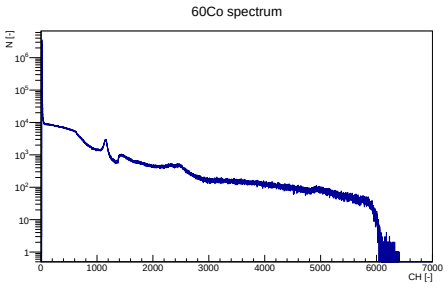

Figure 1: The measured spectrum of ^{60}Co with the silicon photomultiplier.

In close future, we are planning to do simulations in Geant4. These simulations should help us to better understand the measured spectrums. Also using the silicon photomultiplier with 14400 pixels will be a big step in our goal.

References

[1] L. Swiderski, et al. Scintillation properties of csi(co3) and csi(na) crystals for gamma ray detection.

[2] J. T. M. de Haas, et al. Advances in yield calibration of scintillators. *IEEE Transactions on Nuclear Science* **55**(3):1086–1092, 2008.

[3] Hamamatsu photonics k.k. `http://www.hamamatsu.com/us/en/index.html`.

[4] W. J. O'Hagan, et al. Mhz led source for nanosecond fluorescence sensing. *Measurement Science and Technology* **13**(1):84, 2002.

STUDY OF JET PRODUCTION IN AU+AU COLLISIONS IN THE STAR EXPERIMENT

Martin Kocmánek*

Nuclear Physics Institute of the CAS, Na Truhlářce 39/64, 180 86 Prague, Czech Republic

* corresponding author: kocmama2@fjfi.cvut.cz

Abstract. Ultra-relativistic heavy-ion collisions enable us to create the quark-gluon plasma, hot and dense nuclear matter. During hard scattering, partons of incoming nuclei undergo fragmentation and hadronisation which results in jets, collimated sprays of hadrons. Due to interaction of hard partons with QGP, the energy of partons is reduced in comparison to p+p collisions, what is referred to as a jet quenching. Measuring various modifications of jets traversing the medium provides important information about properties of nuclear matter. Recent results of jet analysis at STAR are presented and analysis of fully reconstructed jets produced in Au+Au collisions at $\sqrt{s_{NN}} = 200$ GeV using data recorded during the 2011 RHIC run is described. The study of data quality assurance of events, tracks and neutral towers, response of the BEMC and its time stability is performed. This is followed by application of the anti-kt jet algorithm as a function of centrality and the resolution parameter R to reconstruct jet spectra. Finally, corrections for background effects are included and discussed.

Keywords: quark gluon plasma, jet algorithm, full jet, STAR experiment.

1. Introduction

The STAR experiment is dedicated to study nuclear matter at extremely high temperature and density. It is located at Relativistic Heavy-Ion Collider (RHIC) at Brookhaven National Laboratory, where heavy ions are accelerated to ultra-relativistic velocities and collided in order to create a state of hot and dense nuclear matter, consisting of deconfined partons (quarks and gluons), referred to as a quark-gluon plasma (QGP). QGP is theoretically predicted by Quantum Chromodynamics. During early hard scattering, partons of incoming nuclei undergo fragmentation and hadronization which results in jets, collimated sprays of hadrons. Jets are one of the most important probes of the QGP. Due to interaction of hard partons with surrounding medium, the energy of partons is reduced in comparison to elementary proton-proton collisions that is referred to as a jet quenching. Measurement of modifications of jets traversing the nuclear matter provides important information on properties of hot and dense nuclear matter.

2. Jet reconstruction

Jet-finding algorithms are used for jet reconstruction and their main goal is to cluster a set of particles (charged tracks and neutral towers), which are typically emitted close to each other in angle, and combines their momenta to form the total momentum of a jet. The momentum addition rule is called the recombination scheme. Jet resembles kinematic properties of the original parton, therefore allows to access early stages of the collision. Jet reconstruction is successful in p+p collisions and serves as a fundamental test of QCD and as a reference to A+A collisions. A heavy-ion collision is a high-multiplicity environment with a large and inhomogeneous background, therefore the full jet reconstruction is challenging in such collisions.

An ideal jet algorithm has to fulfill several attributes [1]. It should be fully specified: the jet selection process and the jet kinematic variables are clearly defined. Further requirements are detector and order independence which means that the algorithm behaves equally at the parton, particle and detector level. The ideal algorithm is also collinear and infrared safe - adding of an infrared or collinear particle into an event will not influence existence or shape of measured jets. Finally, due to the enormous number of analyzed data, the jet algorithm should be stable and provide jet identification with a minimum of computer time.

Jet algorithms can be divided into two groups: cone and recombination. A cone algorithm draws a virtual cone around the highest p_T particle and everything inside the cone is defined as a jet. The second category of algorithms are recombination algorithms that are based on selecting a starting particle and then sequentially adding adjacent particles to the arising jet. Recombination algorithms are currently the main tool for jet reconstruction and the most commonly used algorithms are the k_T and the anti-k_T (Figure 1). Both are infrared safe and differ from each other in calculation of the distance between particles. The k_T algorithm recombines first particles with low p_T close to each other in space. The anti-k_T algorithm clusters first particles with the highest p_T. Therefore the anti-k_T algorithm is resilient to the soft background. For the jet reconstruction the FastJet [2] software package is commonly used, which contains jet algorithms and tools for jet analysis.

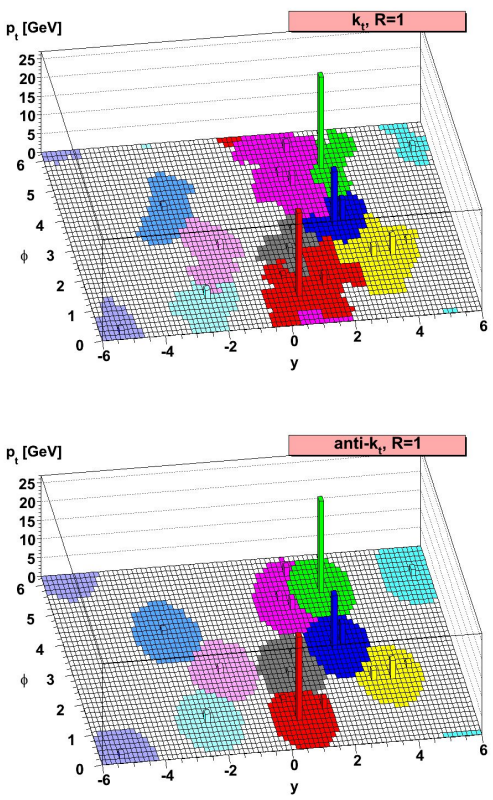

Figure 1: Comparison of the same event reconstructed by the k_T (top) and the anti-k_T (bottom) algorithm [3]. The parameter R determines the radius of a jet.

3. Results of jet analysis at STAR

One of the first attempts to perform full jet reconstruction in the environment of heavy-ion collisions was in the analysis of Au+Au collisions at a center-of-mass energy per nucleon-nucleon pair of $\sqrt{s_{NN}}$= 200 GeV collected in 2007 RHIC run. Figure 2 shows the jet R_{AA} which is the ratio of the jet production in Au+Au and jet production in p+p collisions scaled by binary collisions. Measured jet R_{AA} for $R = 0.2$ jets is more suppressed than the R_{AA} for $R = 0.4$ which is compatible with the unity, within large systematic uncertainties. This fact could indicate jet broadening in heavy-ion collisions, but measurements with smaller uncertainties are needed. There is a difference between algorithms due to their different response to the heavy-ion background. The anti-k_T algorithm is more resilient to the background than the k_T.

The 2011 RHIC run provides higher statistics, therefore the anticipated results are more promising. The increase of statistics enables more precise study of the jet R_{AA} as a function of centrality, it also suppresses systematics errors. Figure 3 presents the quantitative comparison of jet quenching at RHIC and the LHC. It shows semi-inclusive distribution of reconstructed charged jets recoiling from a high-p_T trigger hadron for central and peripheral collisions and compares the jet nuclear modification factor for central and peripheral Au+Au collisions at $\sqrt{s_{NN}} = 200$ GeV for $R = 0.4$ with the result from ALICE in Pb+Pb collisions at $\sqrt{s_{NN}} = 2.76$ TeV for $R = 0.4$. Charged recoil jet spectrum is compared with distribution for p+p collisions at $\sqrt{s} = 200$ GeV calculated using PYTHIA and NLO pQCD. The lower panel under charged recoil jet spectrum shows I_{CP} which is the ratio of central to peripheral distributions. At low p_T the I_{CP} is close to 1. For $p_{T,jet} > 10$ GeV/c, significant jet yield suppression $I_{CP} = 0.2$ can be observed in central collisions. The lowest panel shows ΔI_{AA} which is the ratio of the yield of recoil charged jets in Pb+Pb collisions to that in PYTHIA p+p collisions.

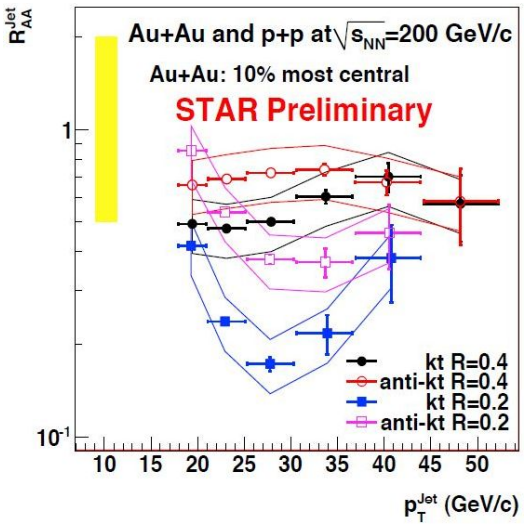

Figure 2: Full jet R_{AA} in Au+Au collisions at $\sqrt{s_{NN}}$= 200 GeV [4].

4. Analysis of full jets

The main aim of my diploma thesis is to study properties of fully reconstructed jets produced in minimum bias Au+Au collisions at $\sqrt{s_{NN}}$= 200 GeV collected in 2014 RHIC run. Large statistics of this data sample (more than a billion events) promises precise measurements of jet cross section and R_{AA}. Full jets are reconstructed from charged tracks measured by the Time Projection Chamber (TPC) and neutral towers measured by the Barrel ElectroMagnetic Calorimeter (BEMC) of the STAR experiment. Full jet reconstruction provides a direct measurement of whole original energy of scattered partons before the energy loss in the medium. We are not limited only to charged particles, but also neutral component of the jet is accepted. This approach enables reconstruction of parton kinematics in an unbiased way and also extends the kinematic reach of jet reconstruction in Au+Au collisions up to higher jet energies.

The first step of the analysis was a selection of suitable events with required properties on triggers, z-position of the primary vertex, reference multiplicity, etc. Then, cuts on p_T, DCA (distance of closest approach) and number of fit points of charged tracks

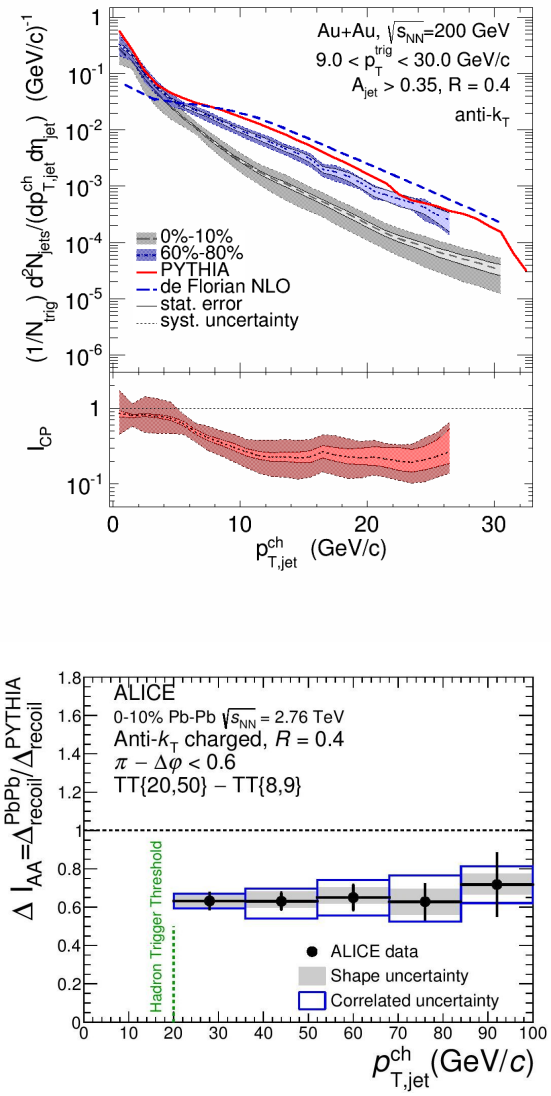

Figure 3: Top: Charged recoil jet spectrum for central and peripheral Au+Au collisions at $\sqrt{s} = 200$ GeV and $R = 0.4$ together with the nuclear modification I_{CP} measured by STAR [5]. Bottom: ΔI_{AA}, the ratio of Δ_{recoil} in Pb+Pb and PYTHIA p+p collisions at $\sqrt{s} = 2.76$ TeV for $R = 0.4$ measured by ALICE at the LHC [6].

were applied. Subsequently, the study of data quality assurance, response of the BEMC and its time stability was performed. In this part it is necessary to exclude runs with non-functional BEMC sectors and hot towers which are towers with excessive energy deposit or hit rate higher than the mean value of all towers. The main part of the analysis is the application of the sequential recombination algorithm anti-k_T in Au+Au collisions as a function of the centrality and the resolution parameter R (0.2, 0.3, 0.4) to reconstruct uncorrected jet spectra. Then, the subtraction of background and the study of its influence on jet spectra follows. Except for real jet constituents, reconstructed jets also contain additional energy contribution from combinatorial event background. To estimate the background, the k_T algorithm is applied on data. The transverse background density ρ for each event is calculated as a median of p_T of all reconstructed k_T jets (excluding 1-2 with the highest p_T) in the event. Uncorrected jet energy for each jet candidate is subtracted by the estimated background energy: $p_{T,jet}^{corr} = p_{T,jet}^{uncorr} - \rho \cdot A_{jet}$, where A_{jet} is the jet area. Combinatorial background is also reduced by imposing reasonable cut on jet area.

The following step is the study of background fluctuations because the above mentioned corrections are not sufficient. It is necessary to find out a correction which would adequately describe a smearing of jet p_T by soft background. Additional particles or simulated jets with defined p_T are embedded into a real event and jet reconstruction is carried out again. Afterwards, embedded particles or jets are matched to real ones and the quantity $\delta p_T = p_{T,jet}^{corr} - p_{T,jet}^{emb}$ which gives a relation between corrected p_T of reconstructed jets and p_T of the embedded object is calculated. This result is utilized for construction of background response matrix, which determines a probability to measure the value of $p_T^{measured}$ for a given real jet p_T^{true}. The measured spectrum is also distorted by detector effects. In order to overcome this problem, response matrix of detector effect is determined utilizing event generator and simulation of detector conditions. Technique for obtaining true jet spectrum from measured one is referred to as an unfolding and requires response matrix that is acquired by multiplication of background and detector response matrix. In this analysis, two unfolding methods: Bayesian [7] and SVD [8] will be used. The Bayesian unfolding is based on Bayes's theorem to calculate reverse probability from the known probability. The SVD unfolding is based on the singular value decomposition of the response matrix. After this process, we get true full jet spectra. The last step of the analysis is the calculation of systematic uncertainties.

5. Conclusions

This proceedings briefly describes motivation for jet physics, the commonly used jet algorithms and recent results of full and charged jet reconstruction from the STAR experiment with comparison to the ALICE results at the LHC. The last section summarizes and shortly explains basic steps of full jet analysis that is currently performed on Au+Au collisions at $\sqrt{s_{NN}}$= 200 GeV collected by the STAR detector in 2014 RHIC run.

References

[1] G. C. Blazey *et al.*, Run II jet physics, hep-ex/0005012.

[2] M. Cacciari, G. P. Salam and G. Soyez, FastJet user manual, Eur. Phys. J. C **72** (2012) 1896 [arXiv:1111.6097 [hep-ph]].

[3] M. Cacciari, G. P. Salam and G. Soyez, The Anti-k(t) jet clustering algorithm, JHEP **0804** (2008) 063 [arXiv:0802.1189 [hep-ph]].

[4] M. Ploskon [STAR Collaboration], Inclusive cross section and correlations of fully reconstructed jets in $\sqrt{s_{NN}}$ = 200 GeV Au+Au and p+p collisions, Nucl. Phys. A **830** (2009) 255C [arXiv:0908.1799 [nucl-ex]].

[5] L. Adamczyk *et al.* [STAR Collaboration], Measurements of jet quenching with semi-inclusive hadron+jet distributions in Au+Au collisions at $\sqrt{s_{NN}}$ = 200 GeV, arXiv:1702.01108 [nucl-ex].

[6] J. Adam *et al.* [ALICE Collaboration], Measurement of jet quenching with semi-inclusive hadron-jet distributions in central Pb-Pb collisions at $\sqrt{\mathbf{s_{NN}}}$ = 2.76 TeV, arXiv:1506.03984 [nucl-ex].

[7] G. D'Agostini, A Multidimensional unfolding method based on Bayes' theorem, Nucl. Instrum. Meth. A **362** (1995) 487. doi:10.1016/0168-9002(95)00274-X

[8] A. Hocker and V. Kartvelishvili, SVD approach to data unfolding, Nucl. Instrum. Meth. A **372** (1996) 469 doi:10.1016/0168-9002(95)01478-0 [hep-ph/9509307].

EXPERIMENTAL STUDY OF ELECTRICAL AND OPTICAL PROPERTIES OF THE MICROTUBULUS

Kristyna Kohoutova*

Department of Physics, Faculty of Nuclear Sciences and Physical Engineering, Czech Technical University in Prague, Brehova 7, 115 19 Prague 1, Czech Republic

* corresponding author: kohoukri@fjfi.cvut.cz

Abstract. Microtubules are very important part of cells, therefore it is very important to study their properties and functions in order to better understand processes inside cells. The first steps leading to the measurement of the specific conductivity of a tubulin dimmer by mechanically-controlled break junction method were realized, for now using calibration proteins BSA instead of tubulin dimmers. Dependence of the capacitance on the distance of the electrodes was measured in order to calibrate the distance. In order to make a correction of the future data, time dependences of the capacitance and the resistivity were investigated as well. A method for the measurement of the area of the active part of the tip was tested as it is necessary to determine this area for the future measurements. Moreover, a new way to create a layer of BSA on the tip was found; in case tubulin dimmers behave the same way, it will be possible to use the tip to measure the conductivity of a layer of tubulin dimmers. Microtubules used for the experiment are going to be observed using a petrographic microscope which was already tested on another objects.

Keywords: microtubule, tubulin, conductivity, capacitance, BSA.

1. Introduction

Microtubules are a component of the cytoskeleton in eukaryotic cells. They are important part of a spindle apparatus, allowing a separation of sister chromatids into daughter cells during eukaryotic cell division. Furthermore, microtubules accompanied by microtubule-associated proteins (MAPs) play major role in the intracellular transport. Moreover, neuronal microtubules are considered by some groups of scientists to be the origin of data processing and storing in human brain. Therefore, microtubules and their changes are expected to be important in such diseases as Alzheimer's disease, Parkinson's disease, and cancer. Requirement of a better treatment for these illnesses leads to the necessity of further microtubules research.

Microtubules are hollow tubes of inner diameter 12 nm, outer diameter 25 nm and length up to 50 µm. They consist of polar tubulin heterodimmers composed of α- and β-tubulin parts. As a result, microtubules are polar. [1] In addition to this, microtubules were found to be optically active. [2]

2. Method

2.1. Microtubules Observation Using Petrographic Microscope

Due to the optical activity of microtubules it is possible to observe them using phase contrast microscopy. This technique combines a magnification by a system of lenses and highlighting optically active objects as light objects on a dark background. Using this approach, it is possible to observe microtubules by an optical microscope despite their size which is not sufficient for regular optical microscopy.

2.2. Conductivity Measurement of the Tubulin Dimmer

The conductivity of the tubuline dimer is going to be measured by so-called mechanically-controlled break junction method shown in the Fig. 1. A plate electrode is situated under a solution containing tubulin dimmers and a tip electrode is located above it. Since tubulin dimmer is polar, it attaches to the electrodes if they are close enough. While moving the tip electrode up, an intense change of resistivity should be observed in distance equal to the dimmer size; this change corresponds to the tubulin dimmer resistivity.

The apparatus will be automated to move the upper electrode using a piezoelectric crystal as shown in the Fig. 2.

3. Results and discussion

3.1. the Distance Dependence of the Capacitance and the Resistivity

As mentioned above, the measurement of resistivity of the tubulin dimmer is going to be automated. For this automation, the distance dependence of the capacitance is going to be used to calibrate distance by capacitance. Early calibration data were measured using a common calibration protein BSA and a plate upper electrode to study this dependence. Unexpected behavior was detected in short distances in both capacitance and resistivity, as it is illustrated in figures

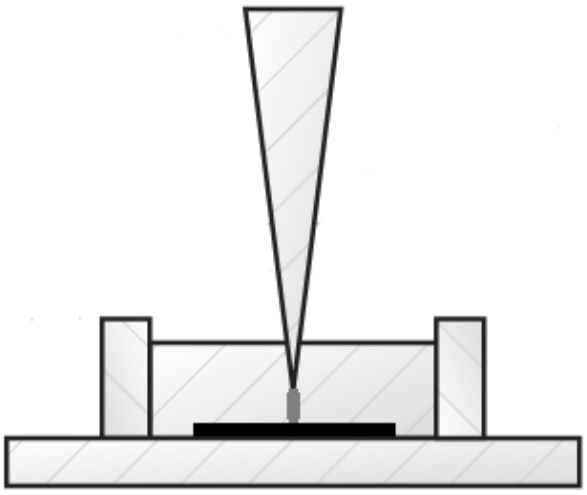

Figure 1: Mechanically-controlled break junction method scheme.

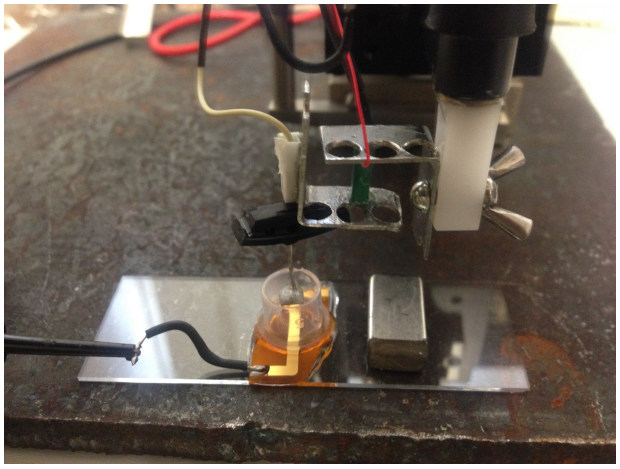

Figure 2: The apparatus.

Fig. 3, 4, 5, 6. These effects can be caused by an abnormal behavior of thin water or solution layers and will be studied in more detail in the future research.

3.2. The Time Dependence of the Resistivity and the Conductivity

The capacitance and the resistivity in stated distance of the electrodes were found to be time-dependent, see Fig. 7. This dependence was studied in order to determine systematic errors of the measured data and to eliminate the influence of the time dependence on our future data using time recalibration. The mechanism of the process is going to be investigated in the future research as well.

3.3. BSA Crystallization

In addition, a new way to crystallize BSA was found. Using a tungsten tip with a small active area as an upper electrode, 2 mg/ml solution of BSA in deionised water, the alternating voltage changing within the range of 10 mV to 1 V, frequencies

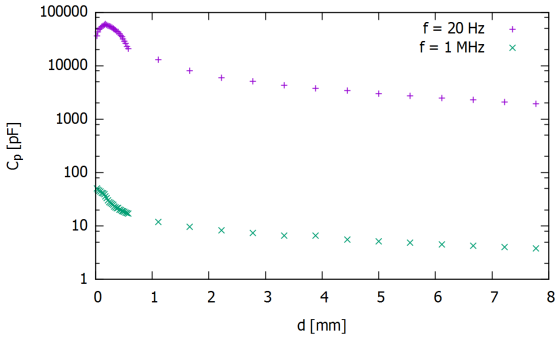

Figure 3: Our results: the distance dependence of the capacitance C_p in deionised water.

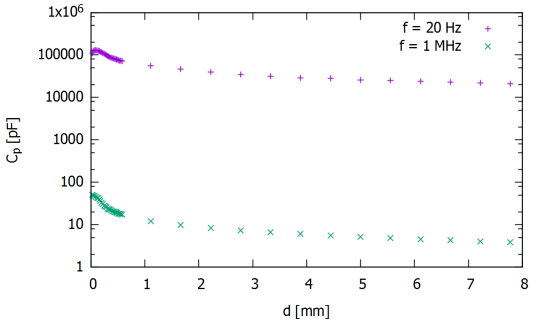

Figure 4: Our results: the distance dependence of the capacitance C_p in the 2 mg/ml solution of BSA in deionised water.

20 Hz to 1 MHz, an observable layer of BSA was deposited on the tip within 45 minutes. This result is remarkable especially in relation to commonly used methods of BSA crystallization where very high concentrations are needed. [3]

4. Conclusions

The apparatus for the measurement of the microtubule conductivity has been constructed and the methodical part of the experiment has been done. The first testing distance - capacitance calibration data were collected using a calibration protein BSA and the time dependence was studied in order to determine a systematic error and examine a possibility of time recalibration. Unexpected effects were observed in case of electrodes very close to each other surrounded by deionised water or BSA solution; these effects will be investigated in more details in the future research. In addition to this, a new method of BSA crystallization has been invented; if tubulin dimmers exhibit the same behavior, a new method to study microtubules' dielectric properties will be available.

Acknowledgements

I want to thank my supervisor doc. RNDr. Vojtech Petracek, CSc. for his advices and help.

References

[1] B. Alberts, et al. *Zaklady bunecne biologie.* Espero Publishing, Usti nad Labem, 1998.

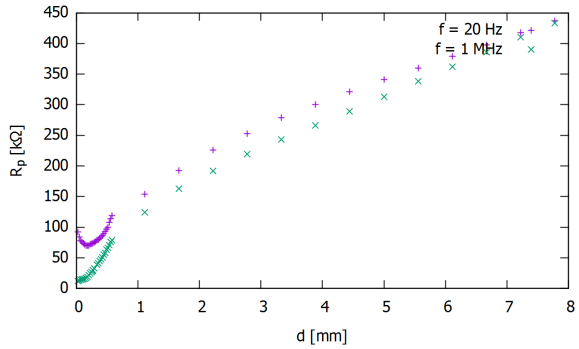

Figure 5: Our results: the distance dependence of the resistivity R_p in deionised water.

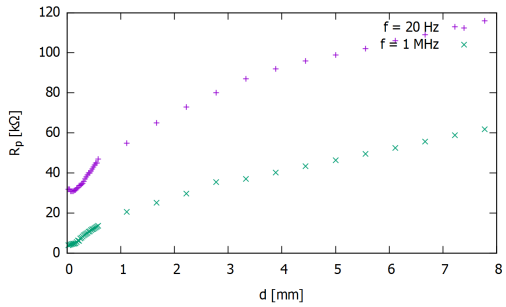

Figure 6: Our results: the distance dependence of the resistivity R_p in the 2 mg/ml solution of BSA in deionised water.

[2] R. Oldenbourg, et al. Birefringence of single and bundled microtubules. *Biophysical journal* **74**(1):645–654, 1998.

[3] A. Bujacz. Structures of bovine, equine and leporine serum albumin. *Acta Crystallographica Section D: Biological Crystallography* **68**(10):1278–1289, 2012.

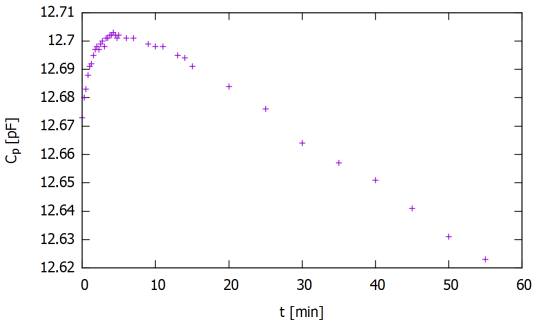

Figure 7: Our results: the time dependence of capacitance C_p in deionised water, alternating voltage $U = 10\,\mathrm{mV}$, frequency $f = 1\,\mathrm{MHz}$.

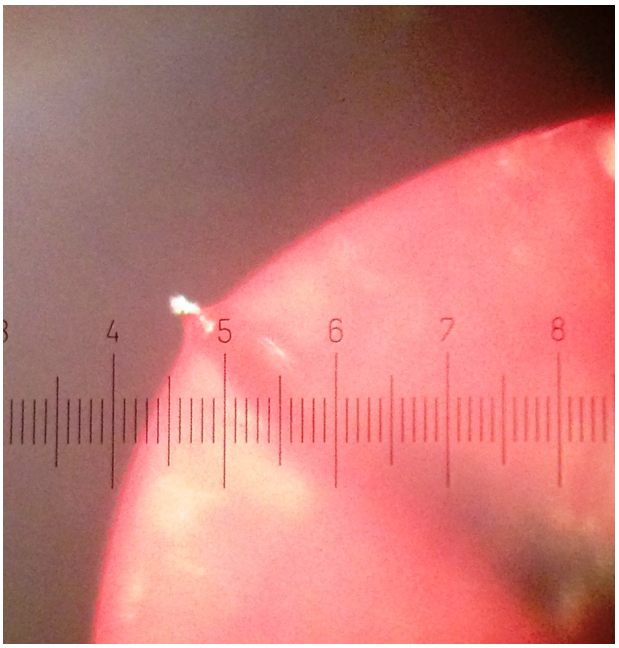

Figure 8: Our results: BSA crystallization.

COLD NUCLEAR MATTER EFFECTS IN PROTON-NUCLEUS COLLISIONS

Lukáš Kramárik*

Department of Physics, Faculty of Nuclear Sciences and Physical Engineering, Czech Technical University in Prague, Břehová 7, Prague 1, Czech Republic

* corresponding author: lukas.kramarik@fjfi.cvut.cz

Abstract. One of the main goals of experiments at Large Hadron Collider in CERN and Relativistic Heavy Ion Collider in BNL is to study hot and dense nuclear matter, quark-gluon plasma, that could be created in collisions of heavy ions. To quantify effects of this hot medium on particle production, study of so-called cold nuclear matter effects is needed. These effects rise from the dense nuclear environment, not from hot medium, and can significantly influence particle production. They can be induced by different phenomena, such as modifications of parton distribution functions of colliding ions, saturations of partons in these ions, initial and final multiple scatterings of created particles. Collisions of protons or deuterons with heavy ions are a great tool to investigate cold nuclear matter effects. Recently, many heavy-flavour results have been published, and they will be summarized in these proceedings.

Keywords: cold nuclear matter effects, heavy flavour, proton-nucleus.

1. Introduction

In ultrarelativistic collisions of heavy ions, hot and dense nuclear matter, quark-gluon plasma (QGP), could be created. Collisions of protons serve as a baseline for observables in heavy ions collisions. However, in order to study QGP effects on produced particles, the quantitative understanding of the effects of the heavy nuclei in the initial stages of collisions is needed.

Proton-nucleus (pA) collisions are studied in order to isolate these, so called cold nuclear matter (CNM) effects. Energy density in such collisions is expected to be too low to create thermalized medium, nevertheless dense nuclear environment could alter colliding nucleons.

CNM effects are studied in proton-lead (pPb) collisions at the Large Hadron Collider (LHC) in CERN, in proton-gold (pAu) and deuteron-gold (dAu) collisions at the Relativistic Heavy Ion Collider (RHIC) in BNL. In this proceedings, results from pPb collisions at energy $\sqrt{s_{\mathrm{NN}}} = 5.02$ TeV from LHC experiments (ALICE and LHCb), pAu at $\sqrt{s_{\mathrm{NN}}} = 200$ GeV and dAu at $\sqrt{s_{\mathrm{NN}}} = 200$ GeV, both from RHIC experiments (PHENIX and STAR), will be shown.

Comparison of particle production in different collisional systems could be quantified by nuclear modification factor measurements. In case of a comparison of particle yield in pA collision of centrality c and particle production cross section in pp collisions σ_{pp}, it is defined as

$$R^c_{\mathrm{pA}} = \frac{N^c_{\mathrm{pA}}}{\langle T^c_{\mathrm{pA}} \rangle \sigma_{\mathrm{pp}}}, \qquad (1)$$

where $\langle T^c_{\mathrm{pA}} \rangle$ is the average nuclear overlap function for the pA collision of centrality class c, usually obtained with Glauber model. If the CNM effects are small or absent in pA collisions, nuclear modification factor is equal to unity. Nuclear modification factor, where central collisions are compared to peripheral ones, not to pp reference, is usually tagged as R_{CP}.

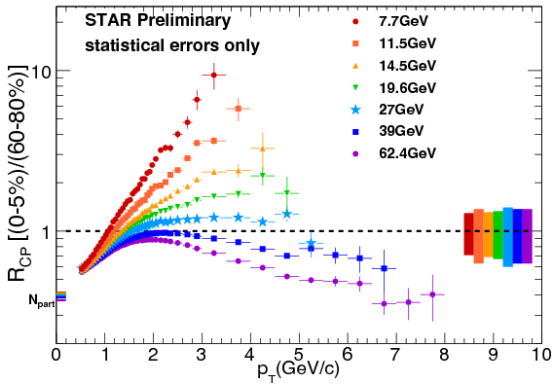

Figure 1: Efficiency corrected charged hadron R_{CP} for RHIC Beam Energy Scan energies vs transverse momentum p_{T}, measured in AuAu collisions. Taken from [1].

Figure 1 shows measurements of R_{CP} for different collision energies from Beam Energy Scan at RHIC. In case of $\sqrt{s_{\mathrm{NN}}} = 200$ GeV, particle production is certainly suppressed. However, suppression turns off at $\sqrt{s_{\mathrm{NN}}} = 39$ GeV. For lower energies, R_{CP} is larger than unity. This enhancement could be caused by Cronin effect, that could make investigation of the parton energy loss more complicated. Thus, it could be observed that quantification of CNM effects is important for further studies of collisions of heavy ions.

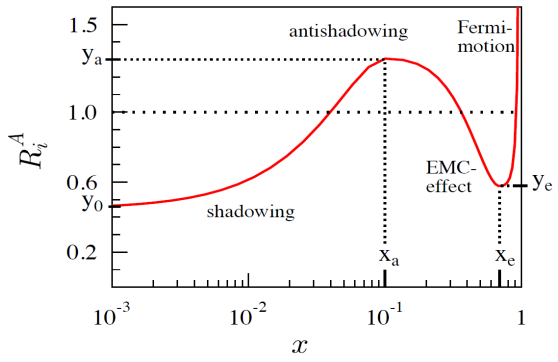

Figure 2: An illustration of the function R_i^A dependency on the Bjorken x, with different regimes of nucleon PDF modification. Taken from [2]

2. Cold nuclear matter effects on heavy flavour production in pA collisions

Heavy quarks are expected to be created in the early stages of collisions, thus they are a great probe of nuclear matter and its effect. Some of the CNM effects, that could be studied with heavy quarks or hadrons in pA collisions are:

- Modification of effective parton distribution functions (PDF) of nucleons in colliding nuclei, with respect to proton-proton collisions. It is expected, that dynamics of partons differ in free protons and in nucleons in colliding nuclei. In relativistic heavy-ions, density of partons could largely grow, effecting parton distribution in nuclei. This nuclear modification depends on the regime of Bjorken scaling x and on the scale of parton-parton interaction Q^2. It could be expressed by a shadowing factor

$$R_i^A(x,Q^2) = \frac{f_i^A(x,Q^2)}{A f_i^{\text{nucleon}}(x,Q^2)}, \qquad (2)$$

  where A is the number of nucleons in the colliding nucleus, f_i^A is the bound nucleon PDF for parton flavour i and f_i^{nucleon} is the free nucleon PDF. Value of R_i^A for different x is shown in Fig. 2. Commonly used terms for different x-regimes (shadowing, antishadowing, EMC-effect and Fermi-motion) are shown as well. In the relativistic collisions of heavy ions, the shadowing regime is present. As it could be seen in Fig. 2, in this regime PDFs of nucleons are hardly modified, because of the phase-space saturation. These modified PDF are usually labeled as nPDF.

- Parton saturation at small x, described by the Colour Glass Condensate (CGC) theoretical framework, that includes multiple-scattering effect on the partons by the dense target.

- Final-state inelastic interactions, such as nuclear absorption of bound states, when passing through the nucleus.

- Partons scatterings in the nucleus, resulting in their energy loss and to the broadening of the transverse momentum (Cronin effect).

- Possible heavy quarkonia dissociation by comovers (partons or hadrons created or moving in the proximity of quarkonia). It is still questionable, if, in pA collisions, comovers at high energy could form a medium with some collectivity.

3. Heavy flavour measurements pA collisions

Heavy flavour hadrons are produced in the early stages of the collisions, thus their production is affected by the parton probability density of the colliding nucleus (nPDF or CGC effect) and further multiple scatterings. Because of their large mass, they could not be measured directly. One of the possible analysis strategy is to measure heavy flavour leptons, coming from decays of these hadrons. Figure 3 shows transverse momentum dependence of nuclear modification factor in dAu collisions at PHENIX for heavy flavour decay leptons, in two centrality classes (central and peripheral) and for three rapidity intervals (midrapidity, forward and backward rapidity). In this figure, as well in other figures that follows, forward (positive) rapidity is in the direction of the colliding proton (deuteron). As it could be seen in Fig. 3 (Right), nuclear modification factor for heavy-flavour leptons is consistent with unity for all of the three shown rapidity ranges in peripheral collision (centrality 60-88%). However, for the central collisions shown in Fig. 3 (Left), nuclear modification factors in forward and backward rapidities strongly deviate from each other and from unity. Currently, such a difference is not explained by theoretical predictions of initial CNM effect.

In the measurements, it is as well possible to distinguish leptons, coming from b decays from other heavy flavour leptons. Nuclear modification factors of b leptons in pPb collisions R_{pPb} at $\sqrt{s_{\text{NN}}} = 5.02$ TeV and in PbPb collisions at $\sqrt{s_{\text{NN}}} = 2.76$ TeV, both measured by ALICE, is displayed in Fig. 4. Within uncertainties, R_{pPb} is consistent with unity, thus the production of electrons from beauty hadrons in pPb scales with the one in pp. It could be concluded, that this measurements confirms, that initial-state effects due to the presence of CNM are small in the measured transverse momentum range.

Another way to study heavy flavour lepton modification is to compare their nuclear modification factors with those of quarkonia. Heavy flavour leptons are expected to come from open heavy flavour decays. Figure 5 shows transverse momentum p_{T} dependence of nuclear modification factor in dAu collisions of inclusive J/ψ and heavy-flavour leptons in three rapidity ranges, as measured by PHENIX. At low p_{T}, J/ψ is clearly more suppressed than heavy-flavour leptons, that could suggest an additional CNM final-state effects on J/ψ production. However, the relation

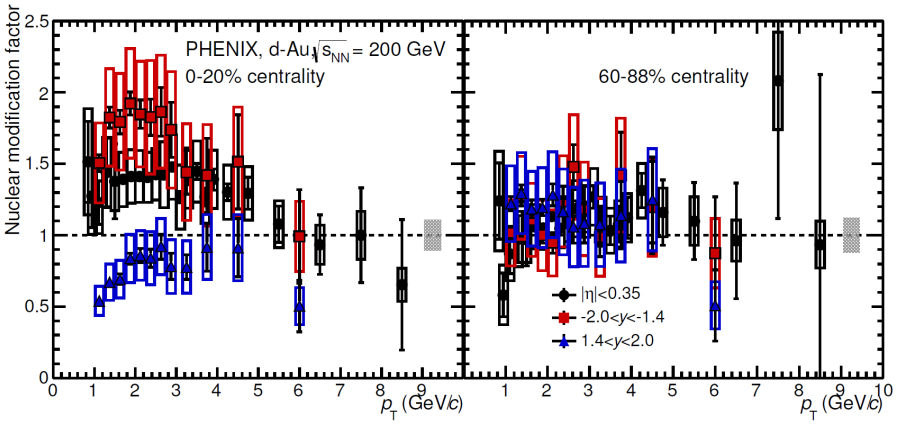

Figure 3: Nuclear modification factor of heavy flavour decay leptons in dAu collisions at $\sqrt{s_{\rm NN}} = 200$ GeV as a function of transverse momentum in the 0-20% (Left) and 60-88% (Right) centrality classes, measured by PHENIX. Taken from [3].

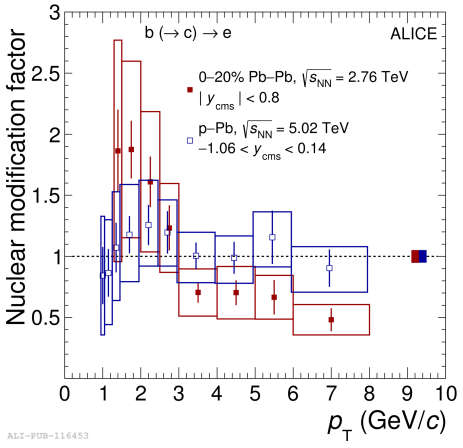

Figure 4: Nuclear modification factors $R_{\rm pPb}$ and $R_{\rm PbPb}$ of electrons from beauty-hadron decays at mid-rapidity as a function of transverse momentum for minimum-bias pPb collisions at $\sqrt{s_{\rm NN}} = 5.02$ TeV and 20% most central PbPb collisions at $\sqrt{s_{\rm NN}} = 2.76$ TeV, measured by ALICE. The data points of the pPb analysis were shifted by 0.05 GeV/c to the left along the $p_{\rm T}$ axis for better visibility. Taken from [4].

between parent quark kinematics and decay lepton kinematics is not straightforward.

3.1. D mesons

Heavy flavour hadrons could be also analyzed through their exclusive decays. For example, D^0 meson decays to K^- and π^+ with branching ratio 3.87%. Kaons and pions could be directly detected at experiments, that allows full reconstruction of D mesons.

Nuclear modification factor of prompt D mesons (as an average of D^0, D^+ and D^{*+}), reconstructed via their hadronic decays, was measured in pPb collisions by ALICE. It is shown in Fig. 6 together with several theoretical model predictions. All of the displayed models (CGC computations, next-to-leading order pQCD calculations, considering nPDF and prediction including nPDFs, $k_{\rm T}$-broadening as well as CNM

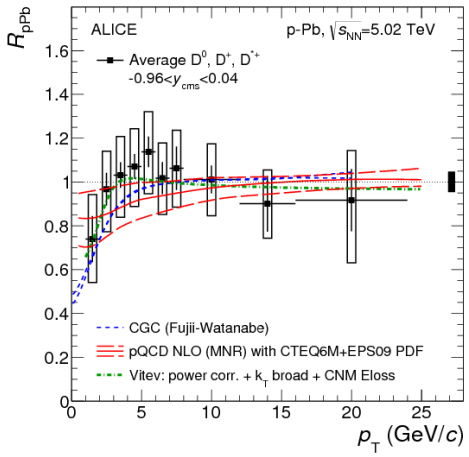

Figure 6: Nuclear modification factor of prompt D mesons in pPb collisions at $\sqrt{s_{\rm NN}} = 5.02$ TeV as a function of transverse momentum $p_{\rm T}$, measured by ALICE, together with theoretical calculations including various CNM effects. Taken from [5].

initial and final state energy loss) describe the measurement. Measured nuclear modification factor of D mesons is consistent with unity within uncertainties, with only small indication of CNM effects.

3.2. Open beauty hadrons

Beauty production could be measured not only by non-photonic electrons and leptons, but also by non-prompt J/ψ (J/ψ, that were not created in the collisions, but in the decays of other hadrons). At RHIC energies, it is expected that the contribution from B meson decays to the inclusive yield of J/ψ is at the level of 3%, at the LHC energies is at the level of 10%. These fractions increase towards mid-rapidity and high-$p_{\rm T}$ region. At LHCb, non-prompt J/ψ are extracted using component fit of the pseudo-proper decay time of the J/ψ along the beam direction.

In the Figure 7, nuclear modification factor $R_{\rm pPb}$ of non-prompt J/ψ, measured by LHCb, is shown.

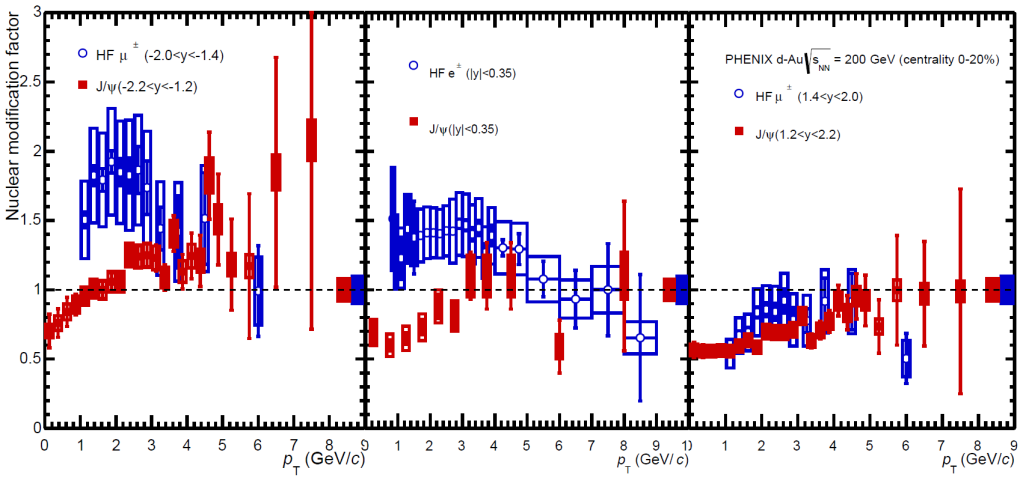

Figure 5: Transverse momentum dependency of nuclear modification factor in dAu collisions at $\sqrt{s_{\rm NN}} = 200$ GeV $R_{\rm dAu}$ of inclusive J/ψ for three different rapidity ranges in 0-20% centrality bin and comparison to heavy flavour electrons and muons, measured by PHENIX. Taken from [3].

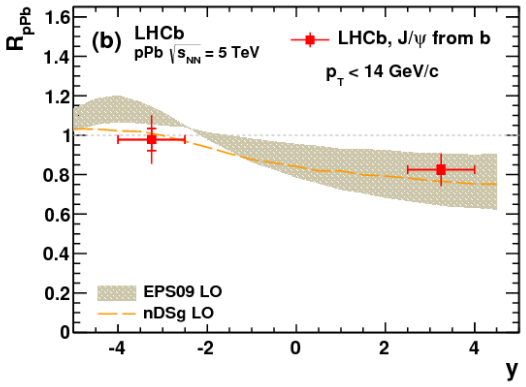

Figure 7: Nuclear modification factor $R_{\rm pPb}$ as a function of rapidity y for J/ψ from b, together with the nPDF-based theoretical predictions, measured in pPb collisions at $\sqrt{s_{\rm NN}} = 5.02$ TeV by LHCb. Taken from [6].

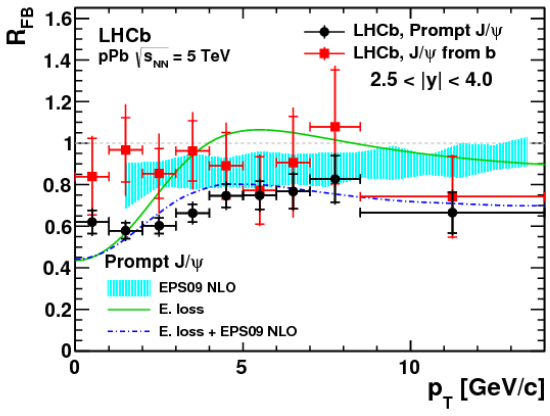

Figure 8: Forward-backward production ratio $R_{\rm FB}$ for prompt J/ψ mesons and J/ψ from b as a function of transverse momentum $p_{\rm T}$, measured in pPb collisions at $\sqrt{s_{\rm NN}} = 5.02$ TeV by LHCb, together with the nPDF-based theoretical predictions for prompt J/ψ. Taken from [6].

At backward rapidity, $R_{\rm pPb}$ is close to unity, but for forward rapidity, it is clearly smaller than one. This backward to forward asymmetry is as well predicted by the LO pQCD calculations, shown in Fig. 7.

Figure 8 shows forward to backward production ratio $R_{\rm FB}$ as a function of transverse momentum, for prompt J/ψ an J/ψ from b decays, measured by LHCb in pPb collisions at $\sqrt{s_{\rm NN}} = 5.02$ TeV. Theoretical predictions in this figure are only for prompt J/ψ, and it can be seen that the one based on parton energy loss and nPDF is in agreement with measurement. Forward production of prompt J/ψ is clearly suppressed in comparison with the backward production. In case of J/ψ from b, despite that $R_{\rm FB}$ values are clearly smaller than one, within uncertainties, the ratio is consistent with unity.

3.3. Charmonium states

Experiments at RHIC and LHC have measured charmonium nuclear modification factor in the large rapidity range, as it can be seen in Fig. 9, together with various theoretical predictions. RHIC data, from dAu collisions at $\sqrt{s_{\rm NN}} = 200$ GeV, shows J/ψ suppression in the whole rapidity range, falling from level of 80% in backward rapidity to nearly 40% in forward rapidity. At backward rapidity, models based on nPDFs overestimate the data. At forward rapidity, NLO nPDFs parametrization, with strong shadowing, is in agreement with smaller nuclear modification factor.

LHC data, from pPb collisions at $\sqrt{s_{\rm NN}} - 5.02$ TeV, shown in Fig. 9 (Right), shows nearly the same suppression in forward rapidities as RHIC data, for both inclusive J/ψ in ALICE and prompt J/ψ in LHCb. However, at backward rapidities, nuclear modification

factor is consistent with unity for inclusive J/ψ (ALICE) and the level of 90% for prompt J/ψ (LHCb). Backward rapidity is well described by nPDF models and models with strong shadowing are in agreement with data for forward rapidities.

Both RHIC and LHC measured relative nuclear modification of inclusive J/ψ to ψ(2S), $R_{\rm pA}(\psi(2S))/R_{\rm pA}(J/\psi)$. ψ(2S) has binding energy 0.05 GeV, that is much lower than J/ψ binding energy, 0.64 GeV. This is why ψ(2S) is expected to be more sensitive to the dense nuclear environment and its suppression relative to the J/ψ suppression is a good probe of CNM effects.

In Fig. 10 (Left), this relative nuclear modification is shown as a function of number of nucleon-nucleon collisions in dAu collisions in PHENIX. For peripheral collisions, the relative modification is compatible with unity, however, through to the central collisions, it is falling to the level of 20%. In Fig. 10, this modification is shown as function of rapidity, as measured by ALICE in pPb collisions at $\sqrt{s_{\rm NN}} = 5.02$ TeV. For the backward rapidities, it is slightly smaller than for forward rapidities, but for both of them, it is smaller than unity and it is at the level of 60%. Theoretical prediction, that uses LO nPDFs and interactions of quarkonia with comovers, is shown as well in Fig. 10. This prediction is in fairly agreement with the data from ALICE and PHENIX.

3.4. Bottomonium states

Despite the fact that bottomonium statistics are not good at RHIC experiments, PHENIX and STAR measured nuclear modification factor of Υ(1S+2S+3S) states in dAu collisions at $\sqrt{s_{\rm NN}} = 200$ GeV, and its rapidity dependency is shown in Fig. 11 (Left). These data does not show evident suppression of upsilons, except the one point for zero rapidity. Here, the suppression is at the unexpected value of 40%. From PHENIX data, slightly higher suppression in backward rapidities is as well observed.

At LHC, LHCb and ALICE measured Υ(1S) nuclear modification factor in pPb collisions at $\sqrt{s_{\rm NN}} =$ 5.02 TeV. Results of this measurement are in Fig. 11 (Right). In this case, for backward rapidity, data are consistent with unity, but in forward rapidity, data are consistently below unity.

Because of relatively large uncertainties of measurements, none of the theoretical models, shown in Fig. 11, can be favored. Models based on nPDFS, coherent energy loss and initial gluon saturation describe data within uncertainties, excepting point from STAR at midrapidity.

4. Conclusions

Heavy flavour is not only the great probe of hot and dense nuclear matter, but it can as well be used to investigate wide range of cold nuclear matter effects. Currently, experiments at LHC and RHIC are able to study pA collisions, in order to quantify these effects. Their actual results on heavy flavour production in these collisions, compared to production in pp collisions, were shown in this proceedings.

Nuclear modification factor of heavy flavour leptons in dAu collisions at $\sqrt{s_{\rm NN}} = 200$ GeV at RHIC shows suppression for forward rapidities in the most central collisions. For backward rapidity in the most central collisions, nuclear modification factor is larger than unity. In case of pPb collisions at $\sqrt{s_{\rm NN}} - 5.02$ TeV, measured by ALICE at LHC, nuclear modification factor is consistent with unity in the mid-rapidity region and in full transverse momentum range.

RHIC experiments measured that leptons from open heavy flavour decays are equally suppressed as J/ψ in forward rapidity, but they differ for other rapidities. Suppression from final-state effects may be at role on J/ψ production at backward and mid-rapidity.

Nuclear modification factor of D mesons is compatible with unity at LHC.

At LHC, J/ψ from b is suppressed in forward rapidity compared to backward rapidity, but this is slight suppression in the full measured transverse momentum range. However, for prompt J/ψ, the ratio of forward to backward production is at the level of 60-80%.

Inclusive J/ψ are suppressed in backward and forward rapidities at RHIC. At LHC, inclusive and prompt J/ψ are suppressed nearly equally and only for forward rapidities.

Comparing ψ(2S) and J/ψ, it can be seen that ψ(2S) is more suppressed towards central collisions at RHIC, as well as at ALICE in full rapidity range. This suggests the presence of final-state cold nuclear matter effects

Bottomonium measurements show only very slight or no asymmetry of forward to backward production for both RHIC and LHC.

Currently, data do not allow to strictly favour or reject specific models, based on nuclear PDF, parton saturation or initial parton energy loss.

Acknowledgements

This work was also supported by the grant LG15001 and LM2015054 of Ministry of Education, Youth and Sports of the Czech Republic.

References

[1] X. Luo. Exploring the QCD Phase Structure with Beam Energy Scan in Heavy-ion Collisions. *Nucl Phys* **A956**:75–82, 2016. 1512.09215.

[2] K. J. Eskola, et al. EPS09: A New Generation of NLO and LO Nuclear Parton Distribution Functions. *JHEP* **04**:065, 2009. 0902.4154.

[3] A. Andronic, et al. Heavy-flavour and quarkonium production in the LHC era: from proton-proton to heavy-ion collisions. *Eur Phys J* **C76**(3):107, 2016. 1506.03981.

[4] J. Adam, et al. Measurement of electrons from beauty-hadron decays in p-Pb collisions at

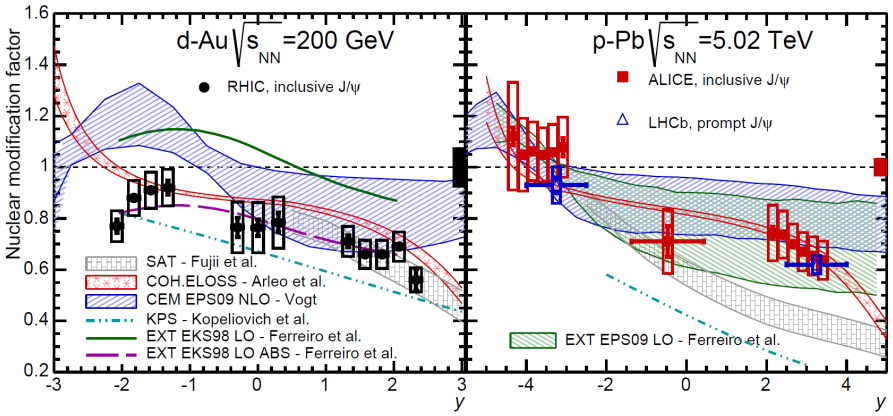

Figure 9: Left: Rapidity dependence of nuclear modification factor R_{dAu} for inclusive J/ψ in dAu collisions at $\sqrt{s_{\mathrm{NN}}} = 200$ GeV R_{dAu} in PHENIX. Right: Rapidity dependence of nuclear modification factor R_{pPb} for inclusive J/ψ at ALICE and prompt J/ψ at LHCb, both in pPb collisions at $\sqrt{s_{\mathrm{NN}}} = 5.02$ TeV. Taken from [3].

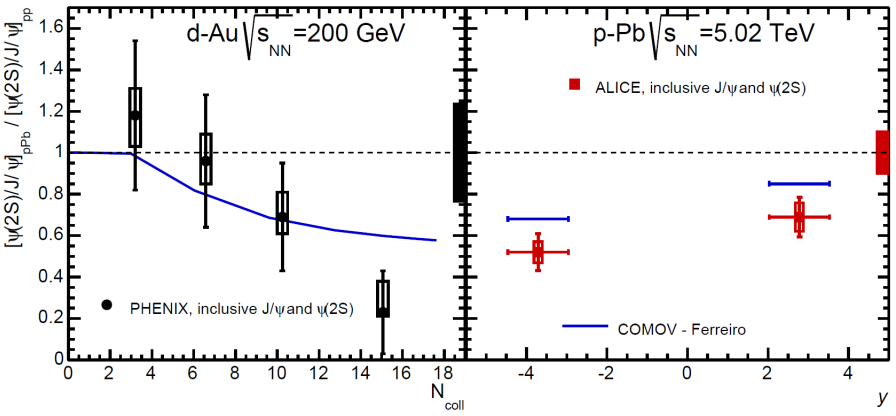

Figure 10: Left: Relative nuclear modification ($[\psi(2S)/J/\psi]_{\mathrm{dAu}}$ / $[\psi(2S)/J/\psi]_{\mathrm{pp}}$) of inclusive J/ψ to $\psi(2S)$ as a function of nucleon-nucleon collisions number in dAu collision N_{coll} in PHENIX. Right: Rapidity y dependence of the relative nuclear modification of J/ψ to $\psi(2S)$ in ALICE. Taken from [3].

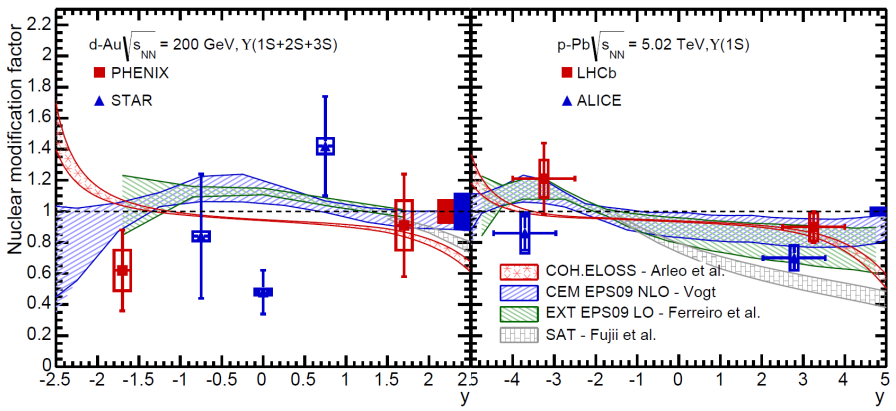

Figure 11: Left: Rapidity dependence of nuclear modification factor for Υ(1S+2S+3S) in PHENIX and STAR. Right: Rapidity dependence of nuclear modification factor for Υ(1S) in ALICE and LHCb. Taken from [3].

$\sqrt{\mathbf{s_{NN}}} = \mathbf{5.02}$ TeV and Pb-Pb collisions at $\sqrt{\mathbf{s_{NN}}} = \mathbf{2.76}$ TeV 2016. 1609.03898.

[5] B. B. Abelev, et al. Measurement of prompt D-meson production in $p - Pb$ collisions at $\sqrt{s_{NN}} = 5.02$ TeV. *Phys Rev Lett* **113**(23):232301, 2014. 1405.3452.

[6] R. Aaij, et al. Study of J/ψ production and cold nuclear matter effects in pPb collisions at $\sqrt{s_{NN}} = 5$ TeV. *JHEP* **02**:072, 2014. 1308.6729.

GEODESIC ACOUSTIC MODES ON THE COMPASS TOKAMAK

Jaroslav Krbec*

CTU Prague, Brehova 7, Prague, Czech Republic

* corresponding author: krbecja1@fjfi.cvut.cz

Abstract. Geodesic acoustic mode (GAM) is axisymmetric oscillation of plasma potential. The mode propagates radially outwards and generates oscillations of a poloidal ExB velocity. Radial gradient of toroidal magnetic field and compressibilty of ExB drift causes oscillations of plasma density at the top and the bottom of plasma column. GAM as a sheared flow plays an important role in turbulence self-regulation and especially in I-mode. The overview of fundamental properties of GAMs (e.g. axisymmetry, frequency scaling with temperature) measured on the COMPASS tokamak are presented.

Keywords: GAM, COMPASS.

1. Introduction

A fusion reactor has to produce more energy than consumes thus at least it has to fulfill Lawson criterion for plasma ignition

$$n\tau_E > 1.5 \times 10^{20} m^{-3} s \tag{1}$$

where n is the ion density and τ_E is energy confinement time which is given by

$$\tau_E = \frac{a^2}{\chi_i} \tag{2}$$

where a is minor radius of tokamak and χ_i koeficient of thermal ion diffusion. It was found the experimental value of χ_i was one order of magnitude larger than theoretical value of chi_i from neoclassical theory. The reason is turbulent transport of particles. There are two methods how to increase τ_E: increase minor radius a of a tokamak or decrease chi_i via decreasing turbulence. Since ZF (Zonal Flows) [1] and GAMs (Geodesic Acoustic Modes) [2] can module amplitude of turbulence level [3] i.e. they represent self-regulation mechanism of turbulence, their importance from the fusion reactor point of view became larger in these days. The poloidal and toroidal structure of GAM magnetic component and frequency scaling of GAM was measured on the COMPASS tokamak.

2. Diagnostics

A magnetic component of GAM was measured by 2 poloidal rings (MC-A and MC-C) of 24 Mirnov coils separated by toroidal angle of 115Âř 1. The electron temperature was measured by Thomson scattering and central ion temperature by NPA (Neutral Particle Analyser).

3. GAM magnetic component

GAM is oscillating axisymmetric sheared flow with m/n = 0/0 plasma potential component. Density

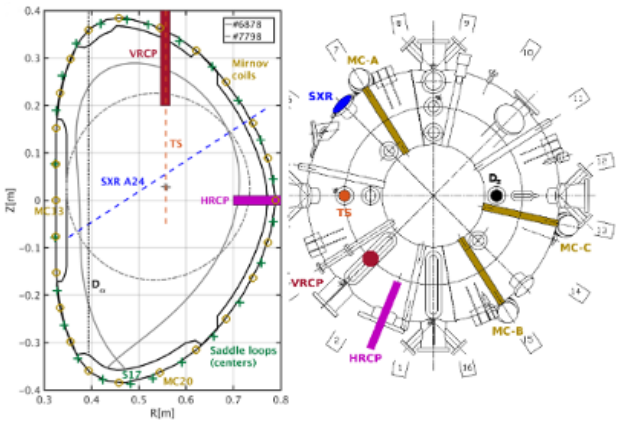

Figure 1: Overview of diagnostics on the COMPASS tokamak used for GAM measurement.

component has m/n = 1/0 structure due to gradient of toroidal magnetic field and ExB drift compressibility thus there is periodical accumulation and loss of electron density at the top and the bottom of the plasma column. Density gradient, diamagnetic current and quasi-neutrality rule produces current along the field lines which generates magnetic component of the GAM with m/n = 2/0 structure in plasma with circular cross-section. Cross-coherence between MC-A and MC-C array show oscillation at frequency cca. 35 kHz which are toroidally symmetric n ≈ 0 2. There can be also seen second harmonic of the GAM and 2/1 and 3/1 tearing mode. Poloidal structure has a standing wave pattern and is much more complex than m/n = 2/0 because of plasma elongation.

4. GAM frequency scaling with temperature

GAM oscillates with frequency

$$f = Gc_s/R_0 \approx \sqrt{T} \tag{3}$$

where G is scaling factor given by plasma shape,

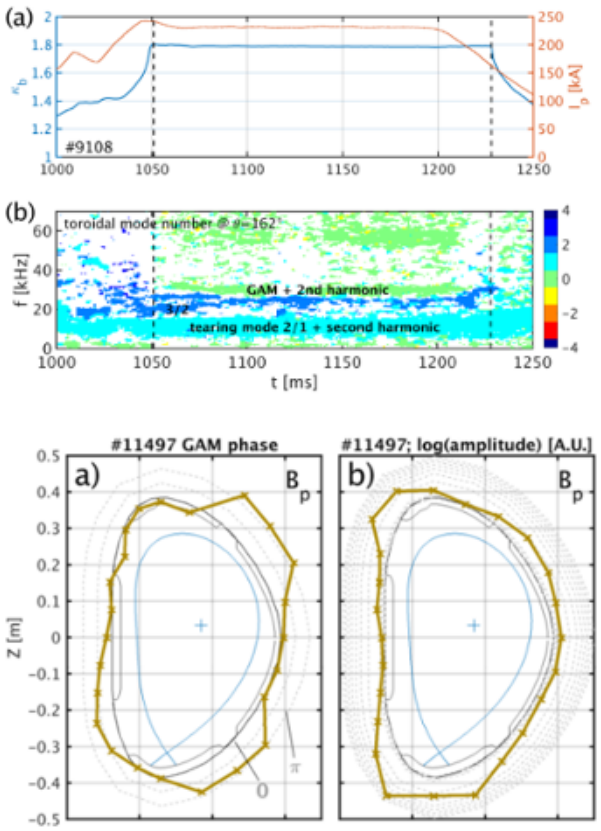

Figure 2: Measurement of toroidal and poloidal structure of GAM magnetic component.

c_s is ion sound speed, R_0 is major radius of tokamak and T is plasma temperature. The plasma discharge with NBI heating was used to change the plasma temperature significantly. Ion sound speed given by plasma temperature and GAM frequency before and during NBI heating is shown in figure 3 and fitted by linear function. The best fit was at radial position $\Psi = 0.85$.

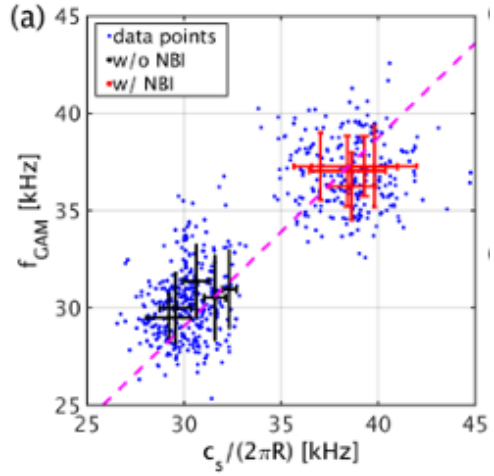

Figure 3: Scaling of GAM frequency with ion sound speed.

5. Conclusion

GAM was successfully identified on the COMPASS tokamak and article about GAM is ready to be published.

References

[1] P. Diamond, et al. Zonal flows in plasmaâĂŤa review. *Plasma Physics and Controlled Fusion* **47**(5):R35, 2005.

[2] N. Winsor, et al. Geodesic acoustic waves in hydromagnetic systems. *The Physics of Fluids* **11**(11):2448–2450, 1968.

[3] T. Lan, et al. Spectral features of the geodesic acoustic mode and its interaction with turbulence in a tokamak plasma a. *Physics of Plasmas* **15**(5):056105, 2008.

SEMICONDUCTOR PIXEL DETECTORS IN RADIATION IMAGING

Mahulena Kuklová*

Department of Physics, Faculty of Nuclear Sciences and Physical Engineering, Czech Technical University in Prague, Břehová 7, Prague, Czech Republic

* corresponding author: kuklomah@fjfi.cvut.cz

Abstract. Semiconductor pixel detectors are versatile devices applicable for example in nuclear medicine, astronomy or particle physics experiments. Each of these utilizations puts different demands on detector performance and characteristics. In high energy physics (HEP) experiments, it is primarily radiation hardness and fast readout. Hybrid pixel detectors have been well proven over many decades in HE/ albeit this technology is relatively complicated and expensive. Monolithic detectors represent a potential cheaper substitute of hybrid pixel detectors, but their properties are generally less suitable for operation in challenging environments, therefore a development and study of new monolithic detecting devices is needed. This work presents an already well-established hybrid detector Medipix and a monolithic detector prototype developed at FNSPE CTU is proposed.

Keywords: semiconductors, pixel detectors, monolithic detectors, hybrid detectors, Medipix.

1. Introduction

Semiconductor pixel detectors are 2D arrays of sensitive elements (pixels) used not only in large particle experiments, but also in astrophysics and many other fields.

Their development boomed at the end of the 20th century, one of the most popular semiconductor detectors are hybrid pixel detectors.

The Center of Applied Physics and Advanced Detection Systems (CAPADS) group based at FNSPE CTU has designed a monolithic chip prototype which aims to be equivalent to hybrid pixel detectors. Since it is a new technology, it needs to be properly analysed and its parameters quantified.

The aim of this paper is to provide a brief introduction to semiconductor pixel detectors physics and present two representatives of both hybrid and monolithic pixel detectors.

2. Technology overview

2.1. Semicondctors

There are three types of solid state materials based on their conducting properties: conductors, insulators, and semiconductors. The conducting properties depend on the energy band structure of the material, namely the "energetic distance" between valence and conduction band, which is called the bandgap.

Semiconductors' size of the bandgap makes it possible for electrons to be lifted from valence to conduction band (when an external source of energy equal or greater than the bandgap energy is present). This process leaves a vacancy (a *hole*) in the valence band.

Depending on the purity of a semiconductor material, one distinguishes between intrinsic and extrinsic semiconductors. Intrinsic semiconductors have an equal number of holes and electrons, while extrinsic semiconductors have one type of majority charge carrier.

Extrinsic semiconductors are fabricated through doping. A pure, intrinsic semiconductor is doped either with a pentavalent or a trivalent dopant. In the first case, electrons become the majority carriers and we call such material a n-type semiconductor; in the latter, a p-type semiconductor is created with holes as its majority charge carrier.

Upon joining a n-type and a p-type semiconductor (creating a p-n junction), the majority carriers of each semiconductor drift to the other side, thus forming a depletion region between both type materials, creating an electric field within the diode.

An external voltage can be applied to the diode. If the p- region is connected to a positive terminal and the n- region to a negative terminal, the depletion region shrinks and one says the diode is forward-biased. In the opposite case the depletion region widens the diode is reversely biased. Semiconductor detectors are operated in a reverse bias mode. If the depletion region spans across the whole diode, the diode is in a state of full depletion. Otherwise it is only partially depleted.

When a bias is applied to the diode, the depletion region behaves like a charged capacitor. For the width of the depletion region applies [1]

$$d \sim \frac{1}{\sqrt{V}}. \tag{1}$$

2.2. CMOS

CMOS stands for Complementary Metal-Oxid Semiconductor and describes a structure that implements both NMOS and PMOS transistors. In CMOS process,

transistors are integrated either directly in a p-type silicon substrate (bulk process) or in epitaxial[1] layer (epi-process) grown on the top of the silicon substrate.

The resistivity of the epitaxial layer is $\sim 10 \cdot$ Ω cm, while the resistivity of the substrate is $\sim$ 1 ÄĞ$dot\Omega$ cm.[2]

CMOS technology is used in front-end electronic chips of hybrid detectors and can be under certain limitations used in monolithic detectors too.

2.3. Silicon on Insulator

SOI technology is a special type of a CMOS process and upgrades the properties of monolithic pixel sensors fabricated in standard CMOS process.[3]

3. Hybrid pixel detectors

A hybrid detector is made of two homogenous parts: a sensor and the front-end electronic chip. These components are mated for example through bump bonding (pixel detectors), a relatively expensive technique, or through wire bonding (strip detectors). This allows for separate optimalisation of both parts of the detector.

A sensor is the part of the detector where the actual interaction with radiation takes place. After being irradiated, it sends a signal to the readout electronics which evaluates the information.

The signal in a hybrid detector is collected by drift because the sensor can be operated in full depletion.

Different types of hybrid detectors are distinguished primarily by their size and the number of sensing elements.

The pixel size of a hybrid pixel detector is below 1 mm^2 and the number of sensing elements is in the order of 10^3-10^4.[4] Because of its dimensions, the sensor has to be connected to the electronics "vertically", by a bump-bond. This high-density connectivity is the main characteristics of a hybrid pixel detector.

This design puts some demands on the construction. For one, the front-end (FE) electronics channel size must match the size of the pixel. The determining restriction for the channel size is Moore's law (which says that the number of transistors which can be fitted in an integrated circuit doubles approximately every two years). Also the electronics unit must be close to the sensor. [4]

An example of hybrid pixel detectors for radiation imaging is the Medipix family developed by the Medipix collaboration.[3]

3.1. Medipix

The Medipix collaboration is aimed at developing single photon counting system for X-Ray radiography. One of their most widely used products is the Medipix2 chip. It contains 256×256 pixels with 55µm pitch, which totals as a 1.982 cm^2 active area.[3]

[1] A process of artificial crystal growth: atoms of a monocrystallic coating material are applied to a monocrystallic substrate, continuously complementing the substrate.

The chip has a 256-bit fast shift register and an excellent signal-to-noise (SNR) ratio. Two threshold values can be set in order to eliminate background noise. More technical details of can be found for example in [5].

Timepix is a slightly modified version of Medipix2 which is able to provide arrival time information and work in a time-over-threshold mode.[3] However, only the lower threshold value can be set.

4. Monolithic detectors

If both the sensitive volume of the detector and the readout circuitry are placed in one piece of silicon, we speak of a monolithic detector. One of the advantages of a monolithic detector is the significant simplicity of the fabrication process – there is no need for up to three different assembly factories (one to construct the sensor, one to construct the front end electronics and one to bond them together). Since monolithic detectors require commercially available technology, the manufactory is significantly cheaper than hybrid detectors'.

The charge in a monolithic active pixel sensor (MAPS) is generally collected by diffusion. This process is much slower than drift and makes the detector more prone to radiation damage.[6] That is a critical disadvantage if one wants to use a monolithic detector in HEP experiments with high event frequencies. Nevertheless, it is possible to build a MAPS in a way enabling to operate the sensor in a fully depleted state, which allows for a faster collection by drift. One of the methods is the silicon on insulator (SOI) technology.

MAPS are already being used in some HEP experiments, the first experiment to include MAPS detectors was STAR at the Relativistic Heavy Ion Collider (RHIC) at Brookhaven National Laboratory. MAPS are integrated in its Heavy Flavour Tracker.

4.1. X-CHIP

X-CHIP-02 is a MAPS prototype developed by Labtech group at FNSPE CTU. It uses a SOI-CMOS technology and contains two pixel matrices. One of them has 21×58 pixels with 50 µm pitch, the other has 14×24 pixels with 100 µm pitch. Each pixel has a 8-bit counter. One threshold value can be set to eliminate background noise.

Apart from a sensitive diode and the front-end electronics, the chip contains multiple test structures. The goal is to use the chip in radiation imaging and dosimetry.

The sensitive parts are made of medium resistivity Si (100 Ω cm), the electronics is processed on a thin epitaxial layer which is separated from the handling wafer by a thin SiO_2 layer.

5. Measurement

5.1. Timepix

We performed several measurements with image quality indicators (IQI). Indicators with thickness spanning from 100 µm to 250 µm were placed in front of a Medipix quad board, which is a 2×2 board of Timepix detectors. They were irradiated by a RTG tube powered on 50 kV.

A flat field correction was applied on the data to clear the noise. Both the original and corrected images are in Figure 1.

A profile analysis of the thickest, 250 µm wire was done, see Figure 2.

5.2. X-CHIP-02

Several measurements have been done to verify functionality of newly developed chip and better understand its features. The first test concerned sensitivity to X-ray radiation and its dependence on bias conditions (namely the threshold and bias voltage of the sensor).

A testing X-RAY scan of Cetonia aurata was done, the resulting images of a leg and the head are in Figure 3.

A measurement of mean hitcount on threshold value dependency was performed, the threshold value was raised in increments of 5 units from 130 to 165. The data are in Figure 4.

A similar dependency of mean hitcount on bias voltage was performed, the data are in Figure 5. The fit function is

$$N(V) = (205 \pm 46)\sqrt{V} - (454 \pm 336). \qquad (2)$$

Both dependencies were reconstructed from data acquired by a 10× integration of a flat field. The shutter speed was in both 100 ms.

6. Discussion

6.1. Medipix

In Figure 1, a comparison of an uncorrected and corrected image is shown. The noise is caused by different amplification levels of each pixel. The peak corresponding to background signal narrowed after the correction as expected. The bump on the peak is caused by the top right chip in the quad board, which systematically detects more hits than the other chips. This could be corrected by scaling down the hits to match the rest of the board.

The data for profile analysis in Figure 2 were acquired as mean hit values from the first 12 rows corresponding to the area where a 250 µm wire was placed. Since the pixel pitch is 55 µm, the wire seems to be only 220 µm thick. This discrepancy is caused by the insufficient resolution of the chip and by diffraction effects.

6.2. X-CHIP-02

In the testing images from X-CHIP, only data from the 50 µm pitch matrix were used. The counters in the other matrix were quick to overflow. Because the counters are only 8-bit in comparison to the 13-bit counter of a Medipix chip, the image has to be integrated in order to get a clearer image.

In Figure 4, a significant raise in sensor sensitivity with increasing threshold (which is equivalent to a lowering minimum energy of a photon required in order for the hit to be counted) is to be seen. This dependence can be used to determine the expected background noise level corresponding to a certain threshold value. At threshold at around 170, the sensor is the most sensitive.

Similarly, from Figure 5 is obvious that the sensitivity of the sensor increases with increasing bias voltage. The square root dependence is derived from a square root dependence of depletion region thickness on bias (1).

7. Conclusions

A couple of testing measurements were performed with hybrid pixel detector Medipix quad board and monolithic pixel detector X-CHIP-2.

We demonstrated the sensitivity of the X-CHIP related to incident X-RAYs, made a couple of first images and measured the dependence of sensor sensitivity on threshold and bias.

In order to compare compare the results, additional measurements with both detectors will have to be performed.

References

[1] G. Lutz. *Semiconductor Radiation Detectors.* 1^{st} edition. Springer-Verlag Berlin Heidelberg, 2007.

[2] M. Havránek. CMOS MAPS (Monolithic Active Pixel Sensors). Lecture. Prague: FNSPE CTU, 2015.

[3] X. L. Cudié. *Design and characterization of 64K pixels chips working in single photon processing mode.* Electronics Design Division, in the Department of Information Technology and Media Mid Sweden University, 2007. Doctoral thesis.

[4] G. Knoll. *Radiation detection and measurement.* 4^{th} edition. John Wiley & sons, Inc., 2010.

[5] X. Llopart, et al. Medipix2, a 64k pixel read out chip with 55 µm square elements working in single photon counting mode. Presented at the IEEE Nuclear Science Symposium and Medical Imaging Conference, San Diego, California, USA, 4-10 November 2001, `http://mcampbel.home.cern.ch/mcampbel/Papers/M7-3-Xavier-Llopart.pdf`.

[6] P. Riedler. Monolithic Pixel Detectors in Hep Experiments. International Conference on Technology and nstrumentation in Particle Physics, Amsterdam, June 2-6 2014, `https://indico.cern.ch/event/192695/contributions/353249/attachments/277175/387771/TIPP2014_priedler0306.pdf`.

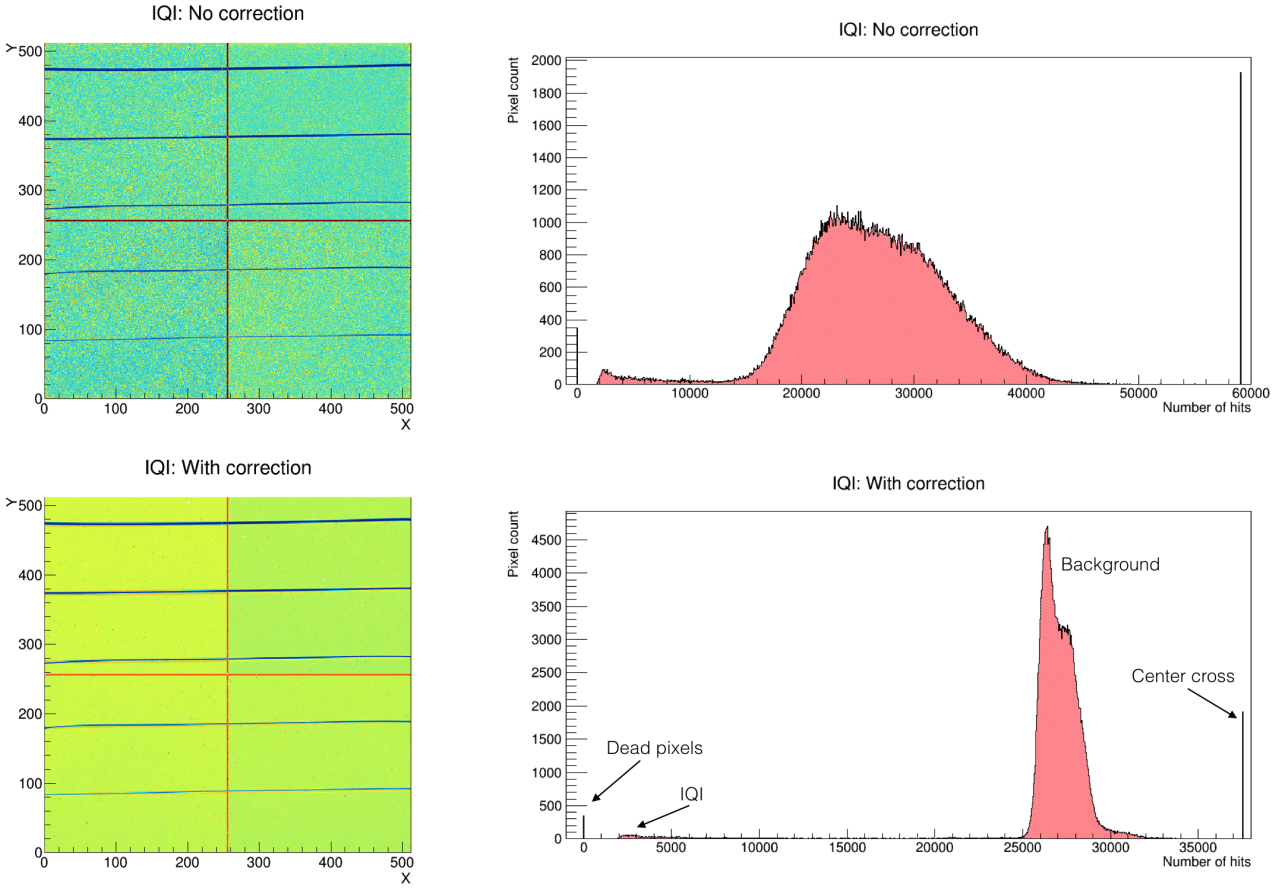

Figure 1: A comparison of an IQI image without (top) and with (bottom) flat field correction. On the left is an image captured by Medipix quad board, on the right is the corresponding histogram.

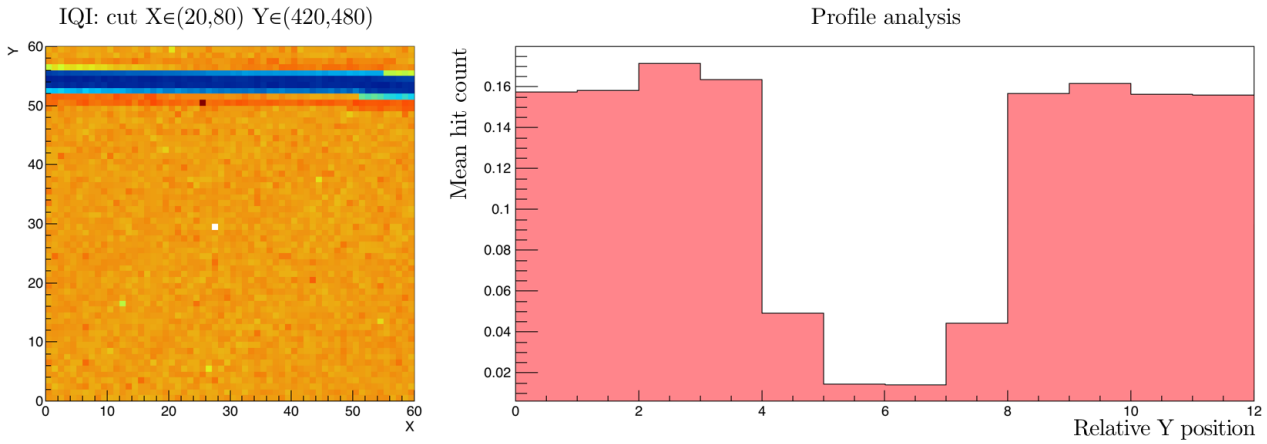

Figure 2: On the left is a detail on a 250 µm wire. On the left is a profile analysis of the first top 12 lines.

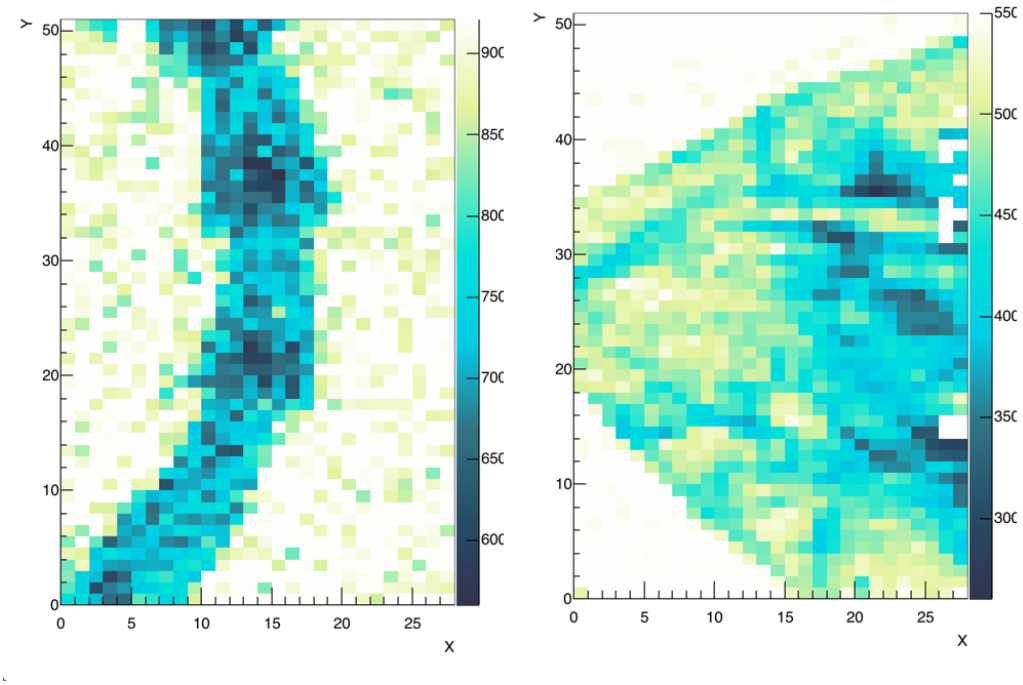

Figure 3: Images captured with the 50 µm pitch matrice of X-CHIP. On the left is a chitin leg with noticable brightness in joint areas, on the right is the head. Both images are results of gradual integration over time.

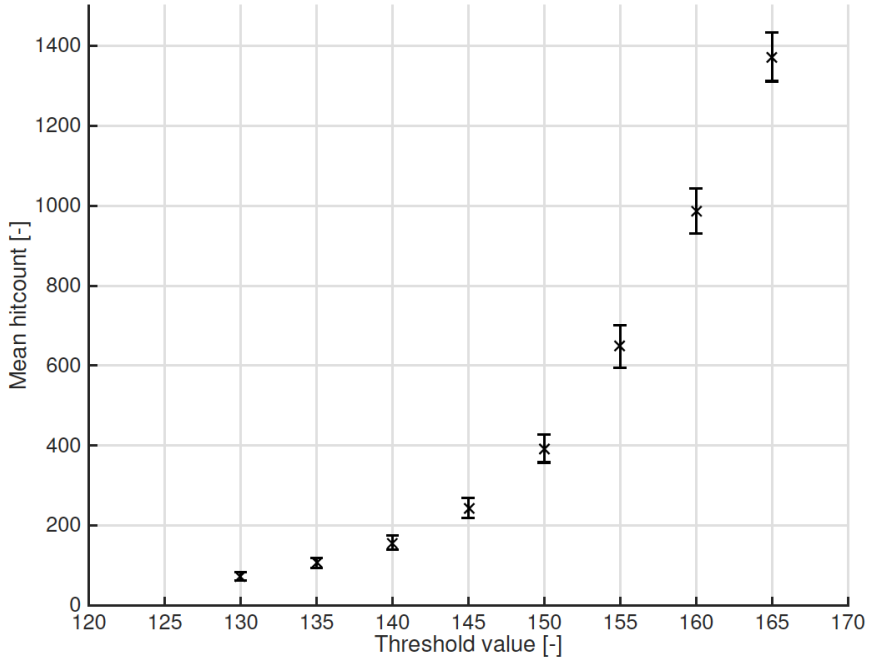

Figure 4: Mean hitcount on threshold dependance, acquired from X-CHIP flat field screenings. Each screening was an integration of ten 100 ms images.

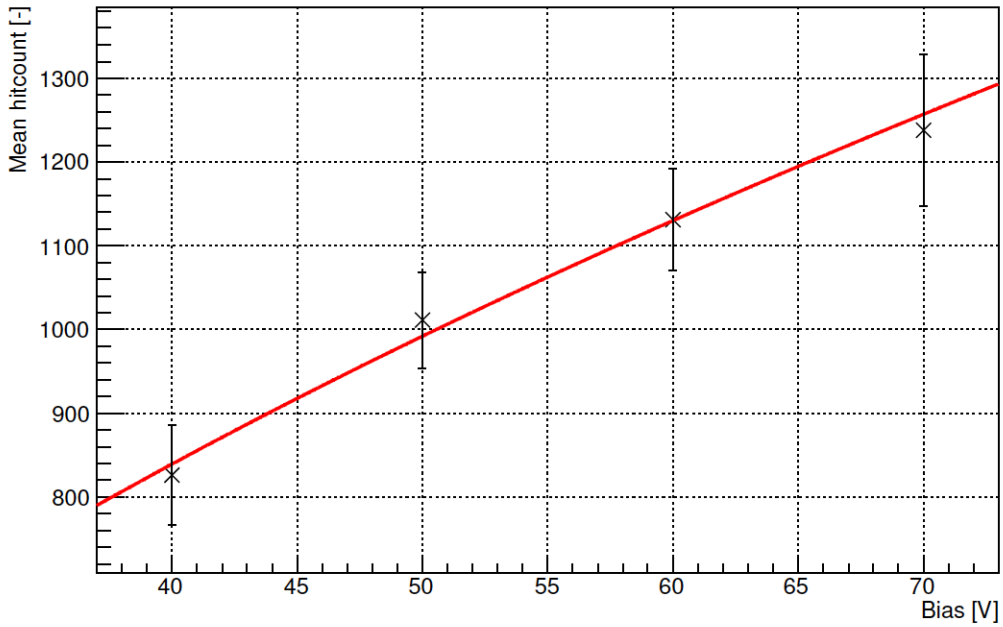

Figure 5: Mean hitcount on bias dependance, acquired from X-CHIP flat field screenings. Each screening was an integration of ten 100 ms images. The fit function is $N(V) = (205 \pm 46)\sqrt{V} - (454 \pm 336)$.

$D^{\pm}$ MESON PRODUCTION IN AU+AU COLLISIONS AT $\sqrt{S_{NN}}$ = 200 GEV MEASURED BY THE STAR EXPERIMENT

Jakub Kvapil*

Faculty of Nuclear Sciences and Physical Engineering Czech Technical University in Prague, Brehova 7, Prague, Czech Republic

* corresponding author: Jakub.Kvapil@fjfi.cvut.cz

Abstract. Charm quarks are mainly created in hard processes at the beginning of heavy-ion collisions and can be used as a tool to study properties of the Quark-Gluon Plasma (QGP). The modification to D-meson production in heavy-ion collisions is sensitive to the energy loss of charm quarks in the QGP. The Heavy Flavor Tracker was installed at the STAR experiment in 2014 and enables the topological reconstruction of the decay vertices for open charm mesons. It significantly improves precision on charm meson measurements. Besides the measurement of D^0, $D^{\pm}$ provides an additional handle and cross-check to study the interaction between charm quarks and the medium. In this poster, we present measurements of $D^{\pm}$ production in Au+Au collisions at $\sqrt{s_{NN}}$ = 200 GeV. $D^{\pm}$ mesons are reconstructed topologically via the hadronic decay channel $D^{\pm} \rightarrow K^{\mp}\pi^{\pm}\pi^{\pm}$ from the data collected in 2014 with the Heavy Flavor Tracker. The invariant yield of $D^{\pm}$ mesons in the transverse momentum range of $2 < p_T < 10$ GeV/c is extracted for 0-10% most central Au+Au collisions, and is found to be consistent with the D^0 yield.

Keywords: Quark-Gluon Plasma, QGP, $D^{\pm}$, Detector efficiency, Invariant yield, R_{AA}.

1. Introduction

Heavy quarks are mostly created in the initial phase of heavy-ion collisions. Therefore they experience the entire evolution of the system and are a good probe to study the properties of the Quark-Gluon Plasma (QGP). The strong suppression of high transverse momentum (high-p_T) D^0 meson yields indicates large energy loss of charm quarks in the QGP. Besides the D^0 meson, $D^{\pm}$ provides an independent handle to study the charm quark interaction with the medium. A good method to express the energy loss of particles in the medium is the Nuclear modification factor (R_{AA}), which example can be seen in Figure 1. Nuclear modification factor is defined as

$$R_{AA}(p_T) = \frac{1}{N_{binarycollisions}} \frac{Yield_{AuAu}}{Yield_{pp}} \qquad (1)$$

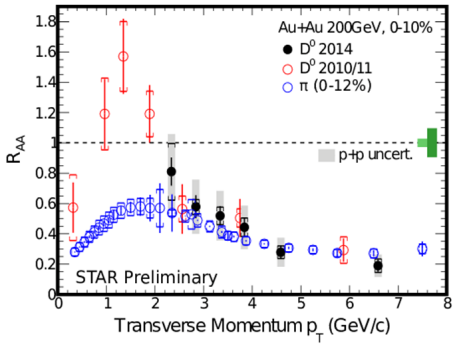

Figure 1: Nuclear modification factor (R_{AA}) of D^0 mesons and π [1].

2. STAR detector

The Solenoidal Tracker at RHIC (STAR) was designed to investigate the strongly interacting matter. It covers full azimuth at mid-rapidity ($|\eta| < 1$) with 0.5 T of solenoidal magnetic field. Main sub-detectors used in this analysis are (Figure 2):

(1.) Time Projection Chamber (TPC): main tracking device, particle identification via specific energy loss dE/dx, momentum reconstruction.

(2.) Time Of Flight (TOF): low p_T particle identification via velocity $1/\beta$.

(3.) Heavy Flavor Tracker (HFT) [2]: new inner tracking system composed of three silicon detectors - the PIXEL made of two Monolithic Active Pixel Sensors layers, Intermediate Silicon Tracker (IST) and Silicon Strip Detector (SSD). Each layer greatly enhance the pointing resolution up to level shown in Figure 3.

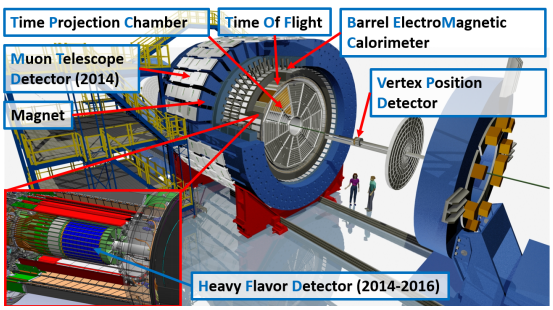

Figure 2: STAR detector with main mid-rapidity detectors.

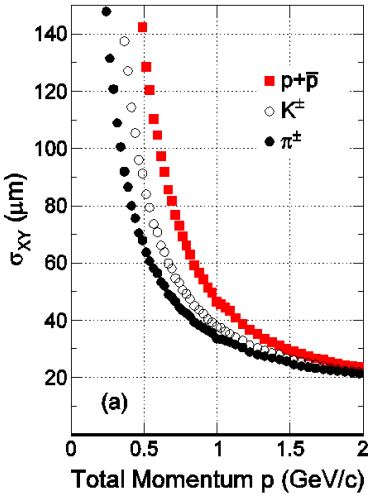

Figure 3: Heavy Flavor Tracker pointing resolution [3].

3. $D^{\pm}$ RECONSTRUCTION

About 900 million minimum-bias Au+Au events at $\sqrt{s_{NN}} = 200$ GeV recorded in year 2014 are used for this analysis. Several selection cuts for tracks were used in order to select good event on further analysis and selection of K, π for $D^{\pm}$ reconstruction. In Figure 4 we can see a three body decay.

(1.) Event selection cuts:

- Vertex position $|V_z| < 6$ cm
- Vertex correlation $|V_z(\text{VPD})\text{-}V_z| < 3$ cm.

(2.) Track selection cuts:

- Hits in the two PIXEL and one IST layers are required.
- At least 20 space points in the TPC for track reconstruction.
- Pseudo-rapidity: $|\eta| < 1$.

(3.) Topological cuts:

- Daughter DCA (Distance of closes approach) to primary vertex: $DCA_{\pi} > 100$ μm, $DCA_K > 80$ μm.
- Pointing angle of reconstructed vertex to primary vertex: $\cos(\theta) > 0.998$.
- $D^{\pm}$ decay length between 30 μm and 2000 μm (PDG $c\tau = 311.8$ μm).
- DCA between daughter pairs: $DCA_{pair} < 80$ μm.
- Longest edge of the triangle formed by reconstructed daughter pair vertices must fulfil $\Delta_{max} < 200$ μm.

(4.) Particle identification:

- Daughter $p_T > 500$ MeV/c.
- TPC: $|n\sigma_{\pi}| < 3.0$ for pions and $|n\sigma_K| < 2.0$ for kaons.
- TOF: $|1/\beta\text{-}1/\beta_{\pi}| < 0.03$ for pions and $|1/\beta\text{-}1/\beta_K| < 0.03$ for kaons. TOF information is used when available, otherwise only TPC is used.

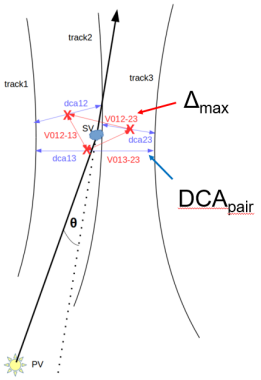

Figure 4: $D^{\pm}$ three body decay with variables used for selection.

4. $D^{\pm}$ RAW YIELD

The hadronic decay channel $D^{\pm} \to K^{\mp}\pi^{\pm}\pi^{\pm}$ is used. Background is estimated via the wrong-sign method: 2 correct-signal ($D^+(K^-\pi^+\pi^+)$, $D^-(K^+\pi^-\pi^-)$) and 6 wrong-signal (background) combinations ($K^-\pi^-\pi^-$), ($K^+\pi^+\pi^+$), ($K^-\pi^+\pi^-$), ($K^-\pi^-\pi^+$), ($K^+\pi^+\pi^-$) and ($K^+\pi^-\pi^+$). $D^{\pm}$ raw yields and significance are calculated using the bin-counting method in the 0-10% central Au+Au collisions for $2 < p_T < 10$ GeV/c where significance is estimated as $\frac{\text{signal}}{\sqrt{\text{signal+background}}}$. Example of raw yield signal in the 0-10% central Au+Au collisions for $3 < p_T < 3.5$ GeV/c can be seen in Figure 5.

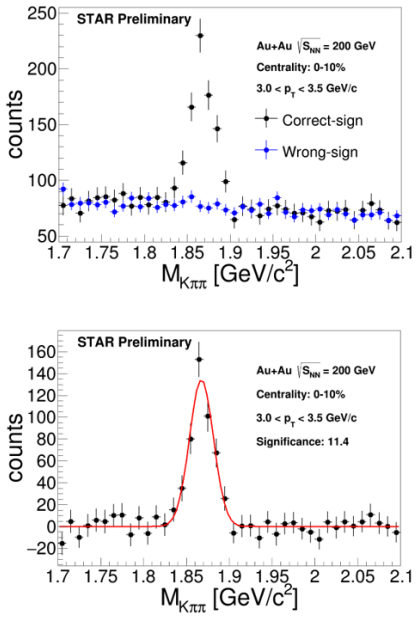

Figure 5: $D^{\pm}$ raw yield signal in the 0-10% central Au+Au collisions for $3 < p_T < 3.5$ GeV/c.

5. Acceptance and reconstruction efficiency

Data-driven fast simulator for acceptance and reconstruction efficiency has been developed. Simulator requires three main inputs: centrality-dependent V_z distributions and ratio of HFT matched tracks to TPC tracks extracted from data and TPC efficiency and momentum resolution from embedding. Fast simulator has been validated with full GEANT simulation. D$^{\pm}$ momentum dependent efficiency×acceptance in the 0-10% central Au+Au collisions is shown in Figure 6.

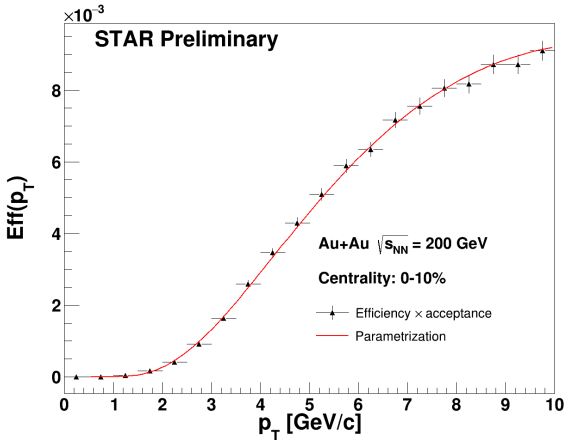

Figure 6: D$^{\pm}$ momentum dependent efficiency×acceptance in the 0-10% central Au+Au collisions.

6. Invariant yield and Nuclear modification factor

The D$^{\pm}$ raw yield is corrected using the following formula:

$$\frac{d^2N}{dp_T dz}\frac{1}{2\pi p_T} = \frac{Yield_{uncorrected}}{2\pi \cdot N_{charge} \cdot N_{events} \cdot BR \cdot p_T \cdot \Delta p_T \cdot \Delta z \cdot Eff(p_T)}, \quad (2)$$

where $N_{charge} = 2$, N_{events} number of events, $BR = (9.13\pm0.19)\%$, Δp_T bin width, Δy rapidity width, $Eff(p_T)$ detector acceptance×efficiency. Systematic uncertainties are estimated by varying cuts on daughter p_T, daughter DCA, DCA$_{\text{pair}}$, Δ_{max}, TPC fit points, changing histogram binning and testing fit stability. The D^0 spectrum in p+p collisions measured using 2009 data is used as the baseline [4].

The invariant yield of D$^{\pm}$ mesons with $2 < p_T < 8$ GeV/c in 0-10% central Au+Au collisions is consistent with that of D^0 mesons within uncertainties and is shown in Figure 7. The nuclear modification factor (R_{AA}) for D$^{\pm}$ also exhibits strong suppression at high p_T, indicating substantial energy loss of charm quarks in the medium and is pictured in Figure 8.

7. Conclusions

The D$^{\pm}$ invariant yield spectrum in 0-10% central Au+Au collisions at $\sqrt{s_{NN}} = 200$ GeV is measured via the hadronic decay channel D$^{\pm} \to K^{\mp}\pi^{\pm}\pi^{\pm}$ for the p_T range of 2-8 GeV/c. The D$^{\pm}$ and D^0 yields are consistent, both indicating strong energy losses of charm quarks in the medium.

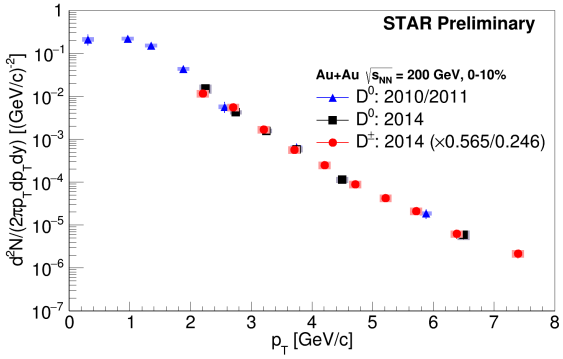

Figure 7: The invariant yield of D$^{\pm}$ mesons with $2 < p_T < 8$ GeV/c in 0-10% central Au+Au collisions.

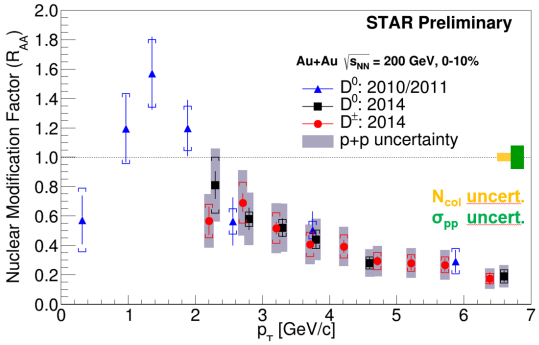

Figure 8: The nuclear modification factor (R_{AA}) of D$^{\pm}$ mesons with $2 < p_T < 8$ GeV/c in 0-10% central Au+Au collisions.

Acknowledgements

J. Kvapil was supported by the grant LG15001 and LM2015054 of Ministry of Education, Youth and Sports of the Czech Republic.

References

[1] G. Xie for the STAR Collaboration. Nuclear modification factor of D^0 meson in Au + Au collisions at $\sqrt{s_{NN}} = 200$ GeV. *Nuclear Physics A* **956**, 2016.

[2] J. Schambach for the STAR Collaboration. A MAPS based micro-vertex detector for the STAR experiment. *Physics Procedia* **66**, 2015.

[3] L. Adamczyk for the STAR Collaboration. Measurement of D^0 azimuthal anisotropy at mid-rapidity in au+au collisions at $\sqrt{s_{NN}} = 200$ GeV. `arXiv:1701.06060`.

[4] D. Tlusty for the STAR Collaboration. Open Charm Measurement in p+p $\sqrt{s} = 200$ GeV Collisions at STAR. `arXiv:1202.5571`.

LOOKING FOR CHARM PRODUCTION IN NOVA

Roman Lavicka[a,*], Keith Matera[b]

[a] *FNSPE CTU, Břehová 7, Prague, Czech Republic*

[b] *Fermilab, P.O.Box 500, Batavia, Illinois*

[*] corresponding author: roman.lavicka@fjfi.cvut.cz

Abstract. Employing a multivariate analysis implemented in ROOT (TMVA) we investigated a possibility to measure a production of charm quark in interactions of muon neutrino from NuMI beam with a near detector of the NOvA experiment. We trained the Boosted Decision Tree method with Monte Carlo simulations (set to summer 2016 collected statistics) of such events using 25 different variables. Applying the trained tree back on the Monte Carlo data we can predict a ratio of signal to background, which in our case is 0.001. This means that with available statistics the signal would be hidden in background events. More gathered data or better understanding of the TMVA process could twist this conclusion.

Keywords: muon neutrino, charm quark, multivariate analysis, NOvA experiment.

1. Introduction

One of the most abundant particles in the universe are neutrinos. The neutrinos are very important in many processes in the nature. The beta decay is a good example for all of them since it is essential for a thermonuclear fusion, an interaction which powers stars. There would not be a live in a form we know today on Earth without the energy provided by the Sun. Therefore it seems to be a good idea to learn more about the neutrinos and processes connected with them. Unfortunately, due to its negligible mass and ability to interact weakly only it is difficult to create, catch or measure them. Scientists all around the world throughout last decades grouped together to build several impressive facilities which focus on a neutrino research. One of them is located near Chicago, Illinois, at Fermi National Accelerator Laboratory (Fermilab).

There are several neutrino experiments at Fermilab. The NuMI Off-axis ν_μ Appearance (NOvA) is an experiment which is looking for neutrino oscillations. Its primary goals are to look for an oscillation of muon neutrino to electron neutrino (appearance) and an oscillation of muon neutrino to muon neutrino (disappearance). Measuring these probabilities one can put new limits on some physics quantities, such as ordering of neutrino masses or symmetry between matter and antimatter. Since the NOvA has become operational in 2014, the experiment NOvA gathered a lot of physics data. Recent results can be found in [1] and [2].

During the summer 2016 we investigated a possibility of a measurement of events, where neutrino interacts with a nucleon and creates a charm quark and muon. This later results in a single or dimuon event visible in a detector. A motivation of this effort is to provide a complementary measurement of the collaboration NOMAD in an energy range from 0 to 20 GeV [3]. Next pages describe and discuss current results.

2. Experiment

Because the collaboration NOvA's physics tasks are motivated with neutrino physics, it needs an intense beam of neutrinos called NuMI. A creation of this beam is sketched in Fig. 1. Everything starts with protons accelerated to an energy of 120 GeV in the Main Injector. These protons are delivered to a graphite target, where they interact and create primarily a lot of charged pions, mainly in a forward and semi-forward direction. The pions are then focused in two magnetic horns and sent to an almost 700 metres long decay pipe. When the pions travel through this pipe, they have enough time to decay into a muon and muon neutrino. Next the beam pass an hadronic absorber, which deflects all remaining protons and mesons made in the initiating collision. Than the beam propagates through a 230 metres of rock, where the rest of the muons is absorbed and only a beam of muon neutrinos with an energy ranging from 1 - 20 GeV remains.

While an axis of the NuMI beam points towards the Soudan Mine in Minnesota (hitting detectors of experiments MINOS and MINERvA), the experiment NOvA is constructed 14.6 miliradians off. This yields in a peak in an energy spectrum of neutrinos around 2 GeV and a long energetic tail, which is a fact we want to exploit in our analysis as it will be described in Sec. 3.

The experiment consists of two detectors - the near detector (ND) and the far detector (FD). As depicted in Fig. 2 the ND is located at Fermilab and the FD is 810 kilometres away in Ash River in Minnesota. The FD is larger so it would be a better idea to use this one for our research. Unfortunately, due to a

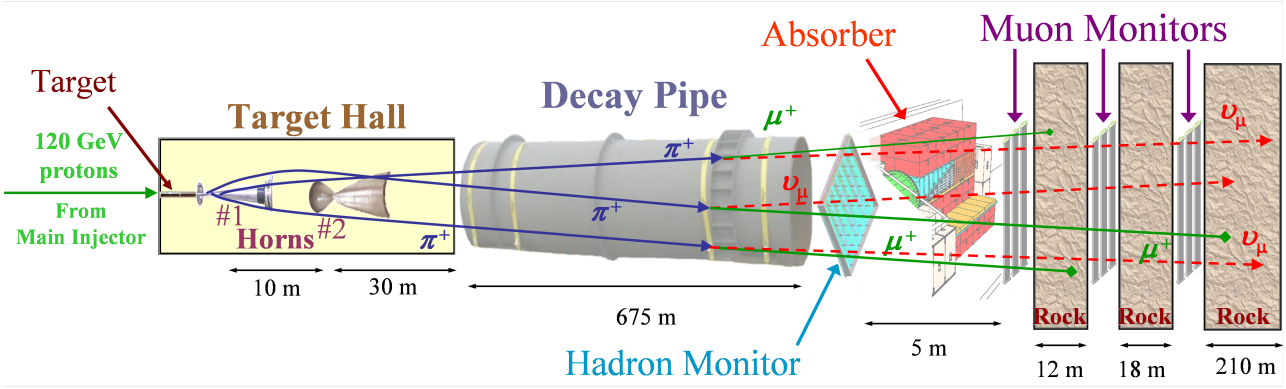

Figure 1: A scheme of the beamline in Fermilab.

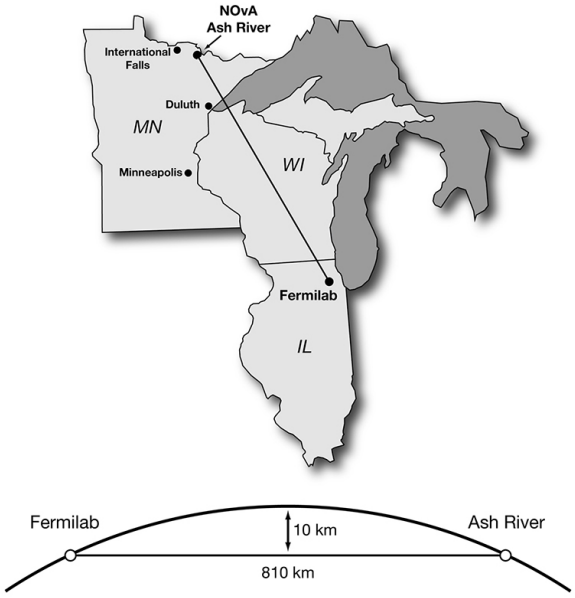

Figure 2: A scheme of the beamline in a macroscopic scale.

long distance a ratio of cross sections of the beam and the detector is much smaller than for the ND. Even if we catch hundreds of neutrinos in the ND per a second, we have only 1 neutrino in the FD per a minute. Therefore we used the near detector in our analysis.

The ND is a compact detector 350 feet underground with dimensions 2.9 x 4.2 x 14.3 m^3 [4]. The body is assembled from modules of extruded Poly Vinyl Chloride loaded with titanium dioxide. The modules are divided into 32 cells with proportions 3.8 x 5.9 centimetres. Each cell is filled with liquid scintillator and read-out with a wave-length shifting fiber which has an avalanche photo-diode on both ends.

3. Theory

Today we classify neutrinos according to their flavour or mass into three types. We can have electron, muon or tauon neutrino or we have 3 different mass states of neutrinos. Each flavour state neutrino consists of an currently unknown mixture of 3 mass state neutrinos. Because of the different masses, each mass state neutrino travels with different velocity and their superposition is changing in time. Therefore the mixture is fluctuating and we observe a flavour state transforming into another flavour state. This is called the neutrino oscillation and this is a primary object of investigation of NOvA collaboration.

But the collected data can be also used for another analysis. In our case it is a usage of the near detector to study a production of charm quark. A general diagram of such a process is shown in Fig. 3. The charm quark then hadronized into a baryon (mostly lambda) or a meson (mostly D-meson). These hadrons have very short lifetime and decay almost immediately through several decays, where some of them produce high energetic muons. In the end we can see one or two high energetic muons in the detector what can be a sign of the charm production.

The multivariate analysis (MVA) or it's ROOT implementation Toolkit for MultiVariate Analysis (TMVA) [5] is a perfect instrument to distinguish between charm events (signal) and the rest (background). This tool includes several packages to solve the problem. In this analysis we used so-called Boosted Decision Tree (BDT). This method as an input needs a set of variables which are further analysed. The method is depicted in Fig. 4. It loops over all possible cuts on each variable. As shown, it takes an event and asks for the first variable, whether it passed a cut or not. According to it, it is sent to one branch or another. In the next node, it is asked again on cut on the next variable (the selection criterion varies from branch to branch). This continues over all variables and in the end the decision whether it is a signal or background is made. This tree needs to be trained using data from Monte Carlo simulations. When the tree is trained, it returns a list of weights for all variables and a cut output value, which represents the best MVA value for the set of variables. The MVA value reflects the efficiency of the acceptance/rejection of data scaled to a general range.

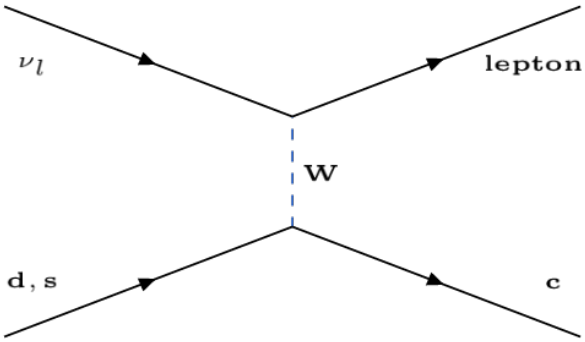

Figure 3: A diagram of a charm interaction. ν_l stands for a neutrino of a specific lepton, W is an intermediate boson and d, s and c are down, strange and charm quarks respectively.

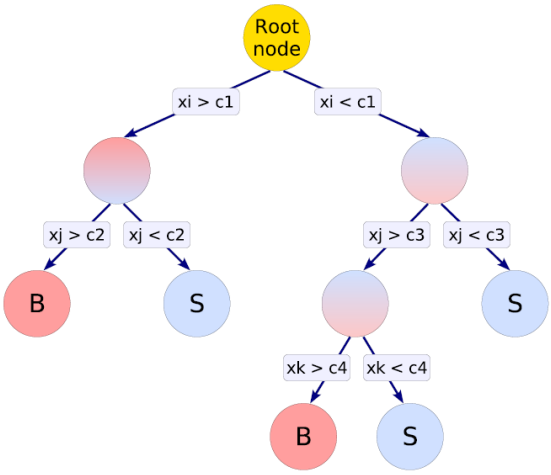

Figure 4: A scheme of a boosted decision tree. Each level represents one decision criterion. B is background, S is signal.

4. Implementation

During 9 weeks of work on this project we had to get acquainted with NOvA computing procedures, to learn with CAFAna tool and a structure of storage of data on a reconstruction level, displaying events, to use GRID for time-eating computations and to apply a multivariate analysis to find the best selections for our data. All this needed to develop several macros, which are described in this section and are saved in a development folder at NOvA hard drives.

4.1. Event displays

Looking at the event displays is one of the less complicated tasks in our analysis from the programming point of view. First, we had to get a specific file containing our wanted event. The macro *find-events.pl* in *EVD* folder serves this purpose. One only need to write correct definition name of the data snapshot and a name of a *.txt* file containing information about event inside the macro. The *.txt* file should in each line (representing 1 wanted event) have the

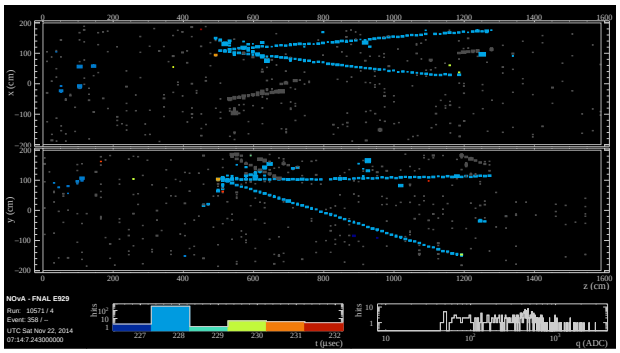

Figure 5: An example event display of an event containing 2 muons obtained from the Monte Carlo simulations.

numbers related to the event in this order: run, subrun, event, slice, cycle and time of the file creation. An example is in a file *dimuon.txt*. Running this macro will download the specific file with the specific event from the tape (SAM) into current folder. One can use a visual framework to look at the event by writing *nova -c evd.fcl -s <samplename.root>* into terminal. The framework is usually set via *edit→Configure Drawing→RawDrawingOptions* where one mark *by time* in a line *Color* and adjust range in a line *TimeRange*. To list through slices it is necessary to mark *slice* in a line *Zoom* in a bookmark *Geometry*. An example of event display with these options on is in Fig. 5. Widely useful option is to use information from the MCTruth module to display trajectories and/or interaction formula. In this case option *trajectories* (*short*) has to be marked in a line *Draw* (*Text*) in a bookmark *Simulation*.

4.2. Monte Carlo variables

To read data form a SAM file and save it in an easy-to-access format was a challenge. Two macros named *charmjob.fcl* and *CharmAnalysis_module.cc* were created and are located in a folder called *fcl*. The *.fcl* file is the one which should be run using ART by typing *nova -c charmjob.fcl* to terminal. This command can be extended with a switch *-s* ⟨*filename.txt*⟩, where the text file contains names of samples of the SAM snapshot which wanted to be processed. The second file is a module, which is called by the *.fcl* file and contains a code, which does with the sample what we want to be done.

A structure of the *.fcl* file is simple and is well commented. We only call attention on the list of input modules in a block called *physics*. Here it is crucial the names match names of modules in the SAM file. This can be easily check by eye using a predefined ART macro by calling *nova -c eventdump.fcl <samplename.root>* in terminal.

The CharmAnalysis module is a little bit more complicated. We only pinpoint important parts of the code in this paragraph. Each time the *.fcl* file loads a data sample, the CharmAnalysis class is constructed, which sets classes (i.e. BackTracker or TFileService)

ART needs for a communication. For each sample *beginJob, respondToOpenInputFile, reconfigure, analyze* and *endJob* functions are called respectively. The *.fcl* file loops over all events the sample contains (usually 2000 events) in the *analyze* function. All histograms or trees needed to store our wanted variables are set in the function *beginJob* and are saved in the function *endJob*. The *reconfigure* function serves to reconnect the input modules with our analyser module and the last function is there to obtain meta data informations about the opened sample.

The most comprehensive part is the analyser module. Here we recover variables we want for our analysis from the SAM files. In the first part we set everything what is needed for the communication with the input modules. The second part is a loop over slices (sub-events). In this part we check the slice and set some switches. Then we obtain and save informations from the sample to local variables. This is done directly in the code when it is necessary or via some functions defined in the header of the class. We should mention the filling of true variables which keep the information about the generated particles (not reconstructed). They are usually stored in an object called MCTruth and each slice contains more of them. Several conditions applied on them should pick only one object per slice. After that we save informations about the presence of the charm quark in the interact, if it comes from the sea quark and the number of muons generated according to the back tracker. The first one is an important variable for us to distinguish between signal and background and the other gives an complementary view helping us to understand what is going on.

At the end of the loop we decide, whether the sub-event was completely reconstructed in the near detector and if it was signal or not. Variables are stored according to it.

One more thing is important to mention about current version of this module. The output can be stored in two different ways. The first way is to store every variable to its own branch in a ROOT object called TTree [5]. To store data in this object is necessary for the multivariate analysis, which is described in Sec. 4.4. The second approach is to fill prepared histograms with the variables. A raw histograms are saved in a *.root* file. A macro called *GetRatio.C* located in a directory *ratio* is written to load this file, set all histograms, make ratios of signal and background for most of the variables and save it in a *.pdf* format.

Because of a pre-defined form of the module, we cannot easily use both methods of data storage simultaneously and one have to switch from one type to another manually commenting and un-commenting some parts of the code. This solution is not optimal and it originated from a development of the code. The next step would be to use a TTree object only to save variables which means the macro *GetRatio.C* needs to be rewritten. Unfortunately we didn't consider this to be a crucial problem, therefore we used our limited time on some other urgent issues.

4.3. GRID

Analysing large amount of events demands a high computational power which would take more than a reasonable amount of time for a laptop. Therefore collaboration NOvA dispose with an array of processors which users can use for their calculations. Once user sets his working environment properly, he can create a project on GRID to run his analysis running a predefined macro called *submit_nova_art.py*. This can be set with options which are listed in [6]. To simplify the act the options can be written in a configuration file which can be append to the macro with a switch *-f*. The configuration file we used is located in a folder *grid* and is named *runcharmjob.cfg*.

A user should set carefully several thing in the file, such as name of the project, where the *.fcl* file is located or which snapshot should be taken. All options are well commented. We will only stress out that for usage of TFileService class one need to set an option *--histTier* with a name which will be appended to a name of an output file.

Each snapshot is usually divided into smaller files. These files contain some number of events. If you want to analyze more events than there are in a single file, you have to express it in the configuration file. An option *--filer_per_job* serves to tell to grid, how many files each job will look at. A number of jobs to be processed is set with *--njobs* option. The power of grid is that it can work on more jobs at the same moment (up to hundreds). An only restriction on users is to set jobs to last between 1 to 6 hours. Therefore the configuration file should contain a proper ratio of number of jobs and number of files per job.

4.4. TMVA

As mentioned before we used ROOT's toolkit for multivariate analysis to train the boosted decision tree method with our Monte Carlo data and to retrieve a selection criterion. Original and adjusted macros from the original ROOT package are located in a folder *TMVA*. There are 3 macros which should be touch.

The macro *classification.C* is the one used to train the tree. It is very well commented and before every use a user needs to take care of several lines. First, names of input and output files had to be set properly in TString objects called *fname* and *outfileName* respectively. Then all used variables has to be assign to the TMVA's object of class Factory via a function *AddVariable*. These have to match with names of branches of TTree objects in the input *.root* file. How to handle this is described in more detail in [7].

Running this macro results in several files. One is the output *.root* file containing histograms for instance with correlations among variables, cut efficiencies or over-training checks. These can be easily accessed

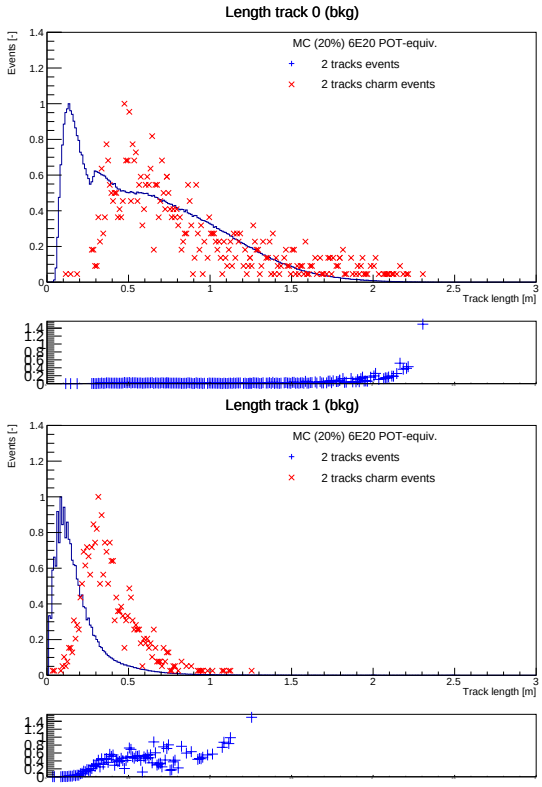

Figure 6: Plots of the lengths of the longest (top) and the second longest (bottom) tracks in an event. Each plot is divided into 2 pads, where the top one contains a histogram for a signal and a background and the bottom one their ratio.

with running a macro *TMVAGui.C* and are automatically plotted into a directory *TMVA/plot*. Other outputs are tables with weights for each variable found by BDT and are stored in *.xml* format in a folder *TMVA/weights*. These are used by a macro *application.C*. This one serves to read the weights using TMVA's object of class Reader and applying them on our data, returning the MVA output value for each event. This can be compared to the cut criterion from the BDT method and accept (or reject) the event. In addition, this macro stores a histogram with numbers of accepted and rejected events into *.root* file made by TFile object called *target*.

5. Results

As it emerges from the previous chapters, our output is mostly graphical. As our input we used Monte Carlo generated data which have a specific definition name used by the NOvA collaboration (available upon request) and contain around 100 millions of event of neutrino interactions with NOvA's near detector.

First, we were able to plot ratio of signal and background for different quantities. These we used to look for some significant differences, which would help us to distinguish between signal and background by a simple cut on a specific variable. In Fig. 6 we have plots of lengths of the longest and the second longest

Variable	Pre-selection
Length of the longest track	>152 cm
Length of the 2. longest track	>16 cm
Hit ratio of the longest track	<0.88
Hit ratio of the 2. longest track	<0.64

Table 1: Pre-selection criteria as suggested by BDT method.

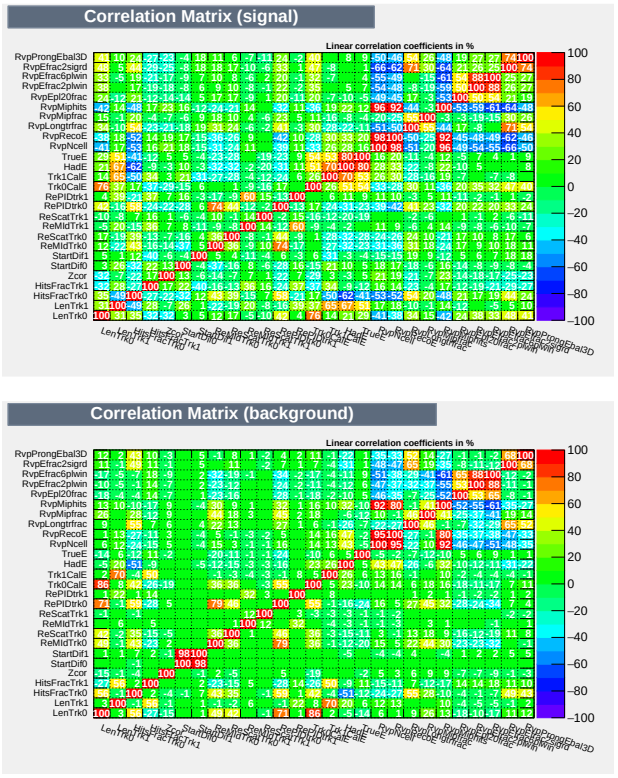

Figure 7: Correlations of variables used by BDT for signal (top) and background (bottom).

tracks in each event as an instance. All produced plots are stored in the *.pdf* file *ratios20M* located in NOvA hard drives. In Fig. 6 we can see that charmed events have more likely longer tracks of muons. This holds with the fact that charmed events should produce more energetic muons than the other. Therefore we believe that a pre-selection cut on track length or muon energy would help.

Except the track length we identified other variables, which could be helpful. Among these belongs a ratio of hits of the track to the other hits (for both tracks). The BDT method can also suggest, which pre-selection criteria use and these are written in Tab. 1. Although we could be more strict according to our plots, we have decided to apply cuts from BDT for consistency.

From the plots we have picked a set of variables. Their correlations are in Fig. 7. As we can see, most of them are not correlated, which is good. But some (like Trk0CalE and LenTrk0) embody large correlations and had to be scratched. In addition, we scratched

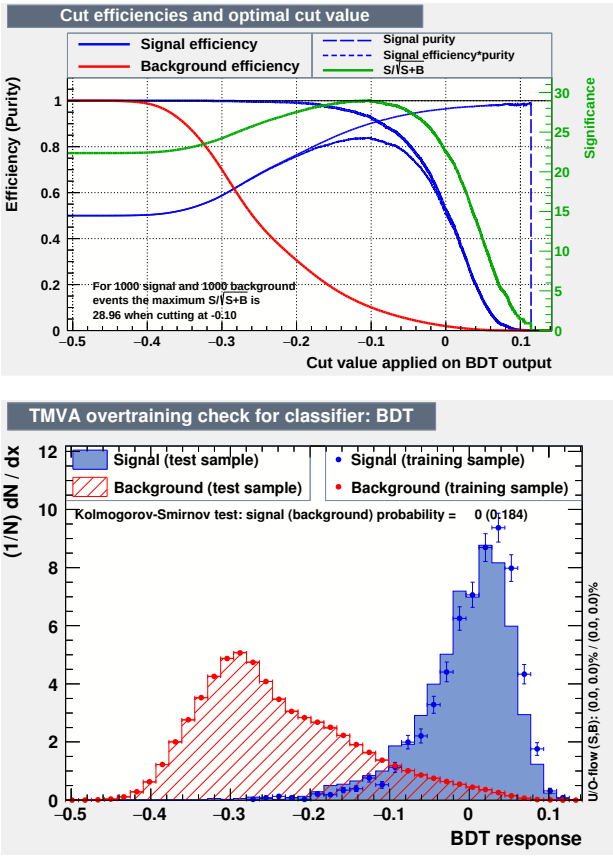

Figure 8: Results of the boosted decision tree method of MVA. The top plot shows efficiencies of the cut on background and signal events. The bottom plot is check for BDT over training.

a variable TrueE and HadE since they represent an information directly from the Monte Carlo generator and we could not use it for real data. On the other hand we kept all variables starting with Rvp. Unfortunately we didn't have time to investigate them more, so we hoped they don't ruin the result. As it will be mention later this is a place where we should pay more attention in future.

When we had prepared trees containing our chosen variables filled with informations from signal and background events, we could start using BDT. The method is described above and results are in Fig. 8. In the top plot the blue line represents an effect of the cut on the signal events, the red line tells us an efficiency of the cut on the background events and the green line shows

$$\frac{S}{\sqrt{S+B}} \tag{1}$$

where S stands for a number of signal events and B for a number of background events. The maximum of the green line gives us a BDT output value, which we use to cut on when looking on a data. The second plot in Fig. 8 tells us, if BDT method was not over trained. It seems it finished well.

Due to a lack of time, we were able to check the efficiency of the found cut only with Monte Carlo. Applying our trained tree on signal (background) and select only those events having the BDT output value > -0.1, we got a percentage of events passing the selection which is 70% (87%). Taking into account that we have 4 705 signal events and 10 441 570 background events we have a ratio of signal to background 0.001, which means that after our selections, we will still have only 1 wanted event between 1000 unwanted events.

6. Conclusions

The resulting ratio is a horrible number and means that we have to repeat a whole process of selection carefully and find any mistake we could make. Appearance of the error is highly likely since we didn't have enough time to properly focus on the BDT method. If we will conclude that we did everything right or we will not be able to find a better selection even after all corrections, we should consider to use a different variables or maybe a different decay modes. If nothing helps, we should start asking, if we are able to measure charmed events with NOvA near detector.

Acknowledgements

R. Lavicka was supported by grant 114-49/15047. R. Lavicka would like to express his gratitude to his supervisor Keith Matera for his invaluable advice and support during the realization of this work. R. Lavicka would also like to thank to RNDr. Milos Lokajicek, DrSc. and everyone from the Italian team, who organized the Summer Students at Fermilab Program, during which this work was done, giving him priceless experience and opportunity to broaden his knowledge and to work side-by-side the best people in the field.

References

[1] P. Adamson, et al. First measurement of electron neutrino appearance in NOvA. *Phys Rev Lett* **116**(15):151806, 2016. 1601.05022.

[2] P. Adamson, et al. First measurement of muon-neutrino disappearance in nova. *Phys Rev D* **93**:051104, 2016.

[3] F. Vannucci. The NOMAD Experiment at CERN. *Adv High Energy Phys* **2014**:129694, 2014.

[4] D. S. Ayres, et al. The NOvA Technical Design Report 2007.

[5] I. Antcheva, et al. ROOT: A C++ framework for petabyte data storage, statistical analysis and visualization. *Comput Phys Commun* **180**:2499–2512, 2009. 1508.07749.

[6] P. Adamson, et al. The nova offline workbook. [2016-10-07], https://cdcvs.fnal.gov/redmine/projects/novaart/wiki/Submitting_NOvA_ART_Jobs.

[7] P. Speckmayer, et al. The toolkit for multivariate data analysis, TMVA 4. *J Phys Conf Ser* **219**:032057, 2010.

UPSILON PRODUCTION AT THE STAR EXPERIMENT

Robert Licenik*

Department of Physics, FNSPE CTU in Prague

* corresponding author: licenrob@fjfi.cvut.cz

Abstract. This paper covers the introduction into the quarkonium (especially Υ) physics and the summary of current and future work in this field. The Υ meson serves as an excellent probe in the QGP as it provides us with a "thermometer" of the hot strongly interacting matter. The production of quarkonia is suppressed in the QGP because the presence of free color charges results in the Debye screening effect and the two constituent quarks are not able to "see" each other so the quarkonium dissolves. The motivation for measurements of the Υ production is the completion of the QCD phase diagram with focus on the QGP-hadronic matter phase transition including locating the critical point. To measure the suppression, the nuclear modification factor R_{AA} is introduced. Recent LHC and RHIC results are presented with main focus on the STAR Au-Au data.

Keywords: quarkonia, Υ meson, quark-gluon plasma, heavy-ion collisions, STAR experiment.

1. Introduction & Motivation

The quark-gluon plasma (QGP) is a state of matter, where the quarks and gluons are free and not confined in hadrons as they are in ordinary matter. This is an interesting field of study as the early Universe is thought to pass through a QGP phase. Since QGP is not observed anywhere in the Universe at the present, it needs to be created by colliding heavy ions (such as Au, Pb, U,...) accelerated to velocities close to the speed of light in vacuum at particle colliders such as the Relativistic Heavy Ion Collider (Fig. 1)

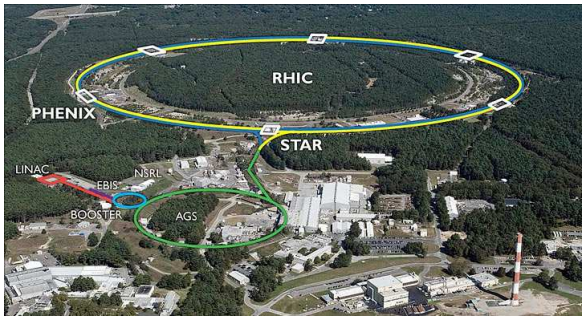

Figure 1: The RHIC accelerator complex at the Brookhaven National Laboratory in Long Island, NY. Source: [1].

The phase transition from hadronic matter to QGP occurs when the medium temperature exceeds a critical temperature $T_c \approx 175$ MeV. Since it is impossible to measure the QGP temperature directly, there is a need for a probe capable of at least approximating the temperature of the hot strongly interacting medium. One of those probes is the measurement of quarkonia (including the $\Upsilon(nS)$ meson - sec. 2) production suppression. Different quarkonia are suppressed at different temperatures so observation of the suppression of a given quarkonium is a good indicator that the temperature of the medium has exceeded certain value. This is illustrated in Fig. 2

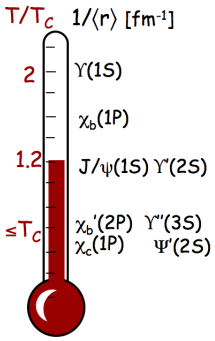

Figure 2: The quarkonium thermometer with different quarkonium states shown along with the temperature above which their production is suppressed. Source: [2].

The ultimate goal is the completion of the QCD phase diagram which can be seen in Fig. 3.

Major progress has been achieved thanks to the RHIC Beam Energy Scan, where the accelerator's unique capability of colliding heavy ions at different energies (several runs with $\sqrt{s_{NN}} = 7.7$ - 200.0 GeV) was utilized. First order phase transition occurs at lower energies (before the critical point) while beyond the critical point the phase transition appears to be a crossover.

2. Bottomonia

The $\Upsilon(nS)$ meson is a part of the bottomonium family (Fig. 4), which is composed of all known $b\bar{b}$ pair bound states. The 3 S-wave states below the open beauty threshold (energy level above which it is more energetically favorable to create a $B\bar{B}$ meson pair)

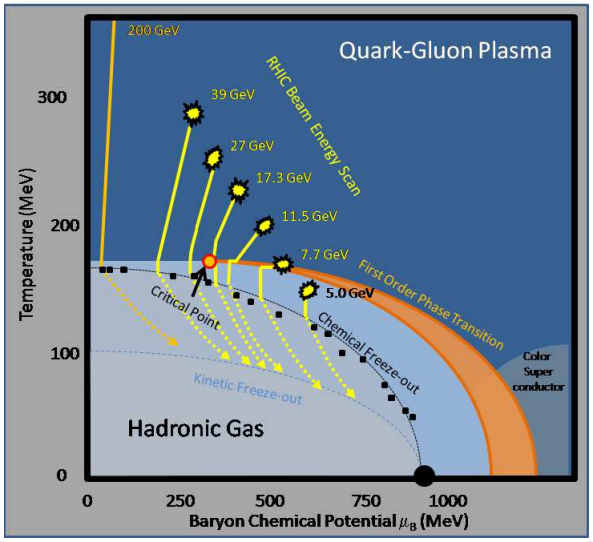

Figure 3: The QCD phase diagram. RHIC Beam Energy Scan results are shown and so is the expected position of the critical point. Source: [3].

are commonly referred to as the $\Upsilon(nS)$ meson where $n = 1, 2, 3$.

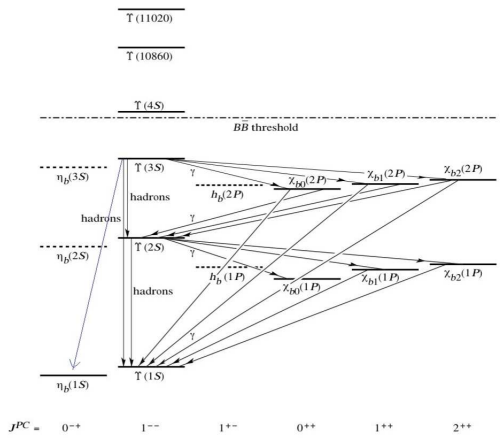

Figure 4: The bottomonium family ascending with increasing rest energy. The Υ states are in the second column. The open beauty threshold and feed down lines are shown as well. Source: [4].

The $\Upsilon(1S)$ meson was the first to be discovered (Fermilab, 1977) and has a rest mass $m_{1S} = 9.5$ GeV/c^2. The other two states were discovered soon afterwards and are slightly more massive. All three states have $J^{PC} = 1^{--}$ and a mean lifetime $\tau \sim 10^{-20}$ s. The $b\bar{b}$ pairs are created exclusively during the hard part of the collision because of their high mass, the main process being the gluon fusion. However, the evolution into the quarkonium state is a soft process so it cannot be described using the perturbation theory. Fortunately, several theoretical models (Color Evaporation, Color Singlet and Color Octet models to name a few) do exist and are an active field of study. Because the bottomonium family is so complex, it is important to study the feed down from resonances. In Fig. 5 the main sources for different quarkonia can be seen. The main source is always direct creation and the most important feed down state is the closest P-state.

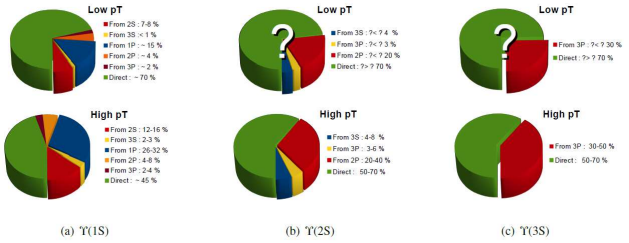

Figure 5: Diagrams showing the amount and sources of feed down for all 3 Υ states, also split into two categories according to their p_T. The main source are always directly created mesons (green) and the largest feed down comes from the closest P-wave state. Source: [5].

2.1. Advantages of Bottomonia

Studying the suppression of bottomonia such as the Υ meson offers several advantages over the charmonium family (which includes the J/ψ and $\psi(2S)$ mesons). One of them is the existence of 3 Υ states below the open flavor threshold in comparison to only two ψ states. This provides us with a finer scaling of the quarkonium thermometer (Fig. 2). These states also occur in a more favorable ratio (7:2:1 compared to 50:1). Furthermore, there is no feed down from the decay of b quarks. Because of the higher mass, there is a lower combinatorial background and the decay products - usually dileptons - are more easily detectable. Since the Υ meson has a large mass, the dileptons have large p_T and also scatter at high mutual angles. One major disadvantage is the lower total abundance of Υ mesons, especially at RHIC energies, while this is not as significant at LHC energies, [5].

3. Theoretical Background

Because the quarkonium is created during the hard scattering, it is also created before the QGP has formed. In vacuum, the quark-antiquark pair can be described by the Cornell potential:

$$V(r, T = 0) = -\frac{4}{3}\frac{\alpha_s(r)}{r} + \sigma r \qquad (1)$$

The first term of the potential is the Coulomb term, while the second is a string term. The Coulomb term is dominant at short distances and is responsible for asymptotic freedom. The string term is responsible for the quark confinement. When increasing the heavy-quark distance the potential increases as well to the point where it is more energetically favorable to create a quark-antiquark pair from vacuum, thus reducing the distance. This can be compared to pulling both ends of a string apart, increasing the tension. Eventually, the string will snap creating two shorter

strings. When the quark-gluon plasma forms around the quarkonium, the potential (1) is modified because of the presence of free color charges:

$$V(r,T) = -\frac{\alpha_{eff}}{r}\exp(-\frac{r}{\lambda_D(T)}) + \sigma\lambda_D(T)[1-\exp(-\frac{r}{\lambda_D(T)} \quad (2)$$

where $\lambda_D(T) \sim \frac{1}{\sqrt{T}}$ is the Debye screening length. In the case of a quarkonium it is the distance beyond which the heavy quark of the quarkonium cannot "see" the heavy antiquark (and vice versa). With increasing temperature the Debye screening length decreases and when it reaches the binding radius of the quarkonium, the quarkonium dissolves and ceases to exist. This can then be measured as a production suppression. First proposed in 1986 by Matsui and Satz [6], quarkonia suppression is now measured to detect whether or not the QGP has formed and how high is the temperature of the medium. This suppression is often described by the nuclear modification factor R_{AA} which uses the yield from p-p collisions - where no QGP is created - as a reference frame. Nuclear modification factor is defined as:

$$R_{AA} = \frac{\frac{\mathrm{d}^2 N_{AA}}{\mathrm{d}p_T \mathrm{d}y}}{\langle N_{coll}\rangle \times \frac{\mathrm{d}^2 N_{pp}}{\mathrm{d}p_T \mathrm{d}y}}, \quad (3)$$

which is the ratio of a A-A collisions yield and a yield from p-p collisions multiplied by the average number of binary collisions in the A-A collisions. This factor includes the effect of both hot (QGP) and cold nuclear matter (CNM). CNM effects include the interaction with the shattered nuclei - effects such as (anti)shadowing and recombination. A comparison with $R_{p/dA}$ (defined similarly to R_{AA}) is used to separate the CNM and QGP effects since it is assumed that in p/d-A collisions there is no QGP created. Current RHIC and LHC measurements indicate nearly complete suppression of $\Upsilon(2S)$ and $\Upsilon(3S)$ states while no direct $\Upsilon(1S)$ is observed. There is significant $\Upsilon(1S)$ suppression, but this is attributed to the suppression of feed down from resonances.

4. RHIC and LHC Results

Quark-gluon plasma is created in high-energy heavy-ion collisions at RHIC (detected by experiments STAR and PHENIX)and LHC (experiments ALICE, ATLAS and CMS). The STAR and PHENIX results from the d-Au and p-p collisions showing a disagreement with theoretical prediction of cross section vs rapidity can be seen in Fig. 6.

In Fig. 7 the STAR results of R_{AA} can be seen. On the left there is a dependence on the collision centrality. At the top there is a measurement of a combined $\Upsilon(1S{+}2S{+}3S)$ production from Au-Au and U-U collisions compared to theoretical predictions and CMS data. The data sets are fairly consistent with theoretical prediction and with each other. At the bottom there is a measurement of $\Upsilon(1S)$ only. Data

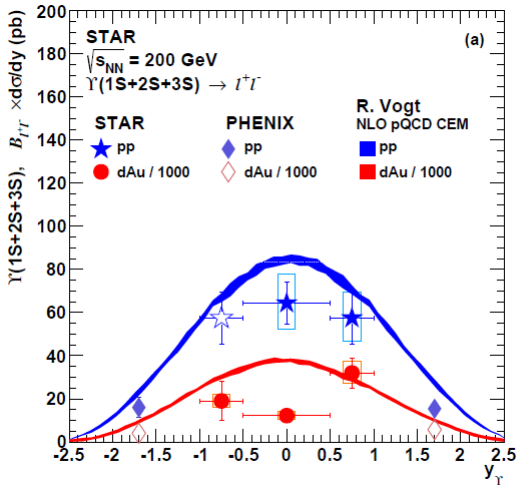

Figure 6: STAR and PHENIX measurement of Υ cross section vs rapidity compared to theoretical prediction. Theory tends to overestimate the data, especially in d-Au collisions. Source: [7].

from Au-Au collisions indicate lower suppression than expected while data from U-U collisions. are fairly consistent with theory and CMS. On the right there is a plot of suppression of different quarkonia types, each of them being suppressed in the A-A collisions.

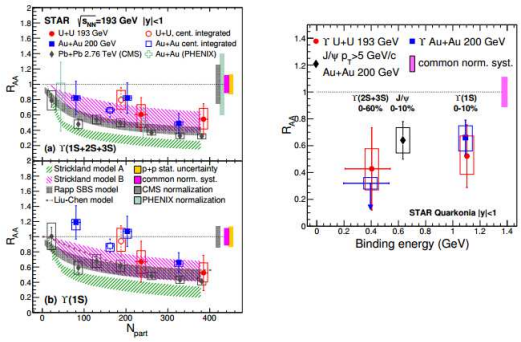

Figure 7: STAR R_{AA} measurement. Left: R_{AA} vs $< N_{part} >$ for Au-Au and U-U collisions indicating high suppression in most central collisions. Right: R_{AA} vs the quarkonium binding energy. Source: [8].

The ALICE experiment in CERN has measured the R_{AA} dependence on rapidity and $< N_{part} >$ in 2.76 TeV Pb-Pb collisions. The results of R_{AA} vs y dependence can be seen in Fig. 8. A strong discrepancy between the data and theoretical predictions is apparent.

The results of R_{AA} vs $< N_{part} >$ can be seen in Fig. 9. It is shown that the theory tends to underestimate the suppression of Υ meson production.

The ATLAS collaboration does not have any results from Pb-Pb collisions, but their results from 5.02 TeV p-Pb collision were published (Fig. 10). The data show little to no suppression of $\Upsilon(1S)$ meson production regardless of $< N_{part} >$, but are somewhat open to interpretation.

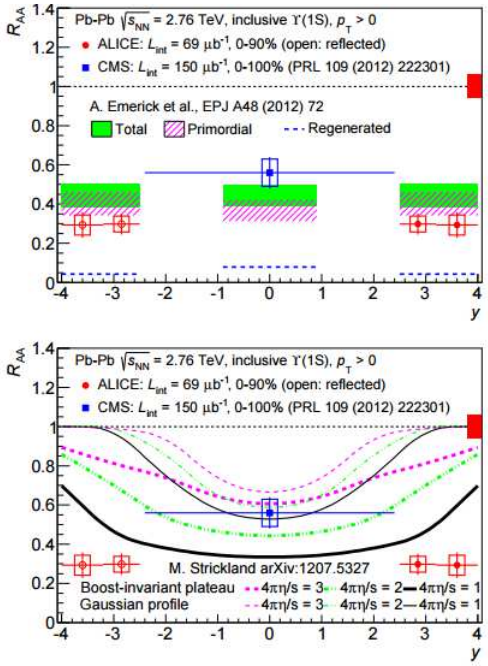

Figure 8: ALICE measurement of R_{AA} dependence on y showing disagreement with theoretical predictions. Source: [9].

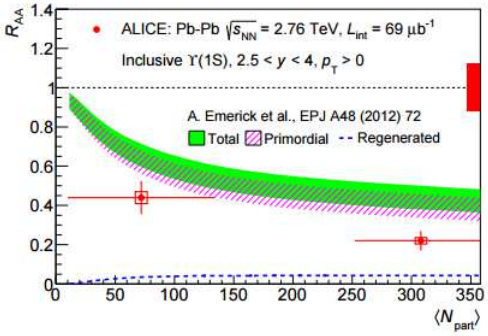

Figure 9: ALICE measurement of R_{AA} dependence on $< N_{part} >$ showing that theory underestimates the suppression. Source: [9].

The CMS collaboration has measured ϒ meson suppression in p-p, Pb-Pb (2.76 TeV) and p-Pb (5.02 TeV) collisions. Results of the dimuon invariant mass spectrum indicate medium suppression in p-Pb collisions and strong suppression in Pb-Pb collisions (Fig. 11). The suppression can be also seen in Fig. 12. This plot of a dimuon invariant mass spectrum from Pb-Pb collisions was scaled by a results from p-p collisions assuming no direct $\Upsilon(1S)$ suppression, showing high level of $\Upsilon(2S)$ and $\Upsilon(3S)$ suppression.

The CMS collaboration has also published their results from R_{PbPb} dependence on $< N_{part} >$ and p_T measurements distinguishing between $\Upsilon(1S)$ and $\Upsilon(2S)$. It can be seen in Fig. 13 that the suppression increases with centrality and is much higher for $\Upsilon(2S)$,

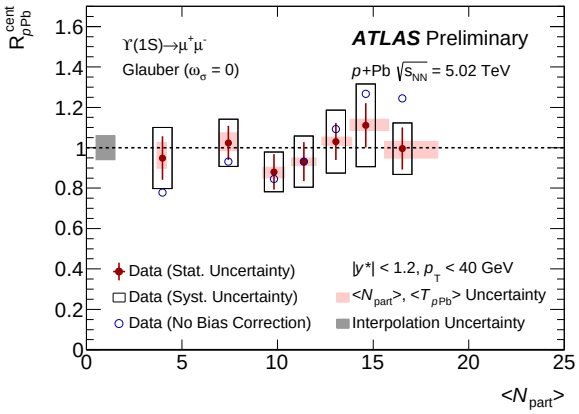

Figure 10: ATLAS results of R_{pPb} vs $< N_{part} >$ showing no significant modification in production. However, results are not conclusive. Source: [10].

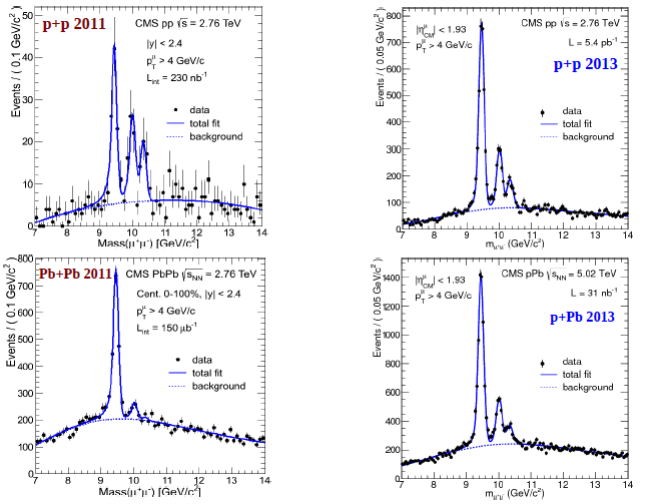

Figure 11: Dimuon invariant mass spectrum from the CMS collaboration. Results indicate high suppression in Pb-Pb collisions and medium suppression in p-Pb collisions. Source: [11].

reaching nearly 0 value, while for $\Upsilon(1S)$ $R_{PbPb} \sim 0.4$ in good agreement with theoretical predictions and available STAR results. The CMS results of R_{PbPb} measurements indicate little to no dependence on p_T for both $\Upsilon(1S)$ and $\Upsilon(2S)$ states again with good agreement with theoretical predictions (Fig. 14).

5. Experimental Setup & Results

The Solenoidal Tracker At RHIC (STAR) experiment is one of the world's most complex devices for particle physics related measurements. The largest part is a 0.5 T solenoidal magnet. Some main detectors include the Time Projection Chamber, the Barrel Electromagnetic Calorimeter, the Time-Of-Flight detector and the Heavy Flavor Tracker. Only the TPC was used for this analysis while the use of the BEMC was planned for future work. An illustration of the STAR detector can be seen in Fig. 15.

The analysis of ϒ meson production in $\sqrt{s_{NN}} = 200$

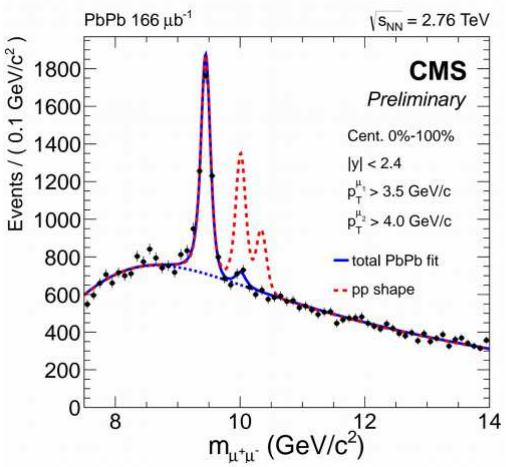

Figure 12: Dimuon invariant mass spectrum measured in Pb-Pb collisions by the CMS collaboration, scaled by the p-p shape. High suppression of excited states is apparent. Source: [12].

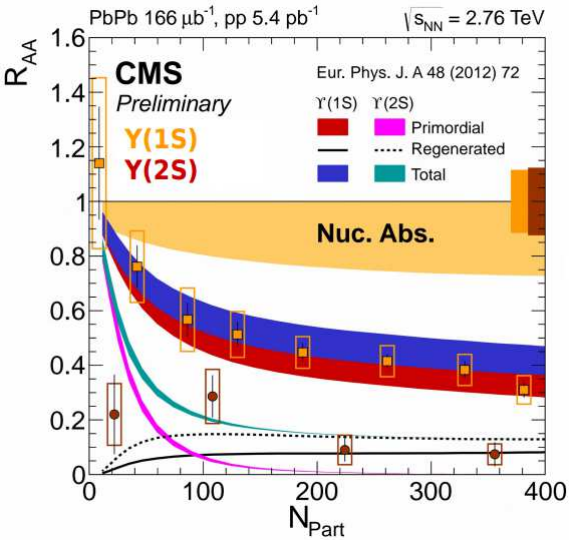

Figure 13: The CMS results for R_{PbPb} vs $< N_{part} >$. Suppression increases with rising number of participants and the effect is more significant for $\Upsilon(2S)$. Source: [12].

GeV Au-Au collisions from Run11 at RHIC as measured by detector STAR had a main goal of reconstructing the invariant mass spectrum from a dielectron channel. Data used were minimum bias and used data filed were the PicoDST. Following analysis cuts were applied to select tracks corresponding with di-electrons. The number of minimum hits in the TPC was set to $N_{fit} \geq 20$ to assure sufficient precision of the track reconstruction. Additionally a cut was set for the ration of fitted versus all possible hits to $\frac{N_{fit}}{N_{max}} \geq 0.51$ to prevent a single track from being attributed to two particles. The Distance of Closest Approach (from the primary vertex) was set to $DCA < 1.5$ cm. Because of the future plan included the BEMC which covers the pseudorapidity range of

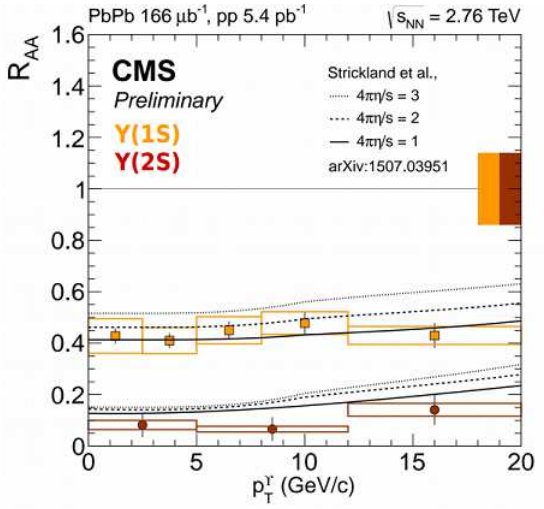

Figure 14: CMS results of R_{PbPb} vs p_T measurements, showing no significant dependence and good agreement with theoretical predictions. Source: [12].

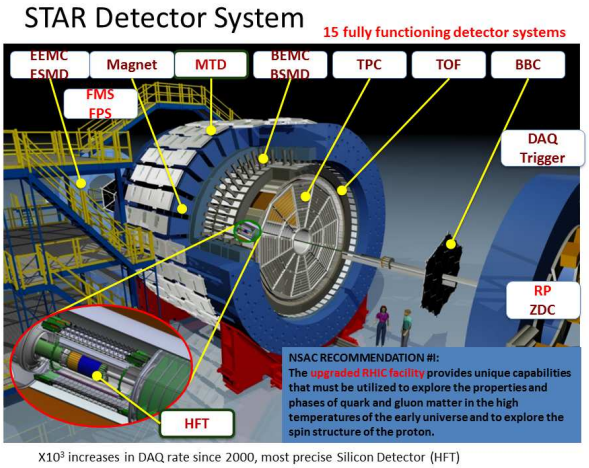

Figure 15: The STAR experiment with its main components - including the TPC used for the presented analysis - highlighted. Source: [13].

$\eta < 1$ this cut was applied as well. To distinguish (di)electrons from other particles such as pions and protons a cut for N_{sigma} was applied. N_{sigma} is derived from the dE/dx behavior of different particles in the TPC and is defined as follows: If a desired particle is an electron, it should have a N_{sigma} value of 0, if we assume Gaussian distribution, N_{sigma} should have values between -3 and 3. Particles outside of this range have only 0.03 percent chance that it is an electron. However, for the particles with $N_{sigma} < 0$ there is also increasing probability of being a proton or a pion. Therefore, to assure that a maximum number of electrons is kept and the contamination by pions and protons is minimized, following cut was applied: $-1 \leq N_{sigma} \leq 3$. The last cut applied was the p_T restriction. Since the Υ mesons are so heavy compared to dileptons, it can be expected that the

decay products will have large values of transverse momentum. Therefore a $p_T \geq 4$ GeV/c cut was applied. The applied cuts are summarized in Tab. 1. From approximately 10^9 analyzed events only 58847 tracks passed the cuts. Unfortunately no invariant mass spectrum was reconstructed.

Analysis Cut	Value(s)
N_{fit}	$\geq$20
$\frac{N_{fit}}{N_{max}}$	≥ 0.51
DCA	< 1.5 cm
$Nsigma$	$\in$ <-1,3>
$\lvert\eta\rvert$	$\leq$1
p_T	≥ 4 GeV/c

Table 1: Table summarizing cuts applied in this analysis.

6. Summary

In conclusion, a brief overview of the Υ meson physics has been presented. Firstly, the introduction to QGP and its relevance in today's research has been shown. The bottomonium family and especially the $\Upsilon(nS)$ meson has been shown, highlighting its main properties and structure. The theoretical background for the Υ use as a probe in the QGP has been presented, including the Debye screening process, created by the presence of free color charges and responsible for the suppression of the quarkonia production. The idea of a quarkonium thermometer and its significance in the quest for obtaining a QCD phase diagram has been summarized. Furthermore, recent RHIC and LHC results were shown, all supporting the quarkonium suppression theory, indicating high suppression in central A-A collisions. There is a nearly 100% suppression of $\Upsilon(2S)$ and $\Upsilon(3S)$ states observed, but the only source of $\Upsilon(1S)$ suppression is the suppression of feed down from resonances. This indicates that the temperature of the QGP presently created at RHIC and LHC is in the range of $1.2T_c < T < 2T_c$. The STAR detector was mentioned, highlighting its key components including the TPC used for the analysis. The analysis of Υ mesons from 2011 STAR data from $\sqrt{s_{NN}} = 200$ GeV Au-Au collisions was not successfully completed - no reconstructed Υ signal from the dielectron channel - despite using correct cuts based on technical and physical properties of the analysis. However, this analysis served primarily as a training for future work which should include the analysis of Υ mesons from 2015 STAR p-Au data.

References

[1] K. Walsh, "Accelerating Particles Accelerates Science âĂŤ With Big Benefits for Society", 3/13/2013, [online cit. 4/16/16], `https://www.bnl.gov/rhic/news2/news.asp?a=3758&t=today`

[2] A. Mocsy, "Potential Models for Quarkonia", 11/3/2008, arXiv:0811.0337 [hep-ph]

[3] "Probing QCD Phase Diagram using Conserved Charge Fluctuations", Lattice Gauge Theory Group, Nuclear Theory, Brookhaven National Laboratory, [online, cit. 6/1/16], `http://quark.phy.bnl.gov/~swagato/USQCD/`

[4] "First Measurement of η_b (ground state of b/anti-b quark pair)" BaBar collaboration, University of Maryland, 2008, [online, cit. 3/15/16], `http://www.physics.umd.edu/news/News_Releases/BaBar2008.htm`

[5] A. Andronic *et al.*, "Heavy-flavour and Quarkonium Production in the LHC Era: From Proton-proton to Heavy-ion Collisions", 6/12/2015, arXiv:1506.03981v1 [nucl-ex]

[6] T. Matsui, H. Satz, "J/ψ Suppression by Quark-gluon Plasma Formation", Phys. Let. B, vol. 178, no. 4, 10/9/1986

[7] A.R. Kesich, "Upsilon Production and Suppression as Measured by STAR in p + p, d + Au, and Au + Au Collisions at $\sqrt{s_{NN}} = 200$ GeV", Dissertation Thesis, UC Davis, 2014

[8] L. Adamczyk *et al.*, "Υ production in U+U collisions at $\sqrt{s_{NN}} = 193$ GeV with the STAR experiment", STAR collaboration, 3/23/2016

[9] B. Abelev *et al.*, "Suppression of $\Upsilon(1S)$ at forward rapidity in PbâĂŞPb collisions at $\sqrt{s_{NN}} = 2.76$ TeV", 10/30/2014, arXiv:1405.4493v3 [nucl-ex]

[10] "Measurement of $\Upsilon(nS)$ production with p+Pb collisions at $\sqrt{s_{NN}} = 5.02$ TeV and pp collisions at $\sqrt{s_{NN}} = 2.76$ TeV", ATLAS collaboration, Quark Matter 2015, Kobe, 9/26/2015

[11] A. Abdulsalam, "Bottomonium production in p+p, p+Pb and Pb+Pb collisions with CMS", CMS collaboration, Quark Matter 2014, Darmstadt, 5/21/2015

[12] M. Jo, "CMS bottomonia results from Run I", CMS collaboration, Quark Matter 2015, Kobe, 9/30/2015

[13] "The STAR Experiment", [online, cit. 4/19/16], `https://drupal.star.bnl.gov/STAR`

KAON FEMTOSCOPY AT THE STAR EXPERIMENT

Jindřich Lidrych*

Faculty of Nuclear Sciences and Physical Engineering, Czech Technical University in Prague, Břehová 7, 115 19 Prague, 1 Czech Republic

* corresponding author: jlidrych@gmail.com

Abstract. Femtoscopic measurements of two-particle correlations at small relative momenta reveal the space-time characteristics of the system created during high-energy nuclear collisions at the moment of particle emission. In comparison to analyses using the most abundant pions, kaons provide a cleaner probe of the emission source as they are less frequently result from resonance weak decays. Additionally, kaons contain strange quarks so these measurements can be sensitive to different effects and earlier collision stages. Pairs of like-sign kaons exhibit correlations due to Coulomb interactions and Bose-Einstein quantum statistics. The system of unlike-sign kaons contains a narrow $\phi(1020)$ resonance in the final state, where femtoscopic measurements have been predicted to be particularly sensitive to the source size and momentum-space correlations. The measurement of space-time extents using unlike-sign kaon correlations can be a complementary study which should provide an additional information about the studied system. In this proceedings, we will discuss the latest STAR results on femtoscopic analysis of like-sign kaon correlations in Au+Au collisions from the RHIC Beam Energy Scan program. The last part of the proceedings is focused on discussion of the analysis of unlike-sign kaons femtoscopic correlations in Au+Au collisions at $\sqrt{s_{\mathrm{NN}}} = 200$ GeV and its comparison to the theoretical predictions.

Keywords: correlation femtoscopy, kaon, STAR experiment.

1. Introduction

Correlation femtoscopy, often called *HBT* as the reference to R. Hanbury Brown and R. Q. Twiss and their pioneering measurements in astronomy [1, 2], is one of the most sophisticated method which can be used for study of the spacial and temporal characteristics of the system created during the ultrarelativistic heavy-ion collisions. In particle physics this method was for the first time employed by the G. Goldhaber, S. Goldhaber, W.-Y. Lee and A. Pais [3], when they observed in proton-anti-proton annihilations an excess of pairs of identical pions produced at the small angles.

Based on their observation the theoretical background of two particle correlation was developed by G. I. Kopylov and M. I. Podgoretsky in the 1970s [4]. They also introduced a new term *correlation function* and demonstrated that this correlation function is sensitive to the spacial and temporal characteristic of the particle emitting source. Since then the femtoscopic measurements of two particles became a standard tool for the extraction of the source sizes. The first measurements were performed with the most abundant particles, with the pions. However, the physics interpretation of results from pion femtoscopy in picture of pure hydrodynamic calculations is quite complicated due to the contribution from long-lived resonance decays which cause non-Gaussian tail in pion source function.

Femtoscopy with heavier particles is significantly more challenging than the corresponding measurements for pions. These measurements are also more statistical challenging since the heavier particles are produced less frequently. Hence the femtoscopic analyses of heavy particle are very often performed just with one-dimensional correlation functions. With these limitations it has been already possible to study pairs of non-identical interacting particles [5, 6]. These measurements can provide valuable information about the particle emitting source and can serve for the additional constrains of the hydrodynamical models which are able to reproduces results from pion femtoscopy. However, for stronger constraint the full three-dimensional information about source is needed. One of possible solution for this problems can be measurement in the region of the resonance [7]. Since it has been predicted the correlation function will be sensitive in the region of the resonance to the spacial and temporal extends, in the system which contains a narrow, near threshold, resonance. In addition, two-particle spectrum rapidly falls with decreasing relative momentum, hence the measurements with the resonance can be statistically advantageous. Pairs of unlike-sign kaons are suitable for such measurements since the system of non-identical kaons contains $\phi(1020)$ resonance. This resonance is characterized by the width Γ=4.3 MeV/c^2 and the decay momentum in the rest frame k^*=126 MeV/c.

2. Two-particle correlation function

Information about the space-time structure of the studied system is encoded into the two-particle correlations, which are measured by the correlation function.

2.1. Theoretical background

In the most general case, the two-particle correlation function can be written as [8]

$$CF\left(p_1,p_2\right)=\int \mathrm{d}^3rS\left(r,k^*\right)\left|\psi_{1,2}\left(r,k^*\right)\right|^2, \quad (1)$$

where $S\left(r,k^*\right)$ is the source function describing the emission of two particles and $\psi_{1,2}\left(r,k^*\right)$ is the relative two-particle wave function characterizing interaction between the two particles. These particles with four-momenta p_1^μ and p_2^μ are emitted at the relative distance r with the relative momentum $\left(2k^*\right)^2=-\left(p_1^\mu-p_2^\mu\right)^2=q_{\mathrm{inv}}^2$.

In case of the identical non-interacting particles, when only Bose-Einstein statistics is used for the construction of the relative two-particle wave function, Eq. 1 can be rewritten as

$$CF\left(p_1,p_2\right)=1+\int \mathrm{d}^3rS\left(r,k^*\right)\exp^{ik^*r}. \quad (2)$$

2.2. Experimental background

Experimentally, the correlation function as a function of the relative momentum is constructed as a ratio of the two-particle distribution from the same events $N_{\mathrm{same}}\left(q_{\mathrm{inv}}\right)$ and uncorrelated two-particle distribution from mixed events $N_{\mathrm{mixed}}\left(q_{\mathrm{inv}}\right)$:

$$CF\left(q_{\mathrm{inv}}\right)=\frac{N_{\mathrm{same}}\left(q_{\mathrm{inv}}\right)}{N_{\mathrm{mixed}}\left(q_{\mathrm{inv}}\right)}. \quad (3)$$

For three-dimensional measurement, the $\vec{q}$ is decomposed into three components: q_{out}, q_{side} and q_{long} in Bertsch-Pratt coordinate systems [8]. This coordinate system, which is often called "out-side-long" system, is connected with emitted pair of particles and is characterized by three axes, namely longitudinal, outward and sideward axis. The longitudinal axis is parallel to the beam direction which typically coincides with z-axis (or beam direction). The direction of the outward axis is parallel to pair transverse momentum k_T and the last axis, the sideward axis, is chosen so that it is perpendicular to the longitudinal and outward axes. As can be seen from the choice of the axes, the Bertsch-Pratt coordinate system is unique for each pair of particles. Then the correlation function is constructed as

$$CF\left(q_{\mathrm{out}},q_{\mathrm{side}},q_{\mathrm{long}}\right)=\frac{N_{\mathrm{same}}\left(q_{\mathrm{out}},q_{\mathrm{side}},q_{\mathrm{long}}\right)}{N_{\mathrm{mixed}}\left(q_{\mathrm{out}},q_{\mathrm{side}},q_{\mathrm{long}}\right)}, \quad (4)$$

where $N_{\mathrm{same}}\left(q_{\mathrm{out}},q_{\mathrm{side}},q_{\mathrm{long}}\right)$ and $N_{\mathrm{mixed}}\left(q_{\mathrm{out}},q_{\mathrm{side}},q_{\mathrm{long}}\right)$ is the three-dimensional two-particle distribution from the same events and mixed events, respectively. In both cases, the uncorrelated two-particle distribution is obtained by the event mixing technique. In order to remove non-femtoscopic correlations, the event mixing technique divide events into sub-classes according to primary vertex position along the beam direction and multiplicity.

Source radii R_{inv} from 1D CF or R_{out}, R_{side} and R_{long} from 3D CF can be extracted by the standard Bowler-Sinyukov fitting method [9, 10], which is based on the separation of the Coulomb interaction from the effect of the Bose-Einstein statistics.

3. STAR Experiment

The results discussed in this proceedings are obtained by the Solenoidal Tracker at RHIC (STAR) [11]. Excellent tracking ability in combination with great identification of charged particles at mid-rapidity with full azimuthal angles coverage makes the STAR detector ideal for multi-particle high statistics measurements. The heart of the STAR detector is the Time Projection Chamber (TPC) [12] which is surrounded by the Time of Flight detector (ToF) [13]. These two detectors are crucial for kaon identification at the STAR detector. When charged particle passes through the gas in the TPC, it ionizes gas and loss energy. The energy loss depends on particle momentum p and is specific for each type of particle. The TPC reconstructs charged particle tracks and measures their momentum p. Particle identification is based on the measurements of the specific ionization loss. Due to a finite resolution of the TPC, the measured energy loss deviates from the theoretically expected value calculated by Bichsel function [14]. In case that the measured distribution of the specific energy loss has a Gaussian distribution with the mean value determined by the theoretical value of $\mathrm{d}E/\mathrm{d}x^{\mathrm{theo}}$ and with the standard deviation σ_{K}, the normalized energy loss for kaon can be defined as

$$n\sigma_{\mathrm{K}}=\ln\left(\frac{\mathrm{d}E/\mathrm{d}x^{\mathrm{meas}}}{\mathrm{d}E/\mathrm{d}x^{\mathrm{theo}}}\right)/\sigma_{\mathrm{d}E/\mathrm{d}x}, \quad (5)$$

where $\mathrm{d}E/\mathrm{d}x^{\mathrm{meas}}$ is the measured value of the energy loss. The normalized energy loss is scaled by the resolution $\sigma_{\mathrm{d}E/\mathrm{d}x}$.

In presented analyses, the tracks were required to have $n\sigma_{\mathrm{K}}$ in the range between -3 and 3. The identification via the ionization energy loss in the TPC can eliminate kaons from charged hadron contamination up to momentum $p\sim$0.55 GeV/c. For higher momentum, the Time of Flight detector has to be used. This detector was fully installed in 2010 [13] and has similar acceptance as the TPC. Thanks to information from the Vertex Position Detector [15], the ToF is able to measure the relative particle velocity β, which is consequently used for the calculation of particle mass m via

$$m=p\sqrt{\frac{1}{\beta^2}-1}, \quad (6)$$

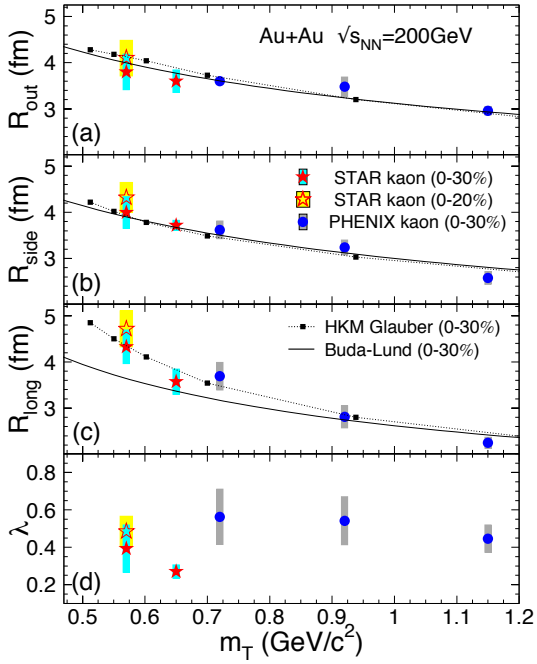

Figure 1: Extracted femtoscopic radii from three-dimensional K^+K^+ & K^-K^- correlation functions from Au+Au collisions at $\sqrt{s_{\rm NN}} = 200$ GeV and comparison to the model calculations. Taken from [16].

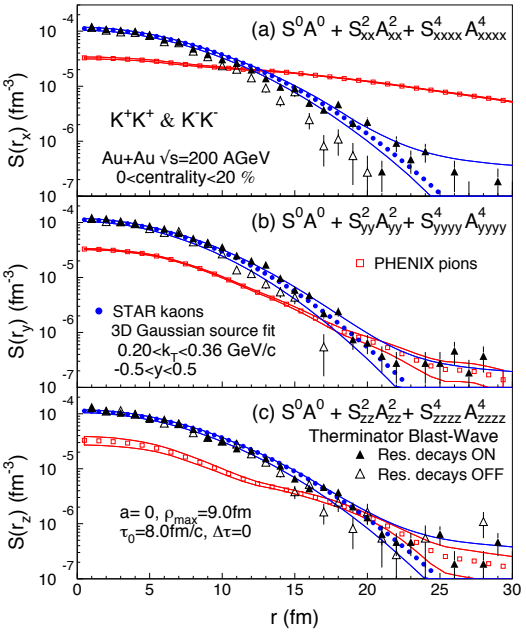

Figure 2: Extracted kaon source function from three-dimensional K^+K^+ & K^-K^- correlation functions from Au+Au collisions at $\sqrt{s_{\rm NN}} = 200$ GeV. The kaon source functions are compared with the pion source function and the Therminator predictions. Taken from [16].

where p is the particle momentum measured by the TPC. The ToF is able to identify the kaons up to momentum $p \sim 1.55$ GeV/c.

4. Recent results from kaon femtoscopy at the STAR

4.1. First measurements at the STAR

The first kaon femtoscopic analysis [16] at the STAR experiment was performed with a total of 20.6 million the most central (0-20%) Au+Au collisions at the energy $\sqrt{s_{\rm NN}} = 200$ GeV collected in year 2004 and 2007. At that time, the kaon identification was able only by the TPC. Hence due to lower yields of kaons, it was necessary without any detailed study merged positive and negative pairs of kaons. Although this analysis was statistically challenges, it provided valuable information about the freeze-out dynamic properties measured via the kaon femtoscopy.

Figure 1 shows the extracted kaon source radii for the most central Au+Au collisions at the energy $\sqrt{s_{\rm NN}}$ = 200 GeV measured by the STAR experiments. The results are presented as a function of the transverse mass $m_{\rm T}$, which is defined as

$$m_{\rm T} = \sqrt{m^2 + k_{\rm T}^2}, \qquad (7)$$

where m is kaon mass and $k_{\rm T}$ is the transverse pair momentum. Figure 1 also presents the comparison of the experimental data with the model predictions. In this analysis, the model calculations from the Buda-Lund model as well as from the hydrodynamic model (HKM) were employed. Both of model predictions for the outward and sideward directions are consistent with the experimental data within the errors. However, there is a significant difference between the HKM and Buda-Lund model predictions for the longitudinal direction. Although Buda-Lund model is able to reproduces the pion source radii in all three directions, kaon source radii favor more HKM predictions. As discussed in [16], this analysis does not support the exact $m_{\rm T}$-scaling for pion and kaon source radii.

Moreover, the novel technique of Cartesian surface-spherical harmonic decomposition of Danielewicz and Pratt [17] was employed in this study for extraction of the kaon source function. The kaon source function $S(r)$ is related to the correlation function via Eq. 1 and can be directly obtained by the fitting of experimentally measured correlation function with the expanded source function into Cartesian harmonics basis elements [16].

Figure 2 presents the STAR results on the extracted source function profiles in the x, y and z directions, i.e. $S(r_{\rm x}) \equiv S(r_{\rm x}, 0, 0)$, $S(r_{\rm y}) \equiv S(0, r_{\rm y}, 0)$ and $S(r_{\rm z}) \equiv S(0, 0, r_{\rm z})$. The x, y and z directions correspond to

the outward, sideward and longitudinal directions. The kaon source function is compared to those for pions together with Therminator model predictions with resonance contributions. The experimental data shows that the kaon source function is more Gaussian that the pion source function and the long tails caused by the resonance decays are not presented.

4.2. Prospect for new high-statistic measurement

Both of two parts of the previous analysis provided important information about the freeze-out dynamics. However statistical limitations leaded to the fairly broad ranges of the centrality bins and the transverse pair momenta bins. As was recently presented by the STAR Collaboration [18], the high-statistic datasets collected during the RHIC Beam Energy Scan I (BES) allow more precise study with the finer binning in the centrality and the transverse pair momenta. The RHIC BES I is one of the main physics program at the STAR which aims at the detailed and systematic study of phase diagram of nuclear matter. The first phase of the RHIC BES I provided sufficiently good dataset from the 8 different collisions energies. In recently presented analysis, the Au+Au collisions at the energy $\sqrt{s_{\mathrm{NN}}} = 7.7, 11.5, 14.5, 19.6, 27, 39, 62.4$ and 200 GeV were used for the kaon femtoscopy. Especially, the high-statistics dataset of 200 GeV collisions with more than 500 million minimum-bias events collected by the STAR Experiment in year 2011 enables the most precise measurements so far. In addition, the STAR detector upgrades for RHIC BES, which includes the full installation of the ToF detector, enables the extension of the kaon identification up to higher momenta $p \sim 1.55$ GeV/c. The high-statistics dataset of Au+Au collisions promises the most precise measurements of two-particle correlation measurements, which can include the extraction of freeze-out parameters by the fitting of Blast-wave model.

5. Conclusions

In this proceedings, the recent results from the kaon femtoscopy at the STAR were presented. The first kaon femtoscopic analysis provided information about the source radii, which were compared to the model calculations. Results from this analysis do not support the exact m_{T}-scaling for pion and kaon source radii. Moreover, the extracted kaon source functions by the Cartesian surface-spherical harmonic decomposition follow the Gaussian distribution and the long non-Gaussian tails caused by the resonance decays are not observed. The second part of the proceedings present the latest results from the kaon femtoscopy with the data from RHIC BES. The high-statistic dataset of 200 GeV Au+Au collisions will allow the detailed study including the fitting by the Blast-wave parametrization. The first preliminary results will be published soon by the STAR Collaboration.

References

[1] R. Hanbury Brown, et al. A New type of interferometer for use in radio astronomy. *Phil Mag Ser7* **45**:663–682, 1954.

[2] R. Hanbury Brown, et al. A Test of a new type of stellar interferometer on Sirius. *Nature* **178**:1046–1048, 1956.

[3] G. Goldhaber, et al. Influence of Bose-Einstein statistics on the anti-proton proton annihilation process. *Phys Rev* **120**:300–312, 1960.

[4] G. I. Kopylov, et al. Correlations of identical particles emitted by highly excited nuclei. *Sov J Nucl Phys* **15**:219–223, 1972. [Yad. Fiz.15,392(1972)].

[5] L. Adamczyk, et al. $\Lambda\Lambda$ Correlation Function in Au+Au collisions at $\sqrt{s_{NN}} = 200$ GeV. *Phys Rev Lett* **114**(2):022301, 2015. 1408.4360.

[6] L. Adamczyk, et al. Measurement of Interaction between Antiprotons. *Nature* **527**:345–348, 2015. 1507.07158.

[7] R. Lednicky, et al. Femtoscopic correlations and narrow resonance formation. *Prog Theor Phys Suppl* **193**:335–339, 2012.

[8] M. A. Lisa, et al. Femtoscopically Probing the Freeze-out Configuration in Heavy Ion Collisions 2008. 0811.1352.

[9] M. G. Bowler. Coulomb corrections to Bose-Einstein correlations have been greatly exaggerated. *Phys Lett* **B270**:69–74, 1991.

[10] Yu. Sinyukov, et al. Coulomb corrections for interferometry analysis of expanding hadron systems. *Phys Lett* **B432**:248–257, 1998.

[11] K. H. Ackermann, et al. STAR detector overview. *Nucl Instrum Meth* **A499**:624–632, 2003.

[12] K. H. Ackermann, et al. The STAR time projection chamber. *Nucl Phys* **A661**:681–685, 1999.

[13] W. J. Llope. Multigap RPCs in the STAR experiment at RHIC. *Nucl Instrum Meth* **A661**:S110–S113, 2012.

[14] H. Bichsel. A method to improve tracking and particle identification in TPCs and silicon detectors. *Nuclear Instruments and Methods in Physics Research Section A: Accelerators, Spectrometers, Detectors and Associated Equipment* **562**(1):154 – 197, 2006.

[15] W. J. Llope, et al. The STAR Vertex Position Detector. *Nucl Instrum Meth* **A759**:23–28, 2014. 1403.6855.

[16] L. Adamczyk, et al. Freeze-out dynamics via charged kaon femtoscopy in $\sqrt{s_{NN}} = 200$ GeV central Au+Au collisions. *Phys Rev* **C88**(3):034906, 2013. 1302.3168.

[17] P. Danielewicz, et al. Analysis of low-momentum correlations with cartesian harmonics. *Phys Lett* **B618**:60–67, 2005. nucl-th/0501003.

[18] STAR Collaboration (J. Lidrych for the collaboration). Kaon femtoscopy in Au+Au collisions at the energy from 7.7 to 200 GeV with the STAR experiment (poster). XXVI International Conference On Ultrarelativistic Heavy-Ion Collisions (Quark Matter 2017), 2017.

INTRODUCTION TO QUANTUM CHROMODYNAMICS AND JET ALGORITHMS

Lukáš Marek*

CTU in Prague, FNSPE, Brehova 7, Prague, Czech republic

* corresponding author: mareklu8@fjfi.cvut.cz

Abstract. One part of the Standard Model of Particle physics is the $SU(3)$ component which represents the quantum chromodynamics (QCD) as the gauge quantum field theory describing the strong interaction between quarks and gluons. First section will concentrate on basic features of QCD: Lagrangian of QCD, running coupling and asymptotic freedom.

Second section will be dedicated to jets and jet algorithms. The theoretical and experimental aspects of the jet algorithms will be discussed.

Keywords: QCD, jets, jets algorithm.

1. Introduction

Symmetry is one of the fundamental principles which is used in the development of modern physics. It could be defined as the invariance of an object under some transformation, where the object can be something in our vicinity with for example spatial symmetry or a mathematical equation and as the transformation is an abstract operation. One of these operations, which plays a fundamental role in the Standard Model, is the local gauge transformation. The invariance of the Lagrangian of some system results in the interaction between particles of the system. In other words, symmetry defines dynamics [1].

2. QCD Lagrangian and local gauge transformation

QCD describes the strong interaction between color charged objects. For this case it is fermion field $\psi(x)$ (quark) with spin $\frac{1}{2}$ and with mass m. Due to the color charge, it has to be symbolized as matrix in the color space (one $\psi_i(x)$ for one color). The Lagrangian of this field can be expressed in dependence on space-time coordinates x as:

$$\mathscr{L}_{free}^{fermion} = \overline{\psi}(x)(i\gamma^\mu\partial_\mu - m)\psi(x), \qquad \psi(x) = \begin{pmatrix}\psi_1(x)\\ \psi_2(x)\\ \psi_3(x)\end{pmatrix}, \tag{1}$$

For QCD, the local gauge transformation is defined as follows:

$$\psi'(x) \equiv \exp(i\alpha_a(x)T_a)\psi(x) = U\psi(x),\ a = 1, ...8, \tag{2}$$

This local gauge transformation forms a $SU(3)$ color group which is nonabelian and generated by T_a. The generators T_a together form a Lie algebra that is standardly represented by Gell-Mann matrices. This representation can be found for example in ref. [2].

Application of the local gauge transformation on field $\psi(x)$ will cause noninvariance of the Lagrangian which can be cancelled by an introduction of a gauge field A_μ and a new derivative, so called covariant derivative:

$$D_\mu \equiv \partial_\mu - igA_\mu,\ A_\mu = A_\mu^a t_a. \tag{3}$$

The gauge field A_μ transforms in the following way:

$$A_\mu^a{}' = A_\mu^a + f_{bca}\alpha_b A_\mu^c + \frac{1}{g}\partial_\mu\alpha_a, \tag{4}$$

where f_{abc} are structure constants of the $SU(3)$ color group. These fields are presented as 8 gauge field bosons, gluons. For the gauge field the invariant tensor can be constructed:

$$F_a^{\mu\nu}(x) = \frac{\partial A_a^\nu(x)}{\partial x_\mu} - \frac{\partial A_a^\mu(x)}{\partial x_\nu} - g f_{abc} A_a^\nu(x) A_a^\mu(x). \tag{5}$$

Connection and usage of all this information leads to the final form of the QCD Lagrangian:

$$\mathscr{L}^{QCD} = \overline{\psi}(x)(i\gamma^\mu\partial_\mu + m_q)\psi(x) + g\overline{\psi}(x)\gamma^\mu\psi(x)T^a A_\mu^a(x) - \frac{1}{4}F^{\mu\nu a}(x)F_{\mu\nu}^a(x), \tag{6}$$

where g is the coupling constant which represents the strength of the interaction and its properties will be discussed later. First part of the $\mathscr{L}^{QCD}$ represents the original Lagrangian of the fermion field $\psi(x)$, second part is the interaction Lagrangian and shows the interaction between the gluon field and the fermion field and last part stands for the Lagrangian of gauge field. The self interaction of three or four gluons can be extracted from the Lagrangian of gauge field which is caused by the nonabelian nature of the $SU(3)$ color group. This is one of the differences of abelian quantum electrodynamics (QED) and nonabelien QCD, where photons, gauge field bosons of QED, can not interact directly together in contrary to gluons [2].

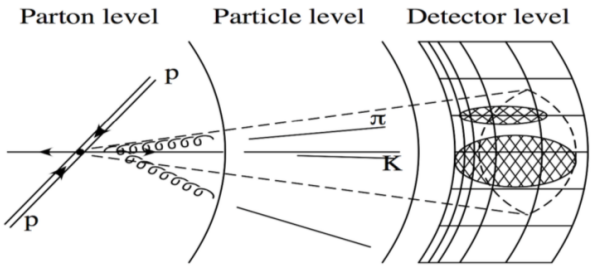

Figure 1: Development of hard collision. Figure taken from [4]

2.1. Running coupling and asymptotic freedom

One of the essential parameters of QCD is the running coupling $g = \frac{\alpha_s^2}{4\pi}$. Generally, QCD is a renormalization theory and as consequence the coupling is a function of renormalised scale μ_R. If the μ_R is taken close to scale of the transfer momentum Q, the running coupling can be described as the effective strength of the interaction. The equation for the running coupling is expressed in following form (as function of Q):

$$Q^2 \frac{d\alpha}{dQ^2} = \beta(Q) = -\left(b_0\alpha^2 + b_1\alpha^2 + ...\right) , \quad (7)$$

where b_0 is the 1-loop coefficient etc. The perturbative approach can be gained from equation (7) and is given by:

$$\alpha_s(Q^2) = \frac{\alpha_s(Q_0^2)}{1 + \frac{7}{4\pi}\alpha_s(Q_0^2) ln(\frac{Q^2}{Q_0^2})} = \frac{1}{b_0 ln(\frac{Q^2}{\Lambda^2})}, \quad (8)$$

where this expression diverges for value: $\Lambda \simeq 0.2\,\mathrm{GeV}$. For large values of the transfer energies, the running coupling $\alpha_s(Q^2)$ decreases and causes the so-called asymptotic freedom. This physical effect can be described as the dependence on the distance between two interacting particles. When the distance is increased the running coupling is rising and the forces between particles are increasing and this is the reason why neither quarks nor gluons are observed as free particles but only as hadrons (compound particles from quarks and gluons). On the contrary with the reduction of distance there is deceasing of the coupling and force that results to free behaviour of the particles [3].

3. Jets and jets algorithm

Experimental ground for QCD focuses on the jets during the hard collisions of hadrons. Generally, the development of the hard collision can be divided in three levels: parton, particle and detector level (Fig. 1.). In the collision, several partons with different momenta can be created. These gluons and quarks can not exist as free particles and must undergo the process of hadronization (creation of hadrons). Energies of these hadrons are reconstructed generally in the calorimeter detectors.

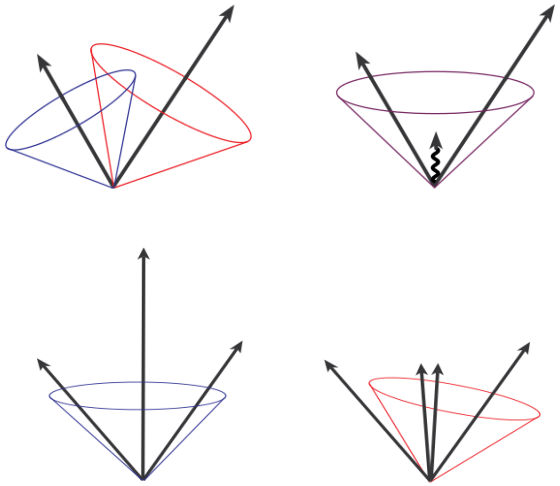

Figure 2: Collinear (bottom) and infrared (top) sensitivity of an algorithm. Figures taken from [5]

Jet can be defined as a group of i-particles with four momenta p_μ^i in some specific (spatial, energetic etc.) relation. The function of the jet algorithm is to select particles according to scheme of algorithm and to combine their momenta. The selecting process of the particles is called the selection scheme and the combining process of momenta is called the recombination scheme.

3.1. Conditions for ideal algorithm [6]

(1.) *Completely defined*: All aspects of the algorithm should be fully specified (kinematics variables of jets, selection process etc).

(2.) *Experiment independence*: There should be no dependence on the experiment.

(3.) *Theoretically correct behaviour*: The collinear and infrared safety are the most desirable. Two problems of this aspects can be seen in Fig. 2. The cross section for the radiation of a soft a gluon is given by:

$$d\sigma_{q\to qg} = \frac{\alpha_s C_f}{\pi} \frac{dE}{E} \frac{d\theta}{sin\theta} \frac{d\phi}{2}, \quad (9)$$

where this cross section diverges for the angle between quark and gluon θ going to 0 or for the energy of gluon going to 0 (a soft gluon). The radiation of soft gluon is highly probable for small angles and this correspond with infrared unsafety as can be seen in top left Fig. 2. This jet algorithm (infrared unsafety) creates two jets in left half of picture as soon as one of them radiates a soft gluon, algorithm changes the organization of jets and finds only one. The collinear unsafe is presented in top left part of the Fig. 2. The algorithm proceeds according to the scheme which chooses that the most energetic particle (seed-based algorithm) and creates the jet

in its surroundings. In the case that most energetic particle is split in two particles with the same total energy, the algorithm chooses a different seed and creates a new jet in its surroundings despite the fact that these two particles have the same energy as the original one. Certain types of jet algorithms are very sensitive to this problem.
Neither the radiation of soft gloun nor the splitting of seed should affect the jet finding.

(4.) *Order independence*: Jet algorithm has to be able to find same jets for each level of development of a hard process (particle, hadron and detector).

(5.) *Time and reconstructive effectiveness*: Jet algorithm should be able to find all experimentally important jets and most effectively in terms of time.

4. Conclusions

QCD is a gauge quantum field theory describing the strong interaction between quarks and gluons. Its Lagrangian shown in the equation (6) is invariant under the local gauge transformation (2).
Jet can be defined as a group of particles in some specific (spatial, energetic etc.) relation. Jet algorithm should be: completely defined, experimentally independent, theoretically well behavioured, order independent and time-reconstructively effective.

References

[1] Cejnar, P. 2007. Symetrie v mikrosvětě *http://www-ucjf.troja.mff.cuni.cz/cejnar/publikace/symetrie.pdf*

[2] F. Novaes, S. 2000. Standard Model: An introduction *https://arxiv.org/abs/hep-ph/0512210*

[3] Chýla, J. 2000. Quarks, partons and quantum chromodynamics *http://www-hep2.fzu.cz/ chyla/lectures/text.pdf*

[4] Hubáček, Z. 2010. Dissertation thesis: Measurement of the Three-jet Mass cross section in $p\overline{p}$ Collisions at $\sqrt{s} = 1.96$ TeV

[5] Zaplatílek, O. 2015. Bachalor thesis: Jet physics at LHC *https://arxiv.org/abs/hep-ex/0005012*

[6] C. Blazey, G. R. Dittmann, J. and col. 2000. Run II Jet Physics: Proceedings of the Run II QCD and Weak Boson Physics Workshop *https://arxiv.org/abs/hep-ex/0005012*

FORWARD DIJET PRODUCTION AS A PROBE OF SATURATION EFFECTS IN DILUTE-DENSE HADRONIC COLLISIONS

Marek Matas*

Faculty of Nuclear Sciences and Physical Engineering, Czech Technical University in Prague, Czech Republic

* corresponding author: matas.marek1@gmail.com

Abstract. One of the ways to study parton saturation effects in hadrons is to study dijet production in p-Pb and p-p collisions. Even though, the two jets have transverse momenta much higher than the saturation scale, the total transverse momentum of the jet pair can be of the order of the saturation scale. Since saturation effects play dominant role in lead rather then in protons, measuring the difference between the dijet production rate in protons and lead can help us determine the validity of the saturation approach to the dipole model.

Keywords: Saturation, Di-jet production, Nuclear modification factor.

1. Introduction

In this work, we shall focus on describing some of the properties of saturation that can be used to detect its signature in experimental data. Then we will describe the processes that have proved to be useful for such experiments and finally we will sketch an outline of the computation that was carried out to quantify the contribution of these effects to the nuclear modification factor. The Balitsky-Kovchegov evolution equation (BK) can be used for obtaining one of the necessary ingredients that go in the computation, the scattering amplitude. This amplitude then describes the gluon distribution in dense hadronic systems that we will consider. In this work, we focus on this equation, because its nonlinear behavior includes saturation effects that we want to quantify and determine the possibility of its measurement.

2. Brief description of saturation

Saturation is a process that influences the gluon distribution inside hadrons in the small-x region. Since gluons, unlike photons, are carriers of charge, a process where one gluon radiates another gluon is allowed. When a gluon undergoes such process, it splits in two gluons, each possessing less energy then the original gluon. Each of these two gluons can undergo the same process thus splitting in a total of four gluons with even smaller momentum. If we therefore look at the gluon distribution functions towards smaller values of Bjorken-x (fraction of the hadron's momentum carried by the considered parton), we see a steep rise. This process is expected to be suppressed by an opposite process, gluon recombination. In this process, two gluons merge into a single one with momentum that is a sum of the two incoming momenta. This process is expected to be more frequent as more gluons emerge in the hadron. Therefore, these two processes are expected to dynamically balance each other out at a certain region of gluon momentum. This dynamical balance is called saturation and this work focuses on describing some of the possible ways of its detection in experimental data.

3. Studied processes

In our approach, to measure the signature of saturation in data, we shall focus on back-to-back events in the forward region in rapidity.

Since we want to go to the region of small Bjorken-x and the energy of the accelerator is fixed, according to

$$x = \frac{Q^2}{2Pq} \tag{1}$$

(where P is the four-momentum of the incoming nucleus, Q^2 is the virtuality of the exchanged photon and q is the four-momentum of this photon) the way to get to this region is to chose events where Q^2 is small. Small Q^2 means small transverse momentum of the studied process, which can prove to be a problem in the detectors with strong magnetic field, since particles with small transverse momentum (k_t) would never reach the devices detecting volume. Therefore we shall focus on dijet processes

$$p(p_p) + A(p_A) \to j_1(p_1) + j_2(p_2) + X \tag{2}$$

where both momenta p_{t1} and p_{t2} are large enough to reach the detector but the total transverse momentum of the jet is on the order of the saturation scale $p_{t1} + p_{t2} \sim Q_s$ (the saturation scale Q_s determines the region of momentum where the gluon parton distribution function starts to be saturated).

It is convenient to study the processes where Bjorken-x of the projectile particle is large and Bjorken-x of the target particle $x_{target} << 1$ (in our case the target particles will be both protons and lead nuclei). We need the $x_{target} << 1$ to see the effects of saturation and large $x_{projectile}$ to be able to describe the projectile particle with the use of the structure

functions of the proton that have been measured previously.

These two conditions can both be reached simultaneously by selecting only the events which fall in the forward rapidity region, since

$$x_{projectile} = \frac{1}{\sqrt{s}}(|p_{t1}|e^{y_1} + |p_{t2}|e^{y_2}) \tag{3}$$

and

$$x_{target} = \frac{1}{\sqrt{s}}(|p_{t1}|e^{-y_1} + |p_{t2}|e^{-y_2}). \tag{4}$$

Because we look in the region where $x_{target} << 1$, on the target side the interacting particles will be mostly gluons. Therefore we shall focus on the following processes.

$$qg \to qg, \qquad gg \to q\bar{q}, \qquad gg \to gg \tag{5}$$

4. Computation of the dijet cross section

The cross section for this process in the TMD factorisation approach reads [1]

$$\frac{d\sigma^{pA\to dijet+X}}{d^2p_t d^2k_t dy_1 dy_2} = \frac{\alpha_s^2}{(x_{pr}x_{tar}s)^2}\sum_{a,c,d}\frac{x_{pr}f_{a/p}(x_{pr})}{1+\delta_{cd}}\cdot$$
$$\cdot\sum_{i=1}^{2}K^{(i)}_{ag\to cd}(p_t,k_t)\Phi^{(i)}_{ag\to cd}(x_2,k_t), \tag{6}$$

where $s = (p_{projectile} + p_{target})^2$ is the total energy of the process, $x_p f_{a/p}(x_p)$ are the parton distribution functions that represent the projectile particle, $K^{(i)}_{ag\to cd}(p_t,k_t)$ are the matrix elements for the considered processes (these have been computed in [2]) and $\Phi^{(i)}_{ag\to cd}(x_2,k_t)$ are the transverse momentum distributions (TMDs) that represent the target particle [3].

Since the parton distribution functions of the projectile particle are obtained from experimental data and the corresponding matrix elements are calculated from QCD, the key missing ingredient for the computation of the cross section are the TMDs.

TMDs can be computed from various parametrisations such as the KS gluon distributions [1] that produce results that are shown in the following sections.

Another way of computing the TMDs is the Fourier transform of the scattering amplitude $N(r,x)$. This can then be obtained in various ways. One of the possible methods are parametrizing the scattering amplitude and fitting its parameters from data (GBW model [4]) or computing it directly as a solution of the Balitsky-Kovchegov evolution equation [5, 6].

5. Solving the BK evolution equation

The Balitsky Kovchegov evolution equation is an integro-differential equation, that does not have an analytic solution and therefore needs to be solved numerically. It describes the evolution of scattering amplitude in rapidity and can be written as

$$\frac{\partial N(r,Y)}{\partial Y} = \int d\vec{r_1}K^{run}(r,r_1,r_2)(N(r_1,Y)+$$
$$+N(r_2,Y)-N(r,Y)-N(r_1,Y)N(r_2,Y)), \tag{7}$$

where $K^{run}(r,r_1,r_2)$ can be expressed as in Eq. 8 and $Y = ln\frac{x}{x_0}$. [7]

$$K^{run}(r,r_1,r_2) = \frac{N_c\alpha_s(r^2)}{2\pi^2}\cdot$$
$$\left(\frac{r^2}{r_1^2r_2^2}+\frac{1}{r_1^2}\left(\frac{\alpha_s(r_1^2)}{\alpha_s(r_2^2)}-1\right)+\frac{1}{r_2^2}\left(\frac{\alpha_s(r_2^2)}{\alpha_s(r_1^2)}-1\right)\right), \tag{8}$$

Here for the dipole size vectors holds that $\vec{r_2} = \vec{r} - \vec{r_1}$. For the running coupling we have used the expression

$$\alpha_s(r^2) = \frac{4\pi}{\beta_{0,n_f}ln\left(\frac{4C^2}{r^2\Lambda^2_{n_f}}\right)}, \tag{9}$$

where

$$\beta_{0,n_f} = 11 - \frac{2}{3}n_f. \tag{10}$$

N_c corresponds to the number of considered colors and n_f to the number of flavors. C^2 is the uncertainty coming from the Fourier transformation that was used to derive this result and is usually fit to data.

This equation can be solved using discrete-value methods such as the Simpson method for integration and Runge-Kutta method for solving the actual differential equation such as in [8].

Solving this equation can be CPU demanding and to optimize the numerical methods used for this computation, one can customize the RK method [9] and precompute the values of K^{run} and r_2 into a three-dimensional grid.

With this equation and setup one can obtain the scattering amplitude and its rapidity dependence as shown in Fig. 1. The MV initial condition as in [8] was used to carry out this computation.

6. Fourier transform of the scattering amplitude

For the computation of the transverse momentum distributions, we first need to shift from the position space to the momentum space of the scattering amplitude by calculating the Fourier transform of it. The two gluon distributions that we need for obtaining the TMDs read

$$x_{tar}G^{(2)}(k_t,Y) = \frac{N_c k_t^2 S}{8\pi^4\alpha_s}\int d^2re^{-ik_t r}[1-N(r,Y)] \tag{11}$$

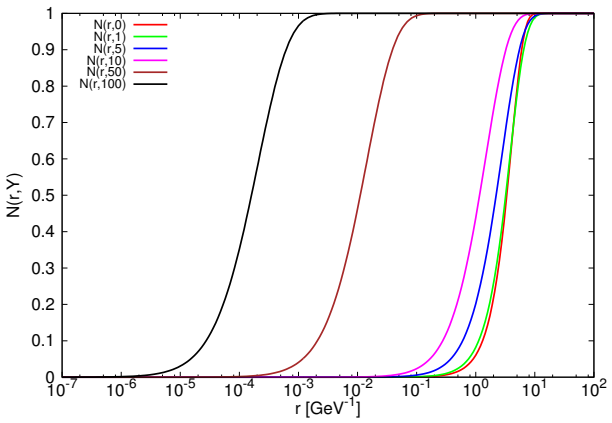

Figure 1: Solution of the BK equation for various values of rapidity.

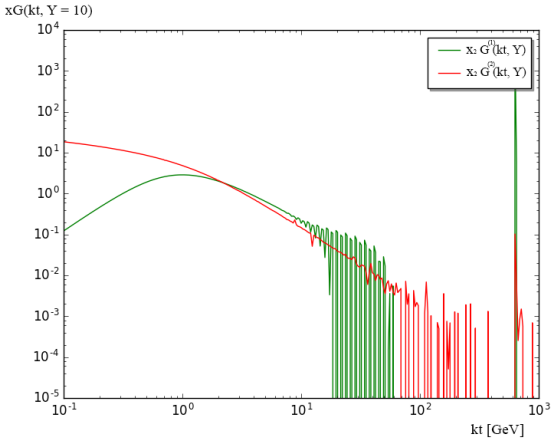

Figure 2: Transformed solution of the scattering amplitude for $Y = 10$ according to Eq. 11 and 12.

and

$$x_{tar}G^{(1)}(k_t, Y) = \frac{N_c S}{4\pi^4 \alpha_s} \int \frac{d^2r}{r^2} e^{-ik_t r} \cdot \cdot [1 - (1 - N(r, Y))^2], \quad (12)$$

where S is a constant that factorizes the dependence of the scattering amplitude on impact factor, N_c is the number of considered colors and α_s is the strong coupling constant.

Since the integrand (apart from the exponential) is a real function, one can convert the integrals into real-valued ones with the use of Bessel functions. These can then be computed using previously mentioned Simpson method. Such transformed scattering amplitudes are shown in Fig. 2. The oscillations in the region of high transverse momentum are non-physical and can be taken out by cutting the distributions and extrapolating the curve of the distribution.

These transformed scattering amplitudes can then be convoluted to obtain the transverse momentum distributions that correspond to the five processes considered in [3]. These TMDs are the missing ingredient in the computation of the cross section that would determine the presence of saturation effects in hadrons with the use of the BK evolution equation. The convolution is however very sensitive to the numerical parameter setup and is very CPU-demanding. Once the TDMs are verified and crosschecked with the expected high-k_t behavior, we can compare them to the results obtained from the KS-gluon distribution parametrisations.

7. Saturation in p-Pb nuclear modification factor

One additional feature of saturation effects needs to be used in order to verify its presence in experimental data: nuclear effects. In nuclei, due to Lorentz contraction, the saturation scale is proportional to $Q_s^2 \sim A^{1/3}$, where A is the total number of nucleons in the nucleus. Therefore, for a lead nucleus, the saturation scale will be ~ 2.4 times larger then the saturation scale of a proton. We can use this phenomenon to manifest the onset of saturation effects through the nuclear modification factor

$$R_{pPb} = \frac{\frac{d\sigma^{p+Pb}}{dO}}{A\frac{d\sigma^{p+p}}{dO}}, \quad (13)$$

where dO stands for $d^2p_t d^2k_t dy_1 dy_2$. Our goal is to produce a plot of the nuclear modification factor versus the angle between produced jets. If we choose jets with similar momenta so that $p_{t1} \sim p_{t2}$, we expect that the modification factor will be about one in the regions where the jets are not back-to-back. As we approach $\Delta\varphi \sim \pi$, we should see that due to saturation, there are fewer gluons in nuclear matter than in hadrons and therefore there should be a visible suppression in the modification factor.

In fact, this is exactly what we observe in the KS gluon distribution approach [3] to the calculation of the TMDs that go in the cross section calculation (Eq. 6).

The next important step is to verify the presence of such behavior in various different models and approaches to this problem, such as the rcBK evolution equation. Comparing the results that were obtained by the KS-gluon parametrisation would determine the validity of these results. This would determine the influence of the saturation effects on the nuclear modification factor in back-to-back dijet events in the forward region in rapidity.

8. Conclusions

A signature of saturation effects can be observed in the suppression of the nuclear modification factor for back-to-back jets in the forward region of rapidity. That is caused by the fact that the total transverse momentum of the jet pair is of the order of the saturation scale even though the transverse momenta of the individual jets are not. Since in nuclei, the saturation effects are stronger than in nucleons, one

can observe that there are fewer gluons available in the momentum region that we impose and this leads to suppression of these events in nuclei. This phenomenon can then be described by the dependence of the nuclear modification factor on the angle between the two jets if they have similar transverse momenta ($p_{t1} \sim p_{t2}$). The influence of these effects was calculated with the use of KS gluon distributions. A complementary calculation of these effects with the use of the scattering amplitude obtained directly from the numerical solution of the rcBK evolution equation is viable to confirm these observations and is being worked on (Fig. 1 and 2) for comparison as well as verification of this approach.

Acknowledgements

I would like to thank Cyrille Marquet for his support and help with understanding this topic as well as for the opportunity to work on extending his work in this field.

References

[1] K. Kutak, et al. Gluon saturation in dijet production in p-Pb collisions at Large Hadron Collider. *Phys Rev* **D86**:094043, 2012. 1205.5035.

[2] P. Kotko, et al. Improved TMD factorization for forward dijet production in dilute-dense hadronic collisions. *JHEP* **09**:106, 2015. 1503.03421.

[3] A. van Hameren, et al. Forward di-jet production in p+Pb collisions in the small-x improved TMD factorization framework. *JHEP* **12**:034, 2016. 1607.03121.

[4] K. J. Golec-Biernat, et al. Saturation effects in deep inelastic scattering at low Q**2 and its implications on diffraction. *Phys Rev* **D59**:014017, 1998. hep-ph/9807513.

[5] I. Balitsky. Operator expansion for high-energy scattering. *Nucl Phys* **B463**:99–160, 1996. hep-ph/9509348.

[6] Y. V. Kovchegov. Small x F(2) structure function of a nucleus including multiple pomeron exchanges. *Phys Rev* **D60**:034008, 1999. hep-ph/9901281.

[7] Y. V. Kovchegov, et al. Triumvirate of Running Couplings in Small-x Evolution. *Nucl Phys* **A784**:188–226, 2007. hep-ph/0609090.

[8] J. L. Albacete, et al. Solving high energy evolution equation including running coupling corrections. *Phys Rev* **D75**:125021, 2007. 0704.0612.

[9] J. Cepila, et al. Rapidity dependence of saturation in inclusive HERA data with the rcBK equation 2015. 1501.06687.

UPSILON MESON PRODUCTION AT THE STAR EXPERIMENT

Oliver Matonoha*

Czech Technical University in Prague, Brehova 7, Prague, Czech Republic

* corresponding author: oliver.matonoha@fjfi.cvut.cz

Abstract. The STAR experiment at Relativistic Heavy Ion Collider (RHIC) belongs to the world's leading experimental facilities in the physics of heavy-ion collisions (HIC). In ultrarelativistic HIC, creation of an exotic state of matter, the quark-gluon plasma (QGP), is expected. Studium of the QGP, a medium of deconfined quarks and gluons, is one of the foci of high energy physics (HEP). Charm and bottom quarkonia (e.g. J/ψ or Υ) exhibit distinctive behaviour in the QGP and thus can be utilised to probe the medium's characteristics. These phenomena and methods are summarised. Furthermore, measurement of the Upsilon meson Υ production at STAR in U+U at $\sqrt{s_{\mathrm{NN}}} = 193$ GeV is presented.

Keywords: heavy-ion collisions, quark-gluon plasma, upsilon, STAR.

1. Introduction

The theory of quantum chromodynamics (QCD) predicts that under extreme conditions, matter may undergo a phase transition and form a quark-gluon plasma. It is hypothesised that this form of matter comprised the universe in its earliest stages. In such medium, quarks and gluons are not confined in hadrons, but exist freely. Said extreme conditions are realised in ultra-relativistic heavy-ion collisions, which are thoroughly investigated at world's particle accelerator facilities.

The short-lived QGP is extremely challenging to experimentally probe. One of the most promising methods to study its properties is the measurement of heavy quarkonia. These tightly bound, massive, and colourless mesons exhibit a specific behaviour in the deconfining medium. Notably, their production suppression by colour screening in the QGP is considered a great tool in estimating the medium's temperature, although other phenomena play a role as well in affecting the production.

2. Heavy quarkonia in HIC

Heavy quarkonia are bound systems of a charm or a bottom quark and its antiquark, i.e. hidden-flavour mesons. There is a variety of these systems, that being said, the ones studied the most are the J/ψ and $\psi(2S)$ for the charmonia and the Upsilons $\Upsilon(1S)$, $\Upsilon(2S)$, and $\Upsilon(3S)$ for the bottomonia. Since the latter are approx. $3\times$ heavier than the charmonia, their behaviour is more distinct. Thus, we will focus on them in the following.

Bottom quark-antiquark pairs $b\bar{b}$ are created in the collision's earliest stages, due to the large mass of b ($\sim 4.5\,\mathrm{GeV}\,c^{-2}$). Bottomonia lifetime (e.g. $\Upsilon(1S) \sim 5\,\mathrm{pm}\,c^{-1}$) is generally a few orders higher than the one expected of QGP. Furthermore, beside the dominant hadronic decay channel, the quarkonia also decay into charged di-lepton pairs. Thus, a bottomonium system has a potential to appear before the QGP, survive its entire existence if unaffected, and decay after it into well-measurable daughters. This makes the quarkonia a great candidate for QGP effects' analysis. [1]

2.1. Quarkonia production models

Despite the fact that the production of heavy quark-antiquark pairs $q\bar{q}$ is relatively easily calculable, the process of how the pair loses its colour and forms a quarkonium meson is less understood. This can be modelled in following ways:

(1.) *Colour Evaporation Model* is a phenomenological model which does not assume correlation between quantum states of $q\bar{q}$ system before and after hadronisation, due to the emission of soft gluons. It describes experimental results on cross sections well. [2]

(2.) *Colour Singlet Model*, on the other hand, forbids the soft gluon emission due to its expected suppression. Its calculations are based on the theory of perturbative QCD (pQCD). [3]

(3.) *Colour Octet Model+NRQCD* permits also the colour octet states to develop into a colourless quarkonium, by emitting a soft gluon. It utilises non-relativistic QCD and allows combination of pQCD and non-perturbative QCD approaches. [3]

2.2. Behaviour in nuclear matter

Existence of heavy quarkonia in nuclear matter present after a heavy-ion collision is affected by several phenomena, which can both suppress and enhance the production. Some of these are related to the existence of QGP, whereas other arise even in hadronic medium *(cold matter effects)*.

(1.) *Quarkonia melting* is caused by the colour screening in QGP. Due to the existence of free colour charge carriers, the quarkonium binding potential

is modified and has an effective range of

$$r_D(T) = \sqrt{\frac{2}{3g^2}}\frac{1}{T}, \qquad (1)$$

where T is the temperature of the medium and g a function of the strong coupling constant. If this so-called Debye radius r_D grows higher than the quarkonium radius $r_{Q\bar{Q}}$, the system dissociates. Furthermore, since the quarkonia states vary in radius, one can utilise studies of their different relative suppression in determining the medium's temperature *(sequential melting)*. [4, 5]

(2.) *Statistical recombination* is a secondary production of quarkonia from pairs of random dynamic heavy q and $\bar{q}$ quarks during the QGP's chemical freeze-out. Its probability is proportionate to the number of heavy quark pairs created in a collision and can be neglected at RHIC energies for bottomonia. [6]

(3.) *Initial state effects* reflect the fact that partons in nuclei behave differently than those in free nucleons, which also results in a difference in the quarkonia production.

- *Nuclear (anti-)shadowing* describes the modification of the parton distribution functions of the partonic content of a nucleon when inside a boosted nucleus.
- *Cronin effect* stems from the energy loss of nucleon's partons by multiple scattering off the nucleus' partons.

(4.) *Inelastic interaction with hadronic system* is the dissociation of the quarkonia off hadrons. These should be negligible for the Upsilons, thanks to their high binding energies.

- *Nuclear absorption* describes the dissociation off nucleonic remnants of the heavy-ions.
- *Co-mover absorption* models suggest breaking of the quarkonia by interacting with mesonic systems created in the medium.

(5.) *Feed-down* is a secondary production of ground quarkonia states from decay of higher excited states. These can comprise a sizeable fraction of the observed production.

3. STAR experiment

The Solenoidal Tracker at RHIC (STAR) is the largest and the only still operating experiment at RHIC in Brookhaven National Lab in the USA. Its primary objective is the study of HIC and the properties of the QGP. It has excellent particle identification (PID) capabilities, full azimuthal coverage and $-1 < \eta < 1$ coverage in pseudorapidity η. The detector is subjected to a 0.5 T magnetic field.

STAR consists of several sub-detectors. Main tracking and momentum measurement is done by the Time Projection Chamber (TPC), along with PID by mean ionisation energy loss. The Heavy Flavor Tracker (HFT), installed in 2014, is a silicon pixel detector and also serves for tracking, most notably for the reconstruction of secondary vertices of open heavy-flavour meson decays. Further PID can be done by means of measuring $1/\beta$ in the Time of Flight (TOF) detector or p/E in the Barrel Electromagnetic Calorimeter (BEMC). BEMC is also used for high-tower triggering. Muon Telescope Detector (MTD), also fully implemented in 2014, enables PID and triggering for muons.

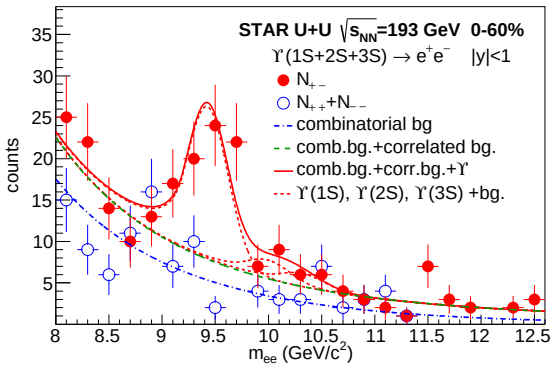

Figure 1: Centrality-integrated reconstructed invariant mass distribution of electron pairs with unlike-sign (solid circles) and like-sign (open circles) from U+U collisions at $\sqrt{s_{\mathrm{NN}}} = 193$ GeV for 0–60% centrality at mid-rapidity. Fits of the Upsilon, correlated background, and combinatorial background contributions are shown as lines. Taken from [7].

4. Recent measurements of Upsilon at STAR

At STAR, analyses of Upsilon production are conducted using both the di-electron and di-muon decay channel. They are measured in various systems, e.g. in Au+Au at $\sqrt{s_{\mathrm{NN}}} = 200$ GeV, U+U at $\sqrt{s_{\mathrm{NN}}} = 193$ GeV, p+Au and d+Au at $\sqrt{s_{\mathrm{NN}}} = 200$ GeV, and p+p at $\sqrt{s} = 200, 500$ GeV. In asymmetric system collisions, cold matter effects can be estimated, since the creation of QGP is deemed unlikely. Results from p+p collisions also serve as normalisation baseline for HIC results. [7, 8]

4.1. $\Upsilon \to e^+e^-$ in U+U

The analysis uses data collected in 2012. Upsilons are reconstructed from electrons in high-tower triggered events, where a tower in the BEMC had a required energy deposit of at least 4.2 GeV. These events correspond to the integrated luminosity of 263.4 μb^{-1}. The data were divided into three centrality bins.

The electron sample is selected by the combination of PID cuts from the TPC and BEMC. In the TPC, electrons need to have energy loss dE/dx close to the value of a given Bichsel function and momentum $p > 1.5$ GeV/c. BEMC is used to further reduce

hadronic background, by imposing cuts on the ratio of tower-cluster energy to particle momentum E_{cluster}/p and on cluster energy distribution. The invariant mass spectrum is shown in Figure 1. The signal was fitted with a Crystal-Ball function to account for bremsstrahlung and TPC momentum resolution, with some of the parameters taken from Monte Carlo simulations. The correlated background, stemming from $b\bar{b}$ decays and Drell-Yan processes, was fitted by the ratio of two power-law functions. The uncorrelated combinatorial background was estimated by fitting a like-sign distribution with a double exponential.

Reconstruction efficiencies were evaluated both from the data and by embedding simulated Upsilon decays into real data. The nuclear modification factor, describing the difference in production between nucleus-nucleus and proton-proton systems, was calculated as

$$R_{\text{AA}}^{\Upsilon} = \frac{\sigma_{pp}^{\text{inel}}}{\sigma_{AA}^{\text{inel}}} \frac{1}{\langle N_{\text{coll}} \rangle} \frac{B_{ee} \times (\mathrm{d}\sigma_{\Upsilon}^{AA}/\mathrm{d}y)}{B_{ee} \times (\mathrm{d}\sigma_{\Upsilon}^{pp}/\mathrm{d}y)}, \qquad (2)$$

where σ^{inel} are the total inelastic cross sections of collisions, $\langle N_{\text{coll}} \rangle$ the mean number of binary nucleon-nucleon collisions, B_{ee} the decay branching ratio, and $(\mathrm{d}\sigma_{\Upsilon}/\mathrm{d}y)$ are the measured Υ cross sections.

R_{AA} as a function of number of participants N_{part} can be seen in Figure 2. In central collisions, significant, albeit not complete, suppression is observed. [7]

5. Summary and Outlook

Basic physics of heavy quarkonia were described in this paper. Moreover, measurements of Upsilon at the STAR experiment were shown. At RHIC energies, significant—but not total—suppression is observed in heavy-ion collisions. On-going analyses via di-electron and di-muon channel on data taken in 2011, 2014, and 2016 with improved statistics may allow for more precise information about suppression of the excited states. Analyses on data from p+A collisions will also shed more light on cold nuclear matter effects.

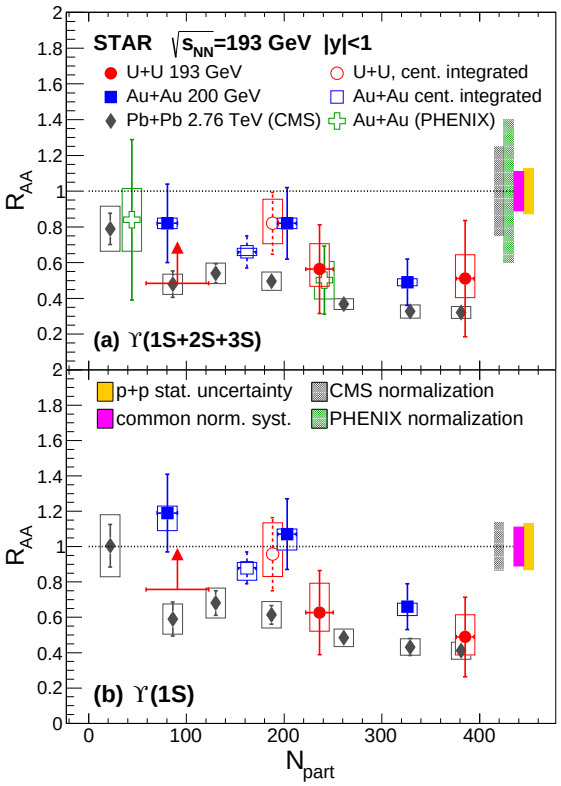

Figure 2: R_{AA} as function of number of participants N_{part} for Υ(1S+2S+3S) (top) and Υ(1S) (bottom) from U+U collisions at $\sqrt{s_{\text{NN}}} = 193$ GeV (circles). Results from Au+Au RHIC at $\sqrt{s_{\text{NN}}} = 200$ GeV (squares, crosses) and Pb+Pb LHC at $\sqrt{s_{\text{NN}}} = 2.76$ TeV (diamonds) are also shown for comparison. Taken from [7].

References

[1] S. Eidelman. Review of particle physics. *Physical Letters B* **592**(1).

[2] A. Andronic. Heavy-flavour and quarkonium production in the lhc era. *European Physical Journal C* **76**(3).

[3] R. Vogt. *Ultrarelativistic Heavy-Ion Collisions*. 1st edition. Elsevier, 2007.

[4] T. Matsui. J/psi suppression by quark-gluon plasma formation. *Physical Letters B* **178**:416–422.

[5] C.-Y. Wong. *Introduction to High-Energy Heavy Ion collisions*. 1st edition. Utopia Press, 1994.

[6] I. Das. Upsilon production measurements in pp, p-pb, pb-pb collisions with alice, qm2015. [2015], `https://indico.cern.ch/event/355454/contributions/838966/`.

[7] L. Adamczyk. Upsilon production in u+u collisions at 193 gev with the star experiment. *Physical Letters C* **94**(1), 2016.

[8] L. Adamczyk. Suppression of upsilon production in d+au and au+au collisions at 200gev. *Physical Letters B* **735**(1):127–137.

MACHINE LEARNING AND DATA ANALYSIS IN PARTICLE PHYSICS

Zuzana Moravcová*

Department of Physics, Faculty of Nuclear Sciences and Physical Engineering, Břehová 7, 115 19, Prague 1, Czech Republic

* corresponding author: Zuzana.Moravcova@fjfi.cvut.cz

Abstract. An inevitable part of physics experiments is data analysis. In last decades, an enormous increase of volume of measured data occured, hence it is crucial to look for new innovative methods of data treatment. The machine learning will be briefly presented, namely neural networks and decision trees. The latter can be improved with boosting method producing so called boosted decision trees (BDT). Application of the BDT algorithm will be shown on the measurement of the Λ_C production on ALICE experiment.

Keywords: machine learning, data analysis, particle physics, boosted decision trees.

1. Machine learning

The term *machine learning* was introduced in the paper *Some Studies of Machine Learning Using the Game of Checkers* written by Arthur Lee Samuel in 1959. Given only the rules of the game, a sense of direction, and a redundant and incomplete list of parameters which are thought to have something to do with the game, but whose correct signs and relative weights are unknown and unspecified [1], after some time, his computer was able to play better game of checkers than himself, a person who wrote the programme. In general it is possible to say that instead of complicated algorithm, the great amount of data is given to computer. Afterward the machine will create its own logic of the treatment.

Machine learning tasks can be divided into two categories, supervised and unsupervised. The difference between them is in the nature of learning. While during supervised learning we know desired outputs that correspond to given inputs, unsupervised learning is left on its own to find connections between inputs. It is clear that for data analysis in particle physics the former is used.

Supervised machine learning can be further subdivided into two types of algorithms, classification and regression. The former has a discrete output, the latter a continuous one. Both have a lot of applications across different fields from facial recognition to particle identification. In particle physics, the algorithms are implemented in a TMVA package (Toolkit for Multivariate Data Analysis) within the analysis framework ROOT.

1.1. Neural networks

Neural networks, as one of the most popular methods, consist of an interconnected group of neurons.[1] Connections are made between neurons across layers, but not within a layer, also they are only in one direction, to avoid a production of a loop. Despite their universality, it is extremely difficult for a human being to understand what is happening during the algorithm. Fortunately, it is possible to transform them to decisions trees which are easy to interpret.

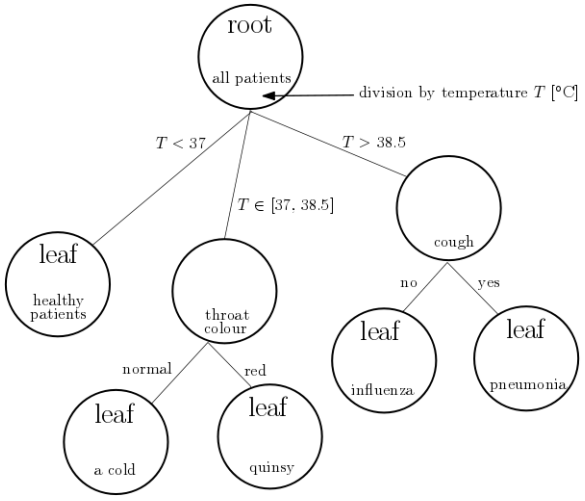

Figure 1: Example of a decision tree. Translated from Ref. [2].

1.2. Decision trees

Unlike neural networks, decision trees are very popular because of the transparency of the procedure and interpretation. Logic beyond them is really simple. In the first step, all data are in the first node called root. Then they are divided using a criteria to disjoint sets. Then, using another criteria (or the same, but with different values) to another sets of data (those are subsets of sets in the previous step). When the criterion is continuous, it has to be divided into finite number of intervals. In Figure 1, an example of a

[1] Neurons are originally nerve cells and the core components of the central nervous system (brain and spinal cord).

decision tree is shown. Patients are divided into three categories based on their temperature. If their temperature is above 37°C, they are further sub-divided into two groups. If no more division is occuring, the node is called leaf. Maximal depth of a decision tree is the maximal distance between one of the leaves and the root, in the example it equals two. The sum of patients in all leaves is equal to the number of patients in the root, so no data is lost during the process.

It is important to say that decision trees have some disadvantages, the most important of them is clearly their great instability. The small change in a training sample can produce a drastically different tree. Fortunately, algorithms to fix this problem exist. The one that is described below is boosting.

1.3. Boosted decision trees

Adding boosting to decision trees is not only that nodes are weighted and improved during iterations while being trained, but also that one does not have a single tree like in the previous case, but a full bunch of them, so a full forest. Furthermore, wrongly classified data from previous tree are used to train the following one. However, there is no need to use the same criterion only with modification of values. Going back to the case with diagnosis in Figure 1, next tree can start for example with a presence (or absence) of a headache, sweating or something completely different. It is known that boosted decision trees are resistant to over-fitting and the correlation between inputs does not influence the quality or precision of them. Also, it has been verified that it is more efficient to use a lot of trees with a small depth instead of a few very deep ones.

Particle physics utilizes usefulness of Boosted Decision Trees (BDT) more and more often, for example in ALICE experiment in CERN laboratory. Actual applications can be found in [3] and [4]. In the following section, ones from the former will be described more particulary.

2. Application of boosted decision trees in particle physics

Extraction of the signal from the $\Lambda_C \to \mathrm{K}^0_S + \mathrm{p}$ decay in p-Pb collisions is challenging because the branching ratio of this channel is only 1.11% which makes the signal to background ratio very small. That is why authors of [3] decided to do a multivariate analysis using boosted decision trees.

Firstly, it is important to congifure the TMVA software. A forest made of 850 individual trees was used, each of them with maximum depth equalled 3. Secondly, the best variable set must have been chosen, since this seems to be more important than fine tunning of the algorithm. Seeing that there is no criteria to choose the set, the following variables were chosen providing the best result:

- impact parameter of the bachelor track with respect to the primary vertex,
- bachelor p_T,
- combined PID for the bachelor track,
- $V0$ invariant mass in the hypothesis that the daughters are π^+ and π^-, i.e. that the $V0$ is a K^0_S,
- impact parameter of the $V0$ with respect to the primary vertex,
- $c\tau$ of the $V0$.

Despite the fact that the BDT analysis and performance is not affected by correlation between inputs, the set of variables listed above allows the correlations between them to be reduced to minimum [3]. Distribution of the input variables for the data and simulations (Monte Carlo for signal and background separately) for transverse momentum of Λ_C in the interval $2 \leq p_T(\Lambda_C) \leq 3$ GeV is shown in Figure 2, for other intervals it is similar and can be found in [3]. All predicted distributions are very similar to the ones from obtained data, but for transverse momentum of bachelor proton which is probably caused by imperfection of the used simulation.

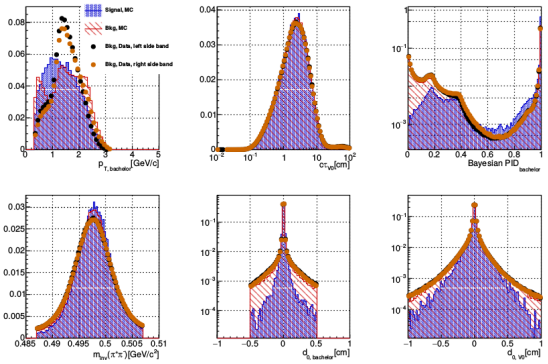

Figure 2: Input variables distribution. Taken from Ref. [3].

For the training and subsequent testing, samples from Monte Carlo simulations were used for both signal and background. Comparison between those two distributions of the classifier is shown in Figure 3. Clearly, the specific choice of training sample does not introduce any bias in the output as applying the BDT classification to the testing sample, one obtains the same output.

Afterwards, BDT classification algorithm can be used on real data. In Figure 4, outputs for classified data and Monte Carlo simulations [2] are shown for each $p_T(\Lambda_C)$ bin.[3] Those results are not very eloquent, but it is helpful to the main goal of the use of BDT – maximization of signal purity. That is done by cutting on the output and retaining the events with

[2] Only the training sample were used.

[3] Authors of [3] decided to divise the interval $2 \leq p_T(\Lambda_C) \leq 12$ GeV/c to six subintervals: 2–3, 3–4, 4–5, 5–6, 6–8, 8–12 GeV/c.

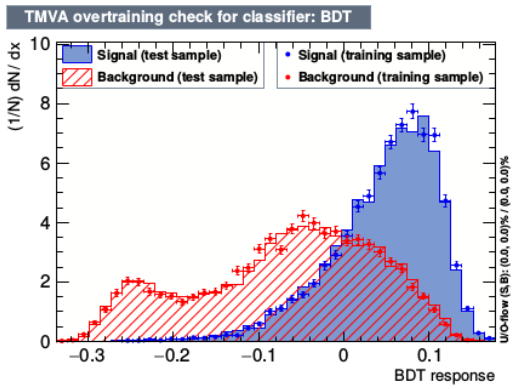

Figure 3: Comparison between the training and the testing distribution of the classifier from BDT analysis. Taken from Ref. [3].

p_T (Λ_C) [GeV/c]	BDT cut
2–3	-0.04
3–4	-0.08
4–5	-0.15
5–6	-0.07
6–8	0.04
8–12	-0.18

Table 1: Table of BDT cuts. Taken from Ref. [3].

the classifier output larger than the cut requirement. Cutting points are reported in Table 1, their choice was based on the quality of extraction of the invariant mass distribution of Λ_C.

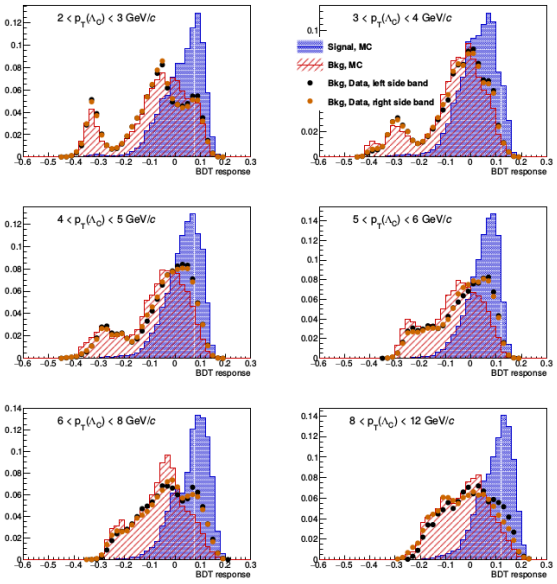

Figure 4: BDT classifier output distributions for data (points) and simulations (areas) for different $p_T(\Lambda_C)$ bins. Taken from Ref. [3].

Finally, after applying BDT cuts, it is possible to plot data with a goal of obtaining invariant mass

p_T (Λ_C) [GeV/c]	sig_1	sig_2
2–3	2.8 ± 2.1	3.5 ± 1.1
3–4	4.0 ± 1.0	4.5 ± 1.0
4–5	4.5 ± 2.1	3.8 ± 1.0
5–6	2.9 ± 1.1	4.2 ± 1.0
6–8	3.3 ± 1.0	4.8 ± 1.1
8–12	4.1 ± 1.1	4.2 ± 1.0

Table 2: Table of significance before (sig_1) and after (sig_2) applying BDT cuts. Taken from Ref. [3].

distributions of Λ_C decaying to a K^0_S and a proton. Those plots are shown in Figure 5. The ones with no cuts are in Figure 6. The fit function contains an order two polynomial function for the background and a Gaussian term for the signal, obtained values are shown in mentioned figures as well. Clearly, the effect of the cut on the output of the BDT classifier is visible in the quality of the fit. Also the significance improves when applying cuts as can be seen in Table 2 (apart from the case of $4 \leq p_T(\Lambda_C) \leq 5$ GeV).

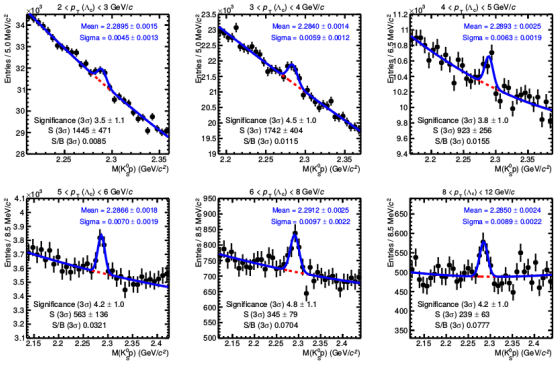

Figure 5: $\Lambda_C \rightarrow K^0_S$ + p invariant mass distribution for six $p_T(\Lambda_C)$ bins *after* applying BDT cuts. Taken from Ref. [3].

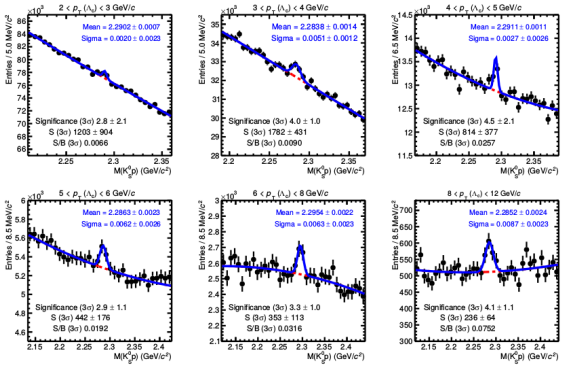

Figure 6: $\Lambda_C \rightarrow K^0_S$ + p invariant mass distribution for six $p_T(\Lambda_C)$ bins *before* applying BDT cuts. Taken from Ref. [3].

3. Conclusion and outlook

With its wide spectra of applications, machine learning recently became very popular in various branches of science. In this text, basic concepts as well as the most known methods used in machine learning, neural networks and decision trees, were introduced. Decision trees can be modified by addition of boosting, thus producing boosted decision trees. These can be used in particle physics to perform various tasks, e.g. to distinguish signal from background in case that the signal to background ratio is very small as presented on the example of the measurement of Λ_C from ALICE experiment (CERN laboratory).

In my bachelor thesis titled *Methods of optimalization of charm hadrons reconstruction* I will look for Λ_C in data from STAR experiment (Brookhaven National Laboratory) using multivariate data analysis. I will apply the facts I have learned by reading $\Lambda_C \rightarrow K^0_S$ *+ p in p-Pb collisions with MVA techniques* [3] and similar papers. Also I would like to focus on machine learning and its application (not only) in particle physics in the future, since machine learning is considered to be a very strong tool with a huge potential.

4. Acknowledgements

This work was also supported by the grant LG15001 and LM2015054 of Ministry of Education, Youth and Sports of the Czech Republic.

References

[1] A. L. Samuel. Some studies of machine learning using the game of checkers. *IBM Journal* **3**:211–229, 1959.

[2] J. Vaňo. Data mining a technika rozhodovacích stromov. *STU* 2008.

[3] A. Alici, et al. $\Lambda_C \rightarrow \mathrm{K}^0_S$ + p in p-Pb collisions with MVA techniques. *CERN* 2016.

[4] M. Figueredo, et al. Measurement of the Λ_C production cross section in the pkπ decay channel in p-pb collisions at $\sqrt{s_{NN}} = 5.02$ TeV using multivariate techniques. *CERN* 2016.

EXCLUSIVE PHOTON-INDUCED PRODUCTION MEASURED WITH THE ATLAS DETECTOR AT THE LHC

Filip Nechansky*

Czech Technical University in Prague

* corresponding author: nechansky.filip@gmail.com

Abstract. In proton-proton collisions, quasi-real photons can be emitted and their interaction can produce various final states. Their measurement is useful for confirmation of the standard model or beyond standard model searches. One such probe for new physics can be production of two W bosons, where the focus is put on an anomalous quartic coupling of two photons and two W bosons. Photon induced processes are obscured by additional interactions between the colliding protons. In order to study exclusive processes, it is necessary to first assess the impact of those interactions. For such study, an exclusive production of two leptons is used due to the precise theoretical description, a relatively large yield and good kinematic properties. Measurement of both processes performed on the ATLAS is presented in this article.

Keywords: Photon induced processes, ATLAS, LHC, dileptons, dibosons.

1. Introduction

In modern experimental particle physics, there is a vast number of areas which need to be studied and understood. Photon-photon interactions are one of them. Even though there is no direct coupling between photons, this constraint can be bypassed by introduction of an interaction through charged propagator.

However, there is an another setback - there is currently no photon source with a sufficient energy and intensity to study such processes. One must then adopt a different approach in order to probe this sector of the standard model.

An ultra-relativistic proton has a deformed electromagnetic field due to a relativistic contraction. The transverse component of such field can be interpreted as a quasi-real photon - a photon with low value of virtuality[1]. On experiments as is the ATLAS at the LHC, a collision of such photons can be studied.

2. The LHC and the ATLAS experiment

The LHC is 27 kilometre long collider with current centre-of-mass energy $\sqrt{s} = 13$ TeV. In four interaction points, the LHC experiments are located. The general purpose detectors ATLAS and CMS are used mainly for standard model measurements and search for new physics and are the most known thanks to their discovery of the Higgs boson. Measurements of a quark-gluon plasma and generally ion physics is studied in the ALICE experiment and finally the LHCb studies mainly b-physics and CP violation.

The ATLAS detector is composed of three main parts. The Inner Detector is composed mostly of silicon detectors and is used to reconstruct trajectories of particles. Around the inner detector are the calorimeters. Electromagnetic Calorimeter is used mainly to detect photons and electrons, while Hadron Calorimeters detect, as the name suggests, hadrons and are used to reconstruct jets. Finally, the Muon Spectrometer reconstructs muons.

[1] Virtuality $Q^2 = -P_\gamma^2$, where P_γ is four momentum of the photon.

3. Dilepton production

Between the great number of final states of photon collision, two particular processes were studied with the ATLAS detector. The first was a production of a dilepton pair, which was performed at $\sqrt{s} = 7$ TeV. The Feynman diagram of this process is in Figure 1. The main reason to study the dilepton production is

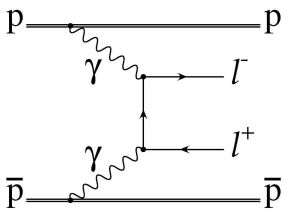

Figure 1: Feynman Diagram of exclusive di-lepton production in proton-proton collision. Taken from [1].

because it serves a standard candle of exclusive processes. Aside from the photon interaction, additional (mostly) strong interaction between the colliding protons can take place. Hence cross-section of exclusive photon induced processes is reduced compared to its theoretical value. This reduction is factorized by survival factor R :

$$\sigma^{meas} = R \cdot \sigma^{theory} \tag{1}$$

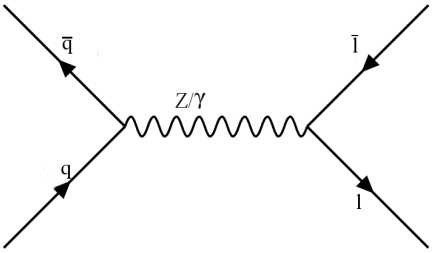

Figure 2: Feynman Diagram of Drell-Yan process.

The interaction of the quasi-real photons is characteristic by a low transverse momentum of the dilepton state. The leptons are therefore back-to-back, which is a factor useful for background subtraction.

The main background to the dilepton production is Drell-Yan process (see Figure 2), which is an annihilation of two quarks to Z or γ boson. Drell-Yan is dominated by a resonance around the mass of the Z boson (approximately 90 GeV). Even though Drell-Yan makes up the majority of the final states containing dilepton, it is usually accompanied by a large number of additional particles and has different kinematic properties than the exclusive production and thus its contribution is significantly reduced by a carefully chosen cuts.

The second most significant background is a photon-induced production associated with dissociation. Single- and double-dissociation (SD,DD) is a process where either one or both colliding protons dissociate - break into variety of final states, most of which have large rapidity. Since the ATLAS detector does not detect all outgoing particles (mainly in the forward rapidity regions), such events are often indistinguishable from the exclusive production. Hence the dissociative contribution is significant even after all cuts and is subtracted using a fit of the exclusive and dissociative distributions to the data, where the fitted normalization constant is taken as the survival factor.

Since there is a large number of collisions per bunch crossing, we cannot simply look for events with only two leptons in the final state. Exclusive events can however be identified by requesting only two particles in proximity of the dilepton vertex. This selection is not perfects - due to the presence of an additional proton interactions in one bunch crossing, another particle can be reconstructed in proximity of the vertex, resulting in rejection of the exclusive events. This fact is described by an exclusive efficiency.

The contribution of the Drell-Yan can be further reduced by removing events in the mass window around the Z-mass peak. Finally, since the leptons are back-to-back and the dilepton system has low transversal momentum, it is useful to select either based on the angle between the two leptons (acoplanarity $= 1 - |\Delta\phi_{ll}/pi|$) or based on the p_T of the dilepton. A spectrum of the dilepton pairs as a function of acoplanarity and p_T from the 7 TeV analysis can be found in Figure 3. Both ATLAS[2] and CMS[3] have performed the

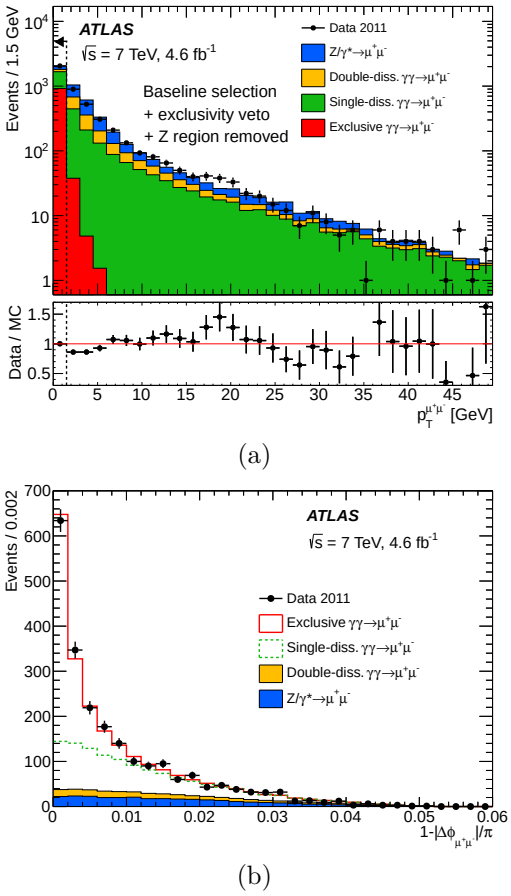

Figure 3: (a) Distribution of p_T^{ll} with the doted line demonstating the final cut. (b) Distribution of acoplanarity used to fit the exclusive and single-dissociative component on data. Taken from [2].

dilepton analysis at 7 TeV. In the ATLAS analysis, selection on p_T^{ll} was chosen while the acoplanarity was to fit the distributions. The results are summarized in Figure 4. The survival factor R was found to be around 80%.

The $\sqrt{s} = 13$ TeV analysis of this process done with the ATLAS detector is almost finished. Since for some period of the 2015 LHC run, a low-p_T muon trigger was used. This allows to do the analysis for lower transverse momentum of the muons, resulting in larger yield of events. Otherwise the situation is similar to 7 TeV and it seems it will not be necessary to make significant adjustments to the selection. Aside from producing results for the new energy, examination of dependence of the survival factor on m_{ll} is performed.

Second process considered is a production of two weak bosons W^+W^-. The lowest level diagrams are depicted in Figure 5. The QGC vertex is especially sensitive to possible beyond the Standard Model physics (BSM). Therefore, aside from standard model measurement, an analysis of this process can serve as a probe of the BSM sector.

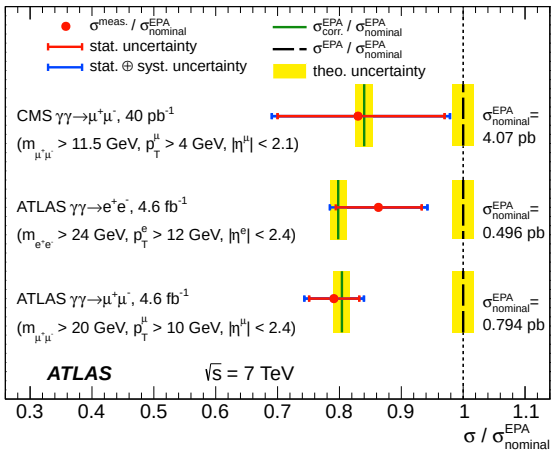

Figure 4: Results of exclusive dilepton analysis at 7 TeV with the ATLAS and CMS experiments. Taken from [2].

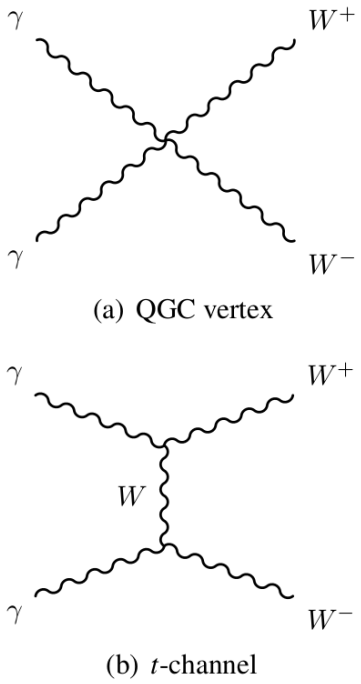

Figure 5: Tree-level diagrams of the $\gamma\gamma \to W^+W^-$ process. Taken from [4].

Since the weak bosons cannot be detected directly, diboson production can be studied only through the decay products. Channel with two leptons (either electron or muon) and two neutrinos is therefore used. Since the neutrinos cannot be detected, they carry away portions of the energy and momentum, leading to more kinematically complicated final state compared to the dilepton analysis. However, aside from the $\mu\mu$ and ee final states, the $e\mu$ channel is also allowed. Its main advantage is an absence of the Drell-Yan background (aside from small contribution of Drell-Yan with $\tau\tau$ in the final state, where one τ decays to μ and the other to e) and its therefore the best channel to study exclusive diboson production.

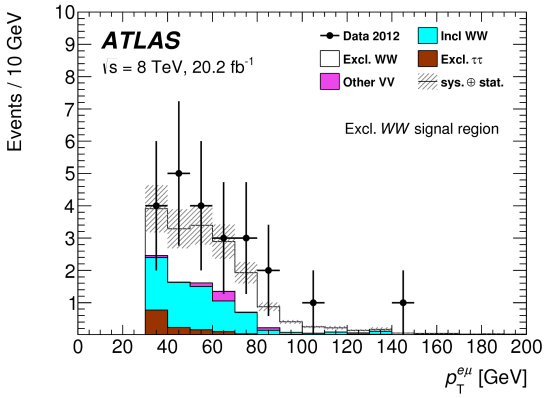

Figure 6: Final event distribution in the analysis of exclusive diboson production as a function of $p_T^{e\mu}$. Taken from [4]

The selection is in many ways similar to the dilepton case. The most important part is the exclusive selection which requires no additional activity in proximity of the dilepton vertex. There are some different kinematic requirements, but the most significant change is a selection on the transverse momentum of the dilepton pair. While for the exclusive dileptons this value is mostly low, the neutrinos carrying away part of the energy result in wider distribution of the transverse momentum. And since one of the dominant background - the Drell-Yan - has mostly low values, it is optimal to select only events with high value of p_T^{ll}.

The final distributions of 8 TeV ATLAS analysis[4] can be found in Figure 6. Due to a low cross-section the resulting yield is low, but it is still possible to derive some restrictions on new physics from it. Both the ATLAS and the CMS[5] found no evidence of beyond the Standard Model physics.

As in the previous case, results from 8 TeV are to be update for the new centre-of-mass energy. Higher energy on one hand means a higher number of collisions per bunch crossing , which results in a lower exclusive efficiency, while on the other hand it leads to increased cross-section. Those two factors combined with higher luminosity for current energy should still lead to a greater yield of exclusive WW events and therefore to higher constraints on new physics.

4. Conclusions

In summary, the exclusive photon-induced processes are great tools for the Standard Model studies and possibly can be used to search for a new physics. Studies of dilepton and diboson final state were performed using the ATLAS detector at centre-of-mass energies 7 TeV, with a $\sqrt{s} = 13$ TeV analyses also planned.

References

[1] M. Albrow, et al. A search for exclusive $z \to ll$ events and a measurement of the $pp \to p\gamma\gamma p \to pllp$ cross section for dilepton invariant mass > 40 gev/c^2. `http://www-cdf.fnal.gov/physics/new/qcd/exclZ_08/exclusive/`. Accessed: 22. 2. 2016.

[2] G. Aad, et al. Measurement of exclusive $\gamma\gamma \to \ell^+\ell^-$ production in proton-proton collisions at $\sqrt{s} = 7$ TeV with the ATLAS detector. *Phys Lett* **B749**:242–261, 2015. `1506.07098`.

[3] S. Chatrchyan, et al. Exclusive photon-photon production of muon pairs in proton-proton collisions at $\sqrt{s} = 7$ TeV. *JHEP* **01**:052, 2012. `1111.5536`.

[4] M. Aaboud, et al. Measurement of exclusive $\gamma\gamma \to W^+W^-$ production and search for exclusive Higgs boson production in pp collisions at $\sqrt{s} = 8$ TeV using the ATLAS detector. *Phys Rev* **D94**(3):032011, 2016. `1607.03745`.

[5] V. Khachatryan, et al. Evidence for exclusive $\gamma\gamma \to W^+W^-$ production and constraints on anomalous quartic gauge couplings in pp collisions at $\sqrt{s} = 7$ and 8 TeV. *JHEP* **08**:119, 2016. `1604.04464`.

$B^{\pm}$ OPPOSITE-SIDE TAGGING

Lukáš Novotný*

CTU FNSPE, Břehová 7, Prague 1, Czech Republic

* corresponding author: novotl23@fjfi.cvut.cz

Abstract. Complex phase in the CKM matrix is one source of CP violation in the Standard Model. This phase can be studied in the decay of $B_s^0 \to J/\psi\phi$. The determination of the initial flavour of neutral B mesons can be inferred using information from the B meson containing other pair-produced b quark. This method is referred to as opposite-side tagging. To study and calibrate the opposite-side tagging method, decays of $B^{\pm} \to J/\psi + K^{\pm}$ are used. The $B^{\pm}$ mass was fitted and the muon from the opposite side was used for the tagging. An efficiency of tagging was determined to be 4.4% for both B^+ and B^- candidates.

Keywords: CP violation, opposite-side tagging, sideband subtraction, ATLAS LHC.

1. Introduction

New phenomena beyond the predictions of the Standard Model (SM) may alter CP violation. The CP-violating weak phase ϕ_s originates from the interference between direct B_s^0 meson decays and decays through $B_s^0 - \bar{B_s^0}$ mixing to the same final state.This phase is small and can be related to Cabibbo-Kobayashi-Maskawa (CKM) quark mixing matrix elements and its value of $\phi_s = -0.0363^{+0.0016}_{-0.0015}$ can be predicted by combining beauty and kaon physics observables [1]. Previous measurements of these quantities have been reported by the LHCb, ATLAS and CMS collaborations ([2],[3],[4]).
The analysis presented here provides a measurement of the charge of the opposite-side muon charge in the decay of $B^{\pm} \to J/\psi + K^{\pm}$. This measurement will be used for calibration of the opposite-side tagging methods used in the decay of B_s^0.

2. Discrete symmetries

Symmetries and conservation laws play a fundamental role in physics. Invariance of system under symmetry transformation leads to the conservation law. For example, the invariance under space translation results in momentum conservation. Generally, there exist two types of symmetries, continuous and discrete. Previously mentioned space translation is an example of continuous symmetry. Three types of discrete symmetry exist, the parity transformation, the charge conjugation and time reversal. These types can also constitute composite symmetries, like parity-conjugation (CP) symmetry or generally known charge-parity-time (CPT) symmetry.

2.1. The parity symmetry

The parity operator P inverts all spatial coordinates, mathematically

$$\mathrm{P}\psi(x, y, z, t) = \psi(-x, -y, -z, t). \qquad (1)$$

The eigenvalues of parity operator are $\mathrm{P} = \pm 1$. Parity conservation implies that any physical process will proceed identically when viewed in mirror image.

The parity had seemed to be conserved in every decay until 1956, when Wu observed an parity violation in ^{60}Co decay [5]. The cobalt nuclei was placed in the magnetic field and then the counting rate was detected in dependence of angle. By inverting the magnetic field direction and thus the polarisation of the cobalt nucleus, a difference in counting rate could be detected. However, the overall counting rate does not change, which means the parity was violated.

2.2. Charge conjugation

The charge conjugation operator C changes the sign of the all quantum charges and does not affect the mass, linear momentum and spin of the particle. This means that the operator C transform the particle into antiparticle. This operator is similarly to parity conserved in electromagnetic and strong interactions and violated in weak interactions.

3. CP violation

As written, the parity and charge conjugation was found violated, but the CP transformation, obtained combining both P and C operators, was still considered to be conserved (see Figure). However, the CP symmetry is violated in certain rare processes.

In 1964, Christenson, Cronin, Fitch and Turlay observed the neutral K meson decay [6]. They were studied eigenstates of two neutral K mesons, called short-lived and long-lived kaons (K_S^0 and K_L^0). If CP is conserved, the final states are only $K_S^0 \to 2\pi$ and $K_L^0 \to 3\pi$ and mass eigenstates are also CP eigenstates. However, K_L^0 also sometimes decays in 2 pions, which means the CP eigenstates are different from the mass eigenstates and the K^0 and $\bar{K}^0$ can oscillate into each other, thus the CP is violated.

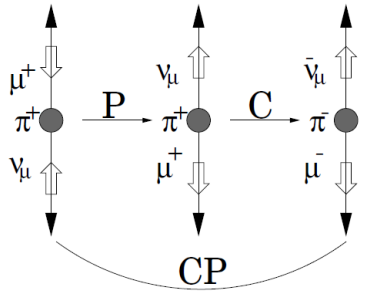

Figure 1: The $\pi^+ \to \mu^+ + \nu_\mu$ decay. The parity and charge conjugation is violated, meanwhile the CP symmetry is conserved.

3.1. Types of CP violation

There are three ways, how the CP can be violated - CP violation in decay, in mixing and in interference of mixing and decay.

The CP violation in decay (also know as direct CP violation) is the only possible source of CP asymmetry in charged meson decays. The decay amplitude of particle M into final state f is different from the decay amplitude of antiparticle into final antistate,

$$\Gamma\left(M \to f\right) \neq \Gamma\left(\bar{M} \to \bar{f}\right). \tag{2}$$

The CP violation in mixing (or indirect CP violation) arises when the probability of oscillation from meson to anti-meson is different from the probability of oscillation from anti-meson to meson,

$$\text{Prob}\left(P^0 \to \overline{P}^0\right) \neq \text{Prob}\left(\overline{P}^0 \to P^0\right) \tag{3}$$

Thus the mass eigenstates are not CP eigenstates.

The CP violation in interference of mixing and decay occurs in case both meson and antimeson decay into the same final state, $M^0 \to f$ and $M^0 \to \bar{M}^0 \to f$. This case occurs for example in the decay $B_s^0 \to J/\psi\phi$, see Figure 2.

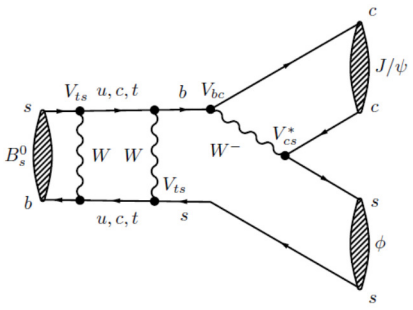

Figure 2: $B_s^0 \to J/\psi\phi$ decay as an example of The CP violation in interference.

3.2. CP Violation in the Standard Model

The GIM mechanism (S. Glashow, I. Iliopoulos and L. Maiani) describing relation between interaction and mass eigenstates for two families of quarks was generalised to three families by M. Kobayashi and K. Maskawa in 1973. The general quark mixing transformation with the unitary Cabibbo, Kobayashi, Maskawa (CKM) mixing matrix is

$$\begin{pmatrix} V_{ud} & V_{us} & V_{ub} \\ V_{cd} & V_{cs} & V_{cb} \\ V_{td} & V_{ts} & V_{tb} \end{pmatrix}. \tag{4}$$

Its element are used for evaluation of vertex factors in Feynman diagrams like Figure 2. This matrix is unitary, which leads to twelve distinct complex relations among the matrix elements. Six of them can represented geometrically as triangles in the complex plane. One of these relations is

$$V_{us}V_{ub}^* + V_{cs}V_{cb}^* + V_{ts}V_{tb}^* = 0. \tag{5}$$

The CP violating phase ϕ_s is defined as the weak phase difference between the $B_s^0 - \bar{B}_s^0$ mixing amplitude and the $b \to c\bar{c}s$ decay amplitude and is related to the angle of the triangle (5), thus

$$\phi_s = -2\beta_s = -2\text{arg}\left(\frac{V_{ts}V_{tb}^*}{V_{cs}V_{cb}^*}\right). \tag{6}$$

4. $B_s^0 \to J/\psi\phi$ analysis

The CP violating phase defined in (6) can be measured in $B_s^0 \to J/\psi\phi$ decay. Before the ϕ_s determination, the b quark or antiquark in B_s^0 has to be identified. B meson at LHC are produced in the hadronization of the $b\bar{b}$ pair. One b quark (it is unknown, whether it is quark or antiquark) are used to form the B_s^0, and second one from the pair is used for the identification when decaying into jets, muon or electron. This method is referred to as opposite-side tagging (OST). However, the B meson formed by the second b quark can decay via the weak interaction and then decay into the jet, muon or electron, so the charge is not always same as the charge of the B meson. To optimize the tagging performance, a muon cone charge variable is constructed, defined (for muons) as

$$Q_\mu = \frac{\sum_i^{Ntracks} q_i \left(p_\text{T}\right)^\kappa}{\sum_i^{Ntracks} \left(p_\text{T}\right)^\kappa}, \tag{7}$$

where q_i is charge of the track, $\kappa = 1.1$ and the sum is performed over the reconstructed ID tracks within a cone $\Delta R = \sqrt{(\Delta\phi)^2 + (\Delta\eta)^2} < 0.5$ around the muon direction.

Events containing $B^\pm \to J/\psi + K^\pm$ decays are used to study and calibrate the OST methods. The initial flavour in this decay is known and then the tag-probability for each B_s^0 candidate is determined from calibrations of $B^\pm$ candidates sample.

5. $B^\pm$ charge tagging

5.1. $B^\pm$ candidate selection

The data used in this analysis was taken on the experiment ATLAS at the LHC in proton-proton collisions

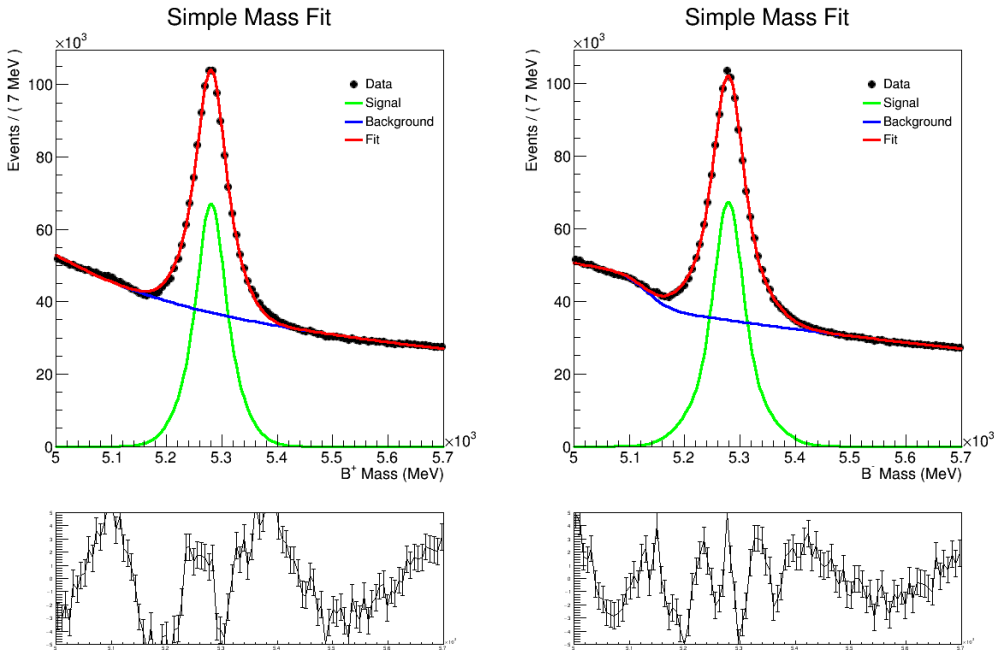

Figure 3: The invariant mass distribution of B^+ (left) and B^- (right) candidates passed the selection criteria. The overall result of the fit is given by the red curve, the signal component is given by the green curve and the background function with the partially reconstructed B is given by the blue curve.

during the whole year 2016. The Good Runs List All Good/data16_13TeV.periodAllYear_HEAD_DQDefects-00- 02-04_PHYS_StandardGRL_All_Good.xml was applied at the Athena level to remove the luminosity blocks that are not available to be used for physics analysis. The B candidate must satisfy mass condition $5.0 < m(B) < 5.7$ GeV and pseudorapidity $|\eta(B)| < 2.5$. Additionally, candidates must pass the transverse distance cut of $L_{xy} > 0.1$ mm (distance of B flight from the primary vertex) is applied to remove prompt component of background and the probability of the vertex fit be at least $\chi^2 < 12$ for one degree of freedom. Additionally, the kaon must satisfy $p_{\mathrm{T}}(K) > 1$ GeV and $|\eta(K)| < 2.5$ and the J/ψ candidates are composed of two oppositely-charged muons with transversal momentum $p_{\mathrm{T}}(\mu) > 4$ GeV and pseudorapidity within $|\eta(\mu)| < 2.5$. The third muon used for opposite tagging passes the $|\eta(\mu)| < 2.5$ and $p_{\mathrm{T}}(\mu) > 2.5$ GeV criteria.

5.2. $B^{\pm}$ MASS FIT

A maximum likelihood fit is performed on the selected data. The likelihood function is defined as a combination of the signal and background probability density functions

$$\begin{aligned}\mathrm{pdf} = & f_{sig}[f_{gauss}G_1(\mu,\sigma_1) + (1-f_{gauss})G_2(\mu,\sigma_2)] + \\ & + (1-f_{sig})[f_{bck1}E(\lambda) + f_{bck2}C + \\ & + (1-f_{bck1}-f_{bck2})AT(sc,of)],\end{aligned}$$

where $G_1(\mu,\sigma_1)$ and $G_2(\mu,\sigma_2)$ are Gauss functions with the same mean μ, $E(\lambda)$ is the exponential function with the slope λ, C is constant function and $AT(sc,of)$ is atanh with the offset of and scale sc. The coefficients f_{sig}, f_{gauss}, f_{bck1} and f_{bck2} are the scale factors between the functions. The results are shown in the Figure 3.

5.3. SIDEBAND SUBTRACTION

This method is used in order to study parameter distribution corresponding to the $B^{\pm}$ signal with the background subtracted. It is assumed that the background distribution of quantity of interest under the signal peak is approximately equal to the distribution of the background away from the peak region.

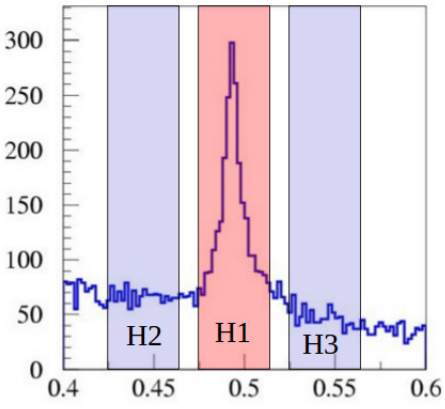

Figure 4: The sideband subtraction method. $H1$ is the signal region with the number of background candidates Nbg_{sigreg}, $H2$ and $H3$ are the sideband regions with the number of background candidates Nbg_{LSB} and Nbg_{RSB}.

There are defined three mass distribution regions.

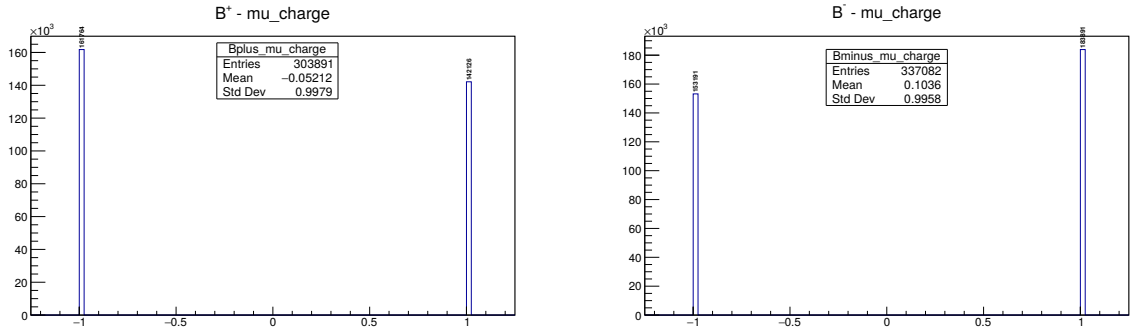

Figure 5: Charge of the third muons after sideband subtraction for B^+ (left) and B^- (right).

The signal region (histogram $H1$ in Figure 4) is defined to be $\pm 2\sigma$ around the Gauss mean, where σ is normalisation-weighted average sigma between the narrow and wide Gauss functions. The left ($H2$ in Figure 4) and right ($H3$ in Figure 4) sideband region are the mass interval $(\mu - 5\sigma; \mu - 3\sigma)$ and $(\mu + 3\sigma; \mu + 5\sigma)$. Approximately 90% of the signal events are retained.

The parameter distribution mention in Fig. 4 can be also used for the opposite side tagging method. Defining histogram of opposite side muons charge for $B^{\pm}$ candidates in mass signal region $G1$ and histograms of opposite side muons charge for $B^{\pm}$ candidates in left and right sideband regions $G2$ and $G3$, the number of charged third muons is

$$G_{final} = G1 - \frac{Nbg_{sigreg}}{Nbg_{LSB} + Nbg_{RSB}} (G2 + G3), \quad (8)$$

where Nbg_{RSB}, Nbg_{LSB} and Nbg_{sigreg} are number of muons defined in the Figure 4. The third muon charge distribution can be seen in Figure 5.

Then the efficiency of tagging ϵ, defined as

$$\epsilon = \frac{N_t agged}{N_B}, \quad (9)$$

where $N_t agged$ is the number the B events which are able to be tagged with a muon on the opposite side and N_B is the number of B events in total. Thus the efficiency of tagging is $\epsilon = 4.4\%$ for both B^+ and B^- candidates.

6. Conclusion

A measurement of tagging efficiency in $B^{\pm} \to J/\psi + K^{\pm}$ decay from a data sample of pp collisions with the ATLAS detector during the LHC Run 2 with central-of-mass energy $\sqrt{s} = 13$ TeV is presented. The calculated efficiency is $\epsilon = 4.4\%$. This result seems to be consistent with the similar measurement in Run 1 [7]. The calculation of dilution and tag power defined in [7] will be performed in future.

References

[1] J. Charles, et al. Predictions of selected flavour observables within the Standard Model. *Phys Rev* **D84**:033005, 2011.

[2] V. Khachatryan, et al. Measurement of the cp-violating weak phase ϕ_s and the decay width difference $\delta\gamma_s$ using the $\mathrm{b}_s^0 \to j/\psi\phi(1020)$ decay channel in pp collisions at $\sqrt{s} = 8$ tev. *Phys Lett* **B757**:97–120, 2016.

[3] V. M. Abazov, et al. Measurement of the CP-violating phase $\phi_s^{J/\psi\phi}$ using the flavor-tagged decay $B_s^0 \to J/\psi\phi$ in 8 fb^{-1} of $p\bar{p}$ collisions. *Phys Rev* **D85**:032006, 2012.

[4] R. Aaij, et al. Precision measurement of CP violation in $B_s^0 \to J/\psi K^+ K^-$ decays. *Phys Rev Lett* **114**(4):041801, 2015.

[5] C. S. Wu, et al. Experimental Test of Parity Conservation in Beta Decay. *Phys Rev* **105**:1413–1414, 1957.

[6] J. H. Christenson, et al. Evidence for the 2π Decay of the K_2^0 Meson. *Phys Rev Lett* **13**:138–140, 1964.

[7] G. Aad, et al. Measurement of the CP-violating phase ϕ_s and the B_s^0 meson decay width difference with $B_s^0 \to J/\psi\phi$ decays in ATLAS. *JHEP* **08**:147, 2016.

THE DEVELOPMENT IN MEASUREMENT OF NARROW STRUCTURE $X(5568)$ IN $B_S^0\pi^\pm$ SPECTRUM

Radek Novotny*

CTU Prague, Brehova 7, Prague, Czech Republic

* corresponding author: Radek.Novotny2@fjfi.cvut.cz

Abstract. In the beginning of 2016, the DØ experiment announced the observation of narrow resonant structure X(5568) decaying into B_s^0 and $\pi^\pm$ with 5.1 σ significance [1]. Since then, several other experiments decided to investigate this resonance and confirm this observation. As well as LHCb [2] and CMS [3], the ATLAS collaboration performs analysis of RUN1 with a goal to search for the resonance of properties declared by D0. In addition ATLAS works on setting an upper limits on a sensitivity for similar resonant states with masses in interval 5550–6000 MeV. The work is in progress, and the current document describes methodology of this research in ATLAS..

Keywords: tetraquark, BsPi, X(5568).

1. Introduction

In the 1960s, M. Gell-Mann [4] and G. Zweig [5] were studying regularities between the lowest lying states of mesons and baryons which were then known. They built a model with an assumption that mesons and baryons are made of constituent particles, called quarks, two for mesons and three for baryons. In 1976 based on M. Gell-Mann, G. Zweig prediction, Jaffe [6] build a model combining two quarks and two antiquarks leading to a structure called tetraquark. The idea of multiquark objects was developed even more for example in 1978 using MIT bag model [7] leading to the structure of four quarks plus one antiquark named pentaquark. Since then, several observations of tetraquark or pentaquark were claimed, but none of them were confirmed until 2015 where the LHCb collaboration observed an $J/\psi p$ resonance in $\Lambda_b^0 \to J/\psi K^- p$ decays [8].

In early 2016, the DØ [1]collaboration announced the observation of narrow structure referred to as X(5568), in $B_s^0\pi^\pm$ spectrum in $p\bar{p}$ collisions at $\sqrt{s} = 1.96$ TeV center-of-mass energy. The most probable explanation of such as exotic state would be the hadron composed of four quarks (b, s, u, d). This exotic state would be very important for the understanding of production mechanism of multiquark objects and in the case of the tightly bound di-quark anti-diquark pair, this may provide an additional information to strong interaction.

2. DØ measurement[1]

The DØ experiment at first made a background study in $B_s^0\pi^\pm$ channel. This background is consist of two components. The first component is produced by combinatorial background under B_s^0 peak and is modeled using real data. The fake B_s^0 signal is taken from sidebands in B_s^0 invariant mass spectrum separated by $\sim 5\sigma$ from the nominal B_s^0 mass. The left and right sideband are then reweighted to give a correct number of the signal under B_s^0 peak in the signal region. The second contribution with real B_s^0 is modeled using Monte Carlo (MC) simulation which is set to produce B_s^0 meson and additional random pion. This contribution from real B_s^0 is then scaled to a number of B_s^0 signal events in the signal region.

After this study, the background shape was fitted and for further studies was fixed. The final fit was made for two set of cuts and can be seen in the figure 1. The first one contain cut on opening angle between B_s^0 and $\pi^\pm$ $\Delta R = \sqrt{\Delta\eta^2 + \Delta\phi^2} < 0.3$ which reduces the background but also put the signal on the edge of the background. The second set of cuts was made without this cone cut but is using only as support measurement. Using the fixed background assumption and cone cut, DØ collaboration measured the signal with 5.1σ significance, mass $m = 5567.8 \pm 2.9(stat)^{+0.9}_{-1.9}(syst)\text{MeV/c}^2$ and natural width $\Gamma = 21.9 \pm 6.4(stat)^{+5.0}_{-2.5}(stat)\text{MeV/c}^2$.

3. LHCb and CMS results [2][3]

The promising result from DØ collaboration was further investigated by other two collaborations LHCb and CMS. Because both of these experiments do not see any evidence of the claimed state $X(5568)$ they published the upper limit on 95% CL of relative production rate of $B_s^0\pi^\pm$ to B_s^0, which is defined as

$$\rho_X \equiv \frac{\sigma(pp \to X + \text{anything}) \times \mathcal{B}(X \to B_s^0\pi^\pm)}{\sigma(pp \to B_s^0 + \text{anything})}, \quad (1)$$

$$= \frac{N(X)}{N(B_s^0)} \times \frac{1}{\epsilon^{\text{rel}}(X)}, \quad (2)$$

where the σ are the cross-sections related to the produced particles within the detector acceptance and $\epsilon^{\text{rel}}(X)$ is a relative efficiency of the $B_s^0\pi^\pm$ state X and the B_s^0 meson.

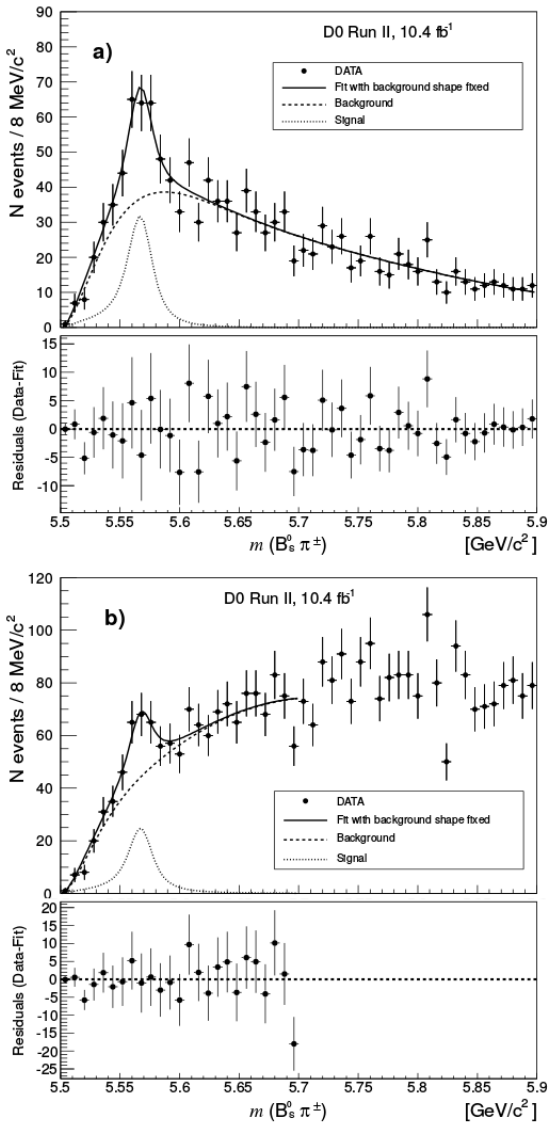

Figure 1: The $m(B_s^0\pi^\pm)$ distribution together with the background distribution and the fit results (a) after applying the cone cut and (b) without the cone cut.[1]

The CMS collaboration set the upper limit using the most conservative estimation of the efficiency ratio, determined from preliminary simulations, to the value of $\rho_X < 3.9\%$ at 95% CL.

The LHCb collaboration made more complex study and set the upper limit for D∅ values in three cuts on $p_T(B_s^0)$

$$\rho_X^{LHCb}(p_T(B_s^0) > 5 \text{ GeV}) < 0.012,$$
$$\rho_X^{LHCb}(p_T(B_s^0) > 10 \text{ GeV}) < 0.024,$$
$$\rho_X^{LHCb}(p_T(B_s^0) > 15 \text{ GeV}) < 0.020.$$

They have also made a mass scans over the region below the 6000 MeV using the 10 MeV steps and varying the width of resonance from 10 to 50 MeV with the same conclusion that there is no significant excess in the $B_s^0\pi^\pm$ spectrum.

4. ATLAS measurement

As well as the LHCb and CMS, the ATLAS decided to investigate this resonance. The studies were made on a data sample recorded with the ATLAS detector corresponding to 4.9 fb^{-1} of pp collision data at 7 TeV and 19.5 fb^{-1} at 8 TeV. Because the data used for this analysis are same as for CPV study in $B_s^0 \to J/\psi\phi$ channel [9], made by the same working group, the quality of the data and triggers was tested and proved in this analysis.

The first step was to make the background study in a similar way as D∅ did and to establish the best background model using real data and MC generated sample. Based on a background study, the following background model was used as default:

$$F_{\text{bck}}(m) = \left(\frac{m - m_{\text{thr}}}{n}\right)^a \cdot \exp\left(\sum_{i=1}^{4} p_i \cdot \left(\frac{m - m_{\text{thr}}}{n}\right)^i\right), \quad (3)$$

where $m_{\text{thr}} = m_{\text{PDG}}(B_s^0) + m_{\text{PDG}}(\pi^\pm)$ and n, a, p_i are free parameters. The S-wave Breit-Wigner PDF was used for a description of signal shape.

To fit total model, consist of background and signal PDF, to data the unbinned maximum-likelihood fit with a per-candidate error was used and contrary to the D∅ analysis, the background shape was given freedom. This approach better reflects the mass dependent resolution of the ATLAS detector thus more precise result can be achieved.

The ATLAS collaboration is looking into data to find a peak in the region claimed by D∅ collaboration, but simultaneously is developing the code to set the upper limit of the relative production rate ρ_X in a similar way as LHCb and CMS.

To calculate the number of B_s^0 candidates in the signal region, the simple fit with double gaussian PDF for signal and linear plus exponential for the background was used.

The last step is to evaluate the relative efficiency ϵ^{rel}. Because the B_s^0 part of efficiency cancel in the fraction, the relative efficiency is dominated by the efficiency of companion pion which consists of two components. The first one is due to the pion reconstruction efficiency within the ATLAS acceptance and the second one is inefficiency for pions under the reconstruction p_T threshold. Both of the contributions are dependent on $p_T(B_s^0)$ that is why the final ϵ^{rel} is calculated as an average of per-candidate efficiency for real data events in the signal region defined by the Breit-Wigner distribution convoluted by mass resolution. Thus for each mass point, where the relative production rate is measured, the relative efficiency need to be calculated separately. Using the constraint that the 99% of the peak is included in the fit window, ATLAS deduced the search interval to 5550–5700 MeV.

The CLs asymptotic calculator implemented in the RooStats package was used to build Asimov dataset which is used to calculate the upper limit. The preliminary results for the upper limit at D∅ position are

comparable with both LHCb and CMS measurements. In addition, the ATLAS made the mass scans over the region below the 5700 MeV and calculate sigma bands for the result.

The ATLAS paper describing in detail the procedure used to study the claimed $X(5568)$ resonance is nearly finished and will be published in the first half of this year.

5. Conclusions

The D∅ observation of tetraquark candidate $X(5568)$ caused a wave of optimism in the field, but further studies carried by the LHCb and CMS collaborations did not confirm the existence of the claimed exotic meson. All concerned experiments set up the upper limits of the relative production rate of $B_s^0\pi^\pm$ to B_s^0 and now are working to correctly describe the D∅ observation.

References

[1] V. M. Abazov, et al. Evidence for a $B_s^0\pi^\pm$ state. *Phys Rev Lett* **117**(2):022003, 2016. 1602.07588.

[2] R. Aaij, et al. Search for Structure in the $B_s^0\pi^\pm$ Invariant Mass Spectrum. *Phys Rev Lett* **117**(15):152003, 2016. 1608.00435.

[3] Search for the X(5568) state in B0s pi+- decays. Tech. Rep. CMS-PAS-BPH-16-002, CERN, Geneva, 2016.

[4] M. Gell-Mann. A schematic model of baryons and mesons. *Physics Letters* **8**(3):214 – 215, 1964.

[5] G. Zweig. An SU(3) model for strong interaction symmetry and its breaking. Version 2 pp. 22–101, 1964.

[6] R. L. Jaffe, et al. Diquarks and exotic spectroscopy. *Phys Rev Lett* **91**:232003, 2003. hep-ph/0307341.

[7] D. Strottman. Multiquark baryons and the mit bag model. *Phys Rev D* **20**:748–767, 1979.

[8] R. Aaij, et al. Observation of $J/\psi p$ Resonances Consistent with Pentaquark States in $\Lambda_b^0 \to J/\psi K^- p$ Decays. *Phys Rev Lett* **115**:072001, 2015. 1507.03414.

[9] G. Aad, et al. Measurement of the CP-violating phase ϕ_s and the B_s^0 meson decay width difference with $B_s^0 \to J/\psi\phi$ decays in ATLAS. *JHEP* **08**:147, 2016. 1601.03297.

FROM THE ZZ CROSS SECTION PRODUCTION MEASUREMENT TO VARIOUS PROCESSES WITH TWO Z BOSONS AT LHC

Ondřej Penc*

Czech Technical University in Prague, Zikova 1903/4, Prague 6, Czech Republic

* corresponding author: penc.ondrej@gmail.com

Abstract. We present an overview of the analyses entangled with the ZZ production in four-lepton channel in proton-proton collisions at the ATLAS and CMS experiments at LHC at CERN. Except the production cross section measurement the document touches anomalous neutral triple gauge coupling limit settings, the search for new resonances in the four-lepton mass distribution, double partons scattering, and ephasise the vector boson scattering in ZZ channel. The overview is focused on Run 1 period of the LHC at 8 TeV centre-of-mass energy and brings the first results from Run 2 at 13 TeV and prospects of ongoing analyses.

Keywords: ATLAS, CMS, ZZ production, aTGC, DPS, VBS.

1. Introduction

The production of two Z bosons in proton-proton collisions in the four-lepton final state, despite its small cross section due to the tiny branching ratio of $B(ZZ \to \ell^-\ell^+\ell^{-\prime}\ell^{+\prime}) = 0.0045$ (electrons and muons only [1]), is a very clean channel because of negligible background contamination. It makes the ZZ production measurement a very good test of the Standard Model at unprecedented energy at LHC. Since the two bosons can be a product of decaying Higgs boson the measurement is also an important background for studies of Higgs boson and the electroweak symmetry breaking mechanism. Four leptons in the final state provide a good opportunity for search of exotic resonances and setting limits on anomalous triple gauge coupling (TGC). The channel consists also a contribution from another two interesting processes the double parton scattering (DPS) and the vector boson scattering (VBS).

2. ZZ production and background

ZZ production at the LHC is dominated by quark-antiquark interactions depicted in Figure 1(left), with a small contribution of the order of 10 % from loop-induced gluon-gluon interactions shown in Figure 1(right).

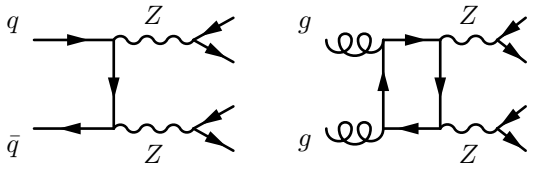

Figure 1: Two feynman diagrams with the biggest contribution to the ZZ production in proton-proton collisions.

The main background contributions originate from the processes with one Z boson and additional jets where a jet or a lepton from a heavy flavour decay is misidentified as an isolated lepton. To estimate such background contribution we identify a sample of events in the data adjacent to the signal region but dominated by events with one or more misidentified *fake* leptons by inversion of certain identification or isolation requirements. We extrapolate then to the signal region using an extrapolation factor (*fake factor*) that is determined in a separate sample which is dominated by *fake* leptons [2].

Additional backgrounds arise from the irreducible sources such as $t\bar{t}Z$ and ZZZ or WWZ decays as well as events with multi-parton interactions producing two separate Z-bosons that can produce four real leptons.

3. Selection and fiducial definition

The selection of events where two Z bosons were produced is rather straightforward although one needs to handle several things such as distinguishing between Z and γ, cosmic muon rejection etc. The measurement phase space is fixed by the detector properties like the acceptance, resolution, and identification and reconstruction performance in general. Such a fiducial phase space defines the measurement and is of special interest in case of inter-experiment comparisons.

The fiducial phase space of the ZZ production cross section measurement is defined similarly across all measurements at various centre-of-mass energies of 7 TeV [3], 8 TeV [2], and 13 TeV [4]. All measurements require a lepton quadruplet formed as a pair of the same flavour opposite charge (SFOC) di-leptons. The mass of each di-lepton has to be within 50 GeV window around the Z pole mass to suppress the γ contribution. The kinematic cut on the objects slightly vary across the measurements and with the increasing pile-up interaction multiplicity the lepton separation cuts are

introduced. The measurement do not consider tau leptons and neutrinos, which rises two pure channels for electrons and muons and one electron-muon mixed channel.

The strategy of event selection can be summarised in two major points.

(1.) Object selection (electrons, muons):
  (a) object quality (detector performance),
  (b) kinematic cuts (detector acceptance),
  (c) overlap removal.

(2.) Event selection (pairs of SFOC di-leptons):
  (a) trigger, primary vertex requirements,
  (b) additional quadruplet quality and hardness,
  (c) lepton isolation, hadronic veto,
  (d) 50 GeV window on di-lepton mass around Z pole mass

4. ZZ production cross section

The cross section is measured in the fiducial phase space and then extrapolated to the total phase space. The measurement is carried out as a counting experiment where the expected number of events is defined as

$$N_{\text{exp}}^{\text{chan}} = \sigma_{\text{tot}}\,\mathcal{L}\,C_{ZZ}^{\text{chan}}\,A_{ZZ}^{\text{chan}}\,BR^{\text{chan}} + N_{DD}^{chan} + N_{Irr}^{chan}$$

where N_{exp}^{chan} is the expected number of events in the channel, σ_{tot} is the total cross section of $pp \to ZZ$, $\mathcal{L}$ is the integrated luminosity, C_{ZZ}^{channel} is the reconstruction correction factor, A_{ZZ}^{chan} is the fiducial acceptance, BR^{chan} is the branching ratio of $ZZ \to$ chan and $N_{\text{DD}}^{\text{chan}}$ and $N_{\text{Irr}}^{\text{chan}}$ are the expected data driven and irreducible background rates in the channel respectively [2]. Both C_{ZZ} and A_{ZZ} factors are calculated using Monte Carlo simulations.

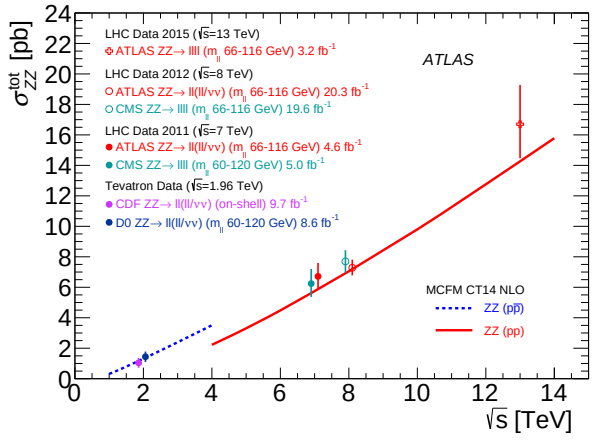

Figure 2: Comparison of experimental measurements and theoretical predictions of the total ZZ production cross section as a function of centre-of-mass energy [2].

The results from various centre-of-mass energies achieved at Tevatron and LHC are summarised in Figure 2. The most right, 13 TeV early measurement [4] on the first data from the second data-taking period at the LHC is in a good agreement with the Standard Model and declare a start of various analysis in the four-lepton ZZ channel.

5. Unfolding

The 8 TeV study unfolded several distributions normalised to the total cross section in the $ZZ \to 4\ell$ channel to correct the detector effects. The leading Z boson distribution serves as an input for the anomalous TGC limit settings, the number of jets distribution gives a first insight to VBS studies, and the $\Delta\phi$ and Δy distributions of the leptons in the quadruplet are sensitive to double parton scattering (DPS). The 13 TeV study is using the same Bayesian iterative unfolding method and promises to bring a wider palette of new unfolded distributions.

6. Anomalous triple gauge coupling

The $ZZ\gamma$ and ZZZ interactions are due to neutral triple gauge coupling (TGC) which is forbidden with respect to the Standard Model. Because such a process would violate S-matrix unitarity that implies non-renormalizability of the perturbative model. The unitarity violation means that the TGC contribution to ZZ production cross section depends on the centre-of-mass energy, therefore one expects the coupling is enhanced at higher energies. A typical signal of non-standard couplings thus will be a broad increase at high energies in the ZZ invariant mass, the Z transverse momentum (p_T) distribution, and the p_T distribution of the Z decay products [5].

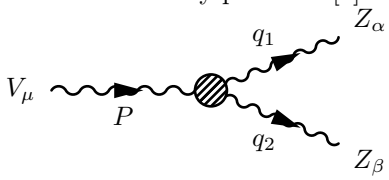

Figure 3: Neutral anomalous TGC vertex.

The vertex factor Γ_{ZZV} for an anomalous $Z_1 Z_2 V$ vertex (shown in figure 3), where Z_1 and Z_2 are on-shell, and $V = Z, \gamma$ may be off-shell, is given by [5]

$$g_{ZZV}\Gamma_{ZZV}^{\alpha\beta\mu} = e\frac{P^2 - m_V^2}{m_Z^2}\left[if_4^V(P^\alpha g^{\mu\beta} + P^\beta g^{\mu\alpha}) + \right.$$
$$\left. + if_5^V \epsilon^{\mu\alpha\beta\rho}(q_1 - q_2)_\rho\right],$$

where m_V is the mass of the V boson, P is the incoming momentum (the partonic centre-of-mass energy of the interaction), e is the proton charge, and q_1 and q_2 are the momenta of the Z_1 and Z_2 bosons, respectively. The anomalous TGCs are f_4^V (CP violating) and f_5^V (CP conserving).

The results by the ATLAS [3] and CMS [6] collaborations are summarised in Figure 4. It can be seen the limits are symmetrical around zero therefore consistent with the Standard Model expectations. The measurement at 13 TeV is about to be published and

promises to set the most stringent constraints on the anomalous couplings.

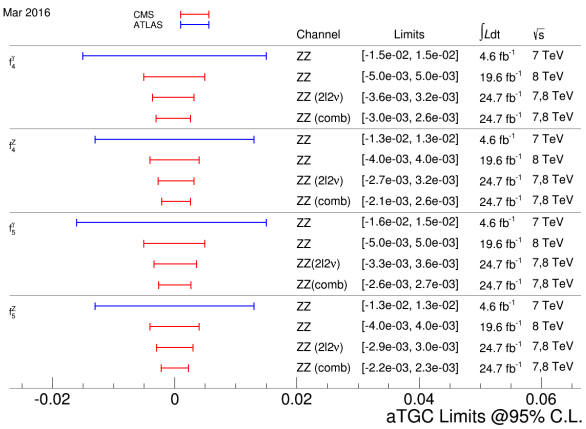

Figure 4: Neutral anomalous TGC results from ATLAS an CMS at Run 1 centre-of-mass energies [3, 6].

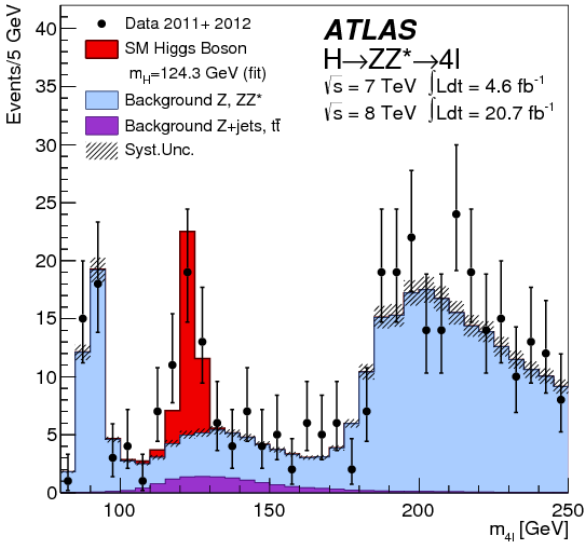

Figure 5: The four-lepton mass spectrum measured on Run 1 data using the ATLAS detector [7].

7. Higgs and other resonances in the 'Golden Channel'

The ZZ production measurement represents a background of the Higgs boson studies and the searches for new resonances because of the Z pole mass window requirement, rather the off-shell Z four-lepton mass and transversal momentum distributions are used in this case.

The four-lepton ZZ^* channel is called *golden* thanks to the large signal-to-background ratio. According to Run 1 studies, at the maximum deviation from the background-only expectation, the significance of the observed Higgs peak in the four-lepton mass spectrum in Figure 5 is 6.6σ, while the expected SM Higgs boson production is 4.4σ. The four-lepton channel alone consist a discovery-level signal [7, 8] and the studies of the Higgs boson properties continue at 13 TeV [9].

Various Standard Model extensions expect one or more neutral gauge bosons, for example the leptophobic Z' resonance originated from an extra Abelian gauge group $U(1)$ [10] that decay to four leptons via a pair of new scalar bosons. The search analyses probe the four-lepton mass spectrum up to 1.2 TeV and above, such as the Z' search analysis at CMS [11] and the additional heavy Higgs boson search analysis at ATLAS [12].

8. Double parton scattering

A Z boson pair can be produced also via two separated parton scatterings in a single proton-proton collision. Such process provides information about the proton structure, like double parton correlations [13]. It also gives a probe of effective proton size, the smaller the size is the larger the probability of double parton scattering (DPS) one gets. The DPS contribution to ZZ cross section is estimated using the following formula

$$\sigma^{\text{tot}}_{Z+Z} = \frac{\sigma^{\text{tot}}_{Z} \times \sigma^{\text{tot}}_{Z}}{2\sigma_{\text{eff}}}$$

where σ^{tot}_{Z} is the cross section to produce one on-shell Z boson and σ_{eff} is an effective area parameter of the proton or its inelastic cross section [14].

The DPS candidate event selection is the main challenge in the measurement. It is impossible to extract them on the event-by-event basis, therefore the usual approach is to fit the distribution variables sensitive to DPS. The ongoing DPS analysis at ATLAS collaboration adopts the basic DPS event selection strategy from four-jet events analysis [15] and adapt them for the four-lepton channel.

9. Vector boson scattering

The vector boson scattering (VBS) is defined by the diagram in Figure 6, where the quarks in protons interact weakly, two weak gauge bosons scatter, and decay to the familiar four-lepton final state. The

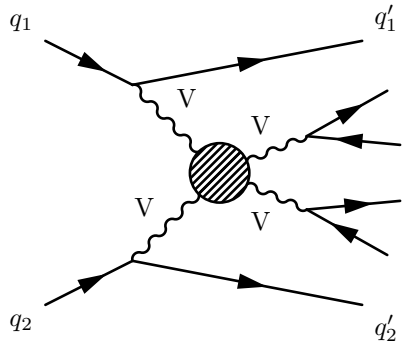

Figure 6: Feynman diagram of vector boson scattering. The grey circle stands for any connected diagram with the given external lines at leading order.

scattering of the bosons is depicted by the blob in the diagram and represent several realisations such as the triple gauge boson vertices in the s, t, and u channel in Figure 7(ordered from left), the quartic gauge boson vertex in Figure 7(most right), and the Higgs boson exchange contribution in Figure 8 in all Mandelstam channels.

Figure 7: VBS contributions from electroweak gauge boson interactions.

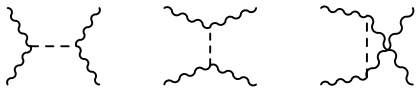

Figure 8: VBS contributions from the Higgs exchanges.

Because of the quarks in the diagram, the VBS analyses require two jets in addition to the lepton selection, so one is interested in $VVjj$ final state where V is W or Z boson.

The first evidence of $VVjj$ electroweak production is reported in the study of VBS in events with two same-charge W and two jets, which take advantage of suppressing the strong production cross section by the same-sign requirement. This analysis was carried out by both ATLAS and CMS experiments [16, 17] at 8 TeV dataset.

The latest efforts in VBS area of ATLAS collaboration in Run 2 are focused on the $ZZjj$ final state which is very unique due to additional di-jet requirements for already rare process. Di-jet mass must be over 500 GeV together with the rapidity difference of jets above 3 to enhance the electroweak signal against the QCD background. The process rarity also demands exploitation of MVA methods for signal enhancement. The ZZ VBS analysis is planned to be carried out on the data collected during the first three years of the 13 TeV data-taking period of the ATLAS detector. The dataset is expected to be up to 80 fb^{-1} and the analysis team expects to observe the electroweak VBS signal of 3σ significance.

10. Conclusions

The presented paper shows a variety of the ZZ studies in four-lepton channel. The processes with two Z bosons are connected with many interesting issues from testing of the Standard Model (ZZ production) to searching for the new resonances (four-lepton mass spectrum) and couplings (neutral TGC) beyond the Standard Model, and to probing the multi-parton interactions and parton distributions in proton.

Many analysis are ongoing and promise interesting results in the current data-taking period, such as the first observation of the electroweak vector boson scattering.

Acknowledgements

O. Penc was supported by grant SGS16/240/OHK4/3T/14.

References

[1] K. A. Olive, et al. Review of Particle Physics. *Chin Phys* **C38**:090001, 2014.

[2] M. Aaboud, et al. Measurement of the ZZ production cross section in proton-proton collisions at $\sqrt{s} = 8$ TeV using the $ZZ \to \ell^-\ell^+\ell'^-\ell'^+$ and $ZZ \to \ell^-\ell^+\nu\bar{\nu}$ channels with the ATLAS detector. *JHEP* **01**:099, 2017. 1610.07585.

[3] G. Aad, et al. Measurement of ZZ production in pp collisions at $\sqrt{s} = 7$TeV and limits on anomalous ZZZ and $ZZ\gamma$ couplings with the ATLAS detector. *JHEP* **03**:128, 2013. 1211.6096.

[4] G. Aad, et al. Measurement of the ZZ Production Cross Section in pp Collisions at $\sqrt{s} = 13$ TeV with the ATLAS Detector. *Phys Rev Lett* **116**(10):101801, 2016. 1512.05314.

[5] U. Baur, et al. Probing neutral gauge boson selfinteractions in ZZ production at hadron colliders. *Phys Rev* **D62**:113011, 2000. hep-ph/0008063.

[6] V. Khachatryan, et al. Measurements of the Z Z production cross sections in the 2l2ν channel in proton–proton collisions at $\sqrt{s} = 7$ and 8 TeV and combined constraints on triple gauge couplings. *Eur Phys J* **C75**(10):511, 2015. 1503.05467.

[7] G. Aad, et al. Measurements of Higgs boson production and couplings in diboson final states with the ATLAS detector at the LHC. *Phys Lett* **B726**:88–119, 2013. [Erratum: Phys. Lett.B734,406(2014)], 1307.1427.

[8] Observation of an excess of events in the search for the Standard Model Higgs boson in the $H \to ZZ(*) \to 4l$ channel with the ATLAS detector. Tech. Rep. ATLAS-CONF-2012-169, CERN, Geneva, 2012.

[9] Study of the Higgs boson properties and search for high-mass scalar resonances in the $H \to ZZ^* \to 4\ell$ decay channel at $\sqrt{s} = 13$ TeV with the ATLAS detector. Tech. Rep. ATLAS-CONF-2016-079, CERN, Geneva, 2016.

[10] P. Langacker. The Physics of Heavy Z' Gauge Bosons. *Rev Mod Phys* **81**:1199–1228, 2009. 0801.1345.

[11] V. Khachatryan, et al. Search for leptophobic Z' bosons decaying into four-lepton final states in proton-proton collisions at $\sqrt{s}$ =8 TeV 2017. 1701.01345.

[12] G. Aad, et al. Search for an additional, heavy Higgs boson in the $H \to ZZ$ decay channel at $\sqrt{s} = 8$ TeV in pp collision data with the ATLAS detector. *Eur Phys J* **C76**(1):45, 2016. 1507.05930.

[13] M. Rinaldi, et al. Double parton correlations in constituent quark models. *Phys Rev* **D87**:114021, 2013. 1302.6462.

[14] I. Sadeh. *Double parton scattering in four-jet events in pp collisions at 7 TeV with the ATLAS experiment at the LHC*. Ph.D. thesis, Tel Aviv U., 2013-01-01. 1308.0587.

[15] Study of hard double parton scattering in four-jet events in pp collisions at $\sqrt{s} = 7$ TeV with the ATLAS experiment at the LHC. Tech. Rep. ATLAS-CONF-2015-058, CERN, Geneva, 2015.

[16] G. Aad, et al. Evidence for electroweak production of $W^{\pm}W^{\pm}jj$ in pp collisions at $\sqrt{s} = 8$ TeV with the atlas detector. *Phys Rev Lett* **113**:141803, 2014.

[17] V. a. Khachatryan. Study of vector boson scattering and search for new physics in events with two same-sign leptons and two jets. *Phys Rev Lett* **114**:051801, 2015.

THREE-BODY INTERACTIONS IN MEAN-FIELD MODEL OF NUCLEI AND HYPERNUCLEI

Jan Pokorny*

Czech Technical University, Brehova 7, Prague, Czech Republic

* corresponding author: pokorj29@fjfi.cvut.cz

Abstract. This work presents results of calculations of Λ single-particle spectra in ${}^{17}_{\Lambda}$O and ${}^{209}_{\Lambda}$Pb, using a mean-field approach. The mean field is constructed self-consistently from realistic NN interaction using the Hartree-Fock method. The Λ hyperon interacts with the nuclear medium through the chiral ΛN interaction. The density-dependent NN and ΛN interaction terms which mimic the three-body interaction were found essential for the realistic description of charge radii and ground-state energies of hypernuclei.

Keywords: hypernuclei, hyperon Λ, mean-field model, three-body interactions.

1. Introduction

Hypernuclei are systems of protons, neutrons and one or more hyperons, baryons with non-zero strangeness $S \neq 0$. Hyperons decay predominantly weakly (with the exception of Σ^0) which results in their long lifetime ($\approx 10^{-10}$ s) compared to the time scale of strong interaction ($\approx 10^{-23}$ s). This allows experimental study of hypernuclei, including their structure and spectra. Furthermore, hyperon propagating in nuclear medium is not affected by Pauli exclusion principle, which makes the hyperon a unique probe of nuclear interior. The study of hypernuclei contributes to our better understanding of baryon-baryon forces, as well as nuclear structure and dynamics [1].

The aim of our work is a theoretical description of a single-particle spectra of Λ hypernuclei. We consider hypernucleus a many-body problem and, subsequently, we calculate its spectra using a mean-field approach. Mean field is constructed self-consistently by the Hartree-Fock method employing realistic N^{2}LO [2] NN and chiral LO ΛN [3] interactions. It has been shown, that three-body NNN interactions have non-negligible effect on nuclear ground-state energies and charge radii [4]. The use of these interactions in nuclear structure calculations is a non-trivial work.

In this work we restrict ourselves on using phenomenological density-dependent NN and ΛN interactions which mimic the effect of three-body interactions.

2. Mean-Field Model

In our calculations, we describe a hypernucleus as a many-body system consisting of a nuclear core and one Λ hyperon. Overal properties of the hypernucleus are given by the Hamiltonian

$$\widehat{H} = \widehat{T} + \widehat{V}^{NN} + \widehat{V}^{\Lambda N} + \widehat{V}^{NNN} + \widehat{V}^{\Lambda NN} - \widehat{T}_{CM}, \quad (1)$$

where $\widehat{T}$ stands for the sum of kinetic operators of each nucleon and Λ, and $\widehat{V}^{NN}, \widehat{V}^{\Lambda N}, \widehat{V}^{NNN}$, and $\widehat{V}^{\Lambda NN}$, denote the sums of two-body NN potential, ΛN potential, and three-body NNN and ΛNN, respectively. The center-of-mass operator $\widehat{T}_{CM}$ is defined as follows

$$\widehat{T}_{CM} = \frac{1}{2M(A+0.18)} \left(\sum_{a=1}^{A} \widehat{P}_a^2 + \sum_{a<b} \widehat{\vec{P}_a} \cdot \widehat{\vec{P}_b} \right), \quad (2)$$

where M is the mass of a nucleon $M \approx 938$ MeV, and A is the number of baryons in the system.

For our present calculations, three-body interactions in Hamiltonian (1) are replaced with two-body density-dependent interaction terms $\widehat{V}^{DD,NN}$ and $\widehat{V}^{DD,\Lambda N}$,

$$\widehat{H} = \widehat{T} + \widehat{V}^{NN} + \widehat{V}^{\Lambda N} + \widehat{V}^{DD,NN} + \widehat{V}^{DD,\Lambda N} - \widehat{T}_{CM}. \quad (3)$$

2.1. The Hartree-Fock Method in Second Quantization

The basic idea of the Hartree-Fock method is to treat a many-body system of interacting particles as a system of non-interacting particles which propagate through the mean field. This mean field is a potential which is obtained by averaging the potentials between all particles.

In our work, we use the Hartree-Fock method in a formalism of second quantization. We show the derivation of the Hartree-Fock method only for identical particles and a two-body interaction. The starting point of this method is the following Hamiltonian of A identical interacting particles

$$\widehat{H} = \sum_{ij} t_{ij} a_i^\dagger a_j + \frac{1}{2} \sum_{ijkl} V_{ijkl} a_i^\dagger a_j^\dagger a_l a_k. \quad (4)$$

In the second quantization, operators are expressed as matrices where $t_{ij} = \langle i|\widehat{T}|j\rangle$ are matrix elements of the kinetic energy operator and V_{ijkl} is the antisymmetrized matrix element of the two-body operator

$$V_{ijkl} = \langle ij|\widehat{V}|kl\rangle - \langle ij|\widehat{V}|lk\rangle = \langle ij|\widehat{V}|kl - lk\rangle. \quad (5)$$

Indices i, j, k, l represent single-particle states. The ground-state A-body wave function can be in terms of creation and annihilation operators expressed as

$$|\mathrm{HF}\rangle = \prod_{i=1}^{A} a_i^\dagger |0\rangle, \tag{6}$$

where $|0\rangle$ denotes the vacuum. By using variational principle

$$\delta\langle \mathrm{HF}|\widehat{H}|\mathrm{HF}\rangle = 0, \tag{7}$$

together with the Wick's theorem [5], the Hamiltonian (4) can be expressed as

$$\begin{aligned}\widehat{H} =& \sum_{ij}\left\{ t_{ij} + \sum_{kl} V^{\mathrm{NN}}_{kilj}\langle \mathrm{HF}|a_k^\dagger a_l|\mathrm{HF}\rangle \right\} \\ &- \frac{1}{2}\sum_{ijkl}\langle \mathrm{HF}|a_i^\dagger a_k|\mathrm{HF}\rangle\langle \mathrm{HF}|a_j^\dagger a_l|\mathrm{HF}\rangle \\ &+ \sum_{ijkl} V^{\mathrm{NN}}_{ijkl} \ :a_i^\dagger a_j^\dagger a_l a_k:, \end{aligned} \tag{8}$$

where $: a_i^\dagger a_j^\dagger a_l a_k :$ denotes the normal ordering of operators $a_i^\dagger a_j^\dagger a_l a_k$. The first line of Eq (8) defines the matrix elements of the mean-field operator

$$u_{ij} = t_{ij} + \sum_{kl} V^{\mathrm{NN}}_{kilj}\langle \mathrm{HF}|a_k^\dagger a_l|\mathrm{HF}\rangle = \varepsilon_i \delta_{ij}. \tag{9}$$

The expression in the second line of Eq. (8) contributes to the ground-state energy E_{HF}

$$\begin{aligned}E_{HF} =& \sum_{i=1}^{A}\varepsilon_i \\ &- \frac{1}{2}\sum_{ijkl}\langle \mathrm{HF}|a_i^\dagger a_k|\mathrm{HF}\rangle\langle \mathrm{HF}|a_j^\dagger a_l|\mathrm{HF}\rangle. \end{aligned} \tag{10}$$

The third line of the equation (8) denote the residual interactions between particles and does not contribute to the ground-state energy of the system.

The many-body problem is then solved iteratively with the following algorithm:

(1.) Express the matrix elements t_{ij}, V_{ijkl} in a single-particle basis defined by operators $a_i^\dagger, a_j$.

(2.) Calculate the matrix (9).

(3.) Diagonalize the matrix (9) and obtain the new single-particle states defined by operators $a_i^{'\dagger}, a_j'$ and the new single-particle energies ε_i'.

(4.) Use the new states as an input for the next iteration.

This loop is repeated until a convergence condition is reached, i.e. when

$$|\varepsilon_i' - \varepsilon_i| < \delta, \tag{11}$$

where δ is a small number. We solve the equations of motion for protons and neutrons separately. The explicit calculations can be performed in an arbitrary single-particle basis. In our calculations, we adopt the spherical harmonic oscillator basis.

2.2. Equations of motion

First, we solve the Hartree-Fock method for the protons and neutrons in the nuclear core without any effects of core polarization. We diagonalize the matrix (9) for protons and neutrons separately and we obtain following equations

$$t^{\mathrm{p}}_{ij} + u^{\mathrm{p}}_{ij} = \delta_{ij}\varepsilon^{\mathrm{p}}_i, \tag{12}$$

$$t^{\mathrm{n}}_{ij} + u^{\mathrm{n}}_{ij} = \delta_{ij}\varepsilon^{\mathrm{n}}_i, \tag{13}$$

where $\varepsilon^{\mathrm{p}}_i$ and $\varepsilon^{\mathrm{n}}_i$ are proton and neutron single-particle energies, respectively. The terms u_{ij} in Eqs. (12) and (13) are defined as

$$\begin{aligned}u^{\mathrm{p}}_{ij} =& V^{\mathrm{pp}}_{ikjl}\langle \mathrm{HF}|a_k^\dagger a_l|\mathrm{HF}\rangle_{\mathrm{p}} \\ &+ V^{\mathrm{pn}}_{ikjl}\langle \mathrm{HF}|a_k^\dagger a_l|\mathrm{HF}\rangle_{\mathrm{n}}, \end{aligned} \tag{14}$$

$$\begin{aligned}u^{\mathrm{n}}_{ij} =& V^{\mathrm{nn}}_{ikjl}\langle \mathrm{HF}|a_k^\dagger a_l|\mathrm{HF}\rangle_{\mathrm{n}} \\ &+ V^{\mathrm{pn}}_{kilj}\langle \mathrm{HF}|a_k^\dagger a_l|\mathrm{HF}\rangle_{\mathrm{p}}. \end{aligned} \tag{15}$$

Then the single particle energies and wave functions of the Λ particle are obtained by solving the equation

$$t^{\Lambda}_{ij} + u^{\Lambda}_{ij} = \delta_{ij}\varepsilon^{\Lambda}_i, \tag{16}$$

where u^{Λ}_{ij} is defined as

$$\begin{aligned}u^{\Lambda}_{ij} =& V^{\mathrm{p}\Lambda}_{kilj}\langle \mathrm{HF}|a_k^\dagger a_l|\mathrm{HF}\rangle_{\mathrm{p}} \\ &+ V^{\mathrm{n}\Lambda}_{kilj}\langle \mathrm{HF}|a_k^\dagger a_l|\mathrm{HF}\rangle_{\mathrm{n}}. \end{aligned} \tag{17}$$

2.3. Three-Body Interactions in the Mean-Field Model

The matrix elements of the two-body operators $V^{\mathrm{pp}}_{ijkl}, V^{\mathrm{pn}}_{ijkl}$, $V^{\mathrm{nn}}_{ijkl}, V^{\mathrm{p}\Lambda}_{ijkl}$, and $V^{\mathrm{n}\Lambda}_{ijkl}$ are matrix elements of sums of the two-body operators and the density-dependent two-body operators. The density-dependent term $\widehat{V}^{NN,DD}$ is defined with the following equation

$$\widehat{V}^{DD,NN} = \frac{C^{NN}_{\rho}}{6}(1+\widehat{P}_\sigma)\rho\left(\frac{\vec{r}_1+\vec{r}_2}{2}\right), \tag{18}$$

where C^{NN}_{ρ} is the coupling constant and $\widehat{P}_\sigma$ is the spin exchange operator. The coupling constant enters into our calculation as a free parameter. The density-dependent ΛN interaction term is analogous to $\widehat{V}^{DD,NN}$,

$$\widehat{V}^{DD,\Lambda N} = \frac{C^{\Lambda N}_{\rho}}{6}(1+\widehat{P}_\sigma)\rho\left(\frac{\vec{r}_1+\vec{r}_2}{2}\right), \tag{19}$$

where $C^{\Lambda N}_{\rho}$ is the coupling constant.

3. Results

For every calculation we need to choose a set of parameters $C^{NN}_{\rho}, C^{\Lambda N}_{\rho}, \hbar\omega$, and $N_{\max}$. Here, $\hbar\omega$ determines the width of the potential well of the spherical harmonic oscillator and $N_{\max}$ denotes the truncation of

the single-particle basis. We performed calculations for the hypernuclei ${}^{17}_{\Lambda}$O and ${}^{209}_{\Lambda}$Pb and studied the impact of the density-dependent interactions on their spectra. The parameter $\hbar\omega$ is fixed to 16 MeV in ${}^{17}_{\Lambda}$O and 12 MeV in ${}^{209}_{\Lambda}$Pb. The convergence of the single-particle states is the fastest with respect to $N_{\max}$ for this choice of $\hbar\omega$. Every calculation was performed with $N_{\max} = 12$ which is the largest available basis at the moment. The values of the coupling constants were chosen as follows:

i.) $C_\rho^{NN} = C_\rho^{\Lambda N} = 0$,

ii.) C_ρ^{NN} was set to match realistic charge density distribution, $C_\rho^{\Lambda N} = 0$,

iii.) C_ρ^{NN} was set to match realistic charge density distribution, $C_\rho^{\Lambda N}$ was set to match the ground-state energy with experimental data.

The values of the coupling constants for calculations i.), ii.), and iii.) for ${}^{17}_{\Lambda}$O and ${}^{209}_{\Lambda}$Pb are written in Table 1 and 2.

	C_ρ^{NN} [MeV·fm^6]	$C_\rho^{\Lambda N}$ [MeV·fm^6]
i.)	0	0
ii.)	1100	0
iii.)	1100	-500

Table 1: The values of the coupling constants for ${}^{17}_{\Lambda}$O.

	C_ρ^{NN} [MeV·fm^6]	$C_\rho^{\Lambda N}$ [MeV·fm^6]
i.)	0	0
ii.)	2500	0
iii.)	2500	-1000

Table 2: The values of the coupling constants for ${}^{209}_{\Lambda}$Pb.

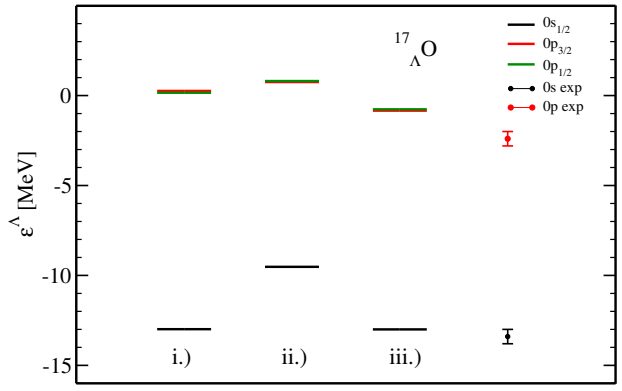

Figure 1: The single-particle energies ε^Λ in ${}^{17}_{\Lambda}$O for different C_ρ^{NN} and $C_\rho^{\Lambda N}$, see in the text. Experimental data are shown as dots with error bars for comparison [6].

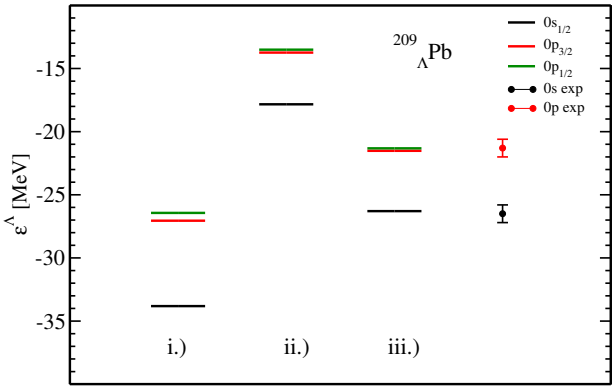

Figure 2: The single-particle energies ε^Λ in ${}^{209}_{\Lambda}$Pb for different C_ρ^{NN} and $C_\rho^{\Lambda N}$, see in the text. Experimental data are shown as dots with error bars for comparison [7].

In Fig. 1 and 2, the single-particle energies ε^Λ are shown for each calculation. Single particle energies ε^Λ depend very strongly on the choice of the coupling constants. This shows non-negligible impact of three-body interactions on charge radii and single-particle spectra of both hypernuclei.

4. Conclusions

In our work, we studied the Λ single-particle spectra of ${}^{17}_{\Lambda}$O and ${}^{209}_{\Lambda}$Pb. We used the Hartree-Fock method in the spherical harmonic oscillator basis to generate the mean field from chiral NN interaction NNLO$_{\rm opt}$. The interaction of the Λ particle with the mean field was described with chiral ΛN interaction. We did not implement three-body interactions fully. Instead, we simulated their effect with density-dependent interaction terms. We fitted the coupling constants of each term to match the charge radii and ground-state energies of considered hypernuclei. We showed strong dependence of the spectra on the choice of the coupling constants.

In future, we plan to implement full three-body NNN and ΛNN interactions into our calculations instead of the density-dependent interaction terms. We also intend to study the effects of $\Lambda - \Sigma$ coupling. It will also be desirable to study the core polarization effects and correlations from beyond mean-field calculations.

References

References

[1] P. Bydzovsky, A. Gal, J. Mares, Lect. Notes Phys **724** (2006).

[2] A. Ekström et. al., Phys. Rev. Lett. **110**, 192502 (2013).

[3] H. Polinder, J. Haidenbauer, U. - G. Meißner, Nucl. Phys. A **779**, 244 (2006).

[4] A. Günther, R. Roth, H. Hergert, S. Reinhardt, Phys. Rev. C **82**, 024319 (2010).

[5] G. C. Wick, Phys. Rev. **80**, 268-272 (1950).

[6] M. Agnello et al., Phys. Lett. B 698, 219 (2011).

[7] T. Hasegawa et al., Phys. Rev. C 53, 1210 (1996).

CORRECTING JET SPECTRA ON DETECTOR EFFECTS

Peter Pribeli*

FNSPE CTU, Břehová 7, Prague, Czech Republic

* corresponding author: peter.pribeli@cern.ch

Abstract. The mathematical basis of the methods used in the correction of various jet spectra on detector effects such as p_T smearing and reconstruction efficiency is laid out. The methods presented are based on Bayes' theorem and the singular value decomposition theorem which are the two most commonly used techniques of jet spectra unfolding.

Keywords: SVD, unfolding.

1. Introduction

In experiments, jets are reconstructed from particles measured by a detector. The jet spectra are therefore affected by various detector effects e.g. inaccurate energy and momentum measurements, the particle reconstruction efficiency etc. Thus corrections of the measured spectra on these detector effects are necessary. The corrections are usually carried out by unfolding.

Suppose that a vector $\vec{b}$ represents a distribution of a physical quantity reconstructed by the detector. If the spectrum is in the form of an histogram, elements of $\vec{b}$ correspond to the bin content of individual bins. It is desired to obtain the distribution of the true, detector-unaffected physical quantity $\vec{x}$. A linear relation of true and measured distributions is often expected. This linear transformation is described by the so-called response matrix $\mathbb{A}$ of the detector which is usually acquired by means of Monte Carlo simulations. Hence one has to solve a linear system

$$\mathbb{A}\vec{x} = \vec{b}. \tag{1}$$

Thus the elements of the response matrix represent *probabilities* that the $i-$th component of the true spectrum will be reconstructed as the $j-$th component of the measured spectrum. The naive inversion of $\mathbb{A}$ does not work because $\mathbb{A}$ is often singular. The process of solving (1) and thereby obtaining $\vec{x}$ is called *unfolding*. Several different algorithms may be used for unfolding. The approaches based on *Singular Value Decomposition* (SVD)[1] and Bayes' theorem[2] are presented.

2. Bayesian unfolding

Bayesian unfolding is based on Bayes' theorem. Let $C_i,\ i \in [1, n_C]$ be independent causes that produce an effect E. Let further $P(\bullet|\bullet)$ be conditional probabilities. The conditional probability of C_i given E is then given by

$$P(C_i|E) = \frac{P(E|C_i)P(C_i)}{\sum_{j=1}^{n}\left[P(E|C_j)P(C_j)\right]}, \tag{2}$$

where $P(C_i)$ is the probability of C_i. Bayes' theorem can be generalized to multiple effects E_j where $j \in [1, n_E]$, for each of which the conditional probability $P(C_i|E_j)$ can be found according to Bayes' theorem. The conditional probability $P(E_j|C_i)$ must be normalised ($\sum_{k=1}^{n_C} P(E_j|C_k) = 1$) which implies that all effects have a cause. While no effects may happen without causes the reverse does not hold true. There might be redundant causes included. Therefore it is convenient to define a measure of efficiency $0 \leq \epsilon_i = \sum_{k=1}^{n_E} P(E_k|C_i) \leq 1$. Given N measurements of an effect E_j, the expected number of effects being caused by a cause C_i is by definition

$$N_{C_i} = N\, P(C_i|E_j). \tag{3}$$

Bayes' theorem has the power to *increase* the knowledge about the initial probabilities $P(C_i)$ iteratively. One can even begin without any *a priori* knowledge of $P(C_i)$ and use a uniform distribution. On the other hand, the conditional probabilities $P(E_j|C_i)$ are not effected by iterations and thus must be calculated beforehand, usually by means of Monte Carlo simulations.

The Bayesian theorem is adapted for spectra unfolding in the following way. One can associate the effect E_j with the $j-$th bin of the measured spectrum. Similarly the cause C_i corresponds to the $i-$th bin of the true spectrum which is represented by the probabilities $P(C_i)$.

Consider again the system of equations (1): $\mathbb{A}\vec{x} = \vec{b}$, where $\vec{x} \in \mathbb{R}^n$ is the true spectrum and $\vec{b} \in \mathbb{R}^m$ is the reconstructed spectrum. Let us identify

$$P(E_j|C_i) = A_{ij}, \tag{4a}$$

$$N_j = b_j, \tag{4b}$$

where N_j is the number of measurements of the effect E_j.

The unfolded spectrum is then given by

$$x_i = \begin{cases} \frac{1}{\epsilon_i}\sum_{j=1}^{n_E} N_j\, P(C_i|E_j), & \epsilon_i \neq 0 \\ 0, & \epsilon_i = 0. \end{cases} \tag{5}$$

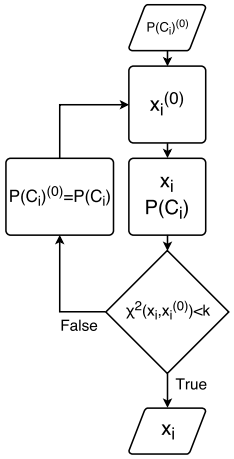

Figure 1: Bayesian unfolding algorithm.

The probability of the causes is then given by

$$P(C_i) = \frac{x_i}{\sum_{j=1}^{n_C} x_j}. \tag{6}$$

2.1. Algorithm

The algorithm for the iterative Bayesian approach to spectra unfolding might be formulated as follows

(1.) Chose an initial $P(C_i)^{(0)}$. In case of complete ignorance pick a uniform distribution. Further, calculate the initial $x_i^{(0)} = P(C_i)^{(0)} N_{ev.obs.}$.

(2.) Compute x_i according to (5) (using $P(C_i)^{(0)}$).

(3.) Determine $P(C_i)$ according to (6).

(4.) Do a χ^2 comparison between x_i and $x_i^{(0)}$, if the χ^2 is too high replace $x_i^{(0)}$ by x_i and $P(C_i)^{(0)}$ by $P(C_i)$ and go to step 2.

(5.) Repeat until χ^2 is sufficiently small.

A flowchart illustrating the procedure can be seen in Figure 1.

3. Singular Value Decomposition

Let $\mathbb{A} \in \mathbb{R}^{m,n}$ be an arbitrary matrix where $n, m \in \mathbb{N}$. Then $\mathbb{A}$ admits a decomposition of the form

$$\mathbb{A} = \mathbb{U}\mathbb{S}\mathbb{V}^T, \tag{7}$$

where $\mathbb{U} \in \mathbb{R}^{m,m}$ and $\mathbb{V} \in \mathbb{R}^{n,n}$ are orthogonal matrices and $\mathbb{S} = \mathrm{diag}(\mathbb{S}_{11}, \mathbb{S}_{22}, ..., \mathbb{S}_{rr})$. The numbers $\mathbb{S}_{11} \geq \mathbb{S}_{22} \geq \mathbb{S}_{rr} \geq 0$ are called the singular values of $\mathbb{A}$ where $r = \mathrm{rank}(\mathbb{A})$.

The dimension of $\vec{x}$ has to be less than or equal to the dimension of $\vec{b}$ in order to make the problem well-posed.

Suppose that $\mathbb{A} = \mathbb{U}\mathbb{S}\mathbb{V}^T$. Substituting in (1) for $\mathbb{A}$ gives

$$\mathbb{U}\mathbb{S}\mathbb{V}^T\vec{x} = \vec{b}, \tag{8}$$

$$\vec{x} = \mathbb{V}\mathbb{S}^{-1}\mathbb{U}^T\vec{b}, \tag{9}$$

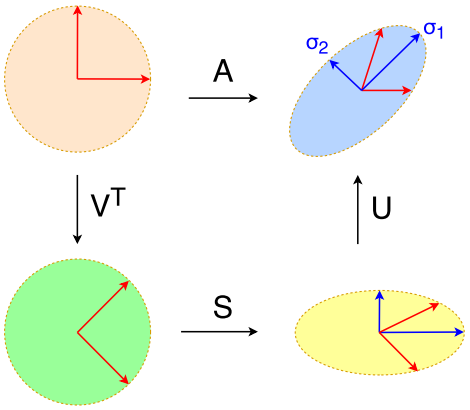

Figure 2: Visualisation of the SVD theorem.

which is easily calculated since $\mathbb{S}^{-1}$ is obtained by replacing the diagonal elements of $\mathbb{S}$ by their respective reciprocal values (provided that $\mathbb{S}^{-1}$ exists). Note that the matrices $\mathbb{U}$ and $\mathbb{V}^T$ might be viewed as rotation operators and $\mathbb{S}$ as a scaling operator for intuitive understanding of the decomposition (see Figure 2).

In the derivation of the equations used in SVD unfolding, the main ideas of [1] are adopted. The problem with SVD arises when the singular values of $\mathbb{A}$ are zero or close to zero. In that case $\mathbb{S}^{-1}$ does not exist. Let us restate (1) as follows

$$\mathbb{A}\vec{x} = \vec{b} \Leftrightarrow (\mathbb{A}\vec{x} - \vec{b})(\mathbb{A}\vec{x} - \vec{b})^T = 0. \tag{10}$$

The problem of finding a convenient substitute for $\mathbb{A}^{-1}$ is therefore equivalent to minimising the corresponding quadratic form.

The components of $\vec{b}$ may have different statistical uncertainties in general. This is accounted for by introducing the inverse covariance matrix $\mathbb{M}^{-1}$ of $\vec{b}$ into the quadratic form.

The problem is thus equivalent to minimising the quadratic form

$$(\mathbb{A}\vec{x} - \vec{b})\mathbb{M}^{-1}(\mathbb{A}\vec{x} - \vec{b})^T = 0. \tag{11}$$

Furthermore, several steps will be carried out which will help eliminate the singular values of $\mathbb{A} \in \mathbb{R}^{n,m}$. First, the matrix $\mathbb{A}$ and the vector $\vec{x}$ are normalized using a presumed shape of the solution—the so-called *prior* spectrum.

Consider $\forall i \in \{1, 2, .., m\}, \forall j \in \{1, 2, .., n\}$

$$y_i = x_i / x_i^{ini}, \tag{12}$$

$$\bar{\mathbb{A}}_{ij} := \mathbb{A}_{ij} x_j^{ini}, \tag{13}$$

where $\vec{x}^{ini}$ is an initial estimate of the solution. It is obvious that $\bar{\mathbb{A}}\vec{y} = \vec{b} \Leftrightarrow \mathbb{A}\vec{x} = \vec{b}$.

The matrix $\bar{\mathbb{A}}$ respects the shape of the expected spectrum and its elements are not probabilities but counts.

The aforementioned transformation is justified for this particular use for several reasons. Using $\bar{\mathbb{A}}$ better

represents errors and weights suppressing less populated bins. Another reason is that if $\vec{x}^{ini}$ is reasonably close to $\vec{x}$ then $\vec{y}$ shall be smooth and nearly constant (varying slowly).

The covariance matrix $\mathbb{M}$ from (11) is symmetric and positive-definite. Using SVD one gets

$$\mathbb{M} = \mathbb{Q}\mathbb{R}\mathbb{Q}^T \Leftrightarrow \mathbb{M}^{-1} = \mathbb{Q}\mathbb{R}^{-1}\mathbb{Q}^{-1}, \tag{14}$$

Where $\mathbb{Q}, \mathbb{Q}^T$ are orthogonal and $\mathbb{R}$ is a diagonal matrix. Substituting (14) in (11) and redefining $\hat{\mathbb{A}} = \mathbb{R}^{-\frac{1}{2}}\mathbb{Q}^T\mathbb{A}$ and $\vec{\hat{b}} = \mathbb{R}^{-\frac{1}{2}}\mathbb{Q}^T\vec{b}$ yields

$$(\hat{\mathbb{A}}\vec{y} - \vec{\hat{b}})(\hat{\mathbb{A}}\vec{y} - \vec{\hat{b}})^T = 0. \tag{15}$$

Thus far the quadratic form (15) is equivalent to (1) which still might be ill defined. The next step is the regularization of the problem. A regularization works around the problem of inverting singular matrices.

To regularise the quadratic form an *a priori* condition on the solution is added

$$(\bar{\mathbb{A}}\vec{y} - \vec{\bar{b}})(\bar{\mathbb{A}}\vec{y} - \vec{\bar{b}})^T + \tau\,(\mathbb{C}\vec{y})^T\,\mathbb{C}\vec{y} = 0. \tag{16}$$

The parameter τ represents the weight of the regularization. While this parameter is strongly problem-dependent and must be determined numerically, the *a priori* condition $(\mathbb{C}\vec{y})^T\,\mathbb{C}\vec{y}$ may be determined from general considerations.

Under the assumption that the prior spectrum has been chosen close enough to the true spectrum, it can be expected that $\vec{y}$ is a slowly varying spectrum. Since the statistical fluctuations induce oscillations in the measured spectrum therefore also in the solution, the next step will be to define and minimalize a measure which represents the curvature of the solution. The degree of oscillations can be conveniently quantified by means of second derivatives. Finite-difference methods may be used to approximate second derivatives as

$$f''(x) \approx \frac{f(x+h) - 2f(x) + f(x-h)}{h^2}. \tag{17}$$

Consider the sum of the squares of second derivatives of $\vec{y}$ with steps $h = 1$ to be the measure of "curvature"

$$(\mathbb{C}\vec{y})^T\,\mathbb{C}\vec{y} = \sum_i \left(y_{i+1} - 2y_i + y_{i-1}\right)^2. \tag{18}$$

The matrix $\mathbb{C}$ from (18) can be expressed as

$$\mathbb{C} = \begin{pmatrix} -1+\varepsilon & 1 & 0 & 0 & \cdots & 0 \\ 1 & -2+\varepsilon & 1 & 0 & \cdots & 0 \\ 0 & 1 & -2+\varepsilon & 1 & \cdots & 0 \\ \vdots & \vdots & \vdots & \vdots & \ddots & \vdots \\ 0 & 0 & 0 & 0 & \cdots & -1+\varepsilon \end{pmatrix}, \tag{19}$$

The small increment ε is added to the diagonal in order to make $\mathbb{C}$ invertible. A sensible choice for ε is on the order of $\varepsilon = 10^{-3}$ [1].

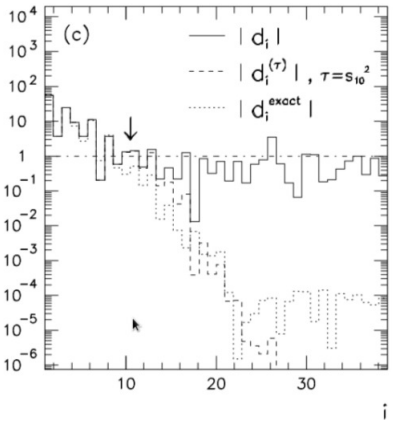

Figure 3: Illustration of $\log|d_i|$ versus i for choosing the optimal value for τ. Taken from [1].

The problem thus leads to an over-determined system of equations

$$\begin{pmatrix} \bar{\mathbb{A}} \\ \sqrt{\tau}\mathbb{C} \end{pmatrix} \vec{y} = \begin{pmatrix} \vec{\bar{b}} \\ \vec{0} \end{pmatrix}, \tag{20}$$

of which the solution is searched by the so-called *damped least squares* method. Equation (20) is rearranged by factoring out $\mathbb{C}$

$$\begin{pmatrix} \bar{\mathbb{A}}\mathbb{C}^{-1} \\ \sqrt{\tau}\mathbb{I} \end{pmatrix} \mathbb{C}\vec{y} = \begin{pmatrix} \vec{\bar{b}} \\ \vec{0} \end{pmatrix}. \tag{21}$$

By applying SVD on

$$\bar{\mathbb{A}}\mathbb{C}^{-1} = \mathbb{U}\mathbb{S}\mathbb{V}^T, \tag{22}$$

one can rewrite the regularized solution of (21) as

$$\vec{y}^{\tau} = \mathbb{C}^{-1}\mathbb{V}\vec{z}^{\tau}, \tag{23}$$

where

$$z_i^{\tau} := \frac{d_i\mathbb{S}_{ii}}{\mathbb{S}_{ii}^2 + \tau}, \tag{24}$$

and

$$\vec{d} := \mathbb{U}^T\vec{b}. \tag{25}$$

The role of τ as a regularisation term is now obvious. When $\mathbb{S}_{ii} \to 0$, z_i^{τ} stays finite. The unfolded distribution $\vec{x}$ is to be obtained by rescaling $\vec{y}^{\tau}$ by $\vec{x}^{ini.}$.

3.1. Determining the regularization parameter

According to [1], the cut-off parameter τ can be determined by plotting $\log|d_i|$ versus i as in Figure 3. The cut-off parameter is then selected to be

$$\tau = \mathbb{S}_{kk}^2 \tag{26}$$

where k is the component indicated by the arrow and $\mathbb{S}_{kk}$ is the $k-$th diagonal element of the matrix $\mathbb{S}$ from SVD. The components of d_i where statistical fluctuations dominate are random numbers following

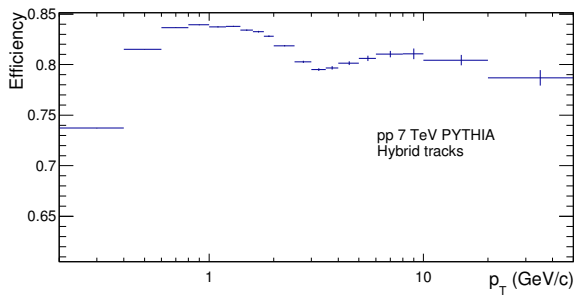

Figure 4: The efficiency of track reconstruction in the ALICE detector as a function of p_T. The track reconstruction efficiency corresponds to the so called hybrid tracks [10].

$|N(0,1)|$, where $N(0,1)$ is the normal distribution with mean 0 and standard deviation 1. If $|d_i|$ vs. i is plotted,these components fluctuate around the expectation value $E[|N(0,1)|] = \sqrt{\frac{2}{\pi}}$.

4. Simulations

A toy Monte Carlo simulaiton has been created to verify SVD unfolding. The goal is to use a reconstructed p_T spectrum of anti-k_t, charged jets and obtain the corresponding true jet p_T spectrum. Using PYTHIA 8 (v. 8.215) tune 5 [3],[4], pp collisions at $\sqrt{s} = 7$ TeV have been simulated. In the used toy Monte Carlo method, the generated particles are distorted by detector effects— reconstruction efficiency and momentum smearing. The jet clusterization routines of FastJet (v. 3.0.3)[5],[6] have been run on the PYTHIA output. The package RooUnfold [7] for the ROOT framework [8] has been used for unfolding.

The cuts used in the analysis are standard in the analyses done in the ALICE collaboration [9].

In the toy Monte Carlo simulation, the set of particles is duplicated. One set will remain unchanged (true particles) while the other is distorted (reconstructed particles) in order to simulate detector effects (reconstruction efficiency and momentum smearing). Particles "reconstructed" by the detector are called *tracks*.

An effect of the track reconstruction efficiency on a generated particle is simulated by a random removal of particles according to the measured track reconstruction efficiency vs. track p_T of the ALICE detector [10], see Figure 4. The selection algorithm is performed as follows. A random number with uniform probability distribution from the interval $[0,1]$ is generated for each track. If the number is greater than the appropriate efficiency shown in Figure 4, the track is discarded.

Furthermore, the transverse momenta of tracks are randomly distorted. The parametrization of the momentum smearing follows the paper [11]. For each track that survived the efficiency cut a random real number is generated according to the Gaussian distribution $N(0,\sigma)$ with mean 0 and standard deviation

$$\sigma = \sqrt{(0.01\, p_T)^2 + (0.007\, p_T^2)^2}. \tag{27}$$

The track p_T is then

$$p_{T,\mathrm{rec}} = p_{T,\mathrm{gen}} + N(0,\sigma), \tag{28}$$

where $p_{T,\mathrm{rec}}$ is the reconstructed transverse momentum, $p_{T,\mathrm{gen}}$ is the generated (true) transverse momentum.

After the distortions, both sets of tracks are clustered by FastJet using the anti-k_t algorithm with $R = 0.4$ using the boost-invariant p_T recombination scheme,the minimum jet constituent p_T of 150 MeV/c and restricting the jet pseudorapidity $|\eta_{\mathrm{jet}}| < 0.5$.

The sets of generated and reconstructed tracks are not identical because of the aforementioned detector effects. Therefore, the correspondence between generated and reconstructed jets is determined by minimizing a metric proportional to the angular distance of the two jets

$$\rho(\phi,\eta) = \sqrt{(\phi_{\mathrm{jet,gen}} - \phi_{\mathrm{jet,rec}})^2 + (\eta_{\mathrm{jet,gen}} - \eta_{\mathrm{jet,rec}})^2}, \tag{29}$$

where $\phi_{\mathrm{jet,gen}}$ is the azimuthal angle of the true jet, $\phi_{\mathrm{jet,rec}}$ is the azimuthal angle of the reconstructed jet, $\eta_{\mathrm{jet,gen}}$ is the pseudorapidity of the true jet and $\eta_{\mathrm{jet,rec}}$ is the pseudorapidity of the reconstructed jet.

First, for each true jet the closest (least ρ) reconstructed jet is sought. Then for each reconstructed jet the closest true jet is sought. The two jets are matched if and only if they are both the closest from the other's perspective. This eliminates the possibility that a true jet will be paired with a reconstructed jet that is closer to another true jet and vice versa.

The paired jets' transverse momenta are subsequently filled in a 2D-histogram. According to the conventions of RooUnfold, the X axis corresponds to the reconstructed jet p_T and the Y axis corresponds to the true jet p_T. A p_T spectrum of true jets is also filled to a 1D-histogram regardless if the true jet has been reconstructed or not. The procedure of the response matrix generation is illustrated by Figure 5. The resulting response matrix is depicted in Figure 6. ince the generation of a significant amount of minimum bias data to fill the response matrix would be extensively time-consuming, a different approach has been used. PYTHIA offers the option to generate collisions with constrained momentum transfer (the parameter p_T hard) which allows to gain statistics in the otherwise sparsely populated, high-p_T regions of the response matrix. This has been exploited to significantly reduce computational time.

The simulation has been split into ten consecutive intervals in p_T hard. Each interval has a fixed maximum and minimum momentum transfer. Equation 30 shows the border values of p_T hard bins (in GeV/c)

$$p_T^{\mathrm{hard}} = \{5, 11, 21, 36, 56, 84, 117, 156, 200, 249, 1000\}\,. \tag{30}$$

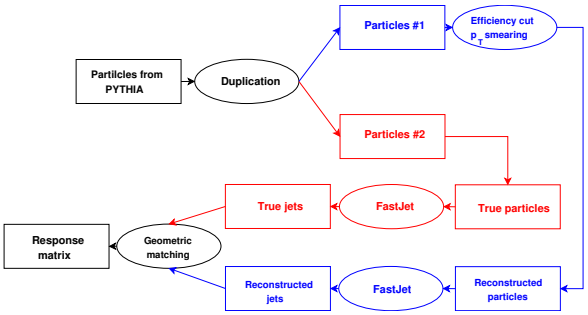

Figure 5: The scheme of the response matrix generation.

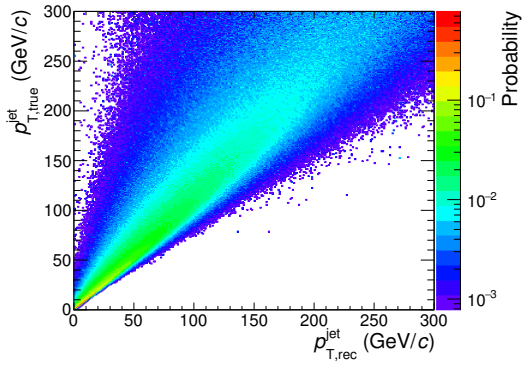

Figure 6: The response matrix of charged, anti-k_T, $R = 0.4$ jets in pp collisions at $\sqrt{s} = 7$ TeV as generated by PYTHIA 8 tune 5.

The resulting data is then added to form the response matrix. Selecting collisions with certain restrictions on p_T hard introduces an obvious bias. The bias is removed by weighting the partial response matrices for each momentum-transfer interval with an appropriate coefficient. The weighting coefficient is determined by the cross-section of the given p_T hard bin and the number of trials for each p_T hard interval according to the following equation

$$\left.\frac{d\sigma_{\text{jet}}}{dp_T^{\text{jet}}}\right|_{\text{MB}} = \sum_{p_T \text{ hard bin}} \frac{\sigma}{N_{\text{trials}}} \left.\frac{dN_{\text{jet}}}{dp_T^{\text{jet}}}\right|_{\text{pT hard bin}}, \quad (31)$$

where MB labels the minimum bias jet p_T spectrum, σ is the cross-section of the collisions in each p_T hard bin and N_{trials} is the number of events per the same p_T hard bin. Both σ and N_{trials} are calculated directly by PYTHIA.

The true and reconstructed spectra used are shown in Figure 7. SVD unfolding has been performed on these spectra using the response matrix in Figure 6. The resulting unfolded spectrum has been folded with the response matrix in order to enable comparison with the reconstructed spectrum. The refolded spectrum in comparison with the reconstructed spectrum is shown in Figure 8. Their respective ratio is plotted in Figure 9. The cut-off parameter has been chosen according to Figure 3. The five rightmost values of the d_i distribution in Figure 10 oscillate around the purple line which shows the mean of $|N(0,1)|$. The best value of k has been chosen as $k = 5$.

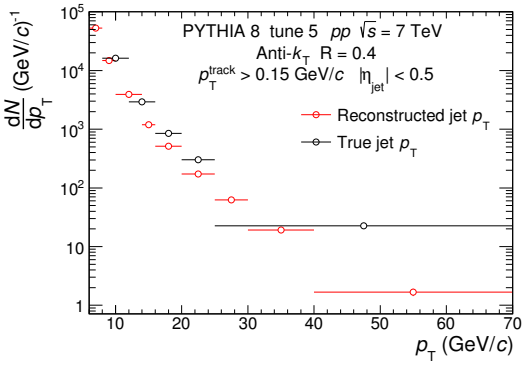

Figure 7: The inclusive p_T spectra of charged, anti-k_T, $R = 0.4$ jets in pp collisions at $\sqrt{s} = 7$ TeV as generated by PYTHIA 8 tune 5. Comparison of the true and reconstructed spectra.

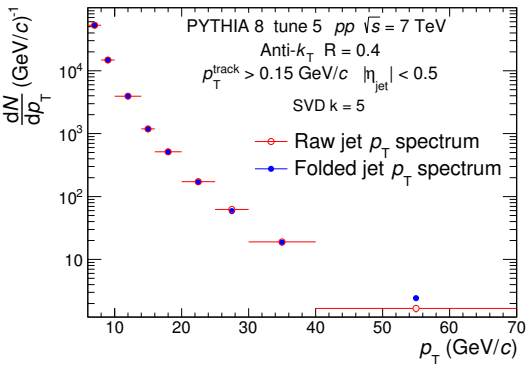

Figure 8: The inclusive p_T spectra of charged, anti-k_T, $R = 0.4$ jets in pp collisions at $\sqrt{s} = 7$ TeV as generated by PYTHIA 8 tune 5. The folded inclusive jet p_T spectrum compared to the raw jet p_T spectrum. SVD unfolding with the regularization parameter $k = 5$ has been used.

The observed differences between the true and unfolded spectra can be attributed to statistical fluctuations in the input true spectrum which are not caught by the unfolding. In general, the regularization should suppress fluctuations and smoothen the unfolded solution.

5. Conclusions

The basic idea behind unfolding with Bayesian and SVD approaches has been laid out. The results have been verified by means of a toy Monte Carlo simulation of anti-k_T jets in proton-proton collisions at $\sqrt{s} = 7$ TeV.

Acknowledgements

I would like to express my gratitude to the Nuclear Physics Institute of the CAS and to RNDr. Filip Křížek, Ph.D. for his guidence.

References

[1] A. Hocker, et al. SVD approach to data unfolding. *Nucl Instrum Meth* **A372**:469–481, 1996. `hep-ph/9509307`.

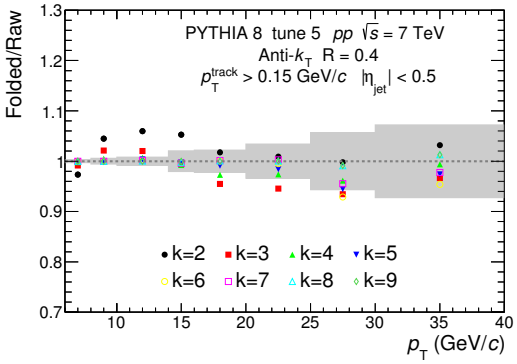

Figure 9: The inclusive p_T spectra of charged, anti-k_T, $R = 0.4$ jets in pp collisions at $\sqrt{s} = 7$ TeV as generated by PYTHIA 8 tune 5. The ratios of folded to raw spectra for various regularization parameters. The grey band represents the relative statistical errors of the raw spectrum.

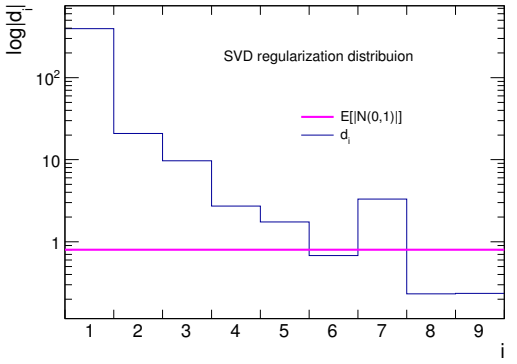

Figure 10: The distribution of the $\vec{d}$ vector components based on which the SVD regularization parameter is chosen. The spectrum was obtained by the unfolding of inclusive spectra shown in Figure 8. The purple line indicates the expectation value $E\left[\,|N(0,1)|\,\right] = \sqrt{\frac{2}{\pi}}$, where $N(0,1)$ is a normal distribution with the mean and width parameters equal to $\mu = 0$ and $\sigma = 1$ respectively. See the text for further details.

[2] G. D'Agostini. A Multidimensional unfolding method based on Bayes' theorem. *Nucl Instrum Meth* **A362**:487–498, 1995.

[3] T. Sjostrand, et al. PYTHIA 6.4 Physics and Manual. *JHEP* **05**:026, 2006. `hep-ph/0603175`.

[4] T. SjÃűstrand, et al. An Introduction to PYTHIA 8.2. *Comput Phys Commun* **191**:159–177, 2015. `1410.3012`.

[5] M. Cacciari, et al. FastJet User Manual. *Eur Phys J* **C72**:1896, 2012. `1111.6097`.

[6] M. Cacciari, et al. Dispelling the N^3 myth for the k_t jet-finder. *Phys Lett* **B641**:57–61, 2006. `hep-ph/0512210`.

[7] H. B. Prosper, et al. (eds.). *Proceedings, PHYSTAT 2011 Workshop on Statistical Issues Related to Discovery Claims in Search Experiments and Unfolding, CERN,Geneva, Switzerland 17-20 January 2011*. CERN, CERN, Geneva, 2011.

[8] R. Brun, et al. {ROOT} âĂŤ an object oriented data analysis framework. *Nuclear Instruments and Methods in Physics Research Section A: Accelerators, Spectrometers, Detectors and Associated Equipment* **389**(1âĂŞ2):81 – 86, 1997. New Computing Techniques in Physics Research V.

[9] K. Aamodt, et al. The ALICE experiment at the CERN LHC. *JINST* **3**:S08002, 2008.

[10] J. Adam, et al. Measurement of jet suppression in central Pb-Pb collisions at $\sqrt{s_{\rm NN}} = 2.76$ TeV. *Phys Lett* **B746**:1–14, 2015. `1502.01689`.

[11] K. Aamodt, et al. Transverse momentum spectra of charged particles in proton-proton collisions at $\sqrt{s} = 900$ GeV with ALICE at the LHC. *Phys Lett* **B693**:53–68, 2010. `1007.0719`.

LUMINOSITY MEASUREMENT AT HADRON COLLIDERS

Jan Pucek*

Faculty of nuclear sciences and physical engineering, Brehova 7, Prague, Czech Republic

* corresponding author: pucekjan@fjfi.cvut.cz

Abstract. In particle physics, one of the ways to study new phenomena is via collisions in particle accelerators. Every process has a characteristic called cross section, which is a probability that the process under study occurs. The cross sections are important, because they contain information about the physics involved in the given process. Experiments in particle physics involve counting the rate of occurrence of a process, which is proportional to the cross section of that process. The proportionality factor is called the luminosity and describes the rate of tries to produce the process that were performed during the experiment. There are several ways of determining the luminosity, but the one used most commonly at the LHC is the van der Meer (VdM) method. The process of a VdM scan will be described and the main inherent assumption in this method will be mentioned.

Keywords: Luminosity, VdM scan, LHC.

1. Introduction

The cross section is a physical quantity, which is well known for some processes, for others only theoretically predicted and for some other processes it is not known. Then it is down to an experiment to measure the cross section. To clarify the topic consider the following example: Imagine two regular balls, which are made to collide, the target ball with a radius R much larger than the other ball, which is thrown at the target covering all possible impact parameters. Then by using classical mechanics the cross section for this particular collision is $\sigma = \pi R^2$, which is the cross section area of the target ball. For particles like protons this is no longer valid and the cross section means something like a probability of interaction.

2. Luminosity

In this article only particle collisions at accelerators will be taken into account. To measure a cross section, the value of the luminosity is needed, because the two are linked by equation (1), where L is luminosity, σ is cross section and R is the rate of the process,

$$R = L\sigma. \tag{1}$$

2.1. Means of measuring luminosity

The most convenient method to measure luminosity would be by counting the rate of a process whose cross section is well known. The problem with this approach is that once the rate is low, the statistical error becomes too high. In other words, the process has to happen often enough to keep the errors down. For example in [1] they estimate an error of the luminosity around 1 to 3% but after using the data of one year. Many other measurements need the luminosity in smaller data samples and a process with a larger rate is needed. Unfortunately it is not known how to compute the cross section of the processes with the largest rates at the LHC. Equation (2) is for this type of measurement, where σ is an unknown cross section, σ_A is the known cross section of a process A with the rate R_A and the rate of the process with cross section σ is R,

$$\sigma = \frac{R\sigma_A}{R_A}. \tag{2}$$

Another way of measuring the luminosity is applying the optical theorem and Coulomb scattering. More about this approach can be found in [1].

Another possibility is to calculate luminosity from beam parameters. This is valid for bunched beams with number of particles n_1 and n_2, with the circulation frequency f, number of colliding bunches N and with the beam density distribution functions S_1, S_2. Formula (3) puts into relation all the parameters stated above with the luminosity,

$$L = KNfn_1n_2 \int_{-\infty}^{\infty} S_1(x,y,z,t)S_2(x,y,z,t)\mathrm{d}V\mathrm{d}t. \tag{3}$$

The volume element is dV and K is the kinematic factor which depends on the collision angle of the beams. For head-on collisions it is equal to 2c. As an example, one can calculate the luminosity for two beams that have Gaussian profiles (each with the variance in x σ_x and in y σ_y), that collide head-on,

$$L = \frac{Nfn_1n_2}{4\pi\sigma_x\sigma_y}. \tag{4}$$

The derivation of equation (4) can be found in [1]. Unlike the variables f, n, N, K the beam density distribution functions are usually unknown. A method has been developed to estimate the probability distributions, the VdM scan.

3. VdM scan

The method was invented by Simon van der Meer in 1968 [2]. It is based on creating offset in the collisions with discreet steps in two perpendicular directions. First in the x-direction and then in the y-direction, while measuring the rate of interactions detected in a given experimental setup, which will provide a reference cross section. The rate is measured by the mentioned detector setup, whose output signal is proportional to the rate of interactions. Once the dependence of rate on separation is measured, one can determine luminosity and reference cross section for the beam parameters. So during the scan and data gathering the luminosity is computed $L = \frac{N}{\sigma_{\text{ref}}}$, where N is the rate detected by the luminosity detector. More information about the VdM scans can be found in [1]

3.1. Factorisation

For the VdM scan there is one assumption. The beam density distribution functions are assumed to be factorisable in the (x,y) plane transverse to the incoming beams. This might not be true as some offset scans show otherwise [3]. The ultimate goal of the author's bachelor thesis would be to study the method used to estimate the uncertainty related to this assumption. This will be done by simulating the VdM scan numerically and applying the non-factorisation methodology to a sample where we know exactly how much non-factorisation is in the beam density functions.

3.2. Simulation benchmarking

To compare different beam shapes, one has to choose them. The factorisable beam will be a Gaussian and the non-factorisable was chosen to be double Gaussian with a correlation. The formula for 2D correlated Gaussian is given by equation (5).

$$G(x,y) = C\exp\left[-\frac{1}{2(1-\rho^2)}\left(\frac{(x-\mu_x)^2}{\sigma_x^2} + \frac{(y-\mu_y)^2}{\sigma_y^2} - \frac{2\rho\,(x-\mu_x)\,(y-\mu_y)}{\sigma_x\sigma_y}\right)\right], \quad (5)$$

where μs are the mean values in the x/y direction, σs are the standard deviations in the x/y direction, ρ is the correlation factor and C is just a scaling constant. The double Gaussian with correlation is easily written by using single Gaussian,

$$G_d = wG_1(x,y) + (1-w)G_2(x,y). \quad (6)$$

The new parameter w is a weight constant of the double Gaussian. Other parameters for double Gaussian are chosen as follows: $\overrightarrow{\mu_{G1}} = \overrightarrow{\mu_{G2}}$, $\overrightarrow{\sigma_{G1}} \neq \overrightarrow{\sigma_{G2}}$ and $\rho_{G1} \neq \rho_{G2}$, where the vectors have components x and y. This choice of distributions is favorable due to the fact of simple integration and that for these two distributions formulas already exist. At the time of writing the VdM scan simulation is not yet implemented, only projections of 2D Gaussians and 2D double Gaussians are created, as might be seen on Fig. (1) and (2).

4. Conclusions

Different approaches can be taken to measure luminosity. The most commonly used at the LHC is the VdM method. One of the problems there are today is the estimation of the uncertainty related to assuming factorisable beam distributions. On Fig. (1) correlated 2D Gaussian histograms are shown, whose mean value changes throughout the x-projection. Although this is a factorisable shape it will be used in comparison with double Gaussian model.

References

[1] G. Anders. *Absolute luminosity determination for the ATLAS experiment.* Ph.D. thesis, CERN, 2013.

[2] S. van der Meer. Calibration of the Effective Beam Height in the ISR 1968.

[3] S. N. Webb. *Factorisation of beams in van der Meer scans and measurements of the ϕ^*_η distribution of $Z \to e^+e^-$ events in pp collisions at $\sqrt{s} = 8$ TeV with the ATLAS detector.* Ph.D. thesis, Manchester U., 2015-06-01.

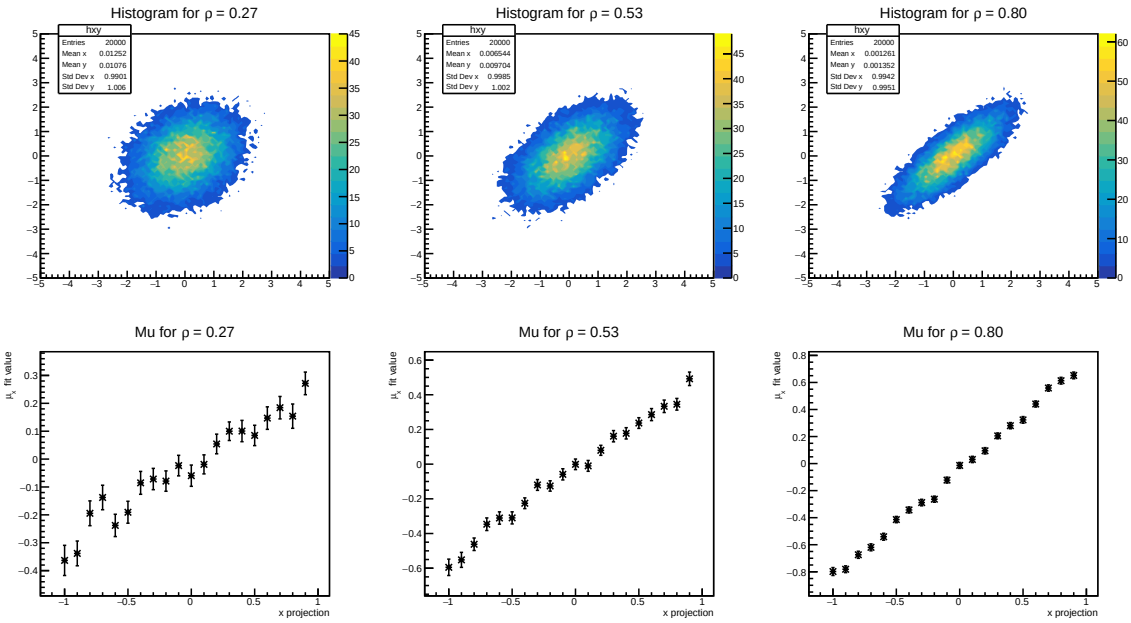

Figure 1: On top 2D Gaussians with different correlation factor. On bottom are graphs of mean values of the x-projection of the histogram on top.

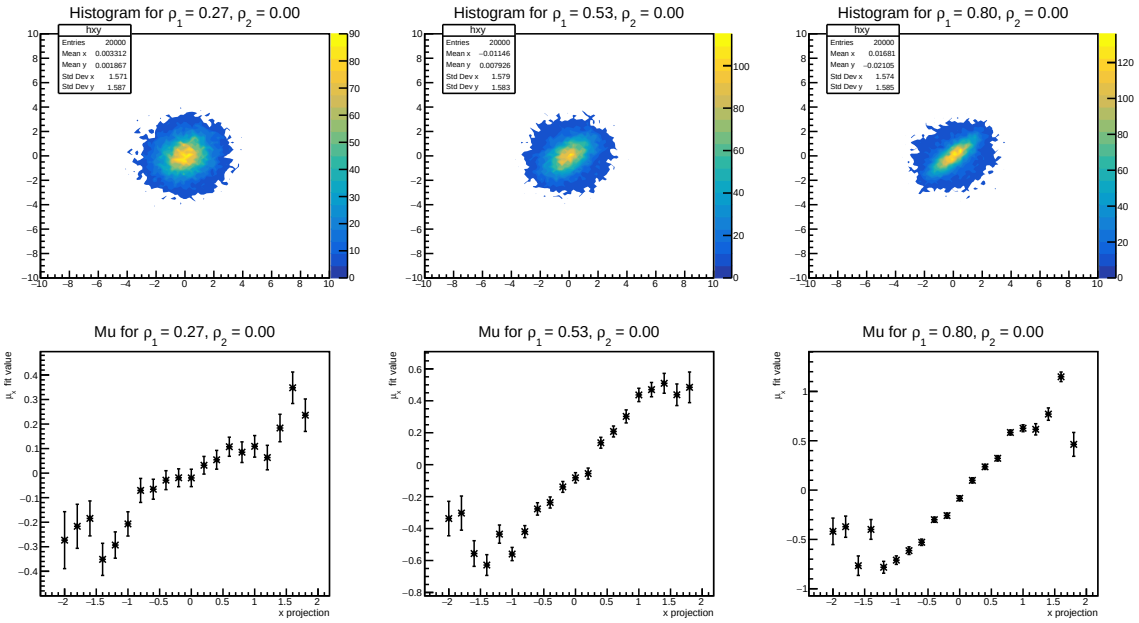

Figure 2: On top 2D double Gaussians with different correlation factor ρ_1. On bottom are graphs of mean values of the x-projection of the histogram on top.

MEASUREMENT OF PROTON FLUX FROM THE U-120M CYCLOTRON USING ACTIVATION FOILS

Valentina Raskina*

Faculty of Nuclear Sciences and Physical Engineering of CTU, Prague

* corresponding author: raskival@fjfi.cvut.cz

Abstract. The experiment ALICE at CERN plans to upgrade its Inner Tracking System detector. All electronic components which are going to be used in the new detector need to be tested whether they sustain the expected radiation load. Radiation hardness tests of new components (cables, FPGA, ...) are therefore needed. For this purpose ALICE group in the Nuclear Physics Institute of the Czech Academy of Sciences (NPI) uses proton beams provided by the isochronous cyclotron U-120M in Řež. The cyclotron provides proton beams with energies up to 35 MeV and currents up to 50 μA. On-line measurement of proton flux is based on corresponding current generated in an ionization chamber. In this paper, we discuss relation between the ionization chamber current and instantaneous proton flux measured by means of activation foils.

Keywords: Proton flux, activation foils, HPGe spectrometer, interaction of ionization radiation with matter.

1. Introduction

In 2019 to 2020, the ALICE experiment in CERN will make a major upgrade of its current Inner Tracking System detector [1] . The new detector will consist of seven coaxial layers of silicon sensors. Throughout 4 years of its operation, all electronic components of the new detector will need to sustain considerable radiation load. For instance, the expected total ionization dose for the sensors in the inner most layer is 2.7 Mrad (including a safety factor of 10). It is thus necessary to test whether all electronics of the new detector is radiation hard and meets requirements of the project proposal.

The NPI ALICE group uses for the purpose of radiation tests the U-120M cyclotron in Řež. Precise estimate of dose rate requires accurate measurement of instantaneous proton flux. For that purpose the group uses the ionization chamber PTW Farmer 30010 [2]. This paper deals with calibration of the ionization chamber response to the incoming proton flux which is assessed using activation foil technique [3].

2. Principle of the method

The activation foil technique determines flux of incoming protons by means of measuring yield of a given nuclear reaction that protons induce in a thin foil of given material. Based on the known cross section of the reaction and the measured yield, the proton flux can be calculated as

$$\Phi = \frac{Y}{\sigma\, n\, t_{\mathrm{irr}}}, \qquad (1)$$

where Y is the number of nuclei of given isotope created by reaction (p, X), σ is the reaction cross section, t_{irr} is time of irradiation and n is the number of target nuclei in the foil, which can be calculated from relation

$$n = \frac{m_{\mathrm{foil}}}{A_{\mathrm{r}} m_{\mathrm{u}}},$$

where m_{foil} is mass of the activation foil, A_{r} is relative atomic mass of given material and $m_{\mathrm{u}} = 1.66 \times 10^{-27}$ kg is the atomic mass unit [4] .

3. Experimental Set-up

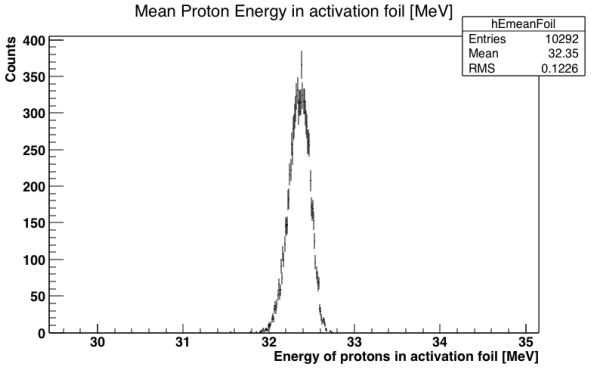

Figure 1: Distribution of proton energy in activation foil calculated using Geant4 simulation. See text for details.

The used activation foils were made of the natural copper. They had a circular shape with a radius of about 1 cm and were about 30 μm thick. The foils were irradiated at the cyclotron U-120M in Řež using proton beam with an energy of 34.8 MeV. The foils were placed approximately 130 cm from the end of cyclotron beam pipe exit window next to the ionization chamber. Since the protons travel the 130 cm distance through air they lose energy by ionization.

The expected mean proton energy in front of the activation foil was estimated by a Geant4 simulation [7] to be 32.35 MeV, see Fig. 1. Another effect of the beam passing through the air is that it gets wider due to multiple scattering. The beam profile was scanned using the ionization chamber which was placed on a movable platform. The beam profile in the transverse plane is a nearly symmetric 2D gaussian with a sigma of 12.5 mm.
The cross calibration measurement of the ionization chamber was done as follows. First the ionization chamber was placed at the beam center for about 1 min. Then the movable platform was shifted such that the activation foil went to the beam center and the ionization chamber continued to measure the proton beam intensity in the tail of the beam profile. From the known ratio between the ionization chamber current when it was at the beam center and when it moved to the tail of the beam profile we could calculate what would be the corresponding ionization current in the center of the beam. The mean value of this current was then correlated with the proton flux obtained from activation of the foil. Let us point out that the beam intensity was kept stable throughout the measurement and exhibited fluctuations of order of 5% around the mean. The gamma radiation from the activated foil was subsequently measured by the HPGe gamma spectrometer.

4. γ SPECTROMETER

The employed gamma spectrometer is a semiconductor detector made of high purity germanium. It registers energy and rate of gamma photons produced in decays of radioactive isotopes.
The peak efficiency gives the probability that an energy of a gamma photon will be fully absorbed by the detector and that it will contribute to the peak of full absorption in the measured spectrum. Peak efficiency of the HPGe spectrometer ε_{p} was estimated using the standard calibration sources ^{133}Ba, ^{152}Eu, ^{57}Co, ^{60}Co, ^{137}Cs, according to the formula

$$\varepsilon_{\mathrm{p}} = \frac{S}{AI_{\gamma}t}, \qquad (2)$$

where S is is the peak area, A is the activity of source, t is the measurement time and I_{γ} is a probability that the line was radiated in decay (table value [6]). The peak efficiency as a function of gamma energy is shown in Fig. 2.The standard calibration sources have known activity and relatively simple decay schemes.

5. CROSS SECTION

In the irradiated foils we analyzed yields of two reactions $^{nat}\mathrm{Cu(p,X)}^{62}\mathrm{Zn}$ and $^{nat}\mathrm{Cu(p,X)}^{63}\mathrm{Zn}$. The cross section of these reactions as a function of proton energy can be seen in Fig. 3 and Fig. 4. The color band gives the uncertainty on the proton energy. The

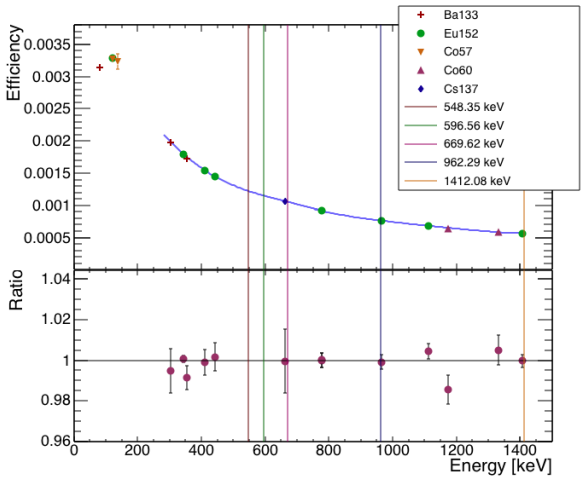

Figure 2: Top panel: Peak efficiency of the HPGe spectrometer as a function of gamma line energy. Data are fitted with a smooth function (blue line). The vertical lines correspond to gamma energies of ^{62}Zn and ^{63}Zn isotopes used in the analysis. Bottom panel: Ratio of the data to the fit.

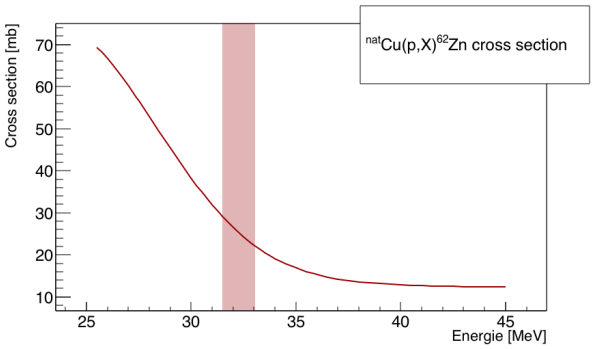

Figure 3: Cross section for reaction $^{nat}\mathrm{Cu(p,X)}^{62}\mathrm{Zn}$ as a function of proton energy. The color band indicates beam energy uncertainty [8].

distribution of proton energies in copper foil was calculated by the Geant4 simulation. The mean cross section of given reaction entering (1) was obtained by folding proton spectrum from Fig. 1 with the energy dependent cross section using

$$\overline{\sigma} = \frac{\sum k(E_i)\sigma(E_i)}{\sum k(E_i)}, \qquad (3)$$

where $k(E_i)$ is the number of protons of given energy (E_i), $\sigma(E_i)$ is cross section for given energy. The calculated mean cross sections are 25.1±1.6 mb for ^{62}Zn and 46.8±1.3 mb for ^{63}Zn.
Produced zinc isotopes have a half life of $T_{1/2}$=9.1 h for ^{62}Zn and $T_{1/2}$=38 min for ^{63}Zn and emit gamma lines 507.6 keV, 548.35 keV, 596.56 keV for ^{62}Zn and 669.62 keV, 962.06 keV, 1412.08 keV for ^{63}Zn. Yield in the corresponding peak of full absorption was evaluated using the software Genie2000 [5] as illustrated in Fig. 5.

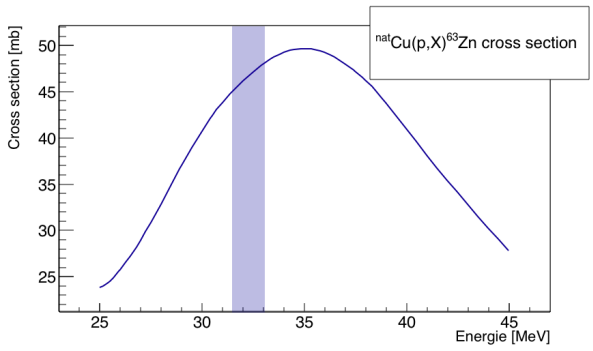

Figure 4: Cross section for reaction $^{nat}\mathrm{Cu(p,X)}^{63}\mathrm{Zn}$ as a function of proton energy. The color band indicates beam energy uncertainty [8].

6. Calculation of proton flux

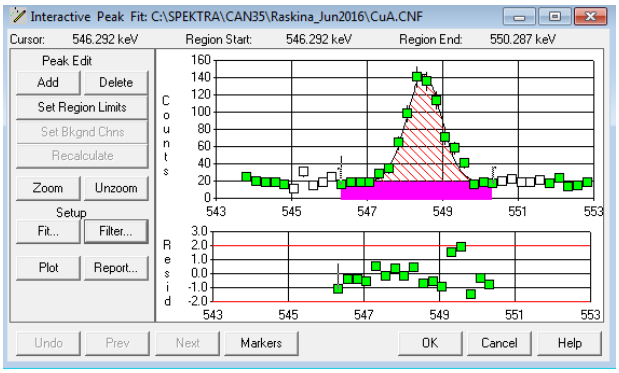

Figure 5: Gamma line of energy 548.35 keV measured by Genie2000 [5] for one of the irradiated copper foils.

The yield Y corrected for decay and detector effects can be calculated as follows

$$Y = \frac{A(E)}{I_\gamma \varepsilon_\mathrm{p}(E)} \frac{t_\mathrm{real}}{t_\mathrm{live}} \frac{\exp(\lambda t_0)}{1-\exp(-\lambda t_\mathrm{real})} \frac{\lambda t_\mathrm{irr}}{1-\exp(-\lambda t_\mathrm{irr})} \quad (4)$$

where Y is the number of nuclei of given isotope created by reaction (p,X), A is area of peak measured by spectrometer see Fig. 5, E is gamma line energy, I_γ is probability that nucleus will emit photon with energy E, ε_p is efficiency of detection of gamma photon with energy E in peak, λ is decay constant, $\lambda T_{1/2} = \ln 2$, t_real is length of measurement by gamma spectrometer, t_live is live time of spectrometer, t_irr is time of irradiation and t_0 is time from the end of irradiation to the start of measurement on HPGe spectrometer.

7. Summary and outlook

Activation foil method is used to calibrate ionization chamber which is used for proton beam monitoring during the tests of radiation hardness. Irradiated foils at cyclotron U-120M were analyzed using HPGe spectrometer. The peak efficiency of the HPGe spectrometer was calibrated with the standard calibration sources. In Fig. 6, the dependence of proton flux on ionization chamber current is shown. The full black markers illustrate proton flux measured by Timepix [2] as a function of Ionization chamber current. Data are fitted with a linear function with the slope parameter $k = (15873 \pm 378)\mathrm{pA}^{-1}\mathrm{cm}^{-2}\mathrm{s}^{-1}$. The inset figure shows the proton flux measurements done by the activation method. The same linear function is plotted. It can be seen, that the same calibration parameterization for small currents (pA) can be used for currents up to 60 nA. In future more corrections (for example $\gamma - \gamma$ coincidence and self absorption) will be added in (4) and proton flux will be calculated with added corrections.

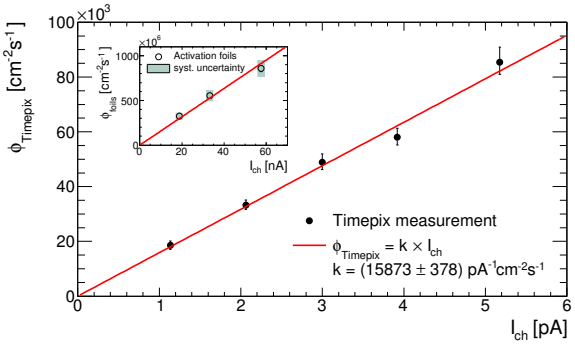

Figure 6: The dependence of proton flux on ionization chamber current fitted with a linear function with the slope parameter $k = (15873 \pm 378)\mathrm{pA}^{-1}\mathrm{cm}^{-2}\mathrm{s}^{-1}$. The inset figure shows the proton flux measurements done by the activation method.

References

[1] *ALICE, Technical Design Report for the Ugrade of the ALICE Inner Tracking System, CERN-LHCC-2013-024*

[2] K. Vysoka. *Low proton flux measurements at the U-120M cyclotron for radiation hardness studies, Thesis, FJFI 2016.*

[3] W.R.Leo. *Techniques for Nuclear and Particle Physics Experiments.* Springer, 2004.

[4] Unified atomic mass unit, `https://en.wikipedia.org/wiki/Unified_atomic_mass_unit`

[5] *Canberra Industries, Genie2000 Operations manual, 2012*

[6] Table of Radioactive Isotopes (August, 2016), `http://nucleardata.nuclear.lu.se/toi/radSearch.asp`

[7] Geant4, `http://geant4.web.cern.ch/geant4/`

[8] Nuclear Data Service, `https://www-nds.iaea.org/medical/monitor_reactions.html`

[9] L. Musilek. *Interaction of ionizing radiation with matter.* Fizmatlit 2004.

[10] V. Hnatowicz. *Handbook of nuclear data for neutron activation analysis.*

JETS AND ENERGY FLOW

Ondřej Sedláček*

CTU FNSPE, Břehová 7, Prague, Czech Republic

* corresponding author: sedlaon4@cvut.fjfi.cz

Abstract. Jets are components of almost every analysis at LHC, because of the high energies they are quite distinguishable. Since jets are in most cases traces of high energy partons it is important to study jets in accordance to understand these partons. Today the most used jet algorithm is Anti-k_T, becouse of the collinear and infrared safety in combination with fast computation time. We used monte carlo generator Pythia 8.219 and to test it we compared the results of our energy flow analysis to real data from ATLAS collected in 2010, run I. Comparsion analysis published in article: [1, 2]

Keywords: Jet, infrared safety, collinear safety, energy flow, ATLAS LHC.

1. Introduction

Firstly basic information about jets is discussed. After this, the infrared and collinear divergence is introduced with examples. Next is described the infrared and collinear safety in terms of jet algorithms and example of widely used jet algorithm $Anti - k_T$ and its properties. In the second part of this text our simulation and the results are shown with some conclusion.

2. Jet

Jets are important in particle physics. Because a jet can be seen as a distinctive flow of energy or a cone of hadrons. However the correct definition is given only by the Jet definition and the set of parameters in concrete jet algorithm. The formation of a jet occurs, when a parton in hard scattering event is given high transverse momentum. In spite of the high momentum, partons (e.g. gluons, quarks) still have color charge so we cannot observe them unbound. Therefore the partons formate hadrons from its momentum and store all of their energy into them. These hadrons can be observed and analyzed. Since invariant energy of the hadrons is negligible compared with the high transverse energy gained in scattering (~ 1 GeV), the transverse momentum of the observed hadrons gives us accurate idea of transverse momentum of the origin parton.

2.1. Infrared and collinear divergence

Infrared and collinear divergence is a problem of divergence of integrals in calculations. The infrared particles means soft or low energy particles. For example when a parton with color charge is accelerated, it emits gluons. The theory states, the infinite number of soft gluons (with low energy) is emitted. The Collinear divergence is similar, only the problem lays in collinear particles. To illustrate the problem:

$$d\sigma_{q->qg} = \frac{\alpha_s C_F}{\pi} \frac{dE}{E} \frac{d\theta}{\theta} \frac{d\phi}{2\pi} \qquad (1)$$

The cross section of quark emitting gluon [2], where α_s is coupling constant of strong interaction, C_F characteristic constant, θ angle between the original quark and emitted gluon, E energy of the emitted gluon and ϕ azimuthal angle. Here when we take in consideration all soft gluons, the formula will diverge, the same occurs when we consider all collinear particles by approaching to zero with θ.

2.2. Infrared and collinear safety of jet algorithms

Infrared safety in terms of jet algorithms refers to the influence of soft particles on the shape and number of jets.

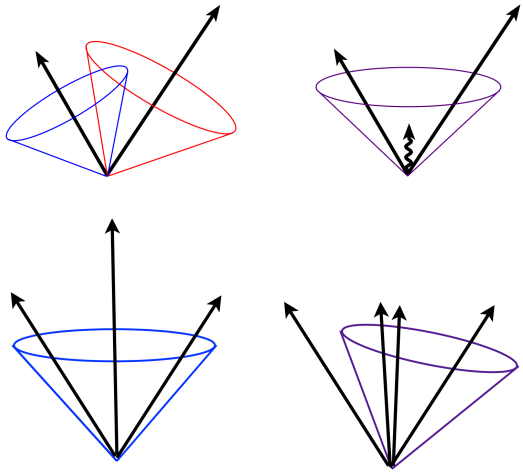

Figure.1 ilustration of the infrared and collinear unsafe algorithms [3].

As can be seen in Figure.1 the upper left, two jets correspond to the two high momentum particles. The upper right example represents infrared unsafe jet algorithm influenced by soft particle in the midle of these two high momentum particles. Collinear unsafe jet algorithm is displayed in bottom part of Figure.1. Since the shape or the number of the jets is influenced by substituting the high momentum particle with two collinear, half of the original momentum particles

2.3. Anti-k_T jet algorithm

This jet algorithm is used very often, for its good qualities. Firstly, since the sequence of the algorithm is dependent on inversed square of the transverse momentum, it prioritizes the hard particles (high energy). Therefore the Anti-k_t algorithm is infrared and collinear safe. Additionally the output is symmetric, hence it is suitable for a calibration of detectors.

3. Simulation

The monte carlo generator Pythia 8.219 was used to generate 10^6 events with central-of-mass energy 7 TeV and option SoftQCD::ALL. We analyzed the data simulated, using minimum bias events. The minimum bias events contain at least two stable, charged particles with transverse momentum greater than 250 MeV [4], in forward region of detector ($|\eta| < 2.5$ where η is pseudorapidity). We used only charged particles with momentum greater than 500 MeV and neutral particles with momentum greater than 200 MeV. Particles with lower momentum has low probability of being detected in real detector. We used mentioned cuts and compared our results with published analysis: [1]

3.1. Results

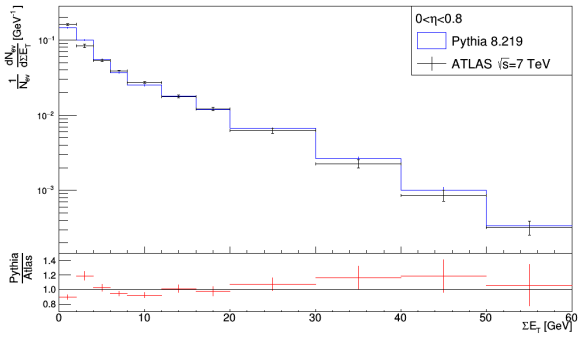

Figure 2. Energy flow in region of $|\eta| < 0.8$.

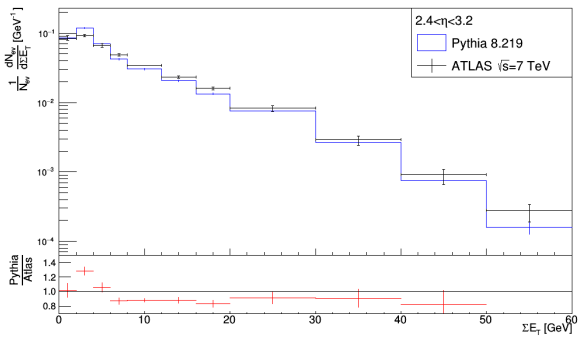

Figure 3. Energy flow in region of $2.4 < |\eta| < 3.2$.

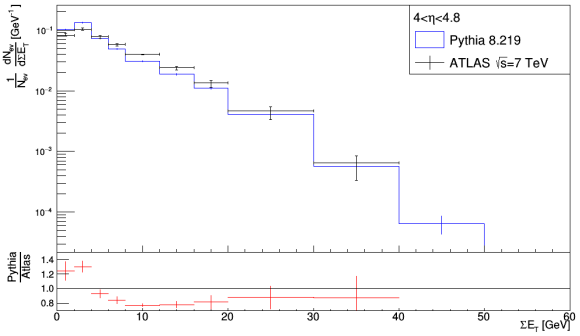

Figure 4. Energy flow in region of $4.0 < |\eta| < 4.8$.

In the Figure 2-4. the comparison of Pythia and ATLAS data can be seen. The number of events found with sum of transverse energy normalized by total number of minimum bias events is plotted against sum of transverse energy in different regions of pseudorapidity.

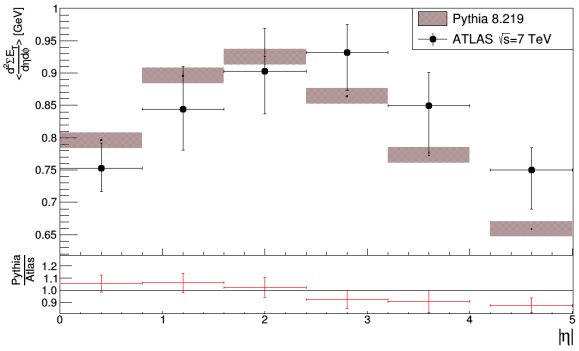

Figure 5. Density of transverse energy $E_T^{density}$

The density of transverse energy $E_T^{density}$ is computed with:

$$E_T^{density} \approx \frac{1}{N_e vent)} \frac{1}{2\Delta\eta} \frac{1}{\Delta\phi} \sum_{x<|\eta|<y} \sum E_T \qquad (2)$$

where N_{event} is number of minimum bias events, $\Delta\eta$ size of interval of pseudorapidity region and $\Delta\phi$ size of interval of azimuthal angle. The size of the interval of azimuthal angle was taken as 2π. In the Figure.5 can be seen comparison of Pythia and ATLAS data.

4. Conclusions

Starting with the most forward region in the Figure 2 of pseudorapidity, the peak is at the lowest sum of transverse energy. With moving towards next regions, Figure 3 and 4, the peak is moving to the right settling down around 4 GeV of sum of transverse energy. The analysis of density of transverse energy $E_T^{density}$, plotted in Figure 5. is most precise to the real data in region of pseudorapidity from 1.6 to 2.4. Since the Pythia with default settings agree with ATLAS data with error up to 20% as can be seen in the comparison graphs, we will use Pythia in further studies of

Jets. This results shows that reconstruction of energy flow of particles in ATLAS by monte carlo generator Pythia 8.219 is sufficient.

Acknowledgements

M.Taševský, Ph.D. my supervisor.

References

[1] C. ATLAS. Measurements of the pseudorapidity dependence of the total transverse energy in proton-proton collisions at sqrt(s) = 7 tev with atlas .

[2] O. Zaplatíle. Jet physics at lhc, 2015. Bachelor thesis, `https://physics.fjfi.cvut.cz/publications/ejcf/bp_ejcf_16_zaplatilek.pdf`.

[3] G. Soyez. Lectures: Qcd in pp collisions, 2015. `http://www.lpthe.jussieu.fr/~soyez/lectures/gsoyez_pp.pdf`.

[4] D. Bendová. Study of diffraction processes at lhc, 2016. Bachelor thesis, `https://physics.fjfi.cvut.cz/publications/ejcf/BP_Dagmar_Bendova.pdf`.

Λ_C BARYON RECONSTRUCTION IN HEAVY-ION COLLISIONS

Miroslav Simko[a,b,*]

[a] *Nuclear Physics Institute of the Czech Academy of Sciences, Na Truhlarce 39/64, Praha, Czech Republic*

[b] *Faculty of Nuclear Sciences and Physical Engineering of Czech Technical University in Prague, Brehova 7, Praha, Czech Republic*

[*] corresponding author: simko@ujf.cas.cz

Abstract. Λ_c is the lightest baryon containing a charm quark and, as such, presents a unique probe into the bahavior the hot and dense QCD medium created at RHIC and the LHC. Together with the measurement of the D^0 meson, we can probe the various modes of hadronization of the charm quark in heavy-ion collisions and bring more insight into the possible process of quark coalescense in the strongly coupled quark-gluon plasma. Λ_c baryons have an extremely small lifetime ($c\tau \sim 60\,\mu m$), therefore an extremely precise vertex detector is needed to distinguish the secondary vertices from the primary ones. The STAR Heavy Flavor Tracker (HFT) upgrade in 2014 has enabled the reconstruction of the Λ_c baryon for the first time in heavy-ion–ion collisions. At the LHC, ALICE has observed a significant signal of Λ_c in p–p and p–Pb collisions. LHCb has a unique measurement at $\sqrt{s_{NN}} = 110\,GeV$ with fixed target with a significant signal of Λ_c. The latter measurements can put constrains on the cold-nuclear-matter effects on Λ_c production. In this paper, we summarize the Λ_c measurements in A+A and p+A collisions at RHIC and the LHC, together with model predictions of the Λ_c production.

Keywords: LambdaC, STAR, ALICE, LHCb, open, charm, baryon.

1. Introduction

In ultrarelativistic heavy-ion collisions, such as the ones produced at Relativistic Heavy Ion Collider (RHIC) and the Large Hadron Collider (LHC), the charm quarks are produced in hard processes in the early stages of the system evolution right after the collision. The reason is that later, the system follows thermal behavior, in which the temperature is not high enough to produce heavy quarks such as charm. Therefore, the charm quarks experience the whole evolution of the collision and can be used as probes of the hot and dense nuclear matter [1].

The Λ_c baryon [2] contains the valence quarks u,d, and c, and is the lightest baryon containing the charm quark. As such, it presents a unique probe into the behavior of the, so called, strongly-coupled quark-gluon plasma (sQGP).

An enhancement of strange baryons compared to mesons has been observed in the intermediate transverse momentum (p_T) range in central heavy-ion collisions at RHIC [3] and the LHC [4]. This phenomenon is known as strange baryon enhancement and is believed to be one of the key pieces of evidence of the existence of the sQGP. This behavior can be explained via hadronization models which include quark coalescence, which is a process in which the quarks are combined to form hadrons, as compared to the quark fragmentation, in which new quarks are created from the vacuum.

The baryon enhancement observed at RHIC is demonstrated in Figure 1, in which the left-hand-side panel shows the ratio of the yield of p and $\overline{p}$ to π^+ and π^-, and the middle panel is a plot of the ratio of Λ^+ and $\overline{\Lambda}^-$ to 2-times the yield of K^0_s. An enhancement in the p_T region of $\sim$2–4 GeV/c is clearly observed in the case of the Λ baryons. The plot in the right-hand-side panel shows theoretical estimates of the ratio of the yields of Λ_c to D^0. The scenario with no coalescence is demonstrated by the green line which was produced using the PYTHIA simulator [5]. The dashed lines (Ko) show two coalescence models [6]: One where the quarks coalesce as the charm quark with a light di-quark structure and one where all three quarks coalesce. No rescattering in the hadron gas is considered in these two models. The darker gray band (Greco) indicates a model with three coalescence calculated in the framework described in [7] with the results from [8], then Λ_c and D meson diffusion are calculated, using an effective T–matrix approach [9]. Note that the denominator for this band is the sum of the yields of all D mesons ($D^{\pm}$, D^0, and $\overline{D^0}$). The light gray rectangle (SHM — Scattering with Hadronic Matter) is a model [10] with coalescence of di-quark and the c-quark. This model uses Λ_c diffusion in the hadronic matter, in which the Λ_c is allowed to change into other hadron species when scattering on other hadrons.

2. Λ_c measurements at the LHC

Λ_c has been measured at the LHC in p+A as well as p+p collisions at two experiments already: ALICE and LHCb.

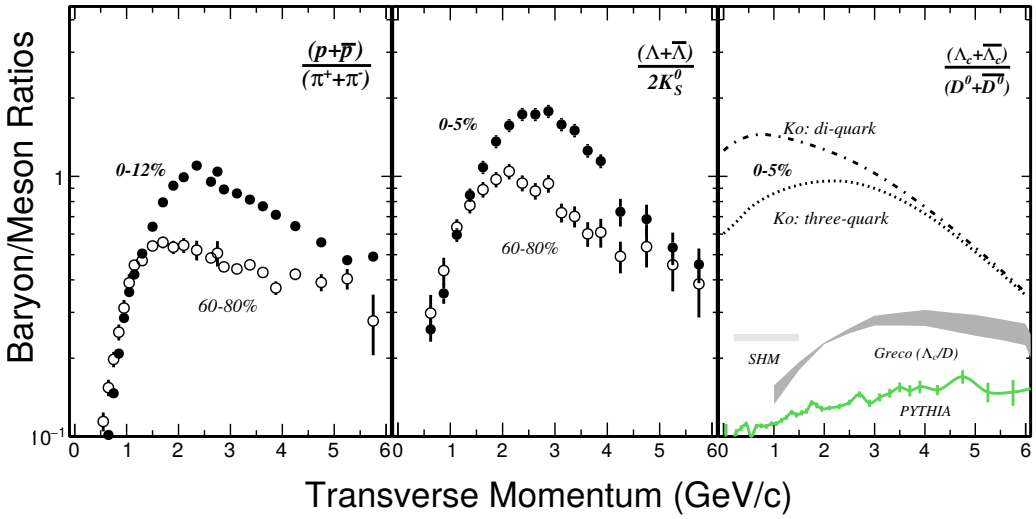

Figure 1: Baryon to meson ratio in RHIC Au+Au collisions with the center of mass energy per nucleon $\sqrt{s_{\mathrm{NN}}} = 200\,\mathrm{GeV}$ vs transverse momentum (p_{T}) [11]. Left: Ratio of the invariant yields of p and $\overline{\mathrm{p}}$ over π^+ and π^- at STAR for the centralities 0–12 % and 60–80 % [3]. Middle: ratio of the yields of Λ over $\mathrm{K}^0_{\mathrm{s}}$ at STAR for central (0–5 %) and peripheral (60–80 %) collisions. Right: Models of ratios of Λ_{c} over D^0 [6, 9, 10].

2.1. Λ_{c} at ALICE

ALICE [12] is a multipurpose detector dedicated to heavy-ion physics with excellent particle-identification (PID) capabilities. The key detectors that enable the Λ_{c} measurement are the Time-Projection Chamber (TPC) for tracking and particle identification (PID), the Time-Of-Flight (TOF) and Transition-Radiation (TRD) detectors, used for additional PID, and importantly, the Inner Tracking System (ITS) for vertexing. The ITS consists of 6 layers of silicon detectors.

The Λ_{c} were reconstructed at ALICE from the three-particle-decay channel $\Lambda_{\mathrm{c}}^{\pm} \to \pi^{\pm} + \mathrm{K}^{\mp} + \mathrm{p}^{\pm}$ with the branching ratio of 5 % with the decay length $c\tau = 60\,\mu\mathrm{m}$ [2]. Another channel $\Lambda_{\mathrm{c}}^{\pm} \to \mathrm{K}^0_{\mathrm{s}} + \mathrm{p}^{\pm}$ was analyzed at ALICE, however the resulting significance is slightly lower.

Two collision systems were analyzed [13] at ALICE: the p-p collisions at the center-of-mass energy $\sqrt{s} = 7\,\mathrm{TeV}$ and p–Pb collisions at the center-of-mass energy per nucleon $\sqrt{s_{\mathrm{NN}}} = 5.02\,\mathrm{TeV}$. For both systems, a Bayesian approach to the PID was used. A particle species is used if the probability that it is this particular particle species is the highest. Somewhat looser topological cuts for the secondary vertices were used compared to the D^0 analyses. For the p–Pb collisions, invariant mass spectra of the p+K+π triplets is shown in Figure 2. The signal can be divided into 6 bins in p_{T}. For both systems efficiency corrections are currently being calculated to obtain the p_{T} spectra.

2.2. Λ_{c} in p+A collisions at the LHCb with SMOG

The LHCb [14] is an experiment dedicated for the physics of beauty and charm which has recently joined the heavy-ion physics program. The System for Measuring Overlap with Gas (SMOG) [15] is a detection system primarily dedicated to precision luminosity measurement. It injects an inert gas (He, Ne, or Ar) with pressure of $\sim 10^{-7}$ mbar into the beam pipe to be able to perform beam-gas imaging, but this inert gas can also serve as a fixed target for the beam. The center of mass energy per nucleon can vary inside $69\,\mathrm{GeV} \leq \sqrt{s_{\mathrm{NN}}} \leq 115\,\mathrm{GeV}$ for the beam energy from 2.5 TeV to 7 TeV. So far, the Λ_{c} have been analyzed in p+Ar collisions at $\sqrt{s_{\mathrm{NN}}} = 110\,\mathrm{GeV}$.

LHCb be is a 20 m long spectrometer arm designed for forward rapidities. The Λ_{c} measurement especially benefits from the new Vertex Locator (VELO) [16] pixel detector. VELO is followed by the first RICH for PID, the main tracker, and the second RICH and calorimeters for additional PID.

Again, the decay channel $\Lambda_{\mathrm{c}}^{\pm} \to \pi^{\pm} + \mathrm{K}^{\mp} + \mathrm{p}^{\pm}$ was used [17]. The invariant mass of the pKπ triplets can be seen in Figure 3. Detector effects are still under study for the Λ_{c} spectra.

3. Λ_{c} measurements in Au+Au collisions at RHIC

The Λ_{c} baryons were measured for the first time in heavy-ion–ion collisions [11] at the STAR experiment at RHIC. STAR [18] is a multipurpose experiment with excellent particle identification capabilities that can measure particles at midrapidity in the full azimuth. In particular, the Λ_{c} measurement was enabled by the Heavy Flavor Tracker (HFT) [19] upgrade that took data in the years 2014–2016. The HFT is a vertex tracker that consists of 4 layers of silicon with a distance-of-closest-approach (DCA) of the tracks to the primary vertex resolution of $\lesssim$30 µm for high-p_{T} particles. This was allowed by the small radius of the first layer, which was placed at 2.8 cm from the center of the accelerator tube, as well as the use of the MAPS technology with excellent granularity for the two innermost layers of the HFT–Pixel detector.

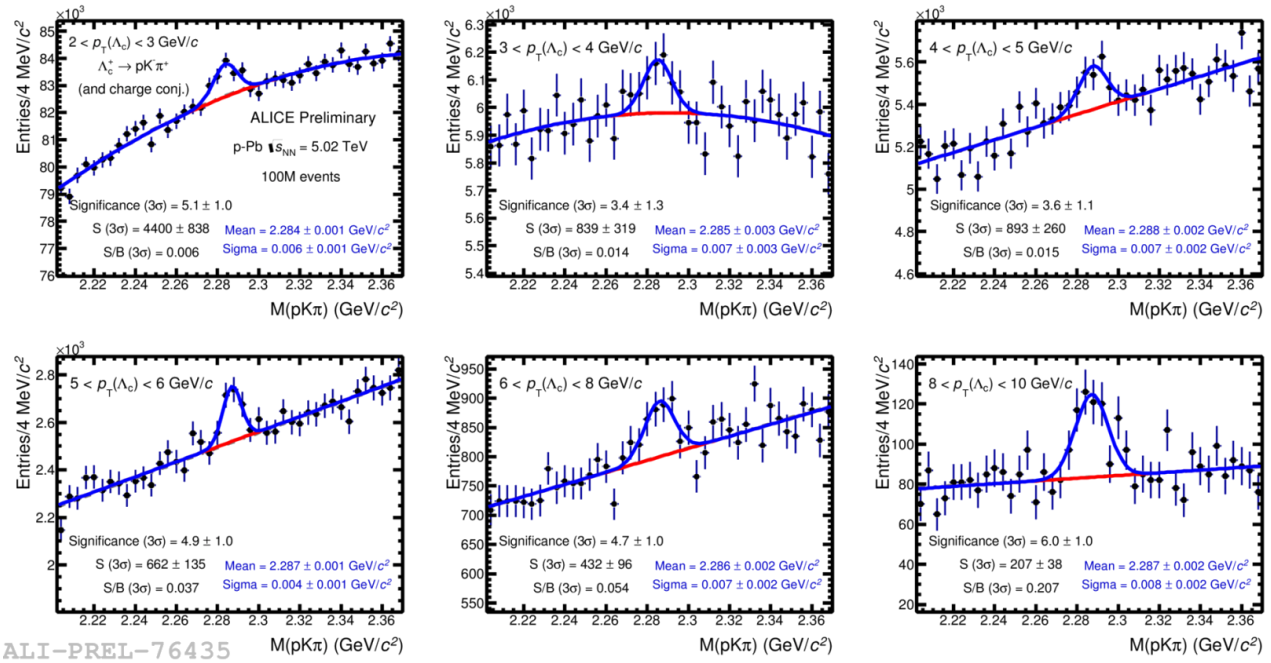

Figure 2: Invariant mass spectra of the p+K+π triplets at ALICE in p–Pb collisions at $\sqrt{s_{\mathrm{NN}}} = 5.02\,\mathrm{TeV}$ divided into p_{T} bins [13].

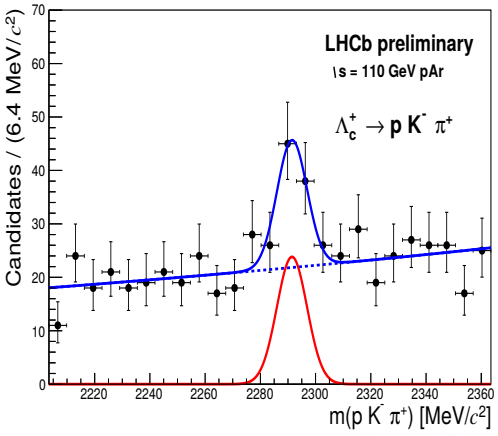

Figure 3: Invariant mass spectrum of the p+K+π triplets in p+Ar collisions with fixed target at $\sqrt{s_{\mathrm{NN}}} = 110\,\mathrm{GeV}$ at LHCb with SMOG [14].

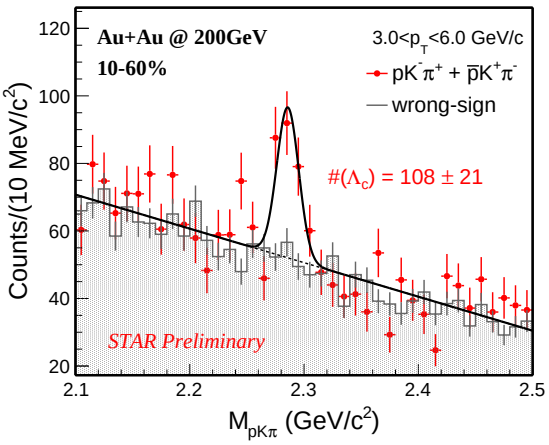

Figure 4: Invariant mass spectrum of the p+K+π triplets in Au+Au collisions with $\sqrt{s_{\mathrm{NN}}} = 200\,\mathrm{GeV}$ at centrality 10–60 % with a transverse momentum cut of $3\,\mathrm{GeV}/c < p_{\mathrm{T}} < 6\,\mathrm{GeV}/c$ [11].

For the run 2014 data, the cuts for reduction of the background were optimized via the Toolkit for Multivariate Analysis Package [20], using the simulated decayed Λ_c particles as signal and background from the measured data. This approach is needed to reduce the background enough to see the peak in the invariant mass spectrum which can be found in Figure 4. A novel data-driven approach to the simulation of the detector effects was developed for the open charm decays at STAR to reduce the computation time and decrease the systematic uncertainties coming from the simulation. Because of the limited statistics in 2014, Λ_c were only analyzed in the p_{T} region of 3–6 GeV/c for centralities of 10–60 %.

In this analysis, the efficiency corrections of the yield were done using the data-driven simulations and the systematic uncertainties were obtained by varying the cuts. The ratio of the yields of the Λ_c and D^0 was calculated from the published D^0 spectrum [21]. The resulting ratio for p_{T} of 3–6 GeV/c and centrality of 10–60 % was calculated as $N(\Lambda_c^+ + \overline{\Lambda_c}^-)/N(\mathrm{D}^0 + \overline{\mathrm{D}^0}) = 1.31 \pm 0.26(\mathrm{stat.}) \pm 0.42(\mathrm{sys.})$.

As can be seen in Figure 5, Λ_c Λ_c are clearly enhanced, compared to the D^0. The data are consistent (within 2σ) with both the di-quark and three-quark coalescence models calculated for the centralities of 0–5 % [6] and are consistent with the "Greco" [9] model calculated for minimum-bias data. Note that the centrality range is different for the the calculations and

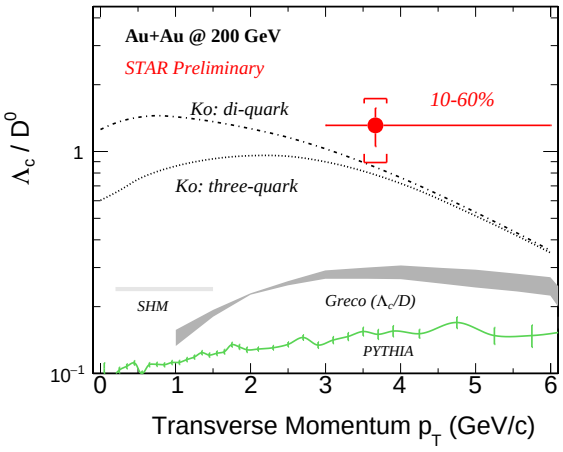

Figure 5: Ratio of the yield of Λ_c over D^0 vs p_T measured at STAR in Au+Au collisions with centrality 10–60 % [11] compared to coalescence models [6, 9, 10] — see description in text.

the data. Currently, STAR is not sensitive in the same p_T range as the "SHM" model [10].

4. Conclusions and outlook

ALICE has measurements of the Λ_c in p–p and p–Pb collisions with good significance in multiple p_T bins. The efficiency corrections and systematic uncertainties are currently being inferred.

For the LHC Run 3, ALICE is preparing a major upgrade of the TPC and, importantly, the ITS which will enable the measurement of Λ_c in Pb–Pb with high statistics.

With the SMOG instrument, LHCb was able to take novel p+Ar data at $\sqrt{s_{NN}} = 110$ GeV, in which the Λ_c were already observed with high significance.

LHCb has recently joined the heavy-ion program at the LHC and has taken high-statistics p–Pb data, in which the Λ_c is being analyzed and, in 2017, LHCb will take Pb–Pb data. As a dedicated experiment for charm and beauty analyses, LHCb can achieve high precision in the Λ_c measurements.

STAR has measured Λ_c for the first time in heavy ion–ion collisions thanks to the addition of the HFT in the years 2014–2016. The ratio of the yields of Λ_c to D^0 was calculated from the Au+Au data taken in 2014 for centralities of 10–60 %. The results point to an enhancement of the Λ_c within the measured range and are consistent within 2σ with theoretical calculations that contain quark coalescence.

STAR has recorded approximately twice more data in 2016 compared to the year 2014 with better performance of the HFT. This will allow to measure the ratio of Λ_c to D^0 in more centrality and p_T bins to put more constrain on theoretical predictions.

Acknowledgements

This work has been supported by the grant LG15001 of the Ministry of Education of the Czech Republic.

References

[1] A. Andronic, et al. Heavy-flavour and quarkonium production in the LHC era: from proton–proton to heavy-ion collisions. *Eur Phys J C* **76**:107, 2016.

[2] C. Patrignani, et al. Review of Particle Physics. *Chin Phys* **C40**:100001, 2016.

[3] G. Agakishiev, et al. Strangeness enhancement in Cu-Cu and Au-Au collisions at $\sqrt{s_{NN}} = 200$ GeV. *Phys Rev Lett* **108**:072301, 2012.

[4] B. Abelev, et al. K^0_S. *Phys Rev Lett* **111**:222301, 2013.

[5] T. Sjöstrand, et al. PYTHIA 6.4 physics and manual. *Journal of High Energy Physics* **2006**:026, 2006.

[6] Y. Oh, et al. Ratios of heavy baryons to heavy mesons in relativistic nucleus-nucleus collisions. *Phys Rev C* **79**:044905, 2009.

[7] V. Greco, et al. Quark coalescence for charmed mesons in ultrarelativistic heavy-ion collisions. *Physics Letters B* **595**:202 – 208, 2004.

[8] H. van Hees, et al. Nonperturbative heavy-quark diffusion in the quark-gluon plasma. *Phys Rev Lett* **100**:192301, 2008.

[9] S. Ghosh, et al. Diffusion of Λ_c in hot hadronic medium and its impact on Λ_c/D ratio. *Phys Rev D* **90**:054018, 2014.

[10] S. H. Lee, et al. Λ_c. *Phys Rev Lett* **100**:222301, 2008.

[11] G. Xie on behalf of the STAR collaboration. Λ_c production in Au+Au collisions at $\sqrt{s_{NN}} = 200$ GeV at STAR. *Poster and Flash talk: QUARK MATTER XXIV* 2017.

[12] K. Aamodt, et al. The ALICE experiment at the CERN LHC. *Journal of Instrumentation* **3**:S08002, 2008.

[13] R. Romita. Observation of the charm baryon Λ_c and future perspectives for measurements with the ALICE upgrade. *Poster, QUARK MATTER XXIV* 2014.

[14] A. A. Alves, et al. The LHCb Detector at the LHC. *Journal of Instrumentation* **3**:S08005, 2008.

[15] The LHCb collaboration. Precision luminosity measurements at LHCb. *Journal of Instrumentation* **9**:P12005, 2014.

[16] LHCb Collaboration. LHCb VELO Upgrade Technical Design Report. Tech. Rep. CERN-LHCC-2013-021. LHCB-TDR-013, 2013.

[17] E. Maurice on behalf of the LHCb collaboration. New high resolution measurements of open and hidden charm production in proton-nucleus collisions at $\sqrt{s} =$ 110 GeV with LHCb. *Presentation: QUARK MATTER XXIV* 2017.

[18] K. H. Ackermann, et al. STAR detector overview. *Nucl Inst Meth A* **499**:624–632, 2003.

[19] J. Kapitán. STAR inner tracking upgrade—a performance study. *Eur Phys J C* **62**:217–221, 2009.

[20] A. Hoecker, et al. TMVA: Toolkit for multivariate data analysis. *PoS* **ACAT**:040, 2007. `physics/0703039`.

[21] L. Adamczyk, et al. Observation of D^0 meson nuclear modifications in Au + Au collisions at $\sqrt{s_{NN}} = 200$ GeV. *Phys Rev Lett* **113**:142301, 2014.

THERMALISATION OF MULTIPLICITY DISTRIBUTION

Radka Sochorová*

Czech Technical University in Prague, Břehová 7, Prague, Czech Republic

* corresponding author: sochorad@fjfi.cvut.cz

Abstract. Overall observed multiplicity of different types of particles from ultrarelativistic nuclear collisions agrees with the statistical model at temperatures above 160 MeV. The phase transition temperature can be determined by lattice QCD methods. It is a temperature at which susceptibility as a function of temperature is changing fastest. This temperature is about 150 MeV. Susceptibility manifests itself in higher moments of the multiplicity distribution.

Keywords: Master equation, multiplicity distribution.

1. Introduction

Overall observed multiplicity of different types of particles from ultrarelativistic nuclear collisions agrees with the statistical model at temperatures above 160 MeV. The phase transition temperature can be determined by lattice QCD methods. It is a temperature at which susceptibility as a function of temperature is changing fastest. This temperature is about 150 MeV. Susceptibility manifests itself in higher moments of the multiplicity distribution. We would like to know how fast different moments of the multiplicity distribution approach their equilibrium value. If an ensemble starts with the multiplicity distribution out of equilibrium, the evolution of multiplicity is described by a master equation, which we shall use.

2. Master equation

Master equation is general evolution equation which is valid for an arbitrary value of $\langle N \rangle$. If we consider a binary process $a_1 a_2 \to b_1 b_2$ with $a \neq b$, eg. $\pi N \to K\Lambda$ the master equation for the probabilities P_n to find n particles has the following form

$$\frac{dP_n}{d\tau} = \epsilon \left[P_{n-1} - P_n\right] - \left[n^2 P_n - (n+1)^2 P_{n+1}\right] \quad (1)$$

where $n = 0, 1, 2, 3....$ Here

$$\epsilon = G \left\langle N_{a_1} \right\rangle \left\langle N_{a_2} \right\rangle / L, \quad (2)$$

and the dimensionless time variable τ is defined as

$$\tau = t \frac{L}{V} \quad (3)$$

so that τ is measured in units of the relaxation time $\tau_0^c = V/L$. In eq. (3) V is the volume of the reaction. In eq. (2) G is defined as $G \equiv \langle \sigma_G v \rangle$ and L as $L \equiv \langle \sigma_L v \rangle$. Here, σ_G and σ_L is momentum-averaged cross section for the gain process $a_1 a_2 \to b_1 b_2$ and for the loss process $b_1 b_2 \to a_1 a_2$, respectively. The ratio of these momentum averaged cross sections is then

$$\frac{G}{L} = \frac{d_{b_1} \alpha_{b_1}^2 K_2(\alpha_{b_1}) d_{b_2} \alpha_{b_2}^2 K_2(\alpha_{b_2})}{d_{a_1} \alpha_{a_1}^2 K_2(\alpha_{a_1}) d_{a_2} \alpha_{a_2}^2 K_2(\alpha_{a_2})} \quad (4)$$

where d_k's are degeneracy factors, $\alpha_k = \dfrac{m_k}{T}$ and K_2's are modified Bessel functions.

Equations (1), (2), (3) and (4) were taken from [1].

The master equation can be converted into the partial differential equation for generating function

$$g(x, \tau) = \sum_{n=0}^{\infty} x^n P_n(\tau). \quad (5)$$

After multiplying eq. (5) by x^n, summing over n and after some adjustments we get for equilibrium

$$x g_{eq.}^{''} + g_{eq.}^{'} - \epsilon g_{eq.} = 0. \quad (6)$$

The solution of eq. (6) is then

$$g_{eq.}(x) = \frac{I_0(2\sqrt{\epsilon x})}{I_0(2\sqrt{\epsilon})}. \quad (7)$$

The average number of $b_1 b_2$ pairs per event in equilibrium is given by

$$\langle N \rangle_{eq.} = g'_{eq.}(1) = \sqrt{\epsilon} \frac{I_1(2\sqrt{\epsilon})}{I_0(2\sqrt{\epsilon})}. \quad (8)$$

In eq. (8) we used

$$I_0^{'}(z) = I_1(z). \quad (9)$$

Equations (5), (6), (7) and (8) were taken from [2].

3. Higher factorial moments in equilibrium state

We can express higher factorial moments by the derivative of the generating function.

The second derivative of the generating function is given by

$$g_{eq.}^{''}(x) = -\frac{1}{2}\sqrt{\varepsilon} x^{-3/2} \frac{I_1(2\sqrt{\varepsilon x})}{I_0(2\sqrt{\varepsilon})} + \varepsilon \frac{1}{x} \frac{I_2(2\sqrt{\varepsilon x}) + I_0(2\sqrt{\varepsilon x})}{2 I_0(2\sqrt{\varepsilon})} \quad (10)$$

and then the equilibrium value of the second factorial moment has the form

$$\langle N(N-1)\rangle_{eq.} = g''_{eq.}(1) = -\frac{1}{2}\sqrt{\varepsilon}\frac{I_1(2\sqrt{\varepsilon})}{I_0(2\sqrt{\varepsilon})} + \frac{1}{2}\varepsilon\frac{I_2(2\sqrt{\varepsilon})+I_0(2\sqrt{\varepsilon})}{I_0(2\sqrt{\varepsilon})}. \tag{11}$$

In eq. (10) we used

$$I_1'(z) = \frac{1}{2}(I_2(z)+I_0(z)). \tag{12}$$

The third derivative of the generating function is given by

$$g'''_{eq.}(x) = \frac{3}{4}x^{-5/2}\sqrt{\varepsilon}\frac{I_1(2\sqrt{\varepsilon x})}{I_0(2\sqrt{\varepsilon})} - \frac{5}{4}\varepsilon\frac{1}{x^2}\frac{I_2(2\sqrt{\varepsilon x})+I_0(2\sqrt{\varepsilon x})}{I_0(2\sqrt{\varepsilon})} + \frac{1}{2}\varepsilon^{3/2}\frac{1}{x^{3/2}}\frac{I_3(2\sqrt{\varepsilon x})+3I_1(2\sqrt{\varepsilon x})}{2I_0(2\sqrt{\varepsilon})} \tag{13}$$

and then the equilibrium value of the third factorial moment has the form

$$\langle N(N-1)(N-2)\rangle_{eq.} = g'''_{eq.}(1) = \frac{3}{4}\sqrt{\varepsilon}\frac{I_1(2\sqrt{\varepsilon})}{I_0(2\sqrt{\varepsilon})} - \frac{5}{4}\varepsilon\frac{I_2(2\sqrt{\varepsilon})+I_0(2\sqrt{\varepsilon})}{I_0(2\sqrt{\varepsilon})} + \frac{1}{4}\varepsilon^{3/2}\frac{I_3(2\sqrt{\varepsilon})+3I_1(2\sqrt{\varepsilon})}{I_0(2\sqrt{\varepsilon})}. \tag{14}$$

In eq. (13) we used

$$I_2'(z) = \frac{1}{2}(I_3(z)+I_1(z)). \tag{15}$$

The fourth derivative of the generating function is given by

$$g^{IV.}_{eq.}(x) = \frac{3}{8}\varepsilon\frac{1}{x^3}\frac{I_2(2\sqrt{\varepsilon x})+I_0(2\sqrt{\varepsilon x})}{I_0(2\sqrt{\varepsilon})} - \frac{15}{8}\sqrt{\varepsilon}x^{-7/2}\frac{I_1(2\sqrt{\varepsilon x})}{I_0(2\sqrt{\varepsilon})} + \frac{5}{2}\varepsilon\frac{1}{x^3}\frac{I_2(2\sqrt{\varepsilon x})+I_0(2\sqrt{\varepsilon x})}{I_0(2\sqrt{\varepsilon})} - \frac{5}{8}\varepsilon^{3/2}\frac{1}{x^{5/2}}\frac{I_3(2\sqrt{\varepsilon x})+I_1(2\sqrt{\varepsilon x})}{I_0(2\sqrt{\varepsilon})} - \frac{3}{8}\frac{1}{x^{5/2}}\frac{I_3(2\sqrt{\varepsilon x})+3I_1(2\sqrt{\varepsilon x})}{I_0(2\sqrt{\varepsilon})} + \frac{1}{8}\varepsilon^2\frac{1}{x^2}\frac{I_4(2\sqrt{\varepsilon x})+2I_2(2\sqrt{\varepsilon x})+I_0(2\sqrt{\varepsilon x})}{I_0(2\sqrt{\varepsilon})} \tag{16}$$

and then the equilibrium value of the fourth factorial moment has the form

$$\langle N(N-1)(N-2)(N-3)\rangle_{eq.} = g^{IV.}_{eq.}(1) = \frac{23}{8}\varepsilon\frac{I_2(2\sqrt{\varepsilon})+I_0(2\sqrt{\varepsilon})}{I_0(2\sqrt{\varepsilon})} - \frac{15}{8}\sqrt{\varepsilon}\frac{I_1(2\sqrt{\varepsilon})}{I_0(2\sqrt{\varepsilon})} - \varepsilon^{3/2}\frac{I_3(2\sqrt{\varepsilon})}{I_0(2\sqrt{\varepsilon})} - \frac{7}{4}\varepsilon^{3/2}\frac{I_1(2\sqrt{\varepsilon})}{I_0(2\sqrt{\varepsilon})} + \frac{1}{8}\varepsilon^2\frac{I_4(2\sqrt{\varepsilon})2I_2(2\sqrt{\varepsilon})+I_0(2\sqrt{\varepsilon x})}{I_0(2\sqrt{\varepsilon})}. \tag{17}$$

In eq. (16) we used

$$I_3'(z) = \frac{1}{2}(I_4(z)+I_2(z)). \tag{18}$$

4. Numeric solution of the master equation

4.1. Initial conditions

On one hand, one can assume that initially the probabilities P_n are distributed according to a Poisson distribution

$$P_n(\tau=0) = \frac{N_0^n}{n!}e^{-N_0}. \tag{19}$$

In this case, the factorial moments obviously start out at 1.

On the other hand, one can assume that initially there is at most one particle in given event. Then the initial conditions are

$$P_0(\tau=0) = 1-N_0, \quad P_1(\tau=0) = N_0, \quad P_n(\tau=0) = 0, n>1. \tag{20}$$

These initial conditions are called binomial. In this case, the factorial moments start at 0.

4.2. Time evolution of the factorial moments

The scaled second factorial moment is given by

$$F_2(\tau) = \langle N(N-1)\rangle / \langle N\rangle^2, \tag{21}$$

the scaled third factorial moment is then

$$F_3(\tau) = \langle N(N-1)(N-2)\rangle / \langle N\rangle^3 \tag{22}$$

and the scaled fourth factorial moment has the form

$$F_4(\tau) = \langle N(N-1)(N-2)(N-3)\rangle / \langle N\rangle^4. \tag{23}$$

4.3. Results

We let the distribution of the multiplicity evolve in time according to the master equation and the results are in the pictures 1, 2 and 3.

5. Conclusions

With the help of master equation we found out that with increasing order of the moment of the multiplicity distribution does not increase the period for which this moment acquires its equilibrium value. We used binomial and poisson initial conditions.

Acknowledgements

I would like to thank Doc. Dr. Boris Tomášik for the help with my work.

References

[1] Fluctuations of rare particles as a measure of chemical equilibration, S. Jeon, V. Koch, K. Redlich, X.-N. Wang, Nucl. Phys. A 697 (2002) 546-562

[2] Kinetic Equation with Exact Charge Conservation, C. M. Ko, V. Koch, Z. W. Lin, K. Redlich, M. Stephanov, X.-N. Wang, Phys. Rev. Lett. 86, 5438 (2001)

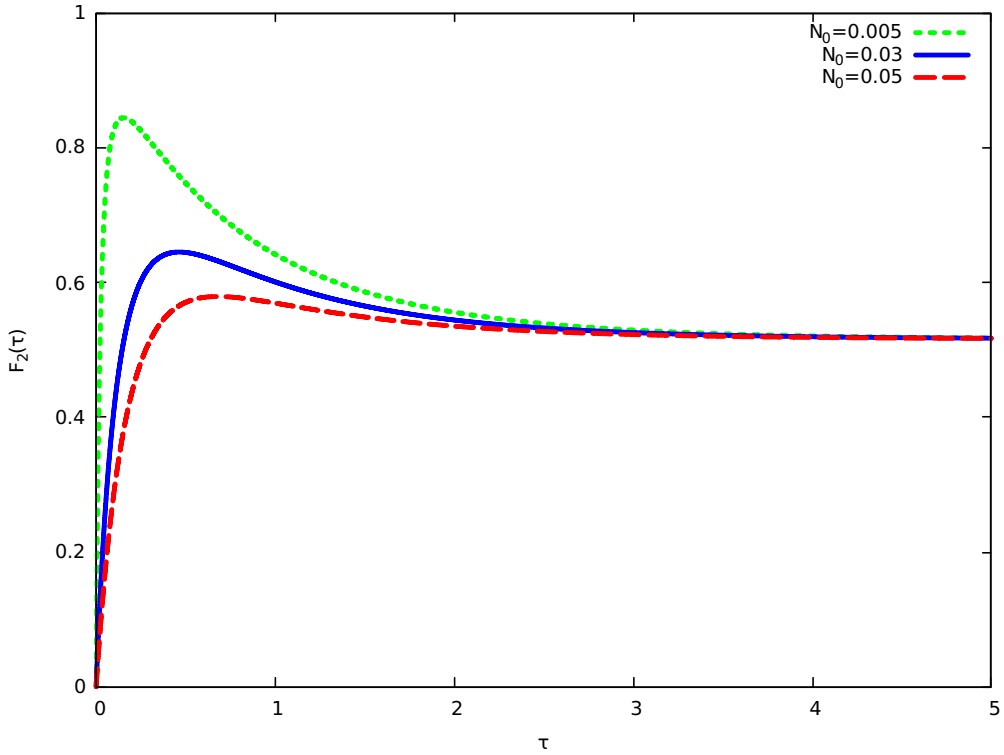

Figure 1: Time evolution of the second factorial moment for the binomial initial conditions. The second factorial moment is shown for different values of the averaged initial number of particles N_0 and for $\epsilon = 0.1$.

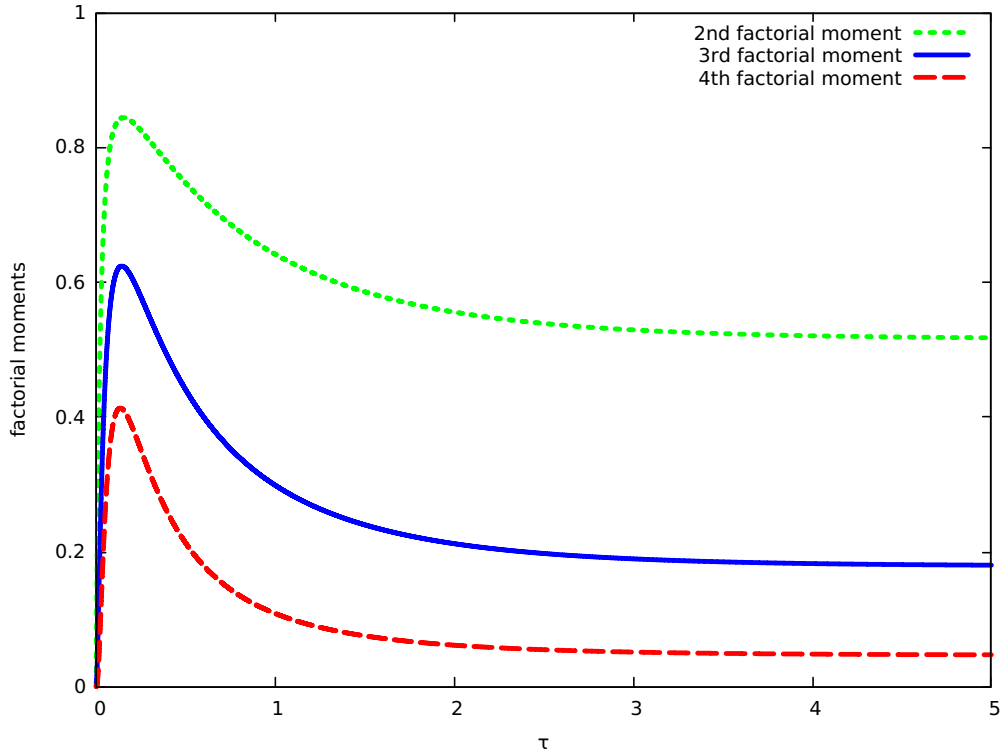

Figure 2: 2nd, 3rd and 4th factorial moment for the binomial initial conditions for $\epsilon = 0.1$ and $N_0 = 0.005$.

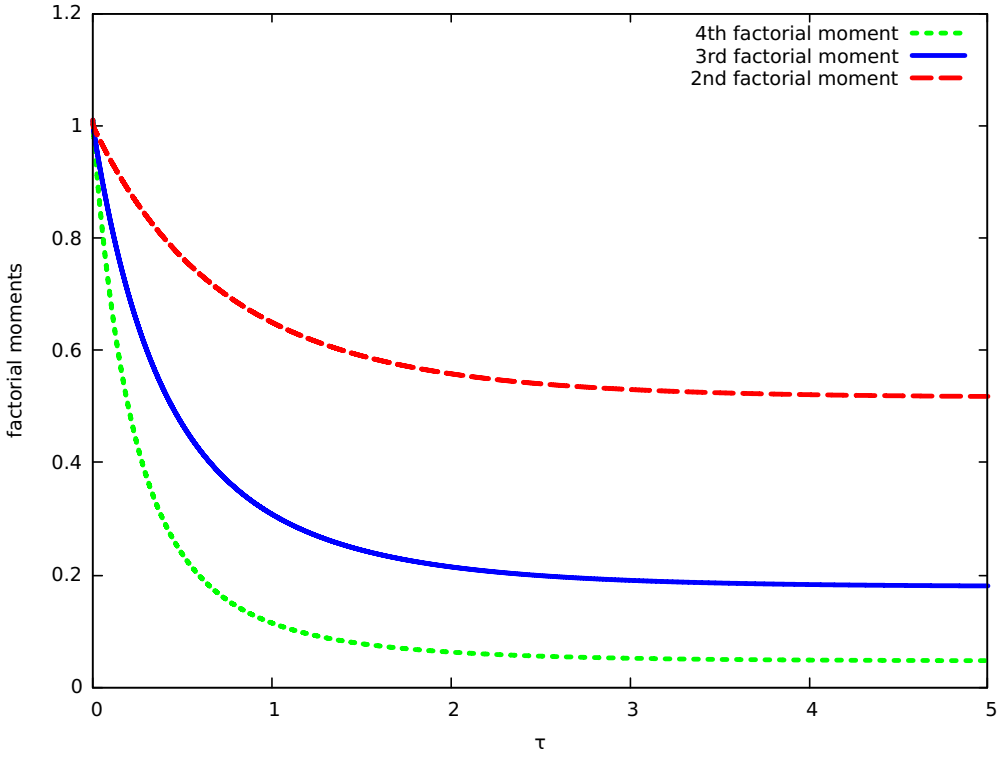

Figure 3: 2nd, 3rd and 4th factorial moment for the poisson initial conditions for $\epsilon = 0.1$ and $N_0 = 0.000009$.

DIFFRACTION AT ATLAS EXPERIMENT AT LHC

Jakub Stula*

Czech Technical University in Prague Faculty of Nuclear Sciences and Physical Engineering, Břehová 7, 115 19 Praha 1, Czech Republic

* corresponding author: stulajak@fjfi.cvut.cz

Abstract. The production of charged particles in proton-proton collisions at a centre-of-mass-energy of 13 TeV is studied at ATLAS at LHC in diffractive processes in proton-proton interaction. Comparison between Monte Carlo simulations of in detector tracks and true particles is made.

Keywords: diffraction, forward proton, ATLAS.

1. Introduction

In 2016 new detector was installed at ATLAS making possible to distinguish specific less frequent diffractive processes from the more abundant non-diffractive[1]. Therefore we can now study differences in particle production in these two kinds of a processes.

2. Description of collision

Total cross-section of an interaction can be factorized into description of individual processes in the interaction. Protons are compound particles, therefore particular partons in colliding protons can interact. Parton distribution function (PDF) describes distribution of momentum amongst partons of incident particle. Because protons are compound objects multi-parton interactions (MPI) occur and description of interaction between the two most energetic partons is not sufficient. MPI accounts for production of additional charged particles in soft interactions of the other, less energetic partons of incident protons.[2]

3. Processes in collision

In proton-proton collisions following processes are observed. In elastic collision protons do not dissociate and merely change direction of movement. Non-diffractive processes produce great numbers of additional particles, on the other hand in diffractive processes less particles are produced. Regions in rapidity without particles produced called rapidity gaps are observed. Non-diffractive processes are well established by model and MC generators, for example Pythia or Herwig, that are tuned for this purpose. However it is not known how accurately these models describe also diffractive processes.

3.1. Single diffraction

Single diffraction is a process in which transferred momentum between protons is typically small. One of the two protons looses only small fraction of momentum emitting pomeron with quantum numbers of vacuum. Fractional momentum loss is defined as $\xi = \frac{|p_b|-|p|}{|p_b|}$, where p is momentum of proton after collision and p_b is momentum of proton in beam[2]. Second proton interacts with the pomeron and dissociates into a high mass object. The first proton stays intact or dissociates to system of similar mass that therefore can be observed.

4. ATLAS detectors

For this study ATLAS forward proton (AFP) and inner tracking detector (ID) are important. Track detector measures charged particles and consists of sensor arrays at several barrel layers and end-cap discs. The whole inner detector is located inside magnetic field parallel to the beam axis. This magnetic field curves tracks of charged particles. The ID measures charge, direction and momentum of each particle. Inner detector acceptance is $|\eta| = 2.5$, i.e. the particle trajectory angle to the beam axis is larger than 0.16 rad. ATLAS is equipped with two forward proton detectors, older ALFA detects elastically scattered protons. AFP, installed in 2016, measures fractional momentum loss of protons from diffractive processes. AFP sensors are located approximately 220 m from the interaction point on both clockwise and counter-clockwise direction in close proximity of proton beam. Diffractively scattered forward protons preserve direction of movement an continue together with the proton beam trough beam pipe until separation from the proton beam by LHC dipoles and deflected upon the AFP sensor.

5. Data selection

The data are Pythia8 MC simulation. Only one proton-proton collision in every event is permitted. True particles have to be primary charged particles or products of short living particles, i.e. with mean life time at least of 300 ps. Trajectory of particle have to be inside the detector range with $|\eta| < 2.5$. Transverse momentum of particle have to be greater than 500 MeV in order for the particle to fly trough all layers of inner detector. For tracks also these requirements $|\eta| < 2.5$ and $p_T > 500$ MeV are applied and 8 hits in the track detector are also required. In order to obtain well reconstructed tracks outgoing from single

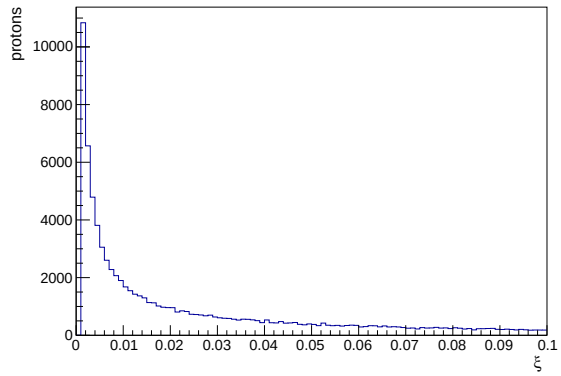

Figure 1: Fractional momentum loss of forward protons in single diffraction.

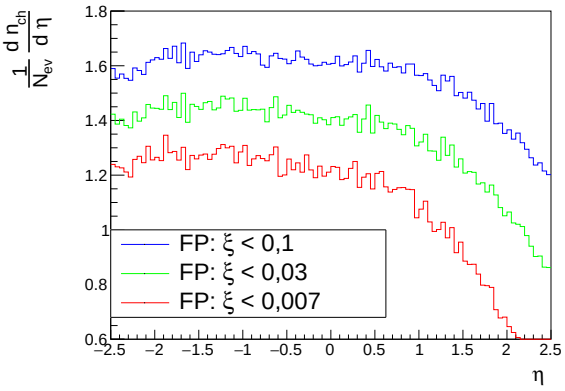

Figure 2: Comparison of multiplicity of charged particles for different fractional momentum losses of forward protons.

interaction point, the tracks comply to $|d_0| < 1.5\,\text{mm}$ and $|z_0 \sin\theta| < 1.5\,\text{mm}$, where d_0 is transversal distance to interaction point and z_0 longitudinal distance to interaction point.

6. Data

Figure 1 shows spectrum of fractional momentum loss of forward protons. In figure 2, there is a spectrum of multiplicity and in 3 are numbers of primary charged particles in comparison for different fractional momentum loss. Depending on how is the MPI implemented influences how many particles per unit of pseudorapidity are produced . In figure 4 track reconstruction efficiency in diffractive events is shown, typical efficiency is around 85% [3]. Efficiency of track reconstruction is counted as ration of true particles and true particles with track assigned in ID.

7. Conclusions

In proton-proton collisions happen soft MPI processes in the background of hard processes. In diffractive processes we observe rapidity gaps and single diffractive events can be selected using data from AFP detector.

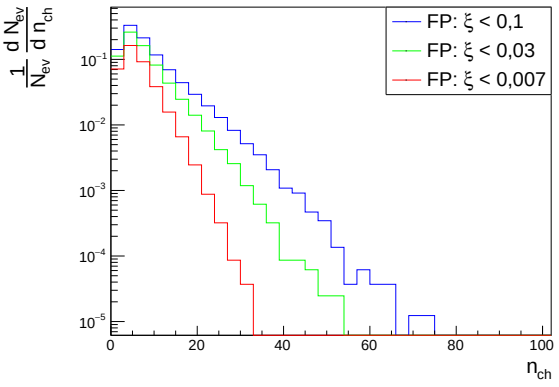

Figure 3: Comparison of total primary charged particles for different fractional momentum loss of forward proton.

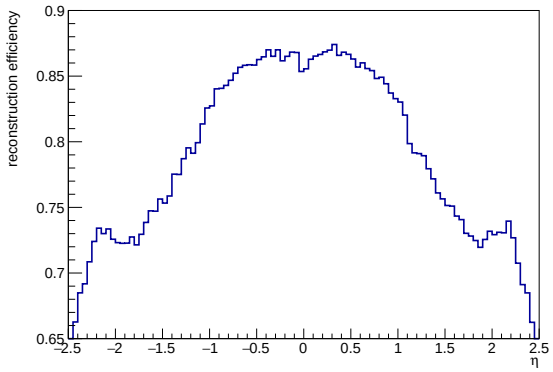

Figure 4: Efficiency of reconstruction in single diffraction events.

Comparing MC simulation and data can determine how are diffractive processes influenced by MPI.

References

[1] ATLAS Colaboration. Rapidity gap cross sections measured with the ATLAS detector in pp collisions at sqrt(s) = 7 TeV.

[2] O. Kepka, et al. *QCD and Diffraction in the ATLAS Experiment at the LHC*. Ph.D. thesis, Prague, Inst. Phys. & Orsay, Orsay, 2009. Presented on 06 Nov 2009.

[3] ATLAS Collaboration. Charged-particle distributions in $\sqrt{s}$=13 TeV pp interactions measured with the ATLAS detector at the LHC.

RUNAWAY ELECTRONS IN TOKAMAKS

Peter Svihra*

Faculty of Nuclear Sciences and Physical Engineering, CTU, Brehova 7, Prague, Czech Republic

* corresponding author: Peter.Svihra@fjfi.cvut.cz

Abstract. Discharges at tokamaks can be rapidly terminated, creating a population of electrons accelerated to high energies. These so-called runaway electrons then behave as if in the particle accelerator and can cause damage to vacuum vessel and other critical components. As the process of generation of runaway electrons is still not well understood, new diagnostic methods, such as usage of semiconductor pixel detectors, are necessary, providing spatial and temporal information about the beam.

Keywords: tokamak, COMPASS, runaway electrons, semiconductor pixel detector, Medipix2.

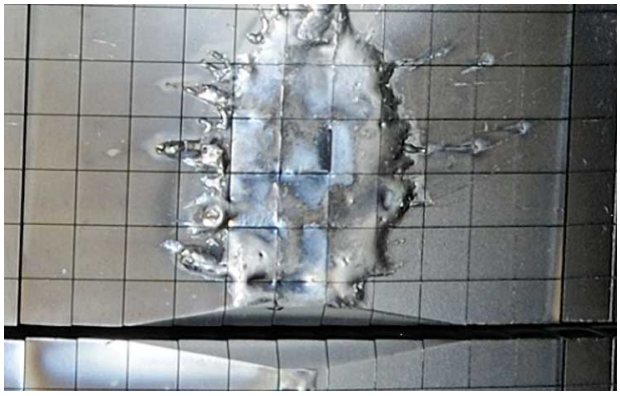

Figure 1: Re-deposited molten beryllium appears on tiles inside the JET vessel after RE experiments [1].

1. Introduction

Tokamaks (from Russian toroidal'naya kamera s magnitnymi katushkami – toroidal chamber with magnetic coils) are devices using electromagnetic induction, microwaves, accelerated neutral atoms or their combination to heat and ionize gas, and then confine it. The confinement is provided by the magnetic field, generated by the coils around the toroidally-shaped chamber, together with the field created by induced electric current in the plasma. By this process, particles receive necessary energy for thermonuclear fusion – standardly a deuterium-tritium reaction, which produces helium and neutron. For a typical tokamak plasma density, the confinement time falls within the range of a few seconds and can be terminated by disruptions.

One of the possible outcomes of a disruption is generation of electrons with high energy – so called runaway electrons (RE). Their generation at a large tokamaks can cause damage to the vacuum vessel, as shown in the figure 1. The worst case scenario is a perforation of the vacuum vessel.

Since the process is still not well understood, new diagnostic methods are needed, providing information about time and position of impact of an electron beam. Semiconductor detectors are widely used in high energy physics (HEP) as particle tracking detectors - due to their sensitivity to ionizing radiation. They can be successfully applied in new system for plasma diagnostic applications.

2. Runaway electrons

The generation of RE happens when the acceleration caused by the electric field is larger than the opposing friction force. It can occur both in space, on the Earth or in artificial plasmas. An example of the process in nature is acceleration of electrons during thunderstorms. In tokamaks this can happen when the intensity of the electric field is increased e.g. during loss of conductivity.

2.1. Derivation

Equation describing the process is derived from Fokker-Planck equation [2] . For one dimensional example, the change in the momentum of electrons is described by:

$$\frac{\mathrm{d}}{\mathrm{d}t}(mv) = eE - C_e\psi(v/v_0) \tag{1}$$

$$\psi(x) \equiv \frac{2}{\sqrt{\pi}x^2}\int_0^x \xi^2 e^{-\xi^2}\mathrm{d}\xi, \tag{2}$$

where m is electron mass, v is standard and v_0 is thermal electron velocity, e elementary electric charge, E external electric field, C_e constant, $\psi(x)$ is Chandresekhar function.

The figure 2 shows dependency of a friction force on an electron velocity. It is a combination of collisional effects (Chandresekhar function) and radiative losses, compared to the accelerating electric force eE. When the friction force is larger than the electric force (up to v_{crit}), electrons are slowed. However, when velocity reaches the critical value, they are accelerated to a pile-up zone (and not further due to the deceleration

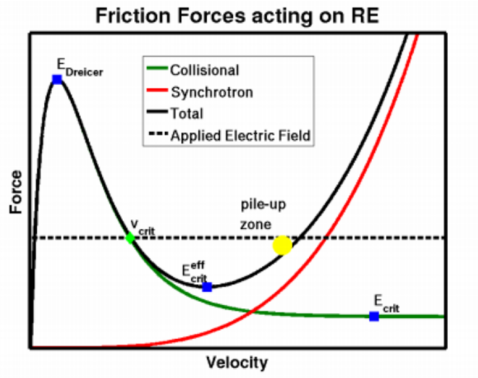

Figure 2: Friction force acting on electron depending on its velocity. Illustrated in arbitrary units according to [3].

caused by radiative processes). Moreover, the collisional force has its local maximum for small velocities in the form of Dreicer electric field E_{Dreicer} [2]

$$E_{\mathrm{Dreicer}} = \frac{n_e e^3}{4\pi\varepsilon_0^2 k T_e} \ln \Lambda. \tag{3}$$

If the intensity of electric field is larger than this value, RE are always generated.

2.2. Generation

Runaway electrons can be divided into two large groups - primary (generated by applied electric field) and secondary (mostly generated by interaction of primarily created RE with other electrons). The processes can be explained in detail on thermal Maxwellian distribution of electrons, plotted in velocity-space in figure 3.

2.2.1. Primary RE

Dreicer The most basic type of RE generation is acceleration of electrons by electric field, as described in section 2.1. Due to the diffusion processes in the velocity distribution (figure 3 top), initially slower electrons can reach the critical velocity and be severely accelerated.

Hot tail When plasma is rapidly cooled by disruptions, velocity of the bulk of the electron is decreased. Since the cooling time of plasma is much shorter than the collisional time of the fastest electrons, they are not decelerated and remain in the hot tail. Moreover, as the temperature and conductivity decrease, intensity of an electric field is increased, which gives ideal conditions for RE generation.

2.2.2. Secondary RE

Avalanche The already created RE can interact with thermal electrons, transferring part of their energy, possibly large enough to get them into the runaway region.

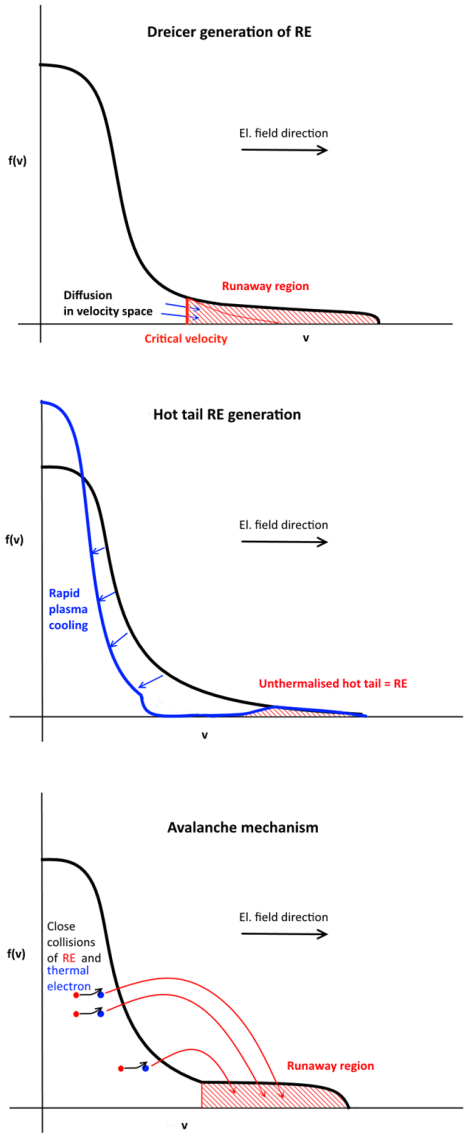

Figure 3: Types of generation processes of RE [4]. Upper figure is classic Dreicer, middle represents hot tail and lower avalanche mechanisms.

3. Semiconductor Pixel Detectors

Silicon semiconductor detectors are the most widely used type of the solid-state detectors in HEP. By doping silicon (or germanium) lattice with donors (lithium, arsenic, phosphorus) and acceptors (boron, aluminium) of electrons, $p-n$ junction is created. Around the junction, a depletion region emerges, which is sensitive to incoming ionizing radiation. The volume of this region can be increased by an applied reverse-bias voltage to the junction.

When incident ionizing particle passes through the sensor, electron-hole pairs are created in the depletion region and move along the electric field lines between $p-$ and $n-$ doped areas, in the opposite directions. These charges then arrive to the collecting electrodes where electric signal is formed and measured.

Such detectors can have detection channels in strip

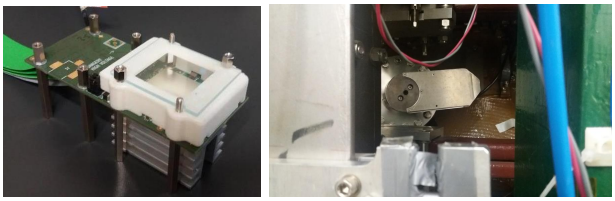

Figure 4: Medipix2 detector (left), pinhole at COMPASS port.

(sensitive lines) or pixel (sensitive matrix) configurations. Each of the detection elements (strips or pixels) is connected to an electronic circuit (micro), in which a conversion from an analog pulse to a digital signal is performed. Readout of the detector is ensured by data acquisition system which provides communication to and from computer.

3.1. Medipix2

Medipix2 is a hybrid pixel detector primarily designed for photon-counting X-ray imaging. It was developed by the Medipix collaboration which is part of the European Organization for Nuclear Research (CERN) The single chip has 256×256 pixels with size 55×55 μm^2, larger coverage area can be achieved by combination of 4 chips as is shown in the figure 4. [5]

3.1.1. Readout

Because of the need for a new and flexible interface, a CoaXPress readout has been developed. It serves as an interface between the detector and a computer, ensuring proper operation and data streaming. Its main advantage is a usage of a coaxial cable between setup and computer, which provides 100 Hz operation - maximum for the Medipix2 chip.

3.1.2. Software

As a mean of controlling the setup from computer, ASPIRE (Adapted Software for PIxel REadout) has been developed. It provides facilities for the detector calibration, data storing and further processing.

4. Results

Medipix2 was attached to a 1 cm thick lead pinhole, which was then connected to a side ports at COMPASS, see figure 4. The port was covered with a beryllium glass which, together with pinhole, should provide geometrical optics system with sufficient spatial resolution of part of the vacuum vessel. Position of the detector, together with other diagnostic types, is shown in the figure 5.

During the measurement, it was found out that the flux and the energy of gamma photons rendered low contrast of the image created by the pinhole. Moreover, large number of Compton electrons from lead shielding was observed. Due to the low contrast, the most relevant information is the temporal distribution of pixel hits.

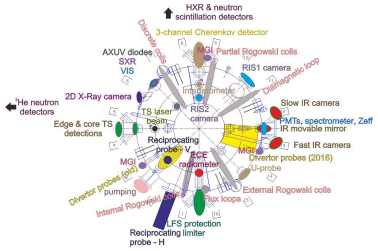

Figure 5: Types of diagnostics during RE campaign. Medipix2 is stated as a 2D X-ray camera.

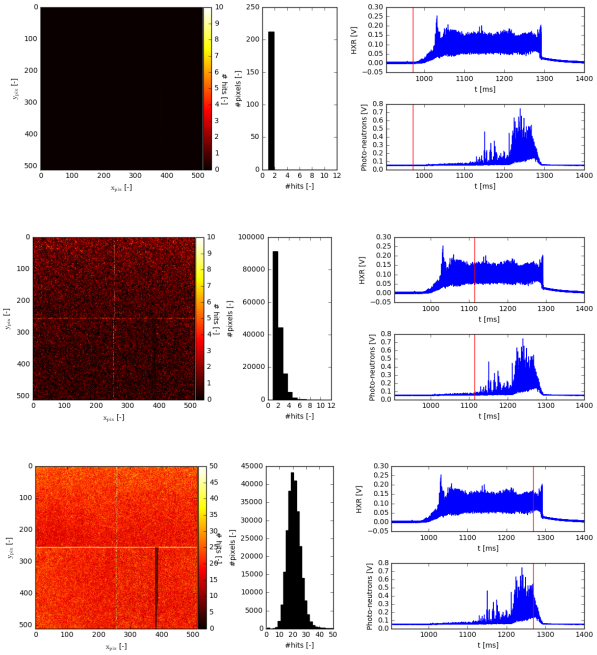

Figure 6: Time development of HXR measured by Medipix2, scintillator (upper) and photo-neutron counter (lower). Red lines represent times 982, 1125 and 1279 ms, discharge starts at 905 ms. Acquisition time per frame is 1 ms, another 10 ms is needed to process and stream data.

The output is in the figure 6, where data from Medipix2 (matrix and histogram) are compared to X-Ray data from a scintillator and from a photo-neutron detector. The preliminary data analysis shows that the number of pixel hits correlates with the acquired X-ray intensities as well as with the flux of photo-neutrons during the end of the discharge.

5. Conclusions

It is crucial that the process of RE creation is well understood as it poses a threat to large tokamaks. Application of semiconductor pixel detectors could serve as a new method of diagnostics, providing both spatial and temporal resolution throughout the plasma discharge.

Proper operation of Medipix2 with newly developed CoaXPress readout and ASPIRE software was successfully tested. Comparison of the measured data with other X-ray diagnostics looks promising, however,

detector was not able to measure significant spatial information. This was mostly due to the high flux and energy distribution of the radiation.

A planned improvement to the measurement will be a change of the position of the detector to another port, so the camera visual field will be positioned perpendicularly to the plasma column. This ensures that the detector is monitoring interaction of electrons with the inner wall. Moreover, Geant4 simulation models will be devised, and subsequent analysis of the simulations of interactions of gamma ans X-rays within the geometrical optics unit and the detector will be performed. Output of the analysis will be the optimal detector position and amount and type of shielding.

Acknowledgements

The work was supported by Technological Agency of the Czech Republic, grant No TE01020069.

References

[1] JET/UKAEA. 2015 Generating runaway electrons in jet to benefit iter. https://www.euro-fusion.org/2015/06/generating-runaway-electrons-in-jet-to-benefit-iter/.

[2] H. Dreicer. Electron and ion runaway in fully ionized gas i. *Physical Review* **115**(238), 1959. http://dx.doi.org/10.1029/2004GL019795.

[3] A. Stahl, et al. Effective critical electric field for runaway-electron generation. *Physical Review Letters* **144**(11), 2015. https://doi.org/10.1103/PhysRevLett.114.115002.

[4] O. Ficker. Generace, ztraty a diagnostika ubihajicih elektronu v tokamacich, 2015. http://physics.fjfi.cvut.cz/publications/FTTF/DP_Ondrej_Ficker.pdf.

[5] X. Llopart. *Design and characterization of 64K pixels chips working in single photon processing mode*. Ph.D. thesis, Mid Sweden University, 2007.

NON-PHOTONIC ELECTRONS RECONSTRUCTION IN HEAVY-ION COLLISIONS

Jan Vaněk*

Czech Technical University, Faculty of Nuclear Sciences and Physical Engineering, Břehová 7, Prague, Czech Republic

* corresponding author: jan.vanek@fjfi.cvut.cz

Abstract. Non-photonic electrons are electrons from semi-leptonic decay of open heavy-flavor mesons, i.e. D and B mesons. These mesons are produced in early stage of relativistic heavy-ion collisions and are used as a probe to the quark-gluon plasma which is created in later phase of such collisions. The non-photonic electrons are studied at STAR experiment in Au+Au collisions at $\sqrt{s_{NN}} = 200\,\mathrm{GeV}$. Contemporary point of interest are data collected by STAR during year 2014 when a new inner tracking system, the heavy-favor tracker, was installed into the STAR detector. The heavy-favor tracker allowed the STAR detector to be able to distinguish the D mesons from the B mesons via the NPE. STAR is for that reason able to study properties of charm and bottom quarks more thoroughly than ever before.

Keywords: Non-photonic electrons, heavy-ion collisions, open heavy-flavor mesons, quark-gluon plasma, STAR experiment.

1. Introduction

A hot and dense state of matter, the quark-gluon plasma (QGP), is studied using ultra-relativistic heavy-ion collisions by STAR experiment. Particles created in hard processes at early stage of the collision are used as a probe to the QGP. These, so called, hard probes pass through the QGP fireball, which is ignited shortly after their creation, and so carry information about the medium. Example of such particles are open heavy-flavor mesons, i.e. D mesons and B mesons.

As these mesons have short lifetime it is not possible to detect them directly, but only via their decay products. A suitable option is to use their semi-leptonic decay containing one electron (or positron), usually referred as the non-photonic electron (NPE). This choice is beneficial as STAR detector is able to detect electrons easily and it can distinguish them from other particles. In addition, the detector is equipped with advanced inner tracking system, the heavy-flavor tracker (HFT), which allows efficient background subtraction.

A brief introduction into NPE analysis using the HFT is presented in following three sections. The first section is dedicated to the STAR detector, the second summarises properties of the open heavy-flavor mesons and the third describes basic NPE analysis principles.

2. STAR detector

STAR (Solenoidal Tracker At RHIC) detector is placed at Relativistic Heavy-Ion Collider (RHIC) in Brookhaven National Laboratory, Long Island, New York. At the moment (2017) it is the only experiment at RHIC which is still taking data and it is dedicated primarily to study of relativistic heavy-ion collisions and spin structure of proton. It consists of several subdetectors which allow efficient particle identification. Only subdetectors relevant to the NPE analysis are presented in this section.

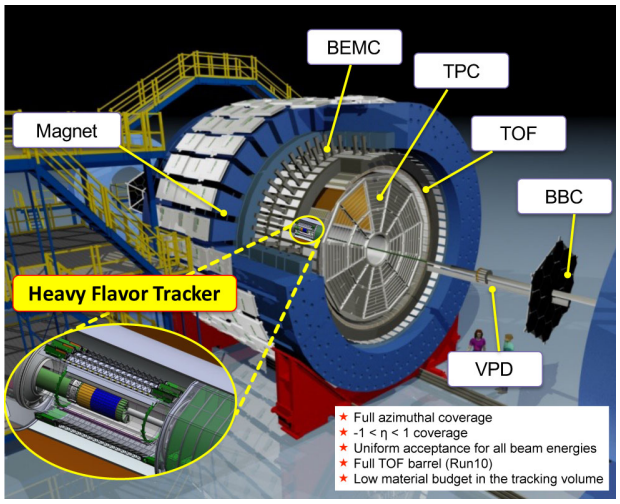

Figure 1: Scheme of the STAR detector and its subdetectors. For details see text. Taken from Ref. [1].

The scheme of the STAR detector is shown in Fig. 1. The HFT is the closest subdetector to the beam. It is a 6-layer silicon detector where two innermost layers are pixel sensors and the remaining four are strip sensors. The main purpose of the HFT is precise measurement of particles containing heavy quarks based on distinction of primary vertex, where these particles are produced, and secondary vertex, where they decay. The precision of the HFT is approximately 30 μm [2], which enables the D mesons to be distinguished from B mesons.

The next subdetector is the Time Projection Chamber (TPC). It is a large, cylindrical, gas-filled detector with MWPC (Muti-Wire Proportional Counter) readout pads. The TPC determines momentum and species of charged particles produced in heavy-ion collision. The momentum can be measured as the particle tracks are curved because of magnetic field of 0.5 T [3]. The particles are identified by their energy loss in the gas. It is the most important subdetector in STAR detector.

The last two detectors help with the particle identification. The firs one is the Time Of Flight (TOF) system. It measures speed of particles based on time difference between signal in Vertex Position Detector (VPD, see Fig. 1) and in Multigap Resistive Plate Chambers (MRPC) placed between TPC and Barrel Electro-magnetic Calorimeter (BEMC). The TOF is efficient in low p_T (transverse momentum) region. For higher momenta, the BEMC is used. It is scintillator type calorimeter with lead absorber.

Combination of these detectors provide all the required information needed to separate NPE signal from the background.

3. Open heavy-flavor mesons

Open heavy-flavor mesons are mesons containing one heavy quark. There are the D mesons containing c-quark and B mesons containing b-quark. Their properties are summarised in Tab. 1. First important point is that all open heavy-flavor mesons have large masses, which means that they are produced predominantly in hard processes of the heavy-ion collisions. The second remark is that B mesons have noticeably longer lifetime than D mesons and for that reason are distinguishable by the HFT.

Meson	M [GeV/c^2]	$c\tau$ [μm]
D^0 ($c\bar{u}$)	1.865	123
D^+ ($c\bar{d}$)	1.868	312
B^0 ($d\bar{b}$)	5.279	459
B^+ ($u\bar{b}$)	5.279	491

Table 1: Properties of open heavy-flavor mesons. Shown is their quark composition (left column), mass M (middle column) and mean lifetime τ (right column). Corresponding antiparticles (not shown) have the same properties (M and τ). Taken from Ref. [4].

Both of these mesons can decay through many decay channels. It is beneficial to select the semi-leptonic channel, more specifically that part of it, where one of the decay products is electron (or positron). First advantage of this choice is that the branching ratio is approximately 10% for all mesons listed in Tab. 1. The second advantage is that only one decay product needs to be reconstructed to obtain information about D and B mesons production in heavy-ion collisions. On the other hand, this method odes not provide information about D and B mesons kinematics. The method is therefore usable just for determination of their production.

4. NPE analysis principles

The NPE analysis at STAR experiment using the HFT has three main steps. The first one is to obtain information about displacement of primary and secondary vertex of the open heavy-flavor mesons from real data. This can be done by measuring the Distance of Closest Approach (DCA) to the primary vertex which is the shortest distance between reconstructed electron track and the primary vertex, see Fig. 2. The DCA is usually measured in plane perpendicular to the beam axis and is denoted DCA_{xy}. STAR detector is able to obtain DCA_{xy} distribution only for D and B mesons combined. To receive desired information about ratio of D and B mesons additional steps are required.

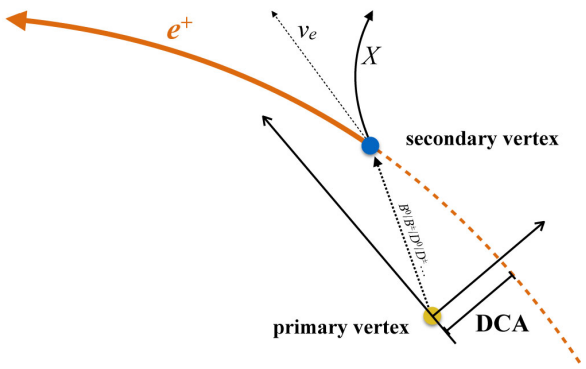

Figure 2: Scheme for illustration of the Distance of Closest Approach (DCA) to the primary vertex. Taken from Ref. [1]

The next one is to generate the DCA_{xy} distributions from simulation. To be more specific to perform so called data-driven fast simulation where acceptance and efficiency of the detector is taken into account. The simulation is performed for D and B mesons separately and also for photonic background (conversion electrons, Dalitz electros). The result of the simulation are three DCA_{xy} distributions where one is for the D mesons, one for the B mesons and one for the photonic background. Distributions simulated this way do not automatically describe experimental data. Therefore sum of the simulated distributions is fitted to distributions from data. The desired ratio of D and B mesons is than obtained from the fit.

5. Conclusions

A new method of NPE measurement is available at STAR experiment since year 2014 when a new inner tracking system was installed into the STAR detector. The method allows direct measurement of open heavy-flavor mesons, the D mesons and B mesons, via their DCA_{xy} distributions. This method should provide

very precise results with smaller statistical and systematical errors, as already proven by ALICE experiment at the LHC [5] which adopted similar procedure.

References

[1] K. OH. Measurements of charm and bottom productions in semi-leptonic channels at STAR. Poster, Quark Matter 2015 (Kobe, Japan).

[2] D. Beavis, et al. The STAR heavy flavor tracker. Technical Design Report, Version 6, 2011.

[3] K.H. Ackermann, et al. STAR detector overview. *Nuclear Instruments and Methods in Physics Research A* **499**:624–632, 2003.

[4] K. A. Olive, et al. Review of particle physics. Chin. Phys. C, 38, 090001 (2014).

[5] The ALICE Collaboration. Measurement of electrons from beauty hadron decays in pp collisions at $\sqrt{s} = 7$ TeV. CERN-PH-EP-2012-229 2013.

EXPERIMENTAL STUDY OF ELECTRIC AND OPTIC PROPERTIES OF TUBULIN AND MICROTUBULES IN VITRO AND IN VIVO

Ales Vlk*

Department of Physics, Faculty of Nuclear Sciences and Physical Engineering, Czech Technical University in Prague, Brehova 7, 115 19 Prague 1, Czech Republic

* corresponding author: alesvlk08@gmail.com

Abstract. Subject of our research are hollow cylindrically shaped filaments of cytoskeleton called microtubules. Some existing theories imply the opportunity of information storing in the structure of microtubules.
For study the information storing in microtubules, the understanding of a transport of an electrical charge in the tubulin molecules and microtubules is needed. Due to the placement of microtubules in water environment, the conductivity could be caused by electron, proton or ion flow.
From experimental point of view, we want to measure AC and DC conductivity of a dielectric layers or single molecule of tubulin and microtubule and study influence of external electric and magnetic fields a optical excitation. Last but not least, we will study an interaction of tubulin and microtubules with quantum entangled photons.

Keywords: tubulin, microtubule, dynamic instability, ferroelectricity.

1. Introduction

Microtubules are long, hollow cylindricaly shaped molecules consisting of α-,β-tubulin dimers. Mostly, they are made of 13 tubulin filaments [1], caled also protofilaments. The inner diameter of mictorubule is about 13 nm, and outer diameter is about 24 nm [2]. This values can vary with respect to type of the cell, placement of microtubule or species of an animal or a plant. Lenght of the microtubule reach values between 8 nm to tens μm. [2, 3]

2. Microtubule polymerization

Microtubules are mostly nucleated and organized by organelles called microtubule-organizing centres (MTOCs). In most cell types is the primary MTOC the censtrosome. Microtubules are nucleated from a circle made of 13 γ-tubulin dimers which is placed in the centrosome. On this γ-tubulin circle are then add α,β-tubulin dimers. This process of adding tubulin dimers is called polymerization.
Polymerization strongly depend on the concentration of tubulin dimers in solution. If the dimer concentration is greater than a critical value, the microtubules grow, but if the concentration is less than the critical, microtubules will depolimerize. This property of microtubules is called dynamic instability. [2, 3]

3. Dynamic instability

Dynamic instability is caused besides by structural differences between α- and β-tubulin molecules, concentration of tubulin dimers in solution and speed of microtubule grow.

The most important factor is presence of a GTP molecule in tubulin and its different properties in α- and β-tubulin. The GTP molecule in α-tubulin is stable, on the other hand the GTP molecule in β-tubulin can be hydrolysed. If the microtubule grow is fast enough, the GTP molecule is not hydrolysed and the microtubule grow. But, if the grow is too slow, the GTP molecule can be hydrolysed causing conformational change in the protein, which makes the protofilaments curved. This leads to a progressive disruption of the microtubule and than its depolymerization. This depolymerization can proceed until the microtubule is completely destroyed, but it can be also interrupted and the microtubule saved.
In laboratories, during measurements, the stability is needed. For this purpose is used for example substance called taxol.

4. Microtubule function

Functions of microtubules are closely related to its dynamic instability.
Microtubules serve as a transport paths for a motor proteins called dyneins and kinesins. These proteins can carry organelles, drugs and other different substances which are needed in different parts of the cell. Second function of microtubules is building of mitotic spindle, used by eukaryotic cells to distribute their chromosomes between two daughter cells.
There are some theories about the function of neuron microtubules. These theories indicate that neuron microtubules help with transmission of a signal along a neuron axon and also that they can store information. These theories are mostly founded on known

ferroelectric properties of microtubules discussed in one of the other sections.

5. Dipole moment of microtubules

One of the first observation of behavior, which indicated that microtubules have nonzero dipole moment, realized Vassilev et al. in 1982 [4]. In their experiment they polymerized microtubules in the presence of pulses of an electric field ($f = 10$ Hz and $E = 25$ mV/cm) and a constant magnetic field ($B = 0.02$ T). Microtubules polymerized under these conditions grew such that their axis of symmetry was parallel to the direction of a vector of the electric or the magnetic field intensity.

The value of the dipole moment was measured for example by Ramalho et al. in 2007 [5]. In their experiment they applied a strong electric field on microtubules, which caused their rotation. An angle, between the axis of the symmetry of a microtubule and a direction perpendicular to the direction of the vector of the applied electric field intensity, was measured. Then from the angle distribution the dipole moment of 5 μm long microtubule was calculated $p = 22661$ D (1 Debye $= 3,33564 \cdot 10^{-30}$ C·m).

6. Ferroelectric properties of microtubules

Ferroelectricity is a material property experimentaly founded in 1920 by Joseph Valasek [6]. Ferroelectric materials are characterized by a spontaneous polarization in a certain temperature interval. The critical temperature for the spontaneous polarization is called Currie temperature. Microtubules belong to ferroelectric materials and several research groups around the world study this phenomenon.

Several theoretical models of the microtubule used for study of its ferroelectric property were proposed for example by J.Tuszynski et al. [7, 8], or Slyadnikov et al. [9, 10]. These models were used for calculating the Curie (critical) temperature of microtubule with several different types of lattice.

For lattice A with 13 protofilament the Currie tempareture is $T_c \simeq 250$ K and all protofilaments are polarized in the same direction and microtubule is fully polarized. Different situation is in the case of lattice B with 13 protofilament. In this case, neighbouring protofilamets are polarized in opposite directions, however odd number of protofilaments ensure full polarization. The Currie temperature is $T \simeq 300$ K. On the other hand mictorubules with latteces 12B and 14B are completely depolarized and Currie temperature for this state is $T \simeq 550$ K.[8]

Slyadnikov et al. estimated the Currie temperature just for an infinite long microtubule with lattice 13A. The temperature is $T \simeq 317$ K.[10]

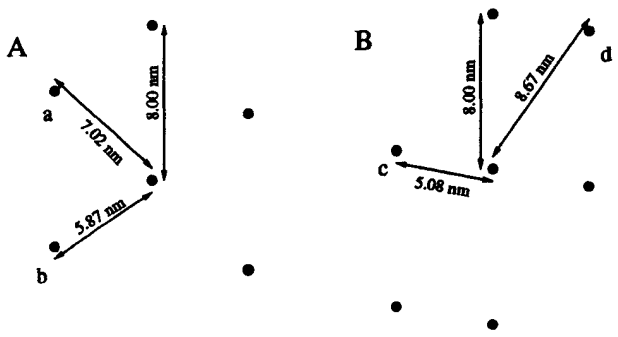

Figure 1: **Two types of microtubule lattice.** There are depicted distances between the centres of tubulin dimers in two types of lattice A and B. [8]

7. Conclusion

Microtubules are very interesting molecules with wide range of properties and potential functions, which are subjects of intensive theoretical and experimental research. In our future work we plan to study and measure some of the quantum mechanical properties of microtubules and this way test existing theories.

Acknowledgements

I want to thank to my supervisor doc. RNDr. Vojtech Petracek, CSc. for valuable advices.

References

[1] P. Dustin. *Microtubules*. Springer Science & Business Media, 2012.

[2] J. L. M. R. K. R. P. W. Bruce Alberts, Alexander Johnson. *Molecular Biology of the Cell, 5th Editon*. New York : Garland Science, 2008.

[3] A. B. et al. *Zaklady bunecne biologie*. Espero Publishing, Usti nad Labem, 1998.

[4] P. M. Vassilev, et al. Parallel arrays of microtubles formed in electric and magnetic fields. *Bioscience Reports* **2**(12):1025–1029, 1982.

[5] R. Ramalho, et al. Microtubule behavior under strong electromagnetic fields. *Materials Science and Engineering: C* **27**(58):1207 – 1210, 2007. {EMRS} 2006 Symposium A: Current Trends in Nanoscience - from Materials to Applications.

[6] J. Fousek. Joseph valasek and the discovery of ferroelectricity. In *Applications of Ferroelectrics, 1994. ISAF'94., Proceedings of the Ninth IEEE International Symposium on*, pp. 1–5. IEEE, 1991.

[7] J. Tuszyński, et al. Ferroelectric behavior in microtubule dipole lattices: implications for information processing, signaling and assembly/disassembly. *Journal of Theoretical Biology* **174**(4):371–380, 1995.

[8] J. Brown, et al. A review of the ferroelectric model of microtubules. *Ferroelectrics* **220**(1):141–155, 1999.

[9] E. Slyadnikov. Physical model and the associative memory of a cytoskeleton microtubule as a system of dipoles. *Technical Physics* **52**(7):898–906, 2007.

[10] E. Slyadnikov. Interrelation between physical and information characteristics near the point of ferroelectric transition in the dipole system of a cytoskeleton microtubule. *Technical Physics* **54**(7):927–938, 2009.

MEASUREMENT OF THE UNDERLYING EVENT AND ITS IMPACT ON TOP MASS DETERMINATION AT THE LHC

Matous Vozak [a,*], Oldrich Kepka[a,b]

[a] *Czech Technical University Faculty of Nuclear Sciences and Physical Engineering, Prague*

[b] *Institute of Physics Czech Academy of Sciences, Prague*

[*] corresponding author: matous.vozak@cern.ch

Abstract. The Large Hadron Collider, situated in Geneva, is a factory for high energy particles, currently capable of colliding protons with 13 TeV. One example of such energetic particle is a top quark with its mass around 172 GeV. As protons have an inner structure, their interaction can be viewed rather as an interplay between their constituents, quarks and gluons -collectively termed as partons, than as the whole. The top quark might emerge from a *hard interaction* between partons where a significant amount of energy is being transferred. However, the collision environment is much stirring and top quark is not the only one in the play. More particles are created in processes that "lie under" the hard interaction. These particles as well as the created top quark carry a colour charge thus might interact strongly which eventually leads to obscuring the top mass. This article contains first measurement of underlying processes at 13 TeV with the ATLAS detector, where various Monte Carlo models are compared to minimum bias data. Moreover, simulations with effects of the underlying processes on top mass reconstruction via the colour exchange were carried out and few examples are provided.

Keywords: underlying event, multi-parton interaction, initial and final state radiation, beam beam remnants, hadronization, colour reconnection.

1. Introduction

The pp collision environment is inhibited by particles from various effects which take place during the collision. These effects can represent contamination for sensitive measurement such as measurement of low energetic jet, top mass determination, etc. Therefore, in order to provide precise measurement, the study of ambient activity is necessary. Unfortunately, some of the contamination effects can not be calculated as they typically represent soft interaction (low momentum transfer) and a different approach is required in order to describe them. For this reason phenomenological models which aim to describe these phenomenas are introduced in Monte Carlo generators.

An example of the ambient effect is an initial and final state radiation (ISR, FSR) [1] of charged particles which as name suggest can take place before and after the pp collision. Another contribution is due to the fact that more parton-parton interactions can participate in the event leading to the so called multi-parton interactions (MPI) [2]. Both examples together with remnants from the beam [3] are collectively termed underlying event (UE) as they "*lie under*" the main hard scattering process.

How to address this additional activity is described in the following section 2. Next, applied event and object selection criteria are listed in section 3 continued by section about correction for the detector effects and systematic uncertainties in section 5. Examples of UE results can be viewed in section 6. In pp collisions it can occur that a string between colour charged objects reattaches to other colour charged object. This effect is called *colour reconnection (CR)* and was introduced to describe mean transverse momenta of charged particles with respect to their multiplicity CITE. Brief description of the CR phenomena can be found in a chapter 7. CR between object from the hard scattering and UE may eventually result in a shift of top mass. How can this occur and how big is the effect is the topic of section 8. Summary can be found in the section 9.

2. UE description

The analysis uses similar approach as in other previous UE measurements [4] and study UE contribution separately in three regions - toward, transverse, away. These regions are defined in azimuthal plane by taking the particle (or track on detector level) with the highest transverse momentum p_T^{lead} termed *leading particle* and measuring the difference in azimuthal angle ϕ from the particle in question 1.

- Toward region $|\Delta\phi| < \pi/3$
- Transverse region $\pi/3 < |\Delta\phi| < 2\pi/3$
- Away region $2\pi/3 < |\Delta\phi|$

The motivation is to separate the contribution of UE from the main event component. As leading particle

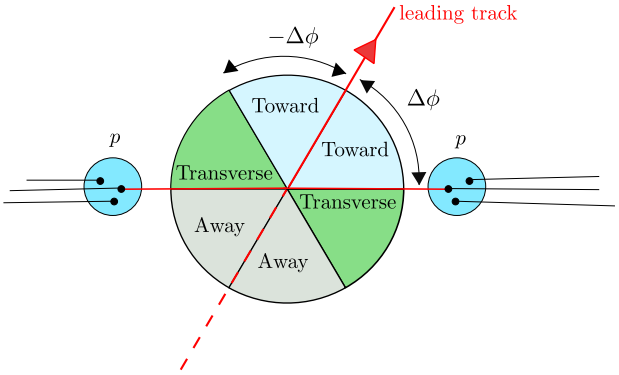

Figure 1: Sketch of plane transverse to the beam axis which is divided into three segments - toward, transverse, away, using the difference in azimuthal angle from ϕ particle/track with the highest transverse momentum called leading particle/track.

is the one coming from the hard scattering, with rising *hardness* of the scale the energy will flow, by definition, mainly in toward and away regions leaving transverse inhabited predominantly by UE.

Various observables are studied in mentioned regions in order to determine the character of UE. These observables are constructed on particle level from primary charged particles, which are charged particles with a mean lifetime $\tau > 300$ ps produced directly from a collision or particles which come from the ones that has a τ lower than 30 ps. This restriction extract strange baryons as their reconstruction significantly varies between models and posses low reconstruction probability. Particles are required to have absolute pseudorapidity η lower than 2.5 due to the ATLAS inner detector acceptance, which was the most significant part for this measurement, and also to have transverse momenta p_T higher than 500 MeV. The same phase-space selection applies for the tracks on detector level with an additional selection described later on in the following chapter. The observables are charged particle multiplicity n_{ch}, their transverse momenta p_T, scalar sum of their momenta Σp_T and their mean transverse momenta $\langle p_T \rangle$ which are plotted either with respect to the p_T^{lead} showing the raise of event hardness or with respect to the difference in azimuthal angle between particles and the event leading particle $\Delta\phi$.

3. Selection

In order to select events of interest and to reduce background effects such as reconstruction of fake tracks, contribution of cosmic radiation etc. following selections were applied.
At least one hit in a Minimum bias trigger scintillator (MBTS) on either side of the detector was required for event to be considered. Additional condition was a presence of vertex with the highest sum of p_T^2 called *primary vertex* which was reconstructed from at least two tracks with $p_T > 100$ MeV. Secondary vertex were allowed only if a number of tracks associated with the vertex was lower than 4 due to the reduction of additional pp collision termed *pile up*.
Except already mentioned kinematic requirements, only tracks with hit in the ATLAS inner pixel detectors were considered. Other selection criteria were concerning the values of transverse and longitudinal impact parameters and χ^2 probability of the track fit to suppress badly reconstructed tracks. To move from isotropic event topologies, typical for minimum bias, to more anisotropic events necessary for this measurement, p_T^{lead} was set to be > 1 GeV.

4. Correction

Observables were corrected in two steps to obtain comparison to particle level. First, tracks were multiplied by weights (*reweighted*) in order to account for detector inefficiencies (loss of particles in detector, ...) which leads to typically lesser activities. Event and track weights were constructed from vertex, trigger and track reconstruction efficiencies which are parametrized by number of selected particles with respect to beam line n_{sel}^{BL}, p_T and η.

$$w_{ev} = \frac{1}{\epsilon_{trig}(n_{sel}^{BL})} \frac{1}{\epsilon_{vtx}(n_{sel}^{BL}, \eta)} \tag{1}$$

$$w_{trk} = \frac{1}{\epsilon_{trk}(p_T, \eta)} \cdot (1 - f_{okr}(p_T, \eta) - f_{np}(p_T, \eta) - f_{sb}(p_T)) \tag{2}$$

f_i (i = okr, np, sb) given in the equation above represents fraction of tracks **o**ut of the **k**inematic **r**egion which migrated inside the studied phase space due to the detector effects, fraction of **n**on-**p**rimary tracks and fraction of **s**trange **b**aryons respectively determined from simulations. It was found out that trigger and vertex reconstruction is merely 100% thus $w_{ev} \sim 1$. On the other hand by applying track weight observables are corrected on average about 15%.
It may happen that a track with the highest momentum is not reconstructed and other track takes its place as leading track which results into the wrong region definition. *Hit backspace once more (HBOM)* [5] method was used on top of detector correction to account for this event reorientation. In principle events are subjected to additional hypothetical propagating through the detector resulting in another loss of tracks and activity. This can be done iteratively in numerous steps, where in each of them the track survival probability is based on the track reconstruction efficiency. Particle level can be achieved by extrapolation from these steps. By default 6 iteration were performed and extrapolation was done using polynomial fit of the second degree. HBOM method was applied for each observable in each bin.

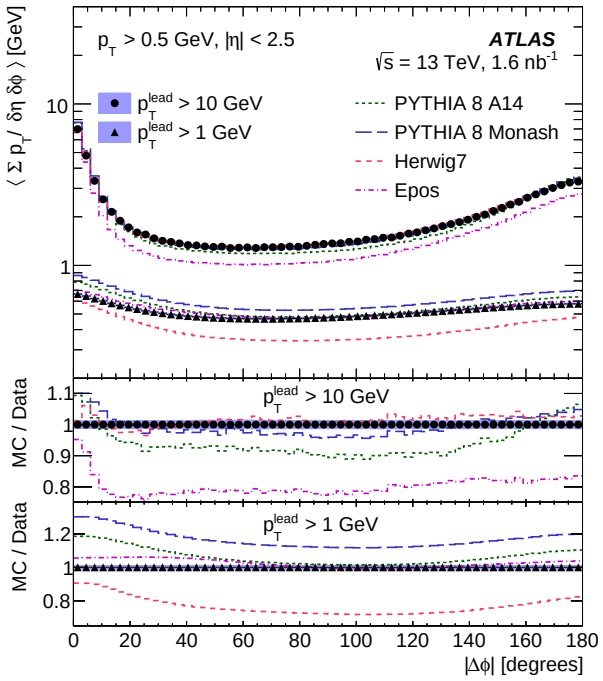

Figure 2: Scalar sum of transverse momentum Σp_T normalized by η-ϕ space plotted with respect to the difference in azimuthal angle between particles and leading particle (excluded from plot) $\Delta\phi$. Two different line shapes in the figure represent events with $p_T^{lead} > 1$, 10 GeV. Data (black dots/triangulars) are compared with given Monte Carlo generators (colour lines) with ratio plots for both p_T^{lead} cut included below the main pad [9].

5. Systematic uncertainty

Systematic uncertainties from vertex and trigger were found to be negligible. Most of the systematic from track reconstruction comes from the imperfect knowledge of material in the detector. Another contribution to systematic uncertainty comes from the estimation of non-primary tracks. The last two parts are from non-closure of HBOM spectra to particle level and parametrization (the choice of given polynomial).

6. UE results

Used data were taken at the beginning of the successful Run II of the LHC machine. Mean number of interaction per buch crossing $\langle\mu\rangle$ of the samples is 0.3-3 % and integrated luminosity L = 1.6 nb^{-1}. Data were compared to various Monte Carlo generators used by ATLAS. These include EPOS [6], Herwig7 [7] and from Pythia8 family [8] A2, A14 and Monash. Only a few examples of UE distributions are presented in here whereas the rest is provided in [9].

Energy flow in the azimuthal plane can be viewed in the Figure 2 where Σp_T is plotted against $\Delta\phi$. As can be seen, with the rising hardness scale more momenta is situated in the toward and away regions, leaving

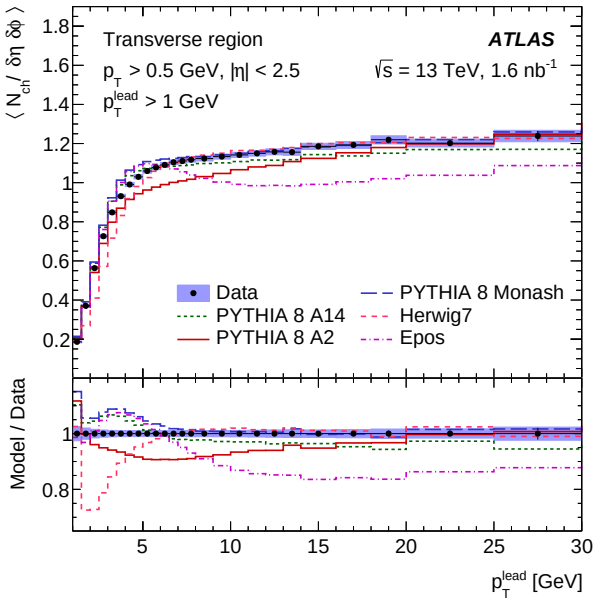

Figure 3: Number of charged particles N_{ch} normalized by η-ϕ space plotted with respect to the momentum of leading particle p_T^{lead} in the transverse region. Data (black dots/triangulars) are compared with given Monte Carlo generators (colour lines) with ratio plots below the main pad [9].

the transverse almost flat. This constant contribution in transverse region is also visible in n_{ch} distribution with respect to the p_T^{lead} Figure 3. At first there is a steep rise of the number of particles in the transverse region which stops at around 6 GeV continuing with a pedestal also called *UE plateau*. Mean number of MPI depends on an overlap integral propriety which basically tells how much the protons overlap during the interaction. If the collision is "head on" meaning the overlap integral reaches the maximum, there are no additional contribution from dominant MPI only from other sources. Therefore, an interesting observation from the measurement is that the additional activity tends to have nearly constant behavior regardless the increasing scale.

7. Colour reconnection (CR)

Colour reconnection is a term for an effect which takes place during a hadronization where all colour charged objects are combined into colour neutral objects (hadrons and mezons). One of the models which aim to describe the hadronization is the Lund string model [10] in which string between $q\bar{q}$ is fragmented into a system of hadrons.
There are several interpretation of CR effect as well. An example is to imagine decay of top quark into b quark and W which further on decays into quarks. There is a string stretched between the quarks from W as they are colour connected. If the b quark carries the same colour charge as one of the quarks from W and happens to be near them in the space-time, it can occur that the string reattaches from quark from W

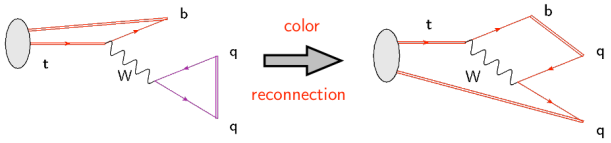

Figure 4: Sketch of colour reconnection in the system where top quark decays into b quark and W which further decays into quarks. Courtesy of S. Argyropoulos.

to b Figure 4.

CR can take place between particles inside jets but also between particles inside and outside jets. Therefore, this can lead to leakage of hadrons from the jet structure as strings may be stretched to underlying event particles outside. If we have a process where top and antitop quark are produced e.g $gg \to t\bar{t}$ and then this system decays into a semi-leptonic channel ($\bar{t} \to bW^- \to l\nu_l$ and $t \to bW^+ \to bq\bar{q}$) we can reconstruct top/antitop mass from its decay product.

$$m^2_{top} = (p(bjet) + p(q) + p(\bar{q}))^2 \quad (3)$$

$$m^2_{atop} = (p(abjet) + p(l) + p(\bar{\nu_l}))^2 \quad (4)$$

As jets are used in reconstruction, change in jet momentum due to CR affects also top mass. Nowadays CR represent one of the systematic in top mass measurement. However, to determine this systematic unrealistic models of CR are compared resulting in the underestimation the uncertainty ($\sim$ 120 MeV for ATLAS measurement [11]). In order to better estimate the uncertainty various models were introduced in Pythia8 generator.

Currently there are about 13 different models in Monte Carlo generator Pythia8 for testing the CR effect. Gluons (strings) between the models are treated differently. For example imagine two systems, the first is $t \to Wbg$ where b radiates gluon and the second is $qq \to qqg$ where one of the final quark radiates gluon as well. Now there are two systems with gluons which are colour connected to quarks Figure 5. These gluons can either exchange colour/anticolour, move completely to other system or exchange single colour index. Each scenario is described by different CR scheme. These schemes also vary in deciding which systems with gluons should be paired by CR effect. This can be done for example randomly but most of the models are based on minimalization of a certain property such as invariant mass of new created system or lambda measure [12]. Studying the spread of top mass between different schemes may lead to better estimation of the uncertainty.

8. Top mass reconstruction

Simulations of $t\bar{t}$ production were made in Pythia8 and Rivet routine [13] was used for further analyzing purposes. Only events with electrons and muons

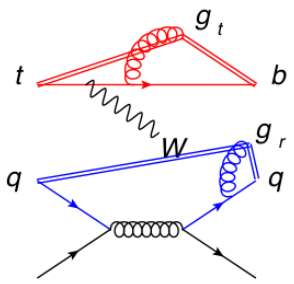

Figure 5: Sketch of two systems with gluons that are colour connected to the quarks. Courtesy of S. Argyropoulos.

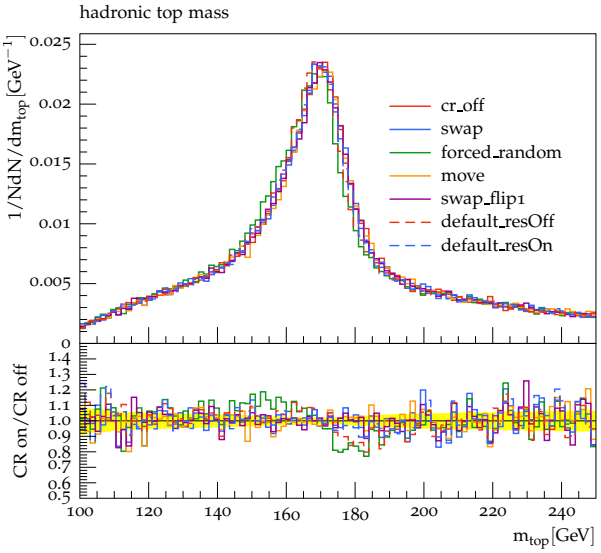

Figure 6: top mass spectrum for various colour reconnection models. Ratio plot where all models are compared to one where colour reconnection is turned off is included below the main pad.

(tau excluded) with $p_T > 25$ GeV and $|\eta| < 2.5$ were considered. Jets were reconstructed using anti-kt algorithm [14] and they were required to have $p_T > 25$ GeV and lying within $|\eta| < 2.5$.

Veto was applied on events where 1) sum of number of muon and electron neutrinos were not equal to 1 2) Jets have overlap in Δ R < 0.5 3) missing transverse energy (MET) < 30 GeV and transverse mass of W $m_T < 35$ for both muon and electron channel 4) number of b tagged jets < 2 and number of jets without b tag < 2 as well.

Example of top mass spectrum for several CR models can be seen in Figure 6 and rough estimates values with uncertainties are provided in Table 1. The spread in top mass ranges from 20 MeV up to 1 GeV (this is done already after tunning some of the CR free parameters). Currently various observables are studied including the typical ones for UE in order to find observable most sensitive to the CR. The aim is to use the observable for further constrains.

CR scheme	m_{top} [GeV]	$\lvert\Delta m_{top}\rvert$ [MeV]
CR off	170.488±0.121	
Default	169.883±0.122	605
Default ERD	170.241±0.122	246
Swap	170.555±0.122	67
Swap + flip	170.468±0.122	20
Move	170.766±0.121	278
Forced random	169.432±0.122	1056

Table 1: Examples of colour reconnection schemes with different result in top mass spectrum. The value and uncertainty of top mass is a rough estimate. The last column represents difference between a given model and model where colour reconnection is turned off.

9. Summary

Study of underlying event at 13 TeV with the ATLAS detector has been presented where several observables sensitive to this effect are analyzed in different azimuthal regions. These observables have provided information about behavior of the underlying event. It has been shown that the contribution from this additional activity tends to have flat character with increasing hard scattering component.
Furthermore, when going into harder scales where $t\bar{t}$ system can be created, colour charged objects forming jets and underlying event may interact via colour reconnection effect which eventually results in a shift of top mass. Further investigation of this effect is currently being carried out using different Pythia8 colour reconnection schemes.

Acknowledgements

I would like to thank to my supervisor Dr. Olrich Kepka for the opportunity to work on an interesting analysis during which I have gained some valuable experiences. My thanks go as well to the rest of the analysis team Dr. Deepak Kar, Dr. Andy Buckley and Dr. Roman Lysak.

References

[1] T. Sjostrand. A Model for Initial State Parton Showers. *Phys Lett* **B157**:321–325, 1985.

[2] T. Sjostrand, et al. A Multiple Interaction Model for the Event Structure in Hadron Collisions. *Phys Rev* **D36**:2019, 1987.

[3] T. Sjostrand, et al. Multiple interactions and the structure of beam remnants. *JHEP* **03**:053, 2004. hep-ph/0402078.

[4] G. Aad, et al. Measurement of underlying event characteristics using charged particles in pp collisions at $\sqrt{s} = 900GeV$ and 7 TeV with the ATLAS detector. *Phys Rev* **D83**:112001, 2011. 1012.0791.

[5] J. W. Monk, et al. The HBOM Method for Unfolding Detector Effects. *Nucl Instrum Meth* **A701**:17–24, 2013. 1111.4896.

[6] T. Pierog, et al. Epos model and ultra high energy cosmic rays. *Nuclear Physics B - Proceedings Supplements* **196**:102 – 105, 2009.

[7] J. Bellm, et al. Herwig 7.0/Herwig++ 3.0 release note. *Eur Phys J* **C76**(4):196, 2016. 1512.01178.

[8] T. Sjostrand, et al. A Brief Introduction to PYTHIA 8.1. *Comput Phys Commun* **178**:852–867, 2008. 0710.3820.

[9] M. Aaboud, et al. Measurement of charged-particle distributions sensitive to the underlying event in $\sqrt{s} = 13$ TeV proton-proton collisions with the ATLAS detector at the LHC 2017. 1701.05390.

[10] B. Andersson, et al. Parton Fragmentation and String Dynamics. *Phys Rept* **97**:31–145, 1983.

[11] K. Y. Wong. New results on top-quark mass in ATLAS, 9th international Workshop on Top Quark Physics Olomouc 2016.

[12] B. Andersson, et al. A Probability Measure on Parton and String States. *Nucl Phys* **B264**:29, 1986. [,145(1985)].

[13] A. Buckley, et al. Rivet user manual. *Comput Phys Commun* **184**:2803–2819, 2013. 1003.0694.

[14] M. Cacciari, et al. The Anti-k(t) jet clustering algorithm. *JHEP* **04**:063, 2008. 0802.1189.

CLOSE-BY EFFECTS

Ota Zaplatilek*,

Faculty of Nuclear Sciences and Physical Engineering at Czech Technical University in Prage, Prage, Czech republic

* corresponding author: ota.zaplatilek@cern.ch

Abstract. A study of close-by effects was performed with multijet events using ATLAS experiment data collected in 2015 at a central mass energy $\sqrt{s} = 13$ TeV and Monte-Carlo event generator Pythia 8. Dependencies of different p_t responses of the closest jets were studied on various metrics with respect to the p_t scale of leading jet. The analysis is based on anti-k_t jets with different radii $R = 0.2/0.4/1.0$ and various types of reconstruction of jets. For example, reclustering procedure was used to obtain large jets ($R = 1.0$). Close-by effects were observed, discussed and also well described by Pythia 8 mostly at 5% level of disagreement.

Keywords: High energy physisc, ATLAS experiment, jet, close-by effects, reclustering, calibrations.

1. Introduction

Contemporary hadrons collider designed for the study of high energy physics produce numbers of highly collimated sprays of color-rich particles in the final states. These sprays, so-called jets, are frequently produced as a product of hard partons interactions from (hard scattering) at proton-proton collisions. Jets became necessary tools for a description and understanding of phenomena acquiring experimental particle physics within and beyond the Standard model.

With ambitions collect to more data effectively with increasing luminosity, also the rate of secondary processes grows. Initial state radiation, multipleparton interactions, underlying events and pile-up became more significant, therefore events, as well as the jets, are affected by them. For illustration, expected contamination from the pile-up at high-luminosity LHC reaches $10 - 20$ GeV per unit area in (y, ϕ) plane.[1]

Nowadays standard jet algorithms and techniques start to fail for sufficiently boosted decaying products of W boson, H boson or top quark. For instance, separation of quarks (as decay products of these boosted objects) becomes smaller than the common radius of jets [2]. Therefore, reconstruction of a single massive jet with large radii R (often called fat jets) represents a solution. Accordingly, it is substantial to develop effective substructure techniques and ways of finding, reconstructing and tagging of these large-R jets.

2. Motivation for close-by effects

Jets as a spray of significant collimated flow of energy could be constructed from various types of objects. Particles, tracks or calorimeter clusters could be used. However, real data have to be corrected back to so-called truth (particle) level.

Most of corrections were developed on well-separated objects to be found in dijets or γ + jet events. Nevertheless reconstruction of different processes (especially those used to search for new physic) possess very different topology for example decay of boosted scalar and vector bosons like $H \to b\bar{b}$, $Z \to b\bar{b}$ or $Z' \to t\bar{t}$. For instance $t\bar{t}$ events count 6 jets at least what could render this process potentially dangerous. Jets may be close enough to alter their properties. Jet properties could be affected by the change of jet shapes or by energy sharing among the closest jets effectively. These causes are the consequences of two phenomena, called energy-flow and color-flow.

Reason from the energy-flow is the energy sharing due to an overlap of jet areas. Since the anti-k_t clustering algorithm (the most often used safe algorithm for jet construction [3]) is used basically and it starts to add particles to the hardest one, hence the energy of the leading jet increases, while the energy of the closest jet decreases. So it is an anti-correlated effect with respect two the closest jets.

Further, in the case of the color-flow, it is assumed that with decreasing mutual distance between two jets also the probability from migration of color-charge particles between two jets increases. This effect is also called correlated out-of cone deposit of energy. Consequently, the particle composition of a jet is changed, which changes its shapes.

Studies of close-by effects have been performed previously in γ + jet and Z + jet events using the anti-k_t $R = 0.4$ jets at $\sqrt{s} = 8$ TeV [5].

This analysis uses collected data in 2015 at a central mass energy $\sqrt{s} = 8$ TeV during pp runs by $ATLAS$ experiment and Monte-Carlo Pythia 8 samples for comparison.

The analysis described in this text, which is based on the analysis [6] uses multijet events and data with higher statistics. Therefore, it is able to investigate a wider range of phase space. Compared with the analysis [5] anti-k_t $R = 0.4$ leading jets are used. The recoil system includes anti-k_t $R = 0.2$ (Small), anti-k_t

$R = 0.4$ (Standard) or anti-k_t $R = 1.0$ (Large) jets. Small and Standard jets were built from calorimeter's towers directly while Large jets in recoil system were obtained by re-clustering of anti-kt Small ($R = 0.2$) jets. Consequently, calibrations and uncertainties of Small jets are propagated, so no more calibrations and systematic uncertainties are needed for jets with larger R. In addition, Large jets are trimmed.

The main goal is to study the close-by effects for jets with different radius $R = 0.2/0.4/1.0$. In dependence on the size of close-by effects, we want to decide, whether an additional systematic uncertainty is necessary to be considered. Results could also verify, whether it is really safe to use $R = 0.2$ jets for reclustering to obtain larger R jets without any complications.

3. Pt-BALANCE AND CLOSEST VARIABLES

Multijet p_t-balance techniques for a study of close-by effects are based on transverse momentum conservation. These methods are applied on so-called back-to-back system. In concrete terms, this is about events, where the leading jet with the highest p_t is produced opposite to the multijets recoil system. Let us denote transverse momentum of leading jet as p_t^{ref} and transverse component of vector sum of all non-leading jet momenta in recoil system as p_t^{recoil}. Hence, variable p_t-balance denoted as p_t^{Bal} could be defined as follows:

$$p_t^{Bal} = \frac{p_t^{ref}}{p_t^{recoil}} \tag{1}$$

In a similar way variable response R could be defined eq. (2), where vector sum of all jet momenta in recoil system is replaced by only two members (leading jet in recoil system with momentum $\vec{p}^{\,L}$ and its the nearest jet with momentum $\vec{p}^{\,Cl}$):

$$R = \frac{(\vec{p}^{\,L} + \vec{p}^{\,Cl})_t}{p_t^{ref}} \tag{2}$$

Hence response R has to be less than unity by definition.

In order to determine the close-by effects, it is necessary to define suitable variable to describe closeness and isolation of jets. Most commonly used ΔR defined by eq. (3) could be used for two jets.

$$\Delta R = \sqrt{\Delta^2\eta + \Delta^2\phi} \tag{3}$$

Where $\Delta\eta$ represents difference in pseudorapidity and $\Delta\phi$ difference in azimuth angle of two considered jets. Variable ΔR will be always related with the leading jet in recoil system and its closest jet for the purpose of the interpretation in the following text.

Information about jet momenta could be also used for description of the closeness like in case of $f_{closeby}$ variable. This variable contains scalar products of jets momenta. Therefore, it has different behavior with respect to ΔR. Increasing $f_{closeby}$ means a decrease of ΔR and hence less separated, or in other words jets are closer. Basic $f_{closeby}$ variable is described by eq. (4), where the sum runs over all jets j with momenta $\vec{p}_j$ in the area ΔR around reference jet.

$$f_{closeby}(jet) = \sum_j \frac{\vec{p}_{jet} \cdot \vec{p}_j}{|\vec{p}_{jet}|^2} \tag{4}$$

Individual contribution of scalar products in $f_{closeby}$ variable corresponds to parallel radiation component of near jet's momenta to the reference jet.

Slight modification of variable $f_{closeby}$ can be done for a system of two jets only. New variables f_{cl1} and f_{cl2} related again to the leading jet in the recoil system and its nearest jets are introduced by eq. (5) using a factor corresponded to response R.

$$f_{cl1} = \frac{\vec{p}^{\,L} \cdot \vec{p}^{\,Cl}}{|\vec{p}^{\,L}|^2} \cdot R \qquad f_{cl2} = \frac{\vec{p}^{\,Cl} \cdot \vec{p}^{\,L}}{|\vec{p}^{\,Cl}|^2} \cdot R \tag{5}$$

These variables f_{cl1} and f_{cl2} contain only one positive contribution, whereas $f_{closeby}$ can include positive as well as negative members of scalar products. Since the normalization by factor $|\vec{p}^{\,L}|^2$ is always greater than $|\vec{p}^{\,Cl}|^2$, the range of f_{cl2} will be larger than the range of f_{cl1}.

The maximum value of f_{cl1} is expected to be 2. Since the most extreme case contains two jets in the recoil system being almost parallel to each other and exactly opposite to the reference jet. If all three momenta will take the same magnitude, then f_{cl1} tends to 2.

Modification by response R in eq. (5) is introduced as otherwise when plotting response R versus $f_{closeby}$ in a particular bin of transverse momenta of leading jet p_t^{ref} the response becomes strongly dependent on $f_{closeby}$ by construction.

4. CONCLUSIONS

The study of close-by effects in multijets events was performed for high-p_t scale of leading jet $200 - 1000$ GeV as well as for the low-p_t scale in range $40 - 200$ GeV. The dependency of even lower transverse momenta could not be used, because the trigger inefficiencies for the softest jets. Since the lowest p_t^{jet} corresponds to 25 GeV, however 100% plateau of trigger efficiency is only reached from 40 GeV.

As all considered distributions of close-by effects include internal ATLAS data, they could not be shown here. However, the results of close-by effect of multijet events can be described as follows.

The most suitable variables for description of close-by effects are f_{cl1} and f_{cl2}, which are most sensitive to these effects.

For high- p_t scale of leading jet ($200 - 1000$ GeV) rather small effects are observed. Spectra of response

R as a function of different variables are almost constant. From the studies dependency on p_t of the leading jet we conclude that the close-by effects are more significant with decreasing transverse momenta of leading jet. This observation was confirmed by low p_t scale analysis in p_t range of leading jet $40 - 200$ GeV.

From the study of different size jets ($R = 0.2/0.4/1.0$) in recoil system, it is seen that the close-by effects are most pronounced for $R = 0.2$ (Small) jets. Verify of safety application small $R = 0.2$ calibrated jets as an input to reclustering procedure to reach large just calibrated jets is still subjets for research. Monte-Carlo predictions with Pythia 8 agree very well ATLAS data within 5% of discrepancy. But it is still a question, whether it is good not to consider this difference as another source of systematic uncertainty for close-by jets.

References

[1] M. Cacciari and G. P. Salam, *"Pileup subtraction using jet areas"*, arXiv:0707.1378 [hep-ph]

[2] ATLAS Collaboration, *"Performance of jet substructure techniques for large-R jets in proton-proton collisions at $\sqrt{s} = 7$ TeV using the ATLAS detector"*, arXiv:1306.4945v [hep-ex]

[3] M. Cacciari, G. P. Salam, *"The anti-k t jet clustering algorithm"*, arXiv:0802.1189v2 [hep-ph]

[4] ATLAS Collaboration, *"Jet Re-clustering in ATLAS"*, tech. rep. ATL-COM-PHYS-2014-1117, CERN, 2014

[5] B. Cooper, P. Starovoitov and F. Vives, *"Studies of Jet Energy Scale Uncertainties due to Close-By Effects in $\sqrt{s} = 8$ TeV Data"*, tech. rep. ATL-COM-PHYS-2013-983, CERN, 2013

[6] J. Hejbal, R. Lysak, *"Close-by jets studies in multijet events"*, tech. rep. ATL-COM-PHYS-2017-067, CERN, 2017

JETS IN PP COLLISIONS AT THE ATLAS DETECTOR

Vladimir Zitka*

FNSPE CTU in Prague, Brehova 7, Prague, Czech Republic

* corresponding author: zitkavla@fjfi.cvut.cz

Abstract. In this article a brief overview of the process of jet production will be put forth. After that basic jet algorithms and MC simulation tools will be touched upon. And an example of dijet analysis and its implementation for the 2012 data from the ATLAS detector will be discussed.

Keywords: Jet, Herwig, ATLAS.

1. Particle jets

Common definition of a particle jet is that it is a shower of particles collimated into a rather narrow spatial angle produced during a collision event. The production of said particle showers takes place for example in a QCD hard scattering process. Jet itself is then the product of the hadronisation of partons scattered during the collision. These partons are characterised by high p_T and their colour charge. Due to the demands of QCD on colour charge confinement there is produced a number of quarks and gluons. This stage is called the parton jet. When asymptotic freedom of the quarks and gluons in the parton jet is no longer feasible, these quarks and gluons combine with each other into particles until the original colour charge is neutralised. And thus a particle jet is born. When one measures a jets in detectors such as the electromagnetic and hadronic calorimeters the jet is then called a calorimeter jet.

2. Monte Carlo simulations

The distinction between the actual particle jets and the measured calorimeter jets is especially noteworthy in MC simulations, where the particle jets are called truth jets. Which is directly tied to the next topic of this article: the monte carlo simulation used. One of the goals of author's bachelor's thesis is to become more knowledgeable of the underlying concepts of MC simulations. The training undergone as of now has encompassed basic usage and understanding of the Herwig 7 program and analysis tools.

Herwig is a C++ based simulation program and it's use is fairly simple. User only needs to create an input file which contains the steering parameters for the generator. There is a number of standardised .in files that come along with the instalation and these contain some standardised parameters such as LHC collisions parameters, so that working from scratch is not required. A little background into the workings of Herwig simulation is now in order.

Herwig 7 needs matrix element of parton collision in order to simulate the hadronisation and other processes undergoing in a event. On its own, Herwig is capable of calculating these matrix elements in leading order. If there is the need to use next to leading order Herwig calls the POWHEG which is a MC generator capable of computing parton collisions up to the next to leading order in perturbative QCD and thus producing desired matrix elements and the partons. Herwig is then capable of simulating the hadronisation from initial and final state shower. Other functions can be enabled in herwig.

For example the computation of multiparton scattering. The process when there is more than one simple collision of partons, but at least one of the partons can interact with the remnants or products of the colliding particles and thus seemingly produce more particles in a jet than one would have naively expected . Studying of this fenomenon can reveal great many things about the underlying event structure.

After all the physics desired processes are computed and accounted for, the jet algorithms are used. The most commonly used algorithms can be found in the FastJets library. And thus the aforementioned truth jets are acquired. That means the particle jets without any detector effects. Thereafter, through the conversion matrix, the same data structure and effects imposed on jets by the detectors can be acquired. The inverse matrix of this conversion is named the unfolding matrix. Its study is of grave importance for those seeking compare actual measured data with MC simulations.

Herwig is also capable of fashioning a visualisation of simulated event. This is useful as an instinctive visual guide to how the interactions occurred and to gain an understanding of the vastness of the number of particles produced in a single collision. In this visualisation one can trace a single particle in the end shower to the original parton that it originated from. Each particle has its own identification number and those of them carrying colour charge are colour-coded according to that.

3. Analysis of 2012 ATLAS data

The third section of this article is dedicated to the description and results of the dijet analysis of MC and

data collected by the ATLAS experiment in the Run 1, Periods A,B,C,D,E,G,H,I,J,L. The measured data used in acquiring the results below were LCTopo calibrated, that means they were locally hadron calibrated and would need an additional recalibration during the final parts of the analysis. The other type of data is the TopoEM globally calibrated ones with calibration from the electromagnetic calorimeter, those are calibrated as well during the final stages of analysis but with different parameters than the LCTopo data. The jet algorithm used for reconstruction was the Anti-k_T from FastJets library with $R = 0.4$. The main p_T cut was set to 25 GeV. The most important rapidity cuts were at 2.4, where the inner detector ends and 4.8 where the calorimeters end. The aim of this analysis is to be applicable on both MC simulated results as well as on the measured data. For MC simulated data there are 19 systematics that are implemented within. These are:

- BCH systematic, that computes the relative error caused by malfunctioning detector segments.
- Pileup systematic, that computes the error caused by the background effects.
- Jet Energy Resolution systematic computes the uncertainty of the detector resolution that is in turn impacting the determination of the energy deposited in calorimeter.
- Punchthrough systematic.
- Closeby jets systematic.
- Jet Energy Scale systematics, 14 independent systematics accounting for detector imperfections on different energy scales.

Alas all of these systematics remain yet to be tested on larger samples of MC data.

The analysis is better tested and functional when it comes to measured data. There are a few corrections implemented to better dispose of bad events and obvious errors[1]. These are:

- Pileup cleaning: The background effect of including tracks into a jet although they don't belong to it, because they are not associated with the vertex where the jet has originated from. Pileup is significant mainly up to 50 GeV. The deciding value used for determination of wheter to kill or leave the jet is the Jet Vertex Fraction[2]:

$$JVF = \frac{\sum p_T(associatedtracks)}{\sum p_T(alltracksinjet)} \quad (1)$$

  If $JVF < 0.5$ then the jet will be killed. Of course most Pileup could be corrected by simply imposing a certain p_T threshold on events, however one must do so cautiously as not to overkill it.
- Hot Tile cleaning: Because the Tile calorimeter was during certain periods malfunctioning in some areas, there is need for killing all events with jets that hit those areas.
- BCH cleaning: Additional correction to the Hot Tile cleaning and other detector effects. At the time this is still under construction and not fully functioning.

Once the data is cleansed of impurities and defects construction of useful histograms can begin. For example there is a histogram that shows how many events have had certain number of jets with rapidity $y < 4.8$ and $p_T > 25$ GeV, see Figure 1. As expected, a declining tendency can be seen, because the more the jets in an event the less likely it is that such an event even occurs.

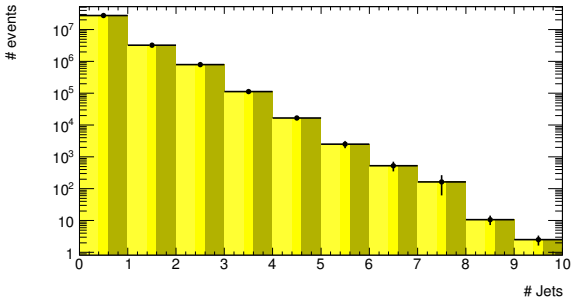

Figure 1: Number of events with certain number of jets.

Another interesting plot can be the histogram of dijet topology, using $\frac{1}{2}|y_1+y_2|$ and $\frac{1}{2}|y_1-y_2|$, where $y_{1,2}$ are the rapidities of jets. In Figure 2 can be seen the topology of events with dijets with rapidity $y < 4.8$ and $p_T > 25$ GeV. It is clear that the majority of dijet events are within back-to-back category and only a small part falls to the space where a slight deviation from momentum conversation is hinted. This beckons that in those events it is needed to inquire as to the cause of this deviation.

Yet another value can shed some light onto the dijet event topology and that is the dijet momentum imbalance $D_n = \frac{p_T^{(pair)}}{p_T^{(1)}+p_T^{(2)}}$ For example if $D_n \to 0$ both jets have approximately equal p_T and are back-to-back. In the Figure 3 can be seen the D_n spectra for $p_T > 25$ GeV. A peak is visible between 0.1 and 0.2 which is consistent with the most dijets being back to back. The rest of the events is clearly some more complex mechanism.

The analysis is of course capable of producing another results than just topological information. In Figure 4 can be found the spectra of leading jet p_t.

The last histogram that is shown in Figure 5 is the dijet mass spectra histogram. We can see that there are big errorbars towards the end of the spectrum and therefore more measurements is needed to amend that.

4. Conclusions

A brief introduction into the Herwig 7 simulation program has been put forth. Once more thorough

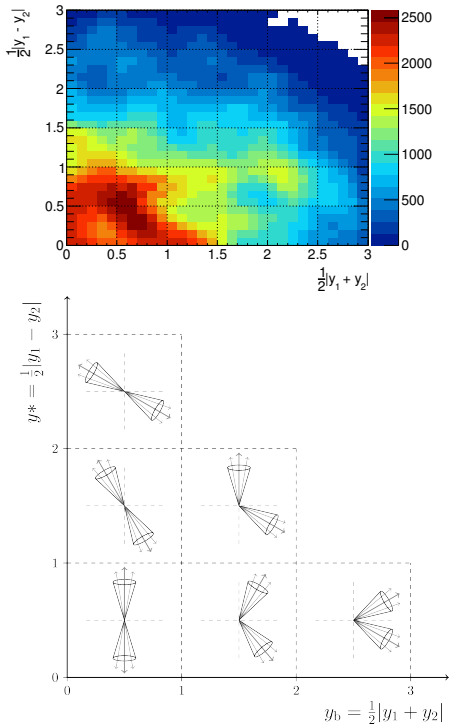

Figure 2: Dijet topology.

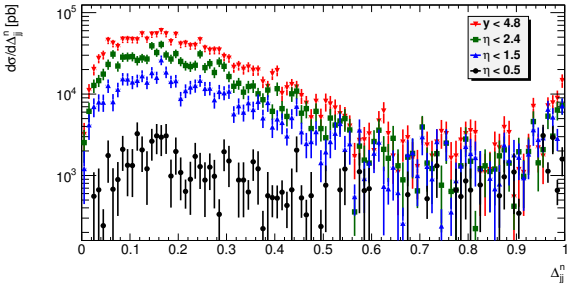

Figure 3: Dijet momentum imbalance spectrum.

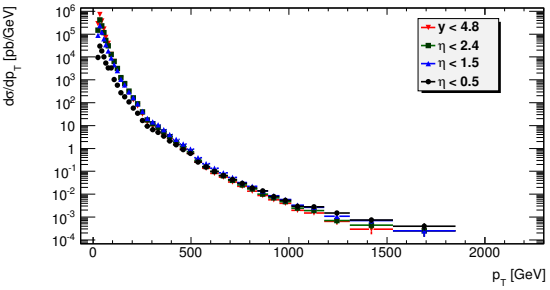

Figure 4: The p_T spectrum of leading jet.

understanding of the MC simulations is achieved and more data can be created that way, the process of testing the capabilities of the analysis on them can begin. At the moment the analysis can be used to acquire insight into the dijet topological attributes, and basic jet parameters such as mass, p_T and energy. As for MC the analysis is well underway to compute systematic errors for a number of different sources.

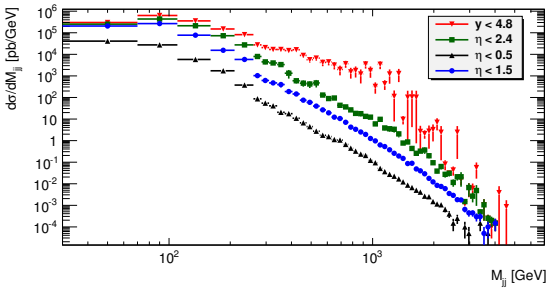

Figure 5: The dijet mass spectra.

References

[1] A. collaboration. How to clean jets 2012. `https://twiki.cern.ch/twiki/bin/viewauth/AtlasProtected/HowToCleanJets2012`.

[2] M. Myska. Double parton scattering contribution to the same-sign w boson pair production at atlas. `https://physics.fjfi.cvut.cz/publications/ejcf/DIS_Miroslav_Myska.pdf`.